Design optimization of double excitation synchronous machines in railway traction

Trung-Kien Hoang

université PARIS-SACLAY

école normale supérieure paris—saclay

NNT: 2016SACLN056

Thèse de doctorat

de

L'Université Paris-Saclay

préparée à

L'École Normale Supérieure de Cachan

Ecole Doctorale N°575

Electrical, optical, bio-physics and engineering

Spécialité de doctorat: Génie électrique

Par:

M. Trung - Kien HOANG

Design Optimization of a Double Excitation Synchronous Machine in Railway Traction

Thèse présentée et soutenue à l'ENS Cachan le 25 novembre 2016:

Composition du Jury:

M. G. BARAKAT	Professeur, GREAH, Université du Havre	Rapporteur
M. T. LUBIN	Maître de conférences, GREEN, Université de Lorraine	Rapporteur
M. M. TA	Professeur associé, Hanoi University of Science & Technology	Examinateur
M. M. BOUSSAK	Professeur, LSIS, Ecole Centrale de Marseille	Président
M. F. GILLON	Maître de conférences, L2EP, Ecole Centrale de Lille	Encadrant de thèse
M. L. VIDO	Maître de conférences, SATIE, Université de Cergy Pontoise	Encadrant de thèse
M. M. GABSI	Professeur, SATIE, ENS Cachan	Directeur de thèse

Design Optimization of a Double Excitation Synchronous Machine in Railway Traction

Trung - Kien HOANG

November 25, 2016

This page intentionally left blank

Acknowledgment

This work has been accomplished in the "Laboratoire des Systèmes et Applications des Technologies de l'Information et de l'Energie" (SATIE) at Ecole Normale Supérieur de Cachan.

First of all, I would like to express my deep thanks to my supervisor Prof. Mohamed GABSI and co-supervisors Dr. Lionel VIDO and Dr. Frédéric GILLON for their guidance and strong encouragements during a long period of time. Their kind patience and acceptances really helped me out of disappointments and gave me confidence to go on.

I sincerely appreciate efforts of Prof. Georges BARAKAT and Dr. Thierry LUBIN in spending theirs precious time reading and evaluating my thesis as well as valuable remarks to improve my work. I would like also to thank Prof. Mohamed BOUSSAK and Assoc. Prof. Cao Minh TA for being parts of the jury.

This work would not have been completed without contributions from my friends and colleagues: Benjamin GAUSSENS, Baptiste CHAREYRON, Emna BEN SEDRINE, Xuan-Linh DANG, Noemi LANCIOTTI, Noureddine FALTAKH, André NASR, Salim ASFIRANE, Hiba BOUKER, Emanuel HOANG, Olivier de la BARRIERE, Sami HLIOUI, Michel LECRIVAIN, Maxime PLOYARD and many others. I actually learned quite a lot through discussions with them.

I would like also to thank administrative staffs (Madam Sophie ABRIET, Madam Béatrice BACQUET, Madam Aurore GRACIA, Mr. Dominique BACH ...) for their kind supports.

My work would have never been done without financial support from Vietnamese government under the 911 program.

Last but not least, my great honor to dedicate this work to my wife (Un In) and my son (Him TC) for always being with me, trusting me, and bringing me hopes.

This page intentionally left blank

Contents

List of Figures

List of Tables

This page intentionally left blank

RESUME

Les véhicules électriques en général et le transport ferroviaire électrique sont largement reconnus comme des modes de transports à haute efficacité énergétique, particulièrement dans un contexte où la réduction de l'utilisation d'énergies fossiles (dont les réserves s'épuisent) et de la pollution est devenue une priorité. Les solutions apportées à ces problématiques sont donc de plus en plus attractives aux yeux des chercheurs qui ont donc redoublé d'efforts pour imaginer et concevoir de nouvelles solutions plus efficaces.

La conception optimale d'un système de traction ferroviaire représente donc un enjeu majeur dont la spécificité réside dans trois aspects principaux :

- D'abord, ce système fait appel à de nombreuses disciplines (électriques, mécaniques, magnétiques, etc.) étroitement couplées entre elles. Les études récentes se sont surtout focalisées sur l'optimisation séparée des composants. L'inconvénient majeur de cette approche est que la combinaison des meilleurs composants ne permet pas d'aboutir à un meilleur système.

- Ensuite, le système de traction ferroviaire fait appel à des sous-systèmes fortement non linéaires. Ces systèmes rendent particulièrement délicat le travail d'analyse des concepteurs et a pour inconvénient d'augmenter le temps de calcul.

- Enfin, contrairement à de nombreuses autres applications où les machines sont conçues pour fonctionner sur quelques points de quelques points de fonctionnement, les applications de traction sont caractérisées par un cycle de fonctionnement pouvant contenir plusieurs centaines de points de fonctionnement (combinaison couple-vitesse) distincts.

La conception optimale est nécessaires obtenir des structures capables de fonctionner à rendement élevé sur divers points de fonctionnement. Dans des études récentes, aucune recherche n'a été n'a pris en compte les trois aspects mentionnés plus haut.

Par exemple, les auteurs de [1] ont présenté une approche pour la conception optimale du moteur

de traction dans le système de propulsion ferroviaire dans laquelle l'aspect multidisciplinaire et le cycle de conduite sont pris en compte, mais les modèles magnétiques utilisés sont linéaires. Dans [2], il est présenté la conception et l'optimisation d'une machine à aimants permanents à commutation de flux pour des applications de véhicules électriques. Dans cette référence, le modèle thermique a été négligé et le modèle de pertes simplifié. Dans [3], une méthode de conception efficace appliquée aux véhicules électriques a été utilisée pour envisager avec rigueur un couplage entre des modèles électromagnétiques et thermiques non linéaires. Pour cela, une surface de réponse est programmée à partir de calcul de couple à l'aide d'un modèle éléments finis mais, une fois de plus, le modèle de perte de fer a été fortement simplifié.

A la recherche d'une meilleure solution en termes d'efficacité énergétique, ce travail est dédié à la traction ferroviaire. Nous examinons plus particulièrement une classe spéciale de machine synchrone appelée machine synchrone à double excitation (MSDE). Le terme Double Excitation indique que le flux inducteur de la machine est créé par deux sources : des bobinages et des aimants permanents. Ce type de machine combine avantages des machines synchrones à aimants permanents (puissance massique élevée et à haute efficacité) et des machines synchrones bobinées (souplesse de commande). Cette propriété est très intéressante dans le contexte des applications avec un cycle de fonctionnement telles que le transport ou la production d'électricité. En effet, en jouant sur le dosage aimants permanents – excitation bobinée, on peut déplacer les zones de meilleur rendement sur les points du cycle les plus sollicités et ainsi améliorer l'efficacité énergétique sur un cycle de fonctionnement.

De ce point de vue la thèse tente de répondre à la question suivante : en termes d'économie d'énergie et de coût, une MSDE st-elle capable de faire mieux que les machines conventionnelles sur un cycle de fonctionnement donné ? Nous analyserons également les circonstances qui favorisent la MSDE par rapport aux machines conventionnelles. Les principales contributions de ce travail de thèse sont ainsi déclinées :

- Considérer une optimisation de la conception d'une MSDE multi-physique, avec l'utilisation d'un modèle magnétique non linéaire générique sur un cahier des charges contenant un cycle de plusieurs points de fonctionnement.
- Répondre à la question : une MSDE peut-elle dominer les machines conventionnelles sur des objectifs de minimisation conjointe de pertes et de coûts ?
- Répondre à la question : généralement, dans quels cas, une MSDE est plus efficace qu'une machine conventionnelle.

A cette fin, la thèse se déroule comme suit :

Le chapitre 1 traite brièvement de l'histoire de la traction ferroviaire. Certains moteurs de traction sont présentés puis comparés dans ce chapitre. En outre, les travaux de recherches récents qui ont été faits sur la traction ferroviaire sont aussi examinés.

Il est mis en évidence que l'électrification du ferroviaire pourrait permettre de baisser les coûts, améliorer la puissance massique et surtout réduire la pollution sonore ainsi que les rejets polluants. Divers moteurs de traction sont disponibles : bien que les machines asynchrones soient les plus populaires dans le cadre de la traction ferroviaire, les moteurs synchrones à aimants permanents apparaissent comme des candidats très prometteurs. En particulier le coût des aimants, qui est un frein à l'expansion des machines synchrones dans le ferroviaire, est réduit si des aimants en ferrite sont utilisés à la place des aimants terres rares. Un autre inconvénient des machines synchrones à aimants permanents réside dans sa difficulté à assurer un fonctionnement adéquat dans la région de fonctionnement à haute vitesse à cause de sa capacité de défluxage limitée. Nous avons donc proposé d'utiliser une machine synchrone à double excitation afin de remédier à ce problème.

Le chapitre 2 est consacré à la présentation et à la description des machines synchrones à double excitation. Le principe fonctionnement et différentes topologies documentées dans la littérature ainsi que celles mises au point dans le laboratoire SATIE sont présentés. Les avantages en termes de contrôle de flux et de rendement sont soulignés. Enfin, un prototype de machine synchrone à double excitation développé au laboratoire est choisi puis étudié finement à l'aide d'une analyse éléments finis 3-D.

Les machines synchrones à double excitation ont un flux d'excitation produit par des aimants permanents et des bobines d'excitation. Ce mixage de sources d'excitation permet d'imaginer une grande variété de structures, qui peuvent être classifiées suivant différents axes. On en propose deux dans cette thèse : en fonction de l'agencement des sources (structures séries ou parallèles) ou en fonction de l'emplacement des sources (rotor, stator, ou mixte). L'agencement peut conduire à des machines dont la structure est en trois dimensions, avec donc des trajets de flux tridimensionnels. Il est aussi rappelé, que même si nous nous focalisons sur des machines tournantes à flux radial, le principe de la double excitation s'étend également à des machines à flux axial. Divers machines utilisant ce principe ont été développées dans le monde entier. Au laboratoire SATIE, certains types ont été fabriqués et testés. Parmi ces prototypes, nous avons retenu celui qui a le meilleur contrôle du flux d'excitation.

Une analyse détaillée de ce prototype est effectuée. Dans ce prototype, certains trajets de flux sont en trois dimensions conduisant à l'utilisation de la méthode des éléments finis 3-D afin de mener l'analyse la plus précise possible. Ces trajets de flux complexes compliquent l'analyse, mais offrent l'opportunité d'envisager plusieurs options afin améliorer les performances de la machine. En raison des temps de calcul nécessaires pour une évaluation à l'aide d'un outil de calcul éléments finis 3-D, une méthode alternative plus rapide a été requise en vue d'e mettre en œuvre un processus d'optimisation avec un grand nombre d'évaluations des modèles. Ce modèle rapide est au centre des chapitres suivants.

Le chapitre 3 se concentre sur la modélisation de la machine en utilisant la méthode généralisée des schémas réluctants dans le but de remplacer le modèle fin de calcul éléments finis 3-D.

L'objectif étant de diminuer le temps de calcul tout en conservant une bonne précision. Cette méthode de modélisation prend en effet compte la saturation magnétique. La validité de cette méthode est vérifiée par des comparaisons avec la méthode de calcul éléments finis. Une partie de ce chapitre est réservée à la discussion du calcul des pertes fer.

La Méthode généralisée des schémas réluctants a prouvé être une méthode rapide d'analyse des machines électriques basée sur son analogie avec un réseau électrique. En termes de temps de calcul, elle est beaucoup plus rapide que la méthode des calculs éléments finis (particulièrement en 3-D, comme c'est le cas ici). Par conséquent, la méthode généralisée des schémas réluctants est tout à fait adapté à la conception, particulièrement dans les phases préliminaires du dimensionnement. Pour le modèle étudié, une méthode nodale généralisée est mise en œuvre. L'idée principale de généralisation est que le nombre de noeuds et les éléments du réseau sont facilement paramétrables. L'élément de reluctance de base du réseau est un bloc de 4 réluctances qui suppose que le flux obtenu est bidimensionnel (x et y dans un système de coordonnées cartésiennes). La signification de "nodale" est que la formulation du système d'équations est basée sur la loi des nœuds de Kirchoffs (par opposition au réseau " maillé " basé sur l'utilisation de la loi des mailles). Le choix d'une base nodale système rend le réseau plus facile à étendre. Cette propriété est très efficace compte tenu de la structure 3-D du prototype puisque la modélisation de l'ensemble de la machine nécessite une connexion des éléments bidimensionnels pour former une modèle tridimensionnel. La saturation magnétique est considérée en résolvant itérativement le système d'équations non linéaires obtenues.

Du point de vue de l'objectif principal de la thèse, à savoir l'optimisation sur cycle de fonctionne, deux aspects les plus importants de le modèle électromagnétique sont le couple et les pertes moyennes sur cycles. En raison des trajets de flux tridimensionnels et des matériaux utilisés (massifs et feuilletés), les pertes fer sont particulièrement difficiles à estimer.

Les comparaisons avec les éléments finis 3-D confirment que les schémas réluctants permettent d'obtenir des résultats plus rapidement tout en conservant une très bonne précision. Afin de calculer plus précisément les pertes Joule, un modèle thermique est également nécessaire. Il permet également d'examiner les températures maximales des enroulements. Ce modèle thermique fait l'objet du chapitre 4.

Le chapitre 4 présente le modèle thermique de la machine. Ce modèle est également basé sur un schéma électrique équivalent à constante localisées. Par rapport aux machines classiques, la machine synchrone à double excitation comporte des enroulements d'excitation additionnels, c'est à dire des sources de chaleur supplémentaire de ces pertes Joule dissipées dans les bobinages d'excitation. En particulier, la difficulté rencontrée ici provient du fait que la résistance thermique entre les bobinages et le stator est élevée, rendant ainsi très problématique l'évacuation de ces pertes Joule supplémentaires. Le modèle thermique est généralement développé en régime transitoire. Le régime permanent est alors facilement déduit. Les pertes mécaniques, notamment les pertes par frottement et celles dans les roulements sont prises en compte afin affiner

l'analyse thermique.

Les aspects thermiques de la machine sont analysés grâce à un modèle similaire au modèle magnétique présenté au chapitre 3. Contrairement au modèle électromagnétique, le modèle thermique nécessite des paramètres (les coefficients thermiques) qui ne peuvent être déterminées que de manière empirique compte tenu de l'état actuel de nos connaissances. Ces coefficients thermiques varient en fonction de différents paramètres mécaniques et sont difficilement applicables sans vérification expérimentale préliminaire. De plus, la structure de machine synchrone à double excitation étudiée est plus complexe en raison des enroulements d'excitation additionnels. Par conséquent, des essais expérimentaux sont nécessaires pour déterminer de nouveau plusieurs coefficients thermiques.

En raison du fait que tous les enroulements sont placés au stator, c'est-à-dire que toutes les principales sources de chaleur sont situées au stator (les pertes rotoriques sont en effet négligeables), le nombre de coefficients thermiques à déterminer sont minimisés. Il convient de noter qu'il est trop difficile de vérifier tous les coefficients thermiques à moins démonter le prototype afin d'effectuer des essais séparés. Par conséquent, le processus de vérification expérimental permet de vérifier la bonne concordance entre les résultats théoriques et expérimentaux.

Le chapitre 5 a pour objet l'optimisation de la machine en tenant compte d'un cycle de conduite en utilisant les modèles multi-physique décrits dans les chapitres précédents. Le processus d'optimisation lancé envisage un cycle de conduite spécifique avec deux objectifs : minimiser les pertes totales et le coût sur le cycle de conduite. Afin de rendre l'optimisation réalisable dans un temps raisonnable, plusieurs hypothèses importantes sont faites : d'abord, on propose un cycle de conduite avec une mise à l'échelle du couple. Deuxièmement, le modèle thermique est utilisé en régime permanent. Troisièmement, les courants d'induit sont supposées sinusoidaux. Malgré ces hypothèses simplificatrices, il reste matériellement impossible de réaliser l'optimisation sur un cycle d'un millier de points. Nous proposons donc de déterminer un ensemble de points représentatifs s'appuyant sur l'énergie des points du cycle.

L'optimisation est traitée en utilisant une approche à deux niveaux et un algorithme basé sur les essaims particulaires. Dans cette stratégie, l'objectif de l'optimisation interne est de trouver les contrôles optimaux pour chaque machine et celui de l'optimisation externe est de rechercher les machines à la géométrie optimale. Visant à réduire le calcul temps, un examen attentif est pris sur l'optimisation interne en utilisant une combinaison appropriée de particules et de générations nécessaires.

Afin de comparer la machine synchrone à double excitation avec une machine conventionnelle, une machine synchrone à aimants permanents est dérivée du modèle de la machine synchrone à double excitation en supprimant les parties spécifiques à la double excitation. Les analyses préliminaires des résultats tendent à montrer que pour les dimensions du prototype, la machine synchrone à aimants permanents semble plus performante que la machine synchrone à double excitation au point de fonctionnement nominal. La machine synchrone à double excitation a

besoin d'un volume plus important principalement à cause des trajets de flux de fuite créés dans cette machine. Cependant, dans les circonstances où la vitesse maximale est beaucoup plus élevée que la vitesse dite de base, la capacité de défluxage de la machine synchrone à double excitation permet d'obtenir des machines plus performantes que les machines à aimants permanents. Ainsi, la capacité de contrôle du flux d'excitation des machines synchrones à double excitation peut s'avérer cruciale dans certains cas et donc dans les applications correspondantes.

Dans l'optimisation, en utilisant la stratégie des points représentatifs, deux cas sont considérés : 3 points représentatifs et 6 points représentatifs (sur 679 points). Il est intéressant de noter que pour générer une optimisation d'un type de machine (machine synchrone à aimants permanent ou machine synchrone à double excitation), un ordinateur de 12 cœurs cadencés à 3,5 Ghz prend environ 6 jours pour finir une optimisation sur 3 points. Cela limite drastiquement le nombre de points maximum à choisir et explique pourquoi nous nous sommes limités à considérer les 2 cas présentés ci-dessus.

Les résultats montrent que pour le cycle initialement envisagé, les machines à aimants permanents optimales sont meilleures que les machines synchrones à double excitation optimales pour les deux objectifs envisagés. La raison principale de la supériorité des machines synchrones à aimants permanents pour le cycle envisagé réside dans le rapport entre la vitesse maximale et la vitesse de base (d'environ 1,7) qui n'est pas suffisamment élevée pour exploiter la capacité de défluxage de la machine synchrone à double excitation. En outre, l'influence du nombre de points (cas avec 6 points) sont est réduite. Afin de vérifier que le ratio entre la vitesse maximale et la vitesse de base est bien la raison principale de la supériorité des machines synchrones à aimants permanents, des optimisations supplémentaires ont été effectuées avec un ratio plus élevé (4 et 5). Le résultat révèle que l'augmentation de ce ratio permet à la machine synchrone à double excitation de présenter de meilleures performances que la machine synchrone à aimants permanents.

Afin de pousser cette étude, plus de cas devrait être étudié dans les travaux futurs : d'abord, l'influence de différentes stratégies dans le choix des points représentatif sur des conceptions optimales. Deuxièmement, l'intégration de stratégies de contrôle ainsi que l'analyse transitoire thermique pour tenir compte des opérations en temps réel sur le cycle de conduite. Troisièmement, l'analyse d'autres structures de machines synchrones à double excitation mérite d'être menée afin d'étendre le périmètre de comparaison.

Introduction

Electric vehicles in general and electrified railways in particular are widely recognized as energy efficient and environmentally friendly solutions, especially in the context of the exhausted fossil fuels and environmental pollution. Energy saving solutions are, therefore, attracting more and more research attention.

A big challenge for optimal designs of a railway traction system lies in three main aspects: firstly, it contains many disciplines (electrical, mechanical, magnetic, etc.) and theirs interactions. Recent studies merely optimized individual components. The major drawback of this approach is that the combination of best components does not surely form a best system. Secondly, nonlinear characteristics make design analyses complicated and time consuming. Lastly, unlike many other applications, where machines are designed to operate at few operating points, traction applications are characterized by a driving cycle, where hundreds of working points (torque-speed combinations) are presented. Optimal designs are required to work with high efficiencies at various points. In recent studies, no research has taken into account all three mentioned aspects. For instances, Kreuawan *et al.* [1] presented an optimal design approach of a traction motor in a railway propulsion system with considerations of a multidisciplinary design and driving cycle; however, a linear model was used. [2] presented a design optimization of a flux switching permanent magnet machine for electric vehicle applications. In that research, the thermal aspect was neglected, and the loss model was much simplified. In [3], an efficient design technique for an electric vehicle was used to actually consider a coupling between the nonlinear electromagnetic and thermal models. The torque output response surface was computed based on a couple of finite element calculations; however, the iron loss model was simplified.

In search of a better energy efficient solution, this work is dedicated to the railway traction with an application of a special class of synchronous machine called **D**ouble **E**xcitation **S**ynchronous **M**achine (DESM). The double excitation term indicates that the field flux of the machine is created by two sources: field windings and permanent magnets. This type of machine combines advantages of permanent magnet synchronous machines (high power density and high efficiency)

and wound field synchronous machines (flexible flux control). This property is very interesting in the context of applications with operating cycles such as the transportation or power generation since this machine type is able to minimize losses, hence the overall efficiency on the operating cycles is improved.

The highlight of the thesis is trying to answer two questions: first, in term of the energy saving approach, is a DESM able to perform better than conventional machines within a given train driving cycle? Second, in which circumstances DESMs are overwhelming? Contributions of the thesis work are briefed as follows:

- Design optimization of a DESM with: **muti-disciplines**, **magnetic non-linearity**, and multiple working points on the **driving cycle**.
- Answer the question: does a DESM machine gain advantages over conventional machines regarding minimizing losses and cost objectives?
- Answer the question: in which circumstance, a DESM performs better than conventional machines?

To this end, the thesis is organized as follows:

Chapter 1 covers briefly the railway traction history. Some common traction motors to date and their comparisons are made in this chapter. Also, researches that have been done on traction applications are briefed.

Chapter 2 is dedicated to the basics of DESMs. The fundamental working principle and different topologies documented in the literature, and ones has been developed in SATIE laboratory are introduced as well. Advantages in term of the flux control and efficiency of DESM machines are emphasized. Finally, a DESM prototype is decided as the analysis model in the thesis. The 3-D FEM analysis for this chosen prototype is conducted in detail.

Chapter 3 concentrates on the machine modeling using generalized Equivalent Magnetic Circuit Network (EMCN) method with the aim to replace the high fidelity model (obtained with FEM) by a cheap-to-evaluate one in term of computation time, while still maintaining a good accuracy. This alternative modeling method takes into account the magnetic nonlinearity. The validity of the EMCN method is verified by comparisons with ones performed by the 3-D FEM. A part of this chapter is reserved for the discussion of the iron loss calculation.

Chapter 4 presents the thermal analysis model by using a lumped parameter thermal network. In comparison with classical machines, a DESM has additional excitation windings, i.e. extra heat sources from these winding's copper losses. In particular, the machine faces a heat evacuation difficulty from its two global excitation windings due to the high thermal resistance between the windings and the stator outer core. The thermal model is generally developed in transient regimes, and the steady state mode can be easily deduced. Mechanical losses including windage and bearing friction losses are briefed for a more comprehensive losses consideration.

Chapter 5 targets optimizations of the machine considering a driving cycle using the multi-physics model. The objectives are to minimize both the material cost and total losses on the driving cycle. Results presented by pareto fronts are derived by using a bi-level optimization approach, in which the lower level is to find the optimal control for each machine and the upper level is to search for the optimal geometries. Taking into account a thousand of points on the driving cycle makes the optimization task impractical and even impossible, though fast models were used. Instead, a set of representative points is derived by using an energy center of gravity technique. Comparisons between the DESM and a classical permanent magnet synchronous machine are conducted. These comparisons are done with the given driving cycle and also with extended speed range to evaluation performance of DESM in different regimes. Finally, a general conclusion is given.

Chapter 3 and 4 deal with conventional modeling techniques yet more complex due to the 3-D magnetic flux and the thermal difficulty with additional excitation windings. Chapter 5 could be considered as an application of all done in its previous chapters to answer the questions of the thesis. The biggest challenge in the optimization is how to deal with the long computation time as a consequence of the nonlinearity and mutiple operating points considerations. Several techniques and assumptions must be made to keep the optimization process feasible.

This page intentionally left blank

Chapter 1

A Brief of Railway Traction

This chapter covers a brief historical perspective of the railway traction dating back from hundred years ago to the current modern railway's technologies.

The earliest record tramway for the mining began in Germany about 1550 [4] due to an advantage of less rolling resistance of wheels on rails compared to those on roads; therefore, heavier loads to be pulled for the same power. This principle applies to all kinds of railway traction. The first engine to replace horse power in locomotives was steam engine in the early 1800's. From its beginning, the steam traction expanded rapidly with larger, faster, and more powerful for the next century. However, the problem with steam engines regardless the fuel used, wood or coal for instances, is the smoke coupled with high a maintenance cost, frequent fueling, and large quantities of water.

Fig. 1.1: Steam locomotive

An alternative way of replacing steam locomotives was to use the diesel fuel. Diesel engines use compression rather than a spark to ignite the fuel were first invented by Rudolf Diesel. However, owing to technical difficulties, this type of traction was not considered until 1920s. Diesel engines have problems associated with the environment, pollution, maintenance, etc. However, because of having higher thermal efficiency (about 40% compared to less than 10% of steam engines [5]) , diesel engines have been widely used to phase out steam engines in railway traction and other

transport sectors, for example passenger cars, buses, trucks, trailers, locomotives, boats, and ships [6, 7].

1.1 Diesel electric traction

Due to the fact that diesel engines face a major problem of lacking a reliable mechanical transmission, its early adoption by railways was prevented. In a new traction system using diesel engines, the power is usually transmitted to the wheels through a form of electric transmission [8]. In this traction system, the diesel engine drives an electric generator conveying electric power to traction motors. A typical system using diesel electric is illustrated in Fig. 1.2 [9]. Depending on the type of traction motor (to be discussed later in this chapter) used, an inverter might be include in this diagram. Also, a battery storage system could be provided to enhance the operation reliability in case of failure happened to the diesel engine or generator.

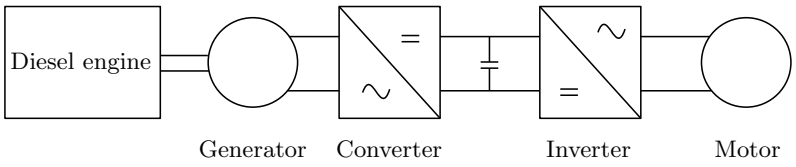

Fig. 1.2: Typical diesel electric traction system

This traction configuration has an obvious advantage of the dependence elimination on the power supply (using electrification system as an example), i.e. failure elimination and the removal of maintenance activities for the power system. In addition to this independence, no big capital investment required for building up a complex power supply system. This facilitates its usage all over the world, especially in developing countries. But the train power is subjected to the power handling capability of the on-board engine, which is limited due to factors such as the engine volume constraint, mechanical system, etc.

1.2 Railway electrification

On the contrary to the traction system using a diesel engine, electrification systems could overcome most of drawbacks that diesel electric counterparts have. Also, the power supply of the electric locomotive is not installed on the train making the overall system could be smaller, lighter, faster, and consequently cheaper. Moreover, it is possible to power several trains at the same time. An electrification diagram is depicted in Fig. 1.3 [10].

Locomotives equipped with regenerative brakes making use of energy sending back into the supply system and/or on-board resistors, which convert the excess energy into heat. Electrification ranges from low speed systems, such as tramways in the cities, to very high speed applications

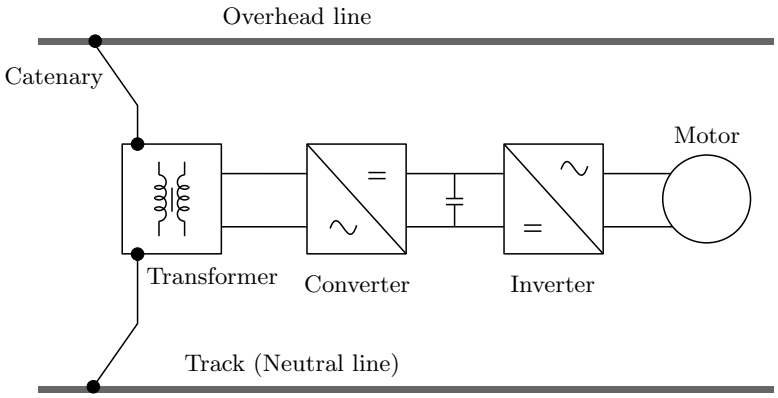

Fig. 1.3: Traction with electrification

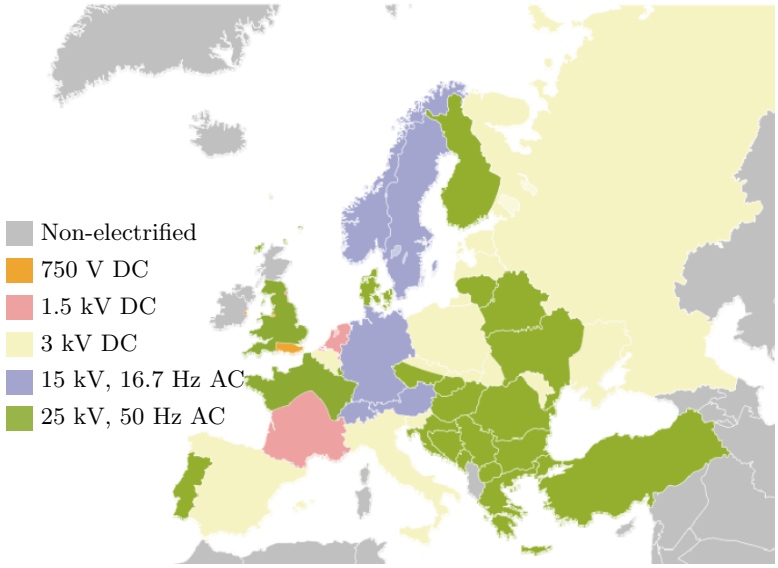

Fig. 1.4: Electrification system in Europe

such as TGVs (France) or Shinkansen (Japan). The electrification distribution map with various kinds and levels of voltage in Europe is shown in Fig. 1.4 [11]. The DC voltage system is simple but requiring thick cables and short distances between feeder stations. This is because of a high current required and also significant resistive losses. On the contrary, with the alternating current system, the voltage can be stepped down inside the locomotive. This permits a much higher voltage can be used along the line, which means much less energy losses along railways.

Main advantages of the electrification include:

- Low running cost of locomotives.
- Low maintenance cost of locomotives.
- High power-to-weight ratio, resulting in:
  - Small number of locomotives.

  - Fast acceleration.
  - High speed limit.
- Less noise and no air pollution from the train itself.

The main disadvantage is the high capital cost of the electrification system. Also, all trains could be brought to standstill due to the overhead-line failures. Therefore, a more reliable system must be assured. Another concern is the high system upgrading cost, especially where tunnels, bridges, and other obstructions have to be altered for the clearance purpose.

With electrification systems, locomotives could take energy by two options either via overhead lines (Fig. 1.3) or a third rail. A third rail is a method of providing the electric power to a railway train through one more rail running in parallel to the main rails. Using a third rail is cheap to install, more compact, and easy for maintenance. The third rail system has its own corridors, which are usually set underground so to avoid the visual pollution like the overhead wires. It is also fully or almost fully segregated from the outside environment to ensure a safety condition. In mos cases, a third rail system supplies the DC power [11].

1.3 Railway traction motors

According to the scope of the thesis, a traction motor is considered to be the most important component in the entire railway system. Various options can be opted among DC motors, induction motors (the most popular one in the industry), and synchronous motors as displayed in Fig. 1.5.

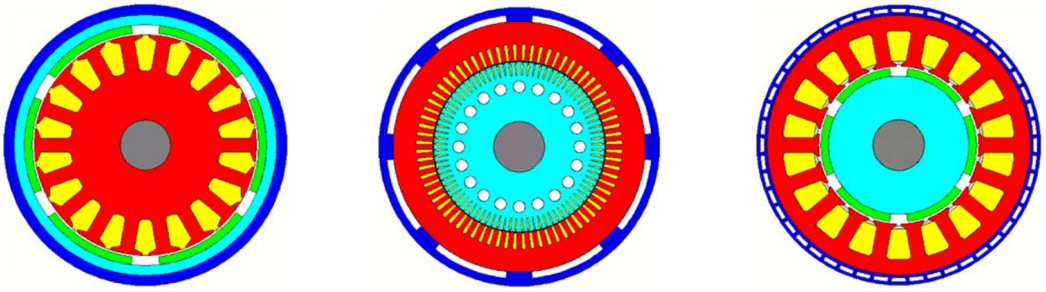

(a) (b) (c)

Fig. 1.5: Popular electric motors used in railway traction. a) DC motor. b) Induction motor. c) Synchronous motor

Briefly, at the early stage of development, DC motors, together with low-voltage DC traction lines, were the main traction power supply methods, due to the simplicity in term of the construction and controlling, i.e. torque characteristic. However, DC motor drives are bulky, inefficient, less reliable, and a high requirement for the maintenance mainly due to the presence of the mechanical commutator [12].

Subsequently, with the development of power electronics, AC motors have come into use providing a lot of advantages. Among them, the induction motor type is the most popular one in industrial applications with the most mature technology among all other AC competitors. A series of advantages of cage induction motors for traction application compared to the DC motors was documented in [13], such as a robust construction, much lower requirement for maintenance, low cost/power ratio, and steep torque-speed characteristic. However, a low power factor is still the disadvantage needed to be improved. Also, as mentioned in [12], the presence of a breakdown torque limits its extended constant-power operation. Moreover, the efficiency at a high speed range may suffer in addition to the fact that induction motor efficiencies are inherently lower than those of permanent magnet (PM) motors. This due to the absence of the rotor winding and rotor copper loss in the PM motors.

The synchronous motor can overcome this disadvantage with high power factor and high efficiency. Although synchronous motors are costly with rather complex structures because it requires additional excitation sources (PMs or excitation windings). However, the operating cost would be lower compared to that of induction motors due to its higher efficiency. Although, this type of motor with PM excitation inherently has a short constant-power region due to their rather limited field weakening capability [12].

A general comparison between DC, induction, and PM motors is summarized in Table. 1.1 based on six factors with a score out of 5 for each [14].

Table 1.1: General comparison between different motors

Feature	**DC**	**Induction**	**PM synchronous**
Power density	2.5	3.5	5
Efficiency	2.5	3.5	5
Controllability	5	5	4
Reliability	3	5	4
Technology maturity	5	5	4
Cost	3	5	4

1.3.1 Traction motor requirements

Motors utilized in the railway traction own some practical differences compared to other industrial machines. This is due to distinguishing requirements to be respected from locomotive's operation [15].

- The traction motors are built-in and carried along by their loads so that they must be physically robust.
- Space limitations for installation.

- Economic operation.
- Harsh environment: vibration, shock, temperature, and humidity
- Limitation on weight for axle/wheel loading.
- More importantly, motors have to satisfy the requirement of variable loading, which is characterized by the traction duty cycle.

The duty cycle consists of various operating modes even at a condition being greater than the rated torque or power, which is subject to the motor thermal constraints. A velocity-time curve of a station-to-station duty cycle with corresponding tractive effort and power requirements is shown in Fig. 1.6 [15].

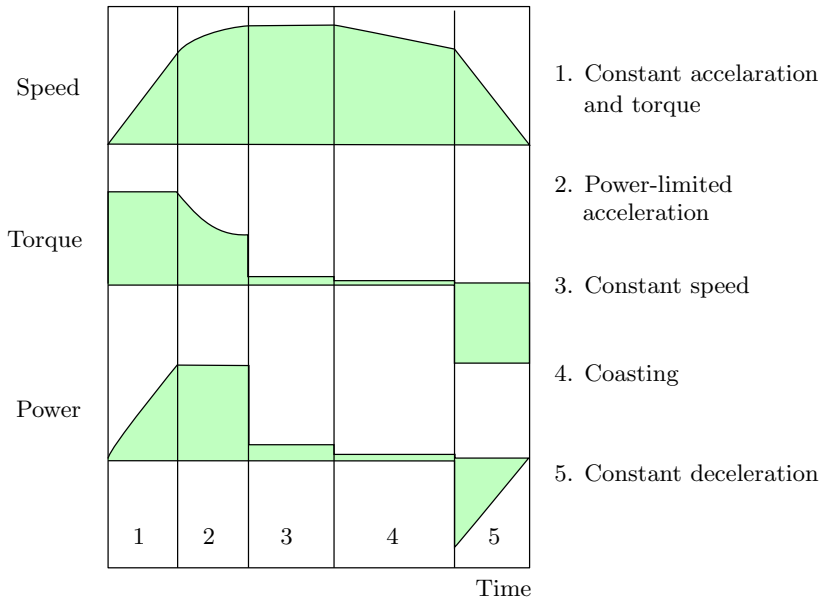

Fig. 1.6: Traction vehicle trajectory, tractive effort and power for station-to-station motion

This duty cycle makes requirements, for example, the nominal torque of the traction motor should be sufficient to achieve the specified acceleration on the maximum slope. DC separately excited, synchronous, and induction motors are all suitable for the traction application. Table. 1.2 compares different motors regarding the traction duty cycle.

1.3.2 Traction motors comparison

Performance guide regarding the traction duty cycle only is; however, insufficient for the motor evaluation. Some other factors below make differences between DC, AC induction, and AC synchronous traction motors:

- Current supply: Power to a DC motor is supplied through a commutator with a sliding contact, this reduces the volume available for the energy conversion, limits the speed, hence the power density, additional losses, and increases the maintenance cost.

Table 1.2: Comparison of machines by traction duty cycle

Regime	DC separately excited	AC induction	AC synchronous
Constant torque	Constant armature current (increase voltage with speed)	Constant flux (increase voltage with frequency)	Constant armature current (increase voltage with speed)
Constant power	Reduced field excitation with constant armature current	Constant voltage and current with increasing slip frequency	Reduce field excitation
Reduced power	Weak field operation with reduced armature current	Constant slip frequency and voltage	Same as constant power

- Efficiency: The induction motor is limited by low power factor and high slip at low speeds leading to a low efficiency.
- Thermal aspect: Both DC and wound field AC synchronous motors, temperature rise happens in both insulated windings in the stator and rotor; hence, more cooling is required. Meanwhile, the AC induction motor is capable to reach a higher temperature due to the uninsulated rotor whose temperature is limited by the bearing.
- Mounting: The mounting space for DC and would field AC synchronous motos are further limited by commutators or slip rings.

However, if permanent magnets are used for the field excitation, thermal problem due to rotor windings and mounting constraint related to the commutator/slip ring can be removed.

A comprehensive comparison between different types of traction motor is a tricky task when considering other factors such as the manufacturing cost and power electronic drive. Table. 1.3 [15] presents a comparison between DC, synchronous, and induction traction motors in term of the power and speed range.

Table 1.3: Power and speed range comparison of various traction motors

	DC	Synchronous	Induction
Maximum power [MW]	2.2	6.55	5.7
Speed range at 2.2 MW [rpm]	940 - 1435	670 - 2000	890 - 1810

This general comparison reveals advantages of the synchronous traction motor over the DC and induction counterparts. With field flux created by PMs instead of field windings, synchronous motors even further make an efficiency improvement and a more compact design. Although, a conventional PM synchronous motor would have a difficulty controlling the air-gap flux but this would be tackled by using additional field windings as will be discussed later on in this thesis.

Conclusion

This chapter has focused on a brief history of railway traction. Various types of traction motor are discussed with their advantages and disadvantages. Although the induction motor has a long development history; therefore, it is currently the most popular machine type in traction application. However, permanent magnet synchronous motors through years appear as a very promising candidate, especially in the context that the PM cost is being reduced. In the next chapter, a special type of permanent magnet machine will be introduced, which is expected to be an energy efficient solution for the railway traction.

Chapter 2

Double Excitation Synchronous Machines (DESMs)

In chapter 1, various traditional traction motors have been briefly discussed including DC, induction, and synchronous motors. In this chapter, a special machine type, which is expected to be a good candidate for traction applications, is addressed. This machine type, namely Double Excitation Synchronous Machine (DESM), belongs to the synchronous type with a special configuration. This chapter aims at reviewing the stage-of-art of DESMs. The basic working principle of the machine as well as different classifications will be presented. Potential advantages of DESMs in railway traction will be discussed, and a prototype will be finally chosen for further analyses in this thesis.

2.1 Basic working principle of a DESM

The wound field synchronous machine (WFSM) could be replaced by permanent magnet synchronous machines (PMSMs) in applications requiring a high power density and high efficiency. Especially in a context that permanent magnet price has become reasonable. However, the problem related to PMSMs is the fact that the flux created by PMs are almost constant. Therefore, it becomes disadvantageous to applications where the air-gap flux control is desirable. Meanwhile, this flux control is easy to tackled with WFSMs. An idea to give a PMSM a good capability of air-gap flux control or in other word, to combine both advantages of WFSMs and PMSMs has given a birth to DESMs. Therefore, a DESM basically proposes additional excitation windings in a PMSM [16–19]. As a result, two flux sources are presented in one machine: one from PMs, and the other from field windings. Although many variants would be realized, but the fundamental working principles are based on flux sources combination: series and parallel principles.

2.1.1 Series DESM principle

In a series configuration as shown in Fig. 2.1, the flux created by the field winding passes through the PM; hence, the series type. By changing the field current, the air-gap flux is

varied accordingly. The most important advantage of the series configuration is the simplicity and the global reduction of the flux density. In this specific example, the air-gap flux is being weakened owing to opposite trajectories of two flux sources. Considering a field winding of N turns carrying a DC current i, hence a magnetomotive force Ni, the air-gap flux is the linear sum of flux created by the field winding and the PM (ϕ_{PM}) (if saturation is neglected) as (2.1):

$$\phi = \frac{Ni}{R_a + R_{\text{PM}} + R_c} + \phi_{\text{PM}} \tag{2.1}$$

where R_a and R_{PM} are reluctance of the air-gap and PM, respectively. R_c is all other reluctances on the flux paths created by field winding.

Obviously, the flux by the field winding is much limited by the PM's reluctance, which is usually high and much higher than R_a and R_c. Therefore, controlling the air-gap flux by the series principle is not quite effective. Also, a risk of demagnetization is likely to occur since the flux from the field winding must pass through the PM. A case study for this series type is demonstrated in Fig. 2.2. With a PM of 15 mm thickness (in the magnetization direction), and the residual flux density $B_r = 0.4$ T. A field winding of 1500 AT. As seen, the air-gap flux is almost canceled out in this case.

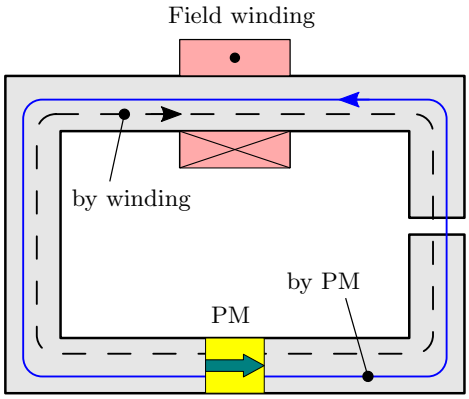

Fig. 2.1: Series combination of flux sources

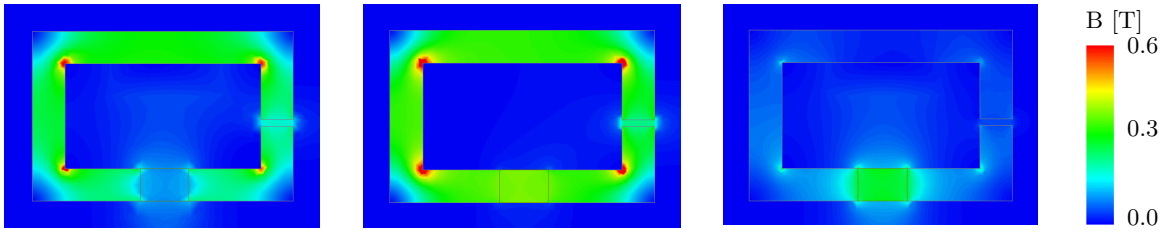

Fig. 2.2: Induction distribution for a series type. a) By field winding. b) By PM. c) Flux combination

2.1.2 Parallel DESM principle

With the parallel principle, the PM does not suffer the flux from the field winding; therefore, the demagnetization is avoided. This principle is demonstrated in Fig. 2.3, with the flux in the air-gap "A" being reinforced due to the same trajectories of two flux sources. For this parallel type, there is no PM reluctance R_{PM} in (2.1); therefore, the field winding become more effective in controlling the air-gap flux. The induction distributions for this case is demonstrated in Fig. 2.4. With a PM of 15 mm thickness, and the residual flux density $B_r = 0.4$ T. A field winding of 500 AT (only one third of one in the series case).

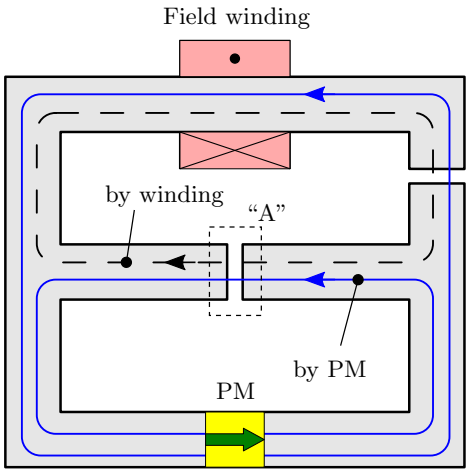

Fig. 2.3: Parallel combination of flux sources

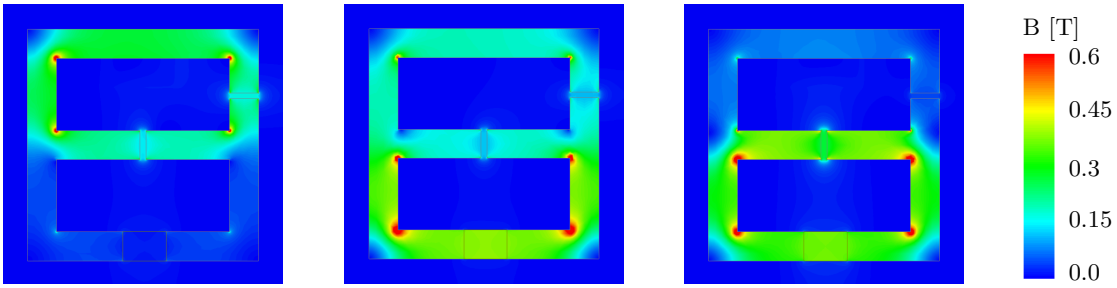

Fig. 2.4: Induction distribution for a parallel type. a) Due to field winding. b) Due to PM. c) Due to flux combination

This parallel principle can deal with disadvantages of the series type; i.e. the demagnetization and low efficiency of the air-gap flux control. Moreover, more configurations could be realized compared to the series one. This is explained by more possible flux trajectories from the field winding compared to the series case (the flux must pass though PM). As a result, this results in more complex structures compared to series counterparts.

Another principle, which is worth mentioning, is juxtaposed circuits displayed in Fig. 2.5, [20]. This type of structure can be considered as the parallel type comprising two rotors placed

together. The stator consists of two longitudinal regions, which are magnetically separated from each other by a stator gap having one or more cooling air passages.

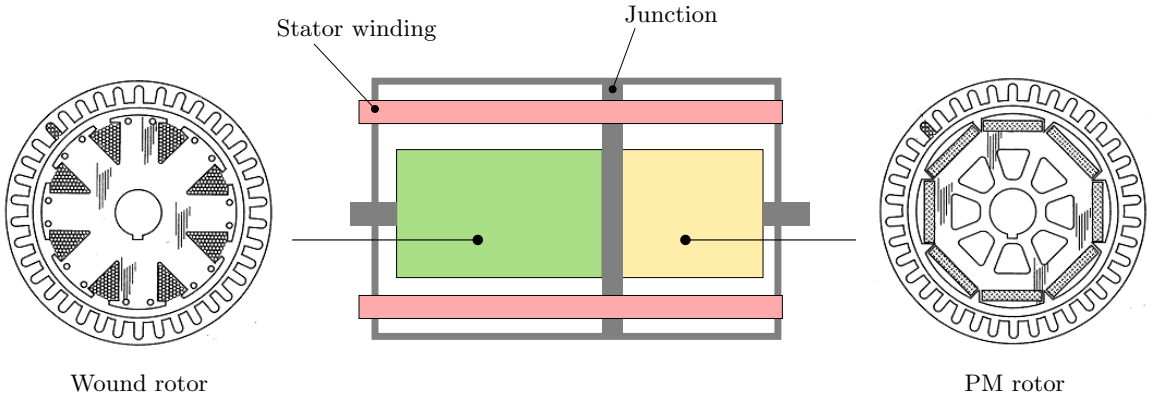

Fig. 2.5: DESM principle with dual rotor

In the rotor combination, one rotor is the wound type, and the other is the PM type. In fact, the flux control is not implemented by reducing the air-gap flux in the PM rotor part. The overall flux is reduced by creating a flux on the wound rotor, which is opposite to that of the PM rotor. The flux control is, therefore, global. One important point discussed in [21] is the axial length of the wound rotor is longer than that of the PM one; this is due to the fact that the flux created by PMs is normally bigger compared to that created by a winding with the same axial length. Therefore, in order to reduce the global air-gap flux, two available options are: using less current with more axial length or more current with shorter length. The first approach results in a lower copper loss compared to the second one.

2.2 Literature review of DESM topologies

The double excitation principle allows a wide variety of structure to be realized. The classification of this machine type could be based on:

- 2-D and 3-D types: This is based on the flux paths are limited to only a 2-D plane (the plane perpendicular to the machine's axis) or extended in the axial direction.
- Series and parallel types (as discussed in 2.1)
- Radial and axial types: Based on air-gap flux is flowing in the radial or axial directions.
- Locations of field winding and PMs: Both sources could be located either in the stator or rotor, or one is placed on the rotor and the other is on the rotor. Placing both field windings and PMs on the stator which is a fixed part would present some advantages from manufacturing and operating points of view, for example avoiding sliding contact, it is also far easier to evacuate losses from fixed parts in comparison with moving ones. Although having both flux sources in the stator together with the armature windings would take

up a lot of space and active stator core is reduced consequently. As a result, saturation is likely to occur.

- Global and non-global excitation windings: with the global type, windings are normally in toroidal shapes wrapping around the periphery of the machine. The air-gap flux is adjusted globally, normally one or two windings are enough. With non-global type, many excitation windings are usually concentrated around teeth, each winding acts locally on air-gap flux in its region.

These classifications are not independent i.e. a 2-D type could be series or parallel, etc. More details with some specific structures will be addressed in the following.

2.2.1 General review

In [22], authors presented a structure with consequent-pole for a 3 kW generator. As shown in Fig. 2.6. This topology belongs to the 3-D parallel type due to the presence of flux in axial direction. This 3-D flux distribution introduces extra losses and increases material and manufacturing requirements [22]. The field winding is set on the stator while PMs are on the rotor.

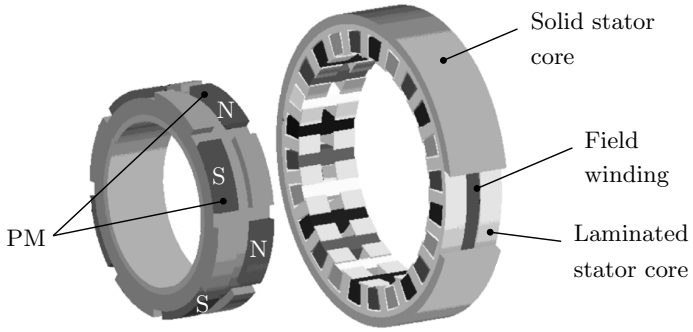

Fig. 2.6: Consequent pole PM machine

In this topology, field flux flows from one iron pole to the next pole through the stator and rotor yoke. Magnetizing and demagnetizing effects are shown in Fig. 2.7. The advantage of this topology is a simple DC current control with no brushes or slip rings required.

Radomski [23] introduced a claw-pole DESM for an alternating current generator. The rotor is shown in Fig. 2.8a) and its circuit principle is shown in Fig. 2.8b). In this topology, the field coil is placed on the rotor connected to slip rings. PMs are also put on rotor and each PM is interposed between and in contact with side surfaces of adjacent poles. When the field coil is not excited, PMs are short-circuited by the rotor and flux developed by PMs does not link the armature windings. When the field coil is energized with an uni-directional current, the magneto-motive force of the field coil opposes the one of PM and thereby causes PM flux to cross the air-gap and link the armature windings.

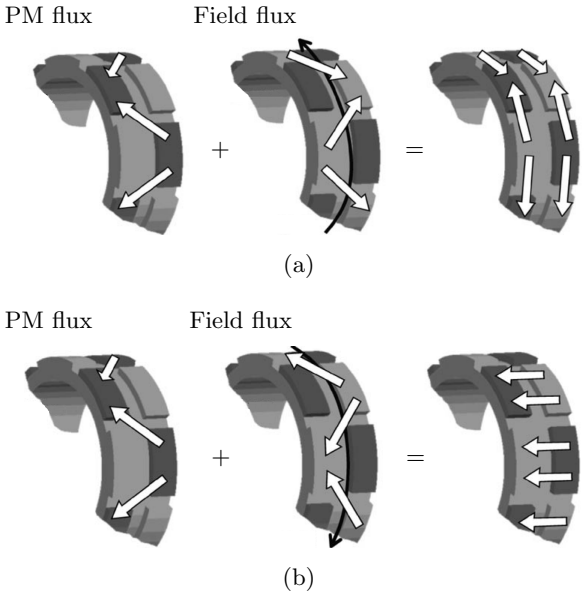

Fig. 2.7: Operations of the consequent pole PM machine. a) Magnetizing effect of field flux. b) Demagnetizing effect of field flux

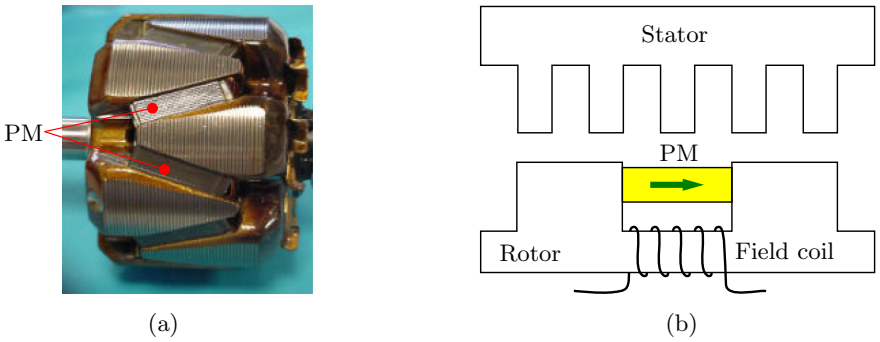

Fig. 2.8: Claw-pole DESM topology. a) Claw-pole rotor. b) Circuit scheme of the machine

One special variant of DESM topology with variable number of pole pairs was presented in [24] with the topology principle is displayed in Fig. 2.9. When the excitation windings are not energized, the number of machine's pole pairs is due to permanent magnets which is 3 and the flux linked to stator windings is minimum. However, when being supplied with currents, these excitation windings will create additional pole pairs to be double i.e. 6 pole pairs.

This machine configuration belongs to the parallel type since flux generated by field windings does not pass through PMs. Also the flux control is global due to the fact that the main flux paths from two sources (PMs and field windings) does not affect each other locally. With this type of DESM, field windings must be placed on the rotor causing a problem with sliding contacts. Another topology with similar working principles are presented in [25].

An application of DESM with axial-gap prototype was discussed in [26] is also presented in Fig. 2.10. This axial flux machine comprises two stators and one rotor which has permanent magnets and pole portions. Without the frame, PM flux closes its path through air-gap, teeth,

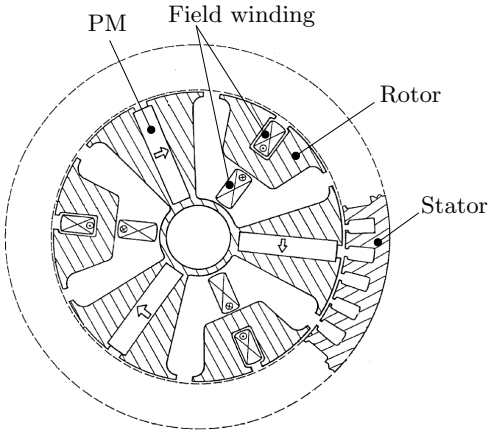

Fig. 2.9: DESM with variable number of pole pairs

yokes and rotor poles. A field coil is not placed neither on stator nor rotor but mounted to the housing and located very close to the rotor. The frame acts as a magnetic path to conduct field coil flux. When the field coil has no current supplied, the PM flux closes its path through the frame. To prevent flux going through the frame, the control current in the field coil produces a countering magneto-motive forces compared to ones from PMs. In the weakening mode, field coild generate flux aiming to reduce flux going through rotor pole.

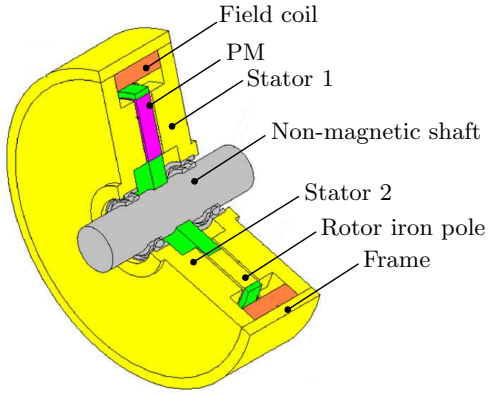

Fig. 2.10: Double excitation principle with axial flux machine

Working based on the idea similar to one using dual rotors presented in Fig. 2.5, authors of [27] proposed a parallel DESM with combination of a variable reluctance machine and a PMSM. The two sections or the machine is seen in Fig. 2.11.

In this prototype, the field windings are naturally wound on the stator of the electrical excitation section. In order to combine two different sections; theoretically, the number of teeth and slots is equal for both sections. Moreover, the numbers of rotor poles in two sections are the same [27]. The core length ratio between two sections should be taken into a careful consideration at least at a point that the stack length of the section with field winding should be large for a efficient field regulation. In contrast, the stack length of PM section is desirable as large as possible to improve the power density.

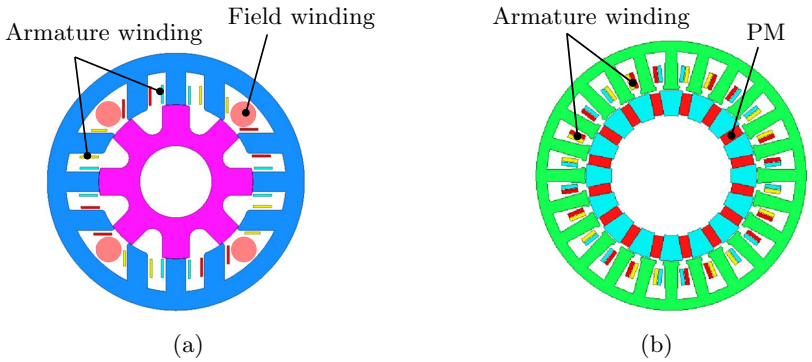

Fig. 2.11: Dual rotor combination in a parallel DESM. a) Electrical excitation section. b) PM section

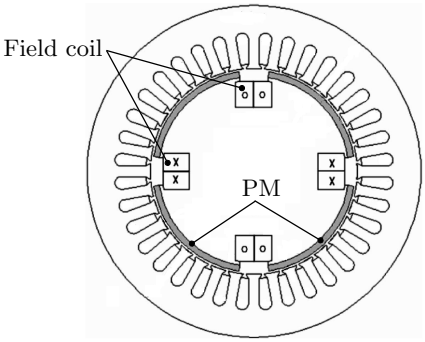

Fig. 2.12: DESM with surface PM type

Another structure also could be explored as in [28] with surface PM type i.e. less efficiency of field windings because of a large equivalent air-gap. The topology principle is demonstrated in Fig. 2.12.

2.2.2 DESMs developed in SATIE laboratory

The rest of this part will be dedicated to some topologies have been developed in SATIE laboratory. Double excitation principle was applied to a flux switching machine introduced in [29] as llustrated in Fig. 2.13.

Both excitation sources are located in the stator and the salient rotor is simply made of stacked soft iron sheets. The operation principle is briefly explained as in Fig. 2.14. This prototype is proposed to be employed to make a high speed motor, or motor for difficult thermal environment [29].

Another topology developed in SATIE which is composed of two magnetically isolated parts was presented in [21]. The split view of the structure is seen in Fig. 2.15.

The stator consists of two identical parts linked together, the rotor consists of two parts: one comprises ferrite magnets (with flux concentration principle) and two teeth and the other being

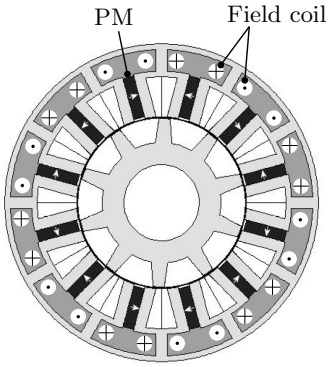

Fig. 2.13: DESM with flux switching permanent magnet machine

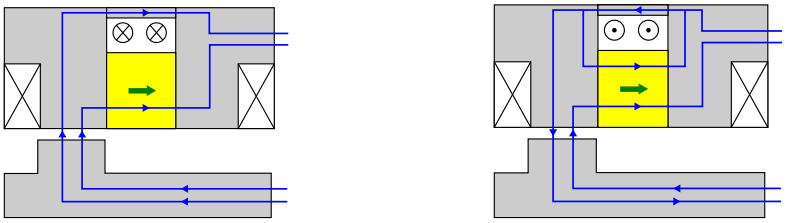

Fig. 2.14: Working principle of hybrid flux switching permanent magnet machine. a) Enhanced field. b) Weakened field

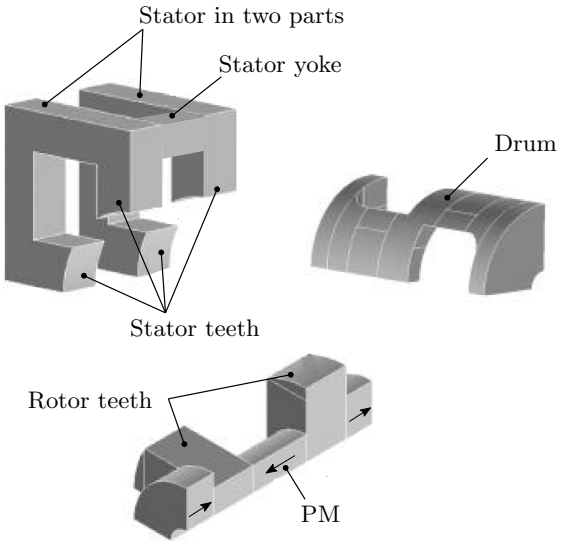

Fig. 2.15: Imbricated DESM principle

the drum. The working principle is illustrated in Fig. 2.16 and Fig. 2.17. More detailed explanation is referred to [21].

According to [21], this topology not only avoids the risk of demagnetization due to the excitation winding but also the risk of demagnetization due to the armature reaction since the flux of armature reaction does not go through the magnet zone. Based on the implicated principle, a

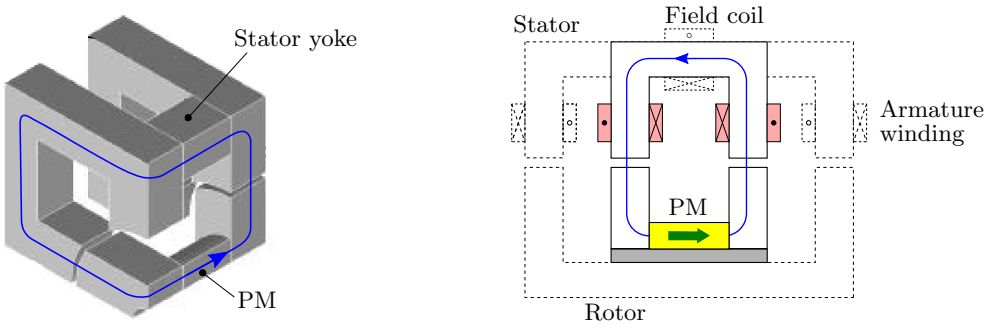

Fig. 2.16: Flux lines principle in the first rotor part by PM

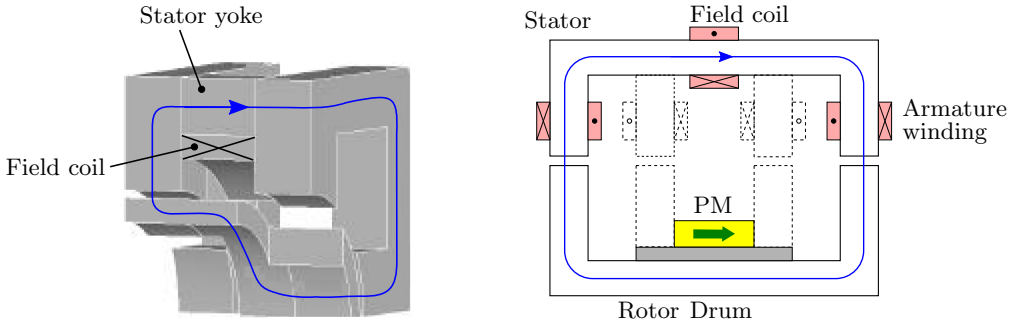

Fig. 2.17: Flux lines principle in the second rotor part by field winding

machine was sized firstly to serve as a car generator as seen in the Fig. 2.18. Authors of [21] suggested the best method of flux weakening is a combination of armature current control and hybrid excitation.

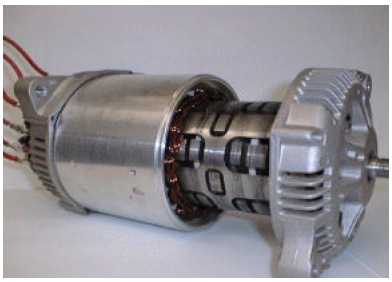

Fig. 2.18: Machine assembly based on imbricated principle

In a research to study the suitability of DESM for vehicle traction applications, authors of [16] worked on a bipolar configuration as in Fig. 2.19 to confirm the advantage of energy efficiency of the double excitation principle. Flux trajectories of the machine are somewhat complex and some are truly 3-D with the homopolar flux paths by PMs displayed in Fig. 2.20.

In this prototype, the blue parts are made of laminated iron sheet and the yellow ones are solid to conduct 3-D flux. Due to the 3-D flux path characteristic, considerations for materials and iron losses should be considered. Another similar variants of this topology were also presented in [30, 31] with modifications.

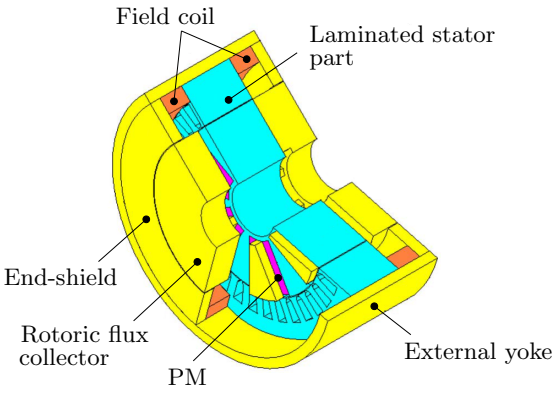

Fig. 2.19: A bipolar DESM topology

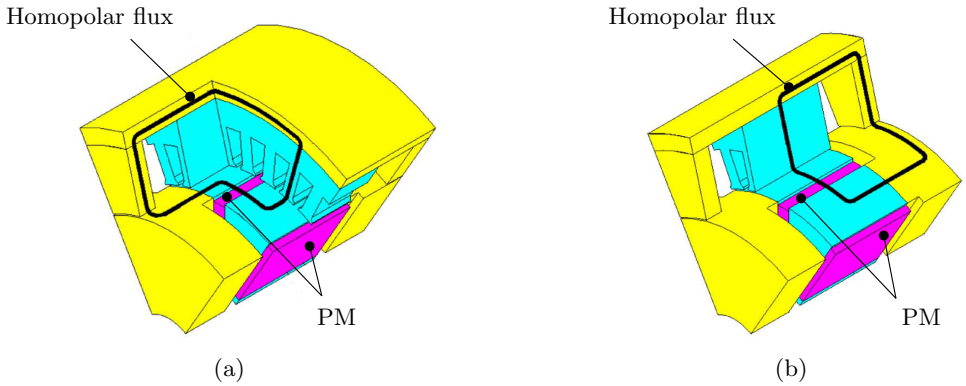

Fig. 2.20: PM flux trajectories. a) First homopolar flux. b) Second homopolar flux

2.3 Efficiency advantage of DESMs

The main advantage of the DESM appears especially in those applications where the electric drives operate under partial loads most of the time. For such applications, the electric motor should not only have the highest efficiency at a given partial load, but should also be able to operate at full load conditions. Unlike classical machines (induction, dc, synchronous), where these requirement are quite difficult to achieve, DESMs, thanks to their hybrid excitation field topology, are able to satisfy these specifications. Frankly, a comprehensive comparative study for comparisons between DESMs and other types of traction motor is a quite challenging task since it requires various factors to consider such as cost, weight, available technology, system being used, etc. Among these factors, a good efficiency should be a priority for every electrical motor used in a traction system. At this early stage, a focus on highlighting advantage of DESMs regarding the efficiency will be presented.

Generally, an efficiency map constitutes a convenient way to assess motor design. Efficiency maps are sketched by isolines of efficiency, it gives an idea about the torque/speed combinations at which a specific motor drive is efficient. An efficiency map of a PMSM is shown in Fig. 2.21 [32] as an example. In most industrial applications, motors usually operate at one or a few predefined

operating points. Therefore, motors could be optimized to have the best performances at these specific points, and the efficiency of the system is well defined [33]. However, it is not the case in propulsion applications such as railway traction where traction motors are expected to perform well in a wide range of torque-speed combination.

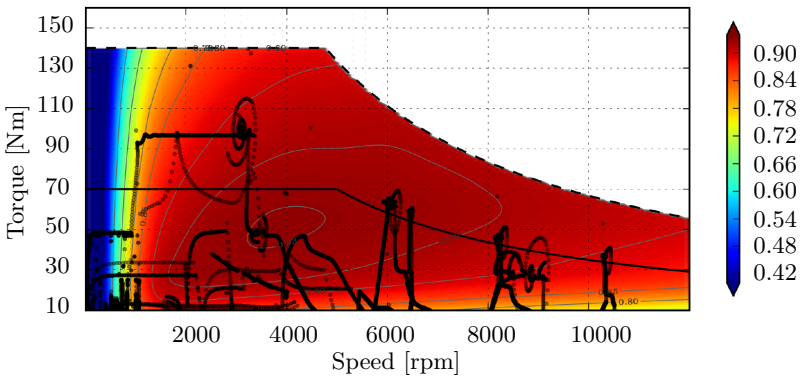

Fig. 2.21: Efficiency map of a PMSM motor with superimposed sampled operation points of a typical drive cycle

Remarked in [34], by a proper control of field current in a DESM and hence the air-gap flux, the torque-speed characteristic can be easily shaped to meet the special requirements. Also, the efficiency map of the motor drive can be optimized throughout the whole operating range. Thus, the efficiency at those operating regions can be improved. As mentioned in [35], using auxiliary field winding to control the speed, the flux density and iron losses are reduced in all motor active parts and as a result an efficiency improvement at wide speed range is achieved. Authors of [35] also pointed out that efficiency of a DESM in a wide speed operation can be improved by control strategy combination: As the motor reaches the rated operating point, a higher speed is obtained through the negative d-axis armature current procedure, then at a certain value of d-axis current, the speed increase is continued by field current injection resulting in a global improved efficiency.

Research done in [16] emphasized advantageous feature of a DESM for vehicle propulsion with higher efficiency compared to a PM and a WFSM motors. Traction motors should have maximum efficiency at the most frequently used operating points. Firstly, a separate comparison between PM and WFSM in term of efficiency map is discussed. Fig. 2.22 [16] draws an efficiency map comparison between a PM motor and a WFSM one excluding mechanical losses and static converter efficiency. As it can be seen, under the base speed, both machines reveals the same maximum efficiency. At high speed; however, PM machine has a lower efficiency that that of WFSM due to a high d-axis current required for flux weakening [33]. WFSM also possesses a better speed range due to the easy of reducing flux compared to the PM case.

In comparison with a PM machine, some DESM topologies are expected to have extended operating area as for a WFSM with the maximum efficiency as same as one of a PM machine. With a combination between PM and WFSM is characterized by a coefficient, namely hybridization

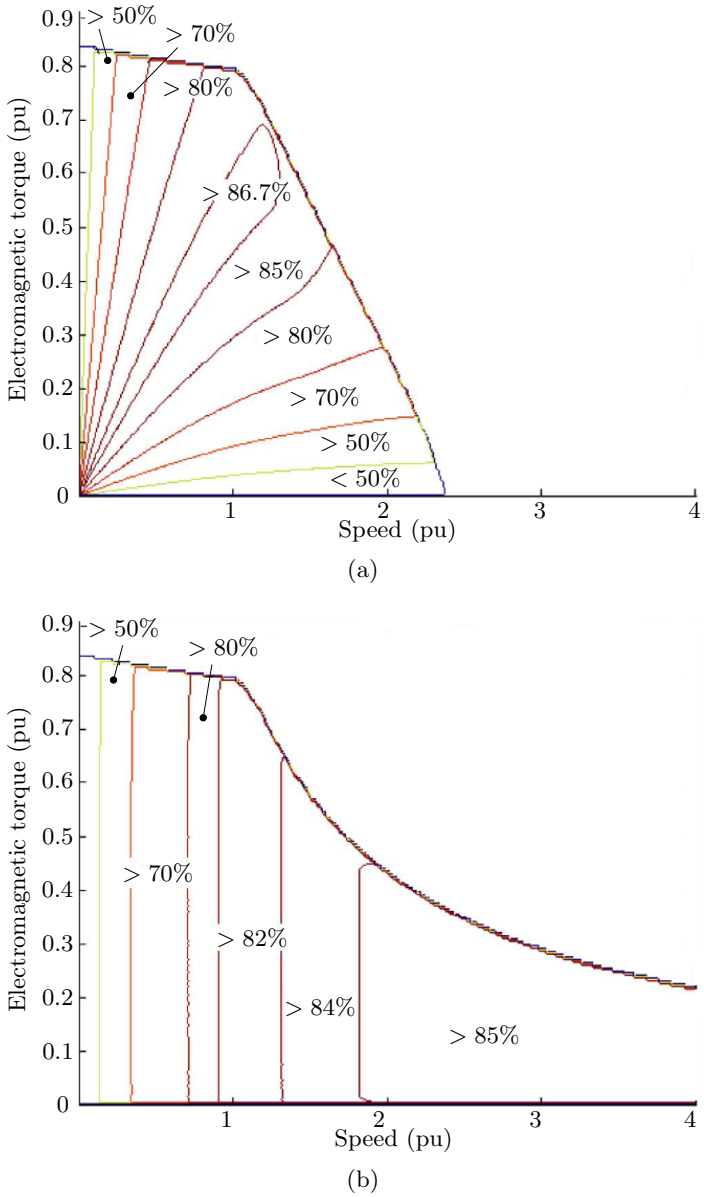

Fig. 2.22: Efficiency maps. a) PM motor. b) Wound field synchronous motor

ratio α defined as (2.2) [16]

$$\alpha = \frac{\Phi_a}{\Phi_{\text{emax}}} \tag{2.2}$$

where Φ_a is PM flux linkage and Φ_{emax} is maximum value of the total excitation flux. $\alpha = 0$ corresponds to the WFSM case and $\alpha = 1$ corresponds to the case where field windings are only for flux weakening but not flux enhancing mode. By adjusting this value, it is possible to shift a high efficiency area into the desired (torque, speed) area. This would significantly increase vehicle range due to energy consumption saving [36]. The studied machine in this research is shown in Fig. 2.19, hybridization ratio is adjusted as $\alpha \approx 0.72$ (both flux weakening and enhancing are available) and $\alpha = 1$ (weakening only). Experiments of efficiency map for these two cases are demonstrated in Fig. 2.23 [16].

As it can be observed in Fig. 2.23, when hybridization ratio changes from 0.72 to 1, the highest

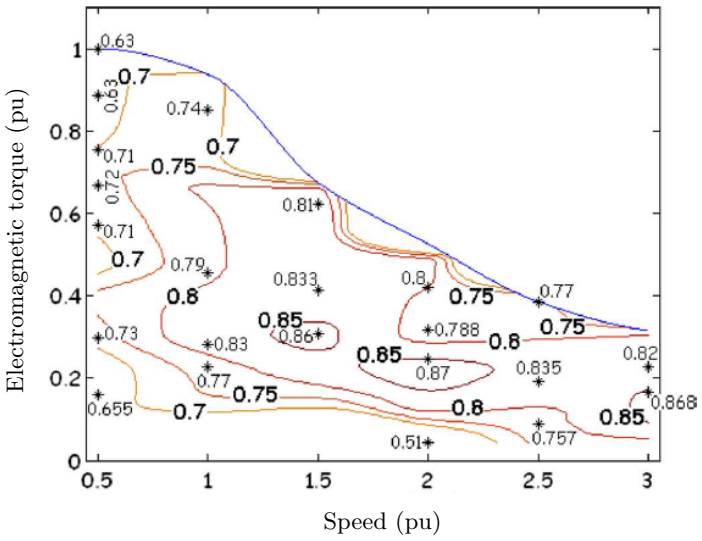

(a)

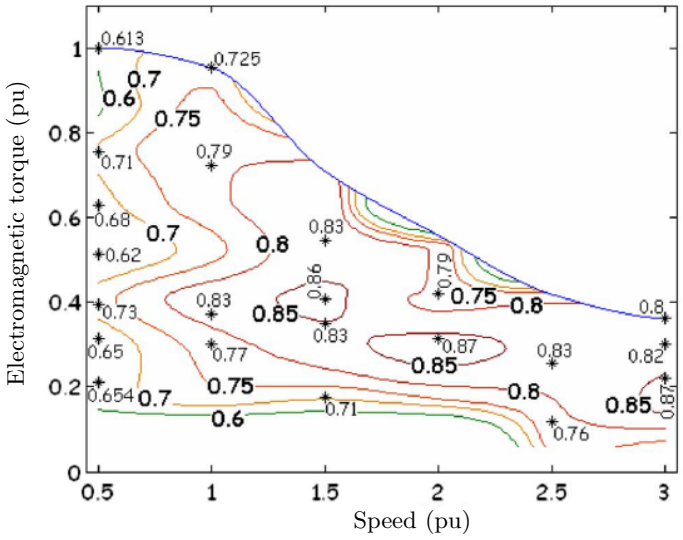

(b)

Fig. 2.23: Measured efficiency maps for a DESM. a) $\alpha \approx 0.72$. b) $\alpha = 1$

efficiency zones are shifted to a higher values of normalized torque.

After all things considered, obviously DESM type could be suggested as a very good candidate for traction applications with flexible operation in flux weakening as well as flux enhancing mode. Also, its energy efficiency is very promising. However, to comprehensively evaluate its performance, more details should be taken into account i.e. its performance in the whole system. In the last section of this chapter, a prototype of DESM will be chosen as the analysis model in the thesis.

2.4 DESM prototype for analysis

In SATIE laboratory, a group of DESM topologies with similar configurations has been developed one of them were already shown in Fig. 2.19. Authors of [30] also presented a work related to this topology group. In detail, three prototypes with power rating of 3 kW will be presented. Two of them are modular; therefore an easy assembly could be made to have different configurations: homopolar and bipolar. Shortly, three prototypes possess identical stators, the difference lies on the rotor parts.

2.4.1 Configurations of different prototypes

This part will briefly summarize work of [30]. Schematic of the first prototype is sketched in Fig. 2.24, corresponding 3-D topology and experimental photo are seen in Fig. 2.25 and Fig. 2.26 respectively. This first topology belongs to the parallel type with two global field windings placed on the stator and PMs are located on the rotor. In order to increase air-gap flux density, flux concentration principle is applied by using side PMs together with azimuth ones as shown in Fig. 2.24. Therefore, PMs with low residual flux density hence low cost could be used. In this case, ferrite PMs are equipped ($B_r = 0.4$ T).

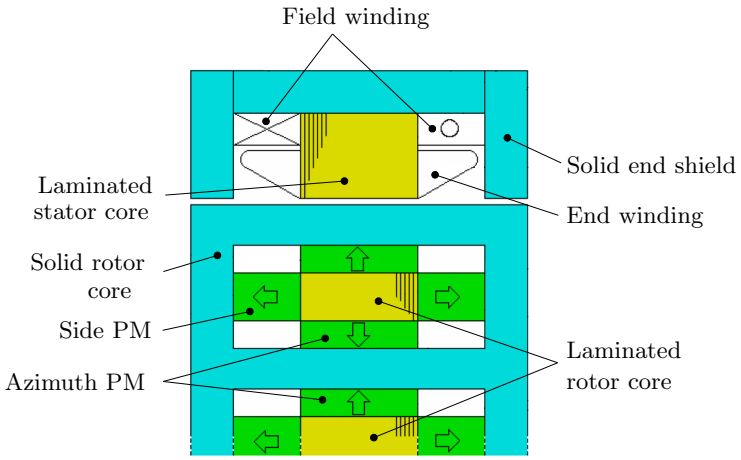

Fig. 2.24: Schematic of the first prototype

The rotor consists of two parts which are magnetically insulated: solid and laminated ones. Due to the existence of some truly 3-D flux paths in the machine (will be explained later in this part), solid material for external stator yoke and end-shield parts are adopted to conduct flux created by field windings (This is also the reason for the solid core part in the rotor). Specifications of the first prototype are detailed in Table. 2.1. These specifications are applied mostly to the second and third prototypes except a slight modification are made. Schematics of the second and third prototypes are correspondingly shown in Fig. 2.27 and Fig. 2.28.

Compared to the rotor of the first prototype, side PMs are removed in these two rotors. In

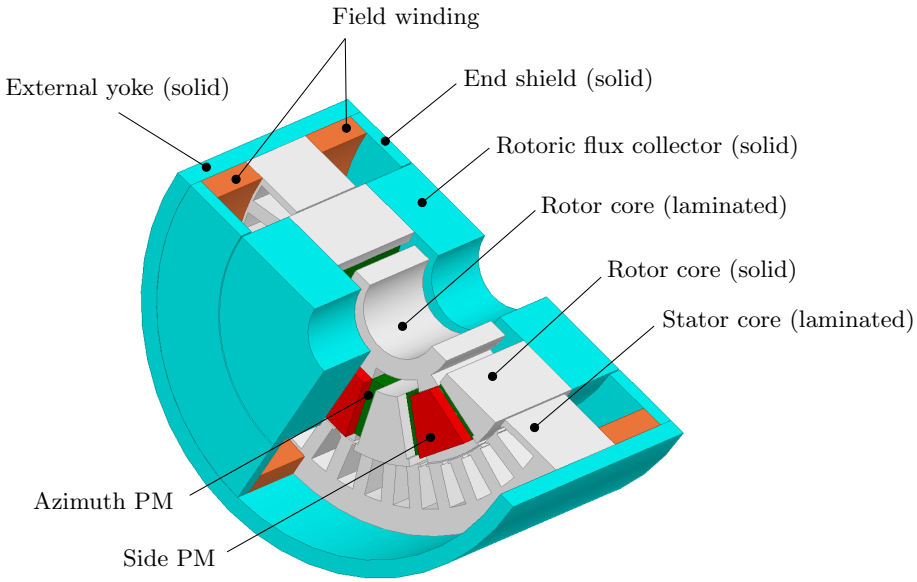

Fig. 2.25: 3-D topology of the first prototype

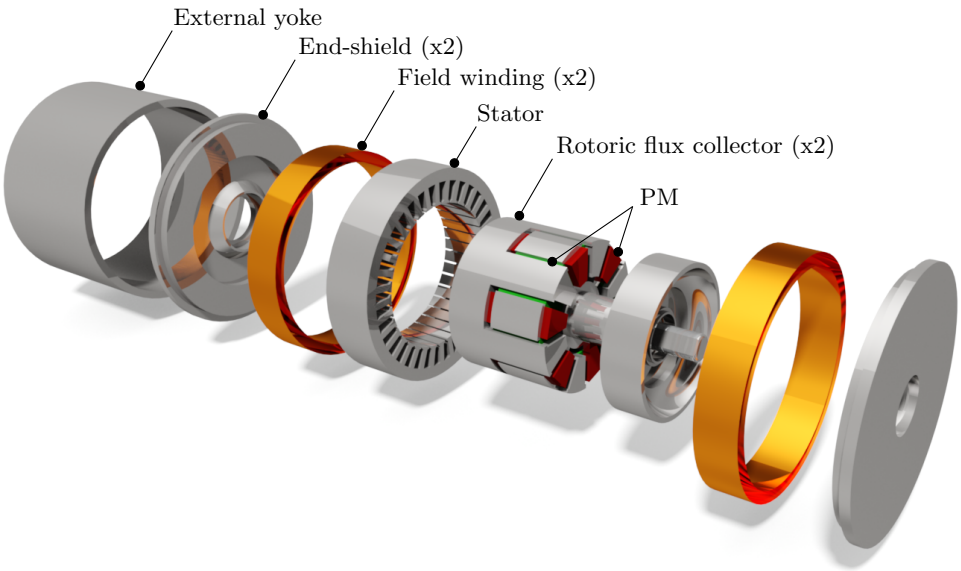

Fig. 2.26: Disassembling of the first prototype

addition, these two rotors are modulated resulting in easy changes in their assemblies to have homopolar of bipolar configurations [30]. One should be noted that if rotating one solid rotor core (for example the lower green part) of rotor in Fig. 2.27b) by one rotor pole, it will turn into the bipolar configuration as seen in Fig. 2.28b). A more detailed difference between these two rotors lies on the laminated rotor cores as displayed in Fig. 2.29. An inner ring is introduced in the laminated rotor part of the third prototype (Fig. 2.29b)) made it simpler compared to that of the second prototype from the construction point of view. However, this in turn increases flux leakage from PMs leading to lower performance.

Table 2.1: Specifications of the first prototype

Parameters	**Value**
Number of phases	3
Number of turns per phase	33
Number of turns per field winding	150
Number of pole pairs	6
Motor length	115 mm
Outer stator diameter	184 mm
Air-gap diameter	114.5 mm
Number of slots	36
Air-gap length	0.5 mm
PM residual flux density	0.4 T (ferrite PM)
Based speed	2000 rpm
Rated power	3 kW

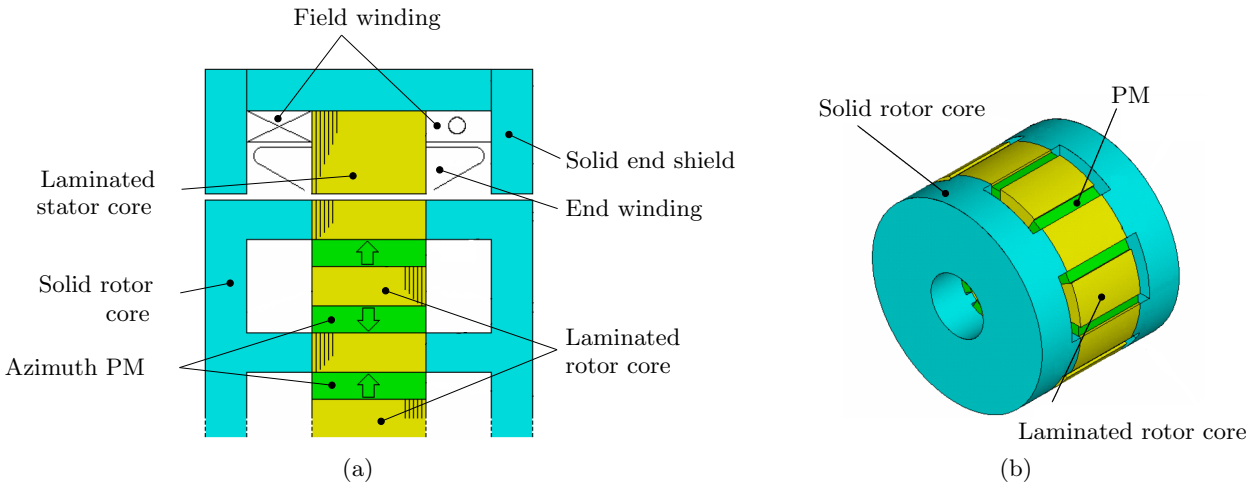

Fig. 2.27: Second prototype with homopolar configuration. a) Schematic. b) Rotor

2.4.2 Comparisons between prototypes

Owing to similar topologies between prototypes and hence similar operation principles. The first prototype will be taken as the representative for the working principle explanation.

2.4.2.1 Homopolar and bipolar flux paths

The double excitation principle creates somewhat complex flux paths in some circumstances especially in cases with operation principle due to flux paths appears in different planes i.e. three dimensional. In these configurations, two kinds of flux path are presented by both PMs and field windings: homopolar and bipolar paths [30, 37]. Simply, homopolar flux paths create

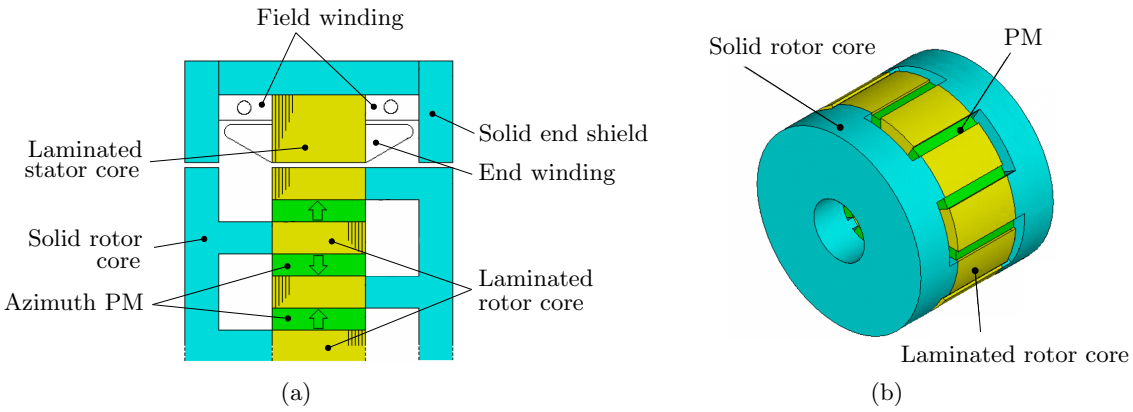

Fig. 2.28: Third prototype with bipolar configuration. a) Schematic. b) Rotor

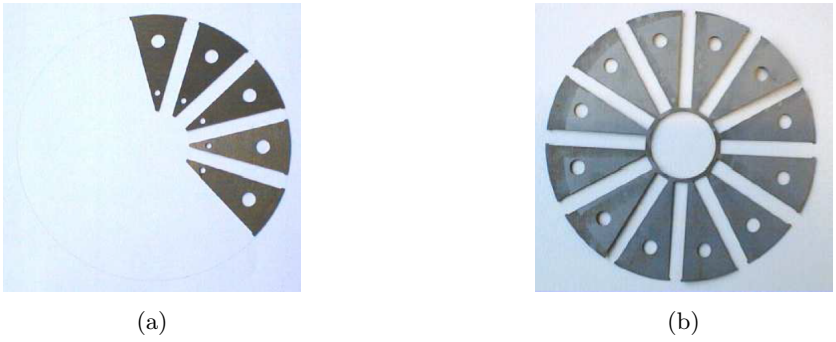

Fig. 2.29: Laminated rotor part for second and third prototypes. a) Second prototype. b) Third prototype

only one type of pole (north or south) under the active part. Meanwhile, bipolar flux paths create north and south poles under the active part. Field windings only generate homopolar flux paths and PMs could have both types. The bipolar flux paths are illustrated in Fig. 2.30. The homopolar flux paths that are more complex are illustrated in Fig. 2.31.

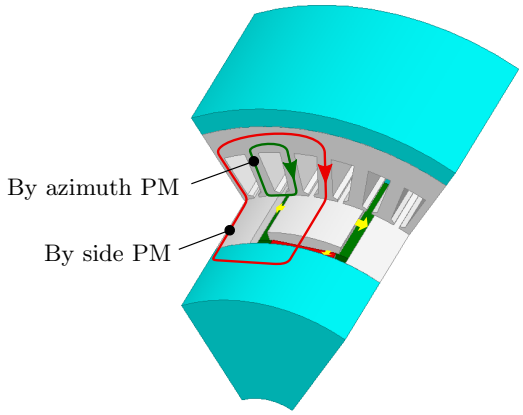

Fig. 2.30: Bipolar flux paths created by PMs

The field winding proposes two different kinds of homopolar flux path namely effective and

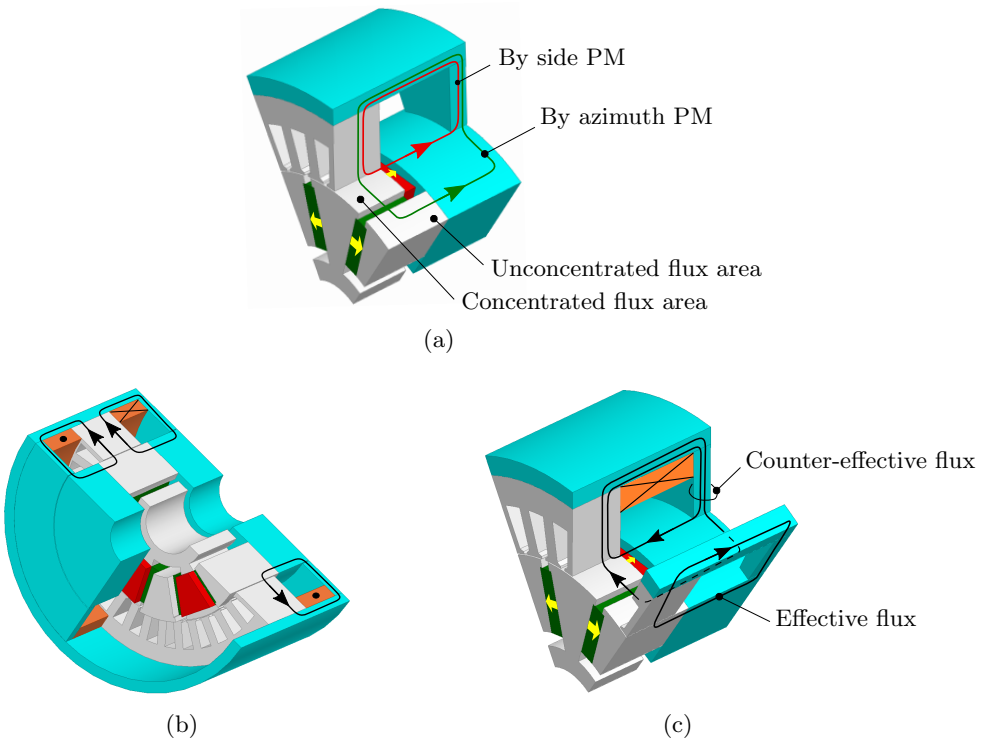

Fig. 2.31: Homopolar flux paths. a) By PMs. b) By field windings. c) Detail by a field winding in the flux enhancing mode

counter-effective flux as in Fig. 2.31c).The effective flux plays the key role for air-gap flux regulation. Meanwhile, counter-effective flux tends to extenuate the the function of effective flux since it generates opposite flux trajectories. For example in the flux enhancing mode, while the main flux from field windings are acting on the unconcentrated flux area to increase air-gap flux, the counter-effective flux are passing through PM in demagnetized direction and they certainly tend to cancel out homopolar flux created by PM i.e. producing a counter-effect. It happens quite similarly in the flux weakening mode except that PMs are not demagnetized as counter-effective flux reverse their directions. Even though the counter-effective flux is generally small compared to main flux because it has to pass through PMs but when the magnetic path of main flux becomes saturated (at highly positive values of field current), any further increase of field current will turn field winding flux into counter-effective, in that situation global flux will reduce.

Due to the presence of these homopolar flux paths, the armature winding arrangement (concentrated or distributed - the case being studied) will affect the its flux linkage distribution in which a DC component may or may not exist. To explain this, aligned and unaligned rotor positions will be examined. Fig. 2.32 shows the case with concentrated windings and homopolar flux paths by side PM (other homopolar flux path type are similar). In direction perpendicular to the paper plane, the armature winding is stacked above. The flux by homopolar path due to the lower side PMs linked armature winding will be in clockwise direction. For the upper side PMs, this will be in counter-clockwise direction. Because of the concentrated arrangement,

these two flux will add up together. At the unaligned position, the flux linkage (usually zero for a classical machine) is shifted by a DC component due to the fact that the armature winding still overlaps a part of side PMs as seen in Fig. 2.32a). At the aligned position, flux linkage will be maximum due to side PMs are entirely overlapped by armature windinga as seen in Fig. 2.33. To summarize, an illustrative flux linkage distribution is seen in Fig. 2.34.

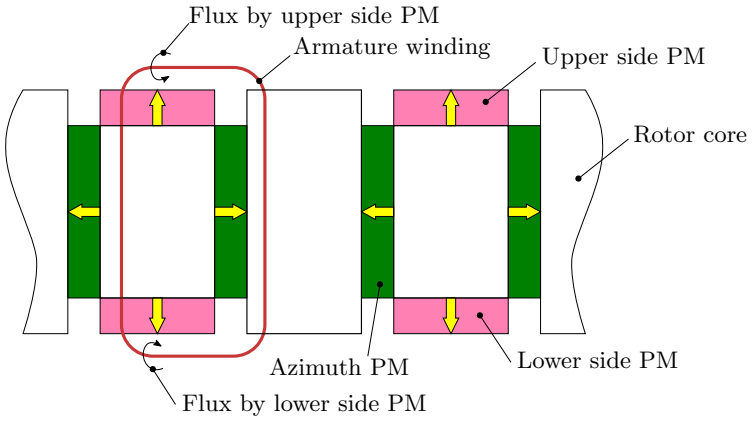

Fig. 2.32: 2-D Illustrative homopolar flux paths by side PMs with concentrated winding

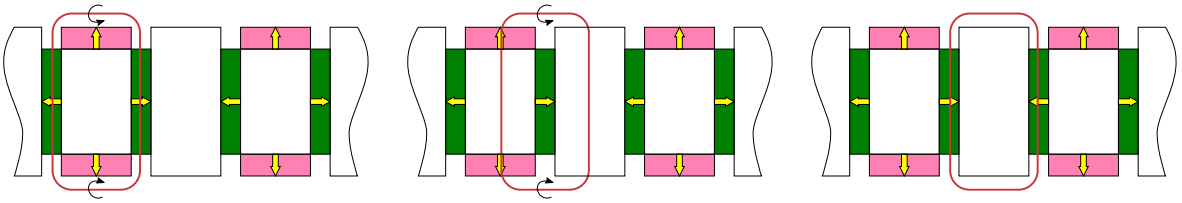

Fig. 2.33: A homopolar flux type created by side PMs with concentrated winding. a) 1st alignment. b) Unalignment. c) 2nd aligment

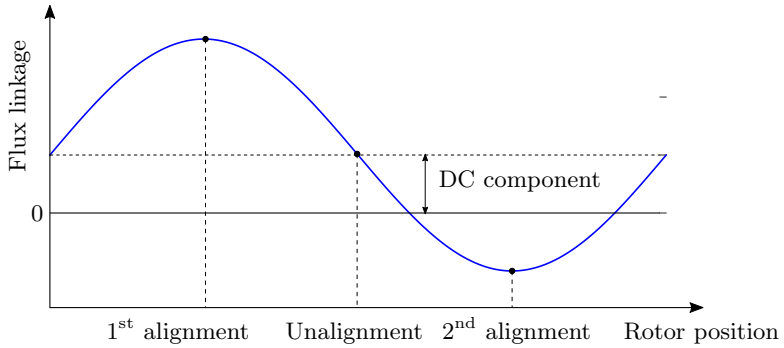

Fig. 2.34: Illustrative phase flux linkage with concentrated winding

The case with a distributed armature winding will be seen in Fig. 2.35. Linked homopolar flux paths by side PMs are seen in Fig. 2.36.

It can be seen that at the 1st aligned position, the flux linked by lower side PMs is maximum whereas one by upper side PMs is zero. At 2nd aligned position in Fig. 2.36a), flux linkage is

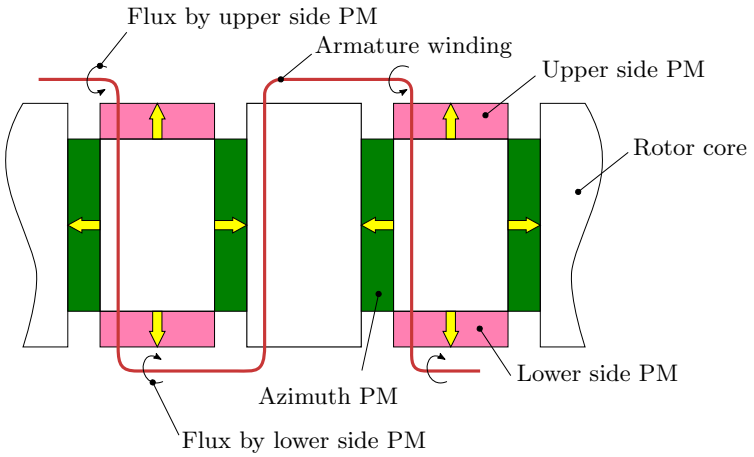

Fig. 2.35: 2-D Illustrative homopolar flux paths by side PMs with distributed winding

reversed with the zero flux linked by lower side PMs and maximum flux linked by upper side PMs. At the unaligned position in Fig. 2.36c), flux linked by upper and lower side PMs will cancel out each other due to the overlapped areas by armature winding for upper and lower PMs are the same and flux direction is reversed as shown in Fig. 2.36b). So that for the distributed arrangement, no DC component is presented in the flux linkage waveform.

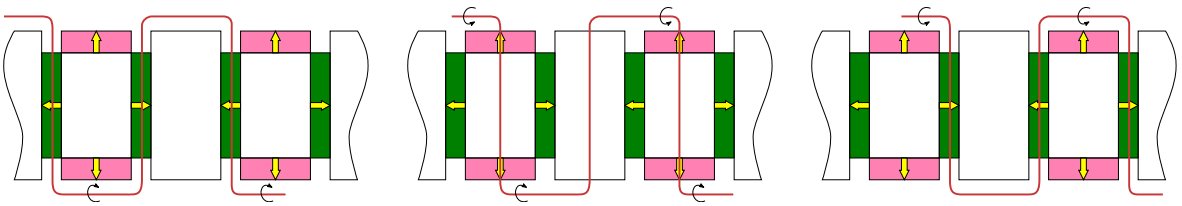

Fig. 2.36: A homopolar flux type created by side PMs with distributed winding. a) 1st alignment. b) Unalignment. c) 2nd aligment

2.4.2.2 A comparison regarding flux control range characteristic

A distinguishing feature of a DESM is air-gap flux control capability. Therefore, a comparison with regard to this characteristic will be examined and on the basic of that analysis, a prototype will be chosen for the further study in this thesis. Also some more factors would be discussed. As mentioned earlier, the second and third prototypes would be modified leading to two configurations: bipolar and homopolar. The experimental result in Fig. 2.37 will show maximum flux per turn with respect to field current in both operation modes: flux weakening and flux enhancing.

As clearly seen, second prototype owns higher flux compared to the third one, this is due to the inner ring introduced in the third prototype making azimuth PM short-circuited and flux linkage is therefore reduced. Though this ring facilitates the fabrication of the rotor core.

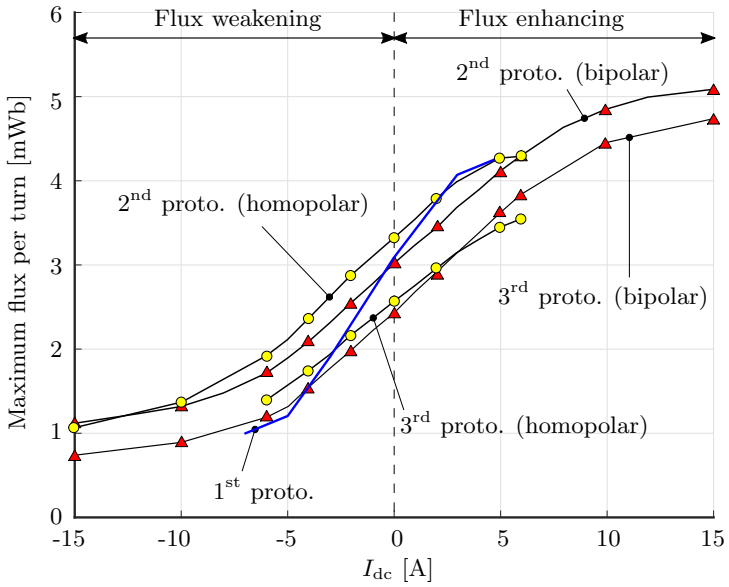

Fig. 2.37: Maximum flux variations comparison

In comparison with the bipolar configuration, the homopolar one has a better performance with field current varies in a small range around zero but it is more highly saturated when field current reaches high. Although two configurations have a same field weakening capability. This is explained by the fact that with homopolar configuration, field current does not act evenly on rotor magnetic poles i.e. one pole would be saturated while the other would not. For bipolar configuration, saturation occurs at the same time for both magnetic poles. For that reason, bipolar will have a wide range of flux variation [30].

A detail comparison for different curves in Fig. 2.37 are shown in Table. 2.2 with slopes are calculated for the linear range around zero field current area.

Table 2.2: Flux control curve characteristic of different machines

Machine prototype	Max. flux [mWb]	Min. flux [mWb]	Flux range [mWb]	Slope [mWb/A]
1st	4.3	1.0	3.3	0.36
2nd (homopolar)	4.3	1.1	3.2	0.23
2nd (bipolar)	5.1	1.1	4.0	0.22
3rd (homopolar)	3.5	1.4	2.1	0.19
3rd (bipolar)	4.7	0.7	4.0	0.23

Regarding the flux control effectiveness, the first prototype exhibits the most efficient solution since the slope of flux variation is biggest i.e. to achieve same flux (either increase of decrease), the first prototype requires a smaller amount of field current leading to a smaller copper loss. This highest slope is due to the use of solid core in the first prototype for the reluctance path of flux created by field windings, while other prototypes utilize laminated cores.

Regarding the flux control range (difference between maximum and minimum flux), bipolar configurations show the best feature among all prototypes and the 2nd prototype is even better than the 3rd one with higher flux level. Even though the 2nd bipolar prototype has the maximum flux of 0.8 mWb higher compared to one with the 1st prototype but it requires too much field current (9 A more) causing much copper loss and temperature increased as well.

Due to this dominance in flux control over the others, the first prototype will be chosen for a further investigation. In the next part, more analysis result done by 3-D FEM will be conducted.

2.4.3 3-D FEM analysis of the first prototype

This part performs a more detailed analysis of the first prototype. Due to a 3-D flux path characteristic, a 3-D FEM is necessarily required. In this study, 3-D FEM ANSYS Maxwell will be employed. Thanks to the symmetry property, only one pole pair (corresponds to 60 mechanical degree) will be analyzed. Periodic boundary condition is used to ensure the magnetic vector potential are exactly the same on the boundary surfaces. To begin, Fig. 2.38 shows the B-H magnetization curve for the FeSi core material at 50 Hz.

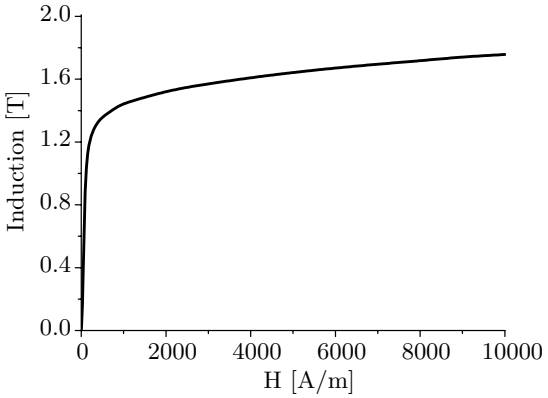

Fig. 2.38: B-H characteristic of a 0.35 mm FeSi lamination

3-D mesh for a part of the motor is presented in Fig. 2.39 with about 60,000 elements. Unlike some other solutions, for example in [38] the 3-D mesh is derived from an extrusion of a 2-D mesh, the mesh created in Maxwell program is truly 3-D.

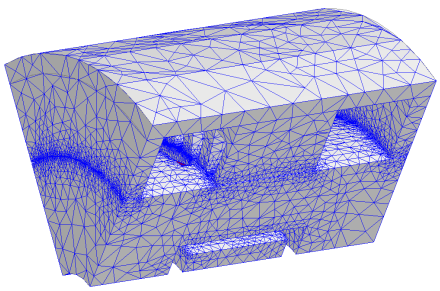

Fig. 2.39: 3-D mesh of a part of the studied prototype

Owing to one pole pair corresponding to 60 mechanical degree, 60 points with a step of one mechanical degree will be analyzed. An interesting point is that for quantities related to winding such as current, back electromotive force (EMF), analysis data for one sixth of one pole pair is enough because of winding symmetry i.e. data could be deducted from the first one sixth. Thus saving computation time if only winding quantities are calculated. This is explained as follows:

Without loss of generality, one could assume:

$$\begin{cases} x_a &= X\sin(\omega t - 2\pi/3) \\ x_b &= X\sin(\omega t + 2\pi/3) \\ x_c &= X\sin(\omega t) \end{cases} \tag{2.3}$$

where x represents phase quantities (current, voltage, etc.), X is the amplitude, t is the time variable. If quantity x is equally divided into 6 periods: $\{x_1, x_2, ..., x_6\}$. Then quantities for x_i $(i = 2 \div 6)$ could be deducted from $\left\{x_{a(1)}, x_{b(1)}, x_{c(1)}\right\}$ such as (2.4):

$$\begin{cases} x_{a(2)} = -x_{b(1)} & x_{a(3)} = x_{c(1)} \\ x_{a(4)} = -x_{a(1)} & x_{a(5)} = -x_{a(2)} \quad x_{a(6)} = -x_{a(3)} \end{cases} \tag{2.4}$$

Flux density distribution is displayed in Fig. 2.40 at no-load condition and field windings are not excited ($I_{\text{dc}} = 0$). The effect of homopolar flux paths could be observed in this map that the flux densities in the stator teeth (let's say teeth-1 group) facing the concentrated flux area are higher than others (teeth-2 group). However, when exiting field windings with a current of

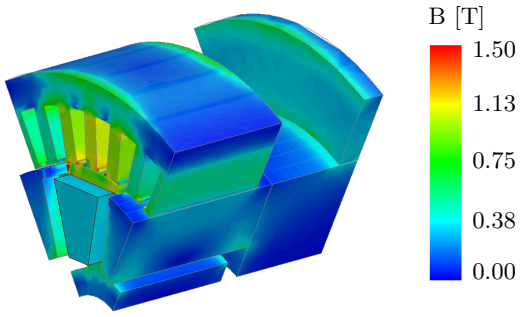

Fig. 2.40: Flux density distribution at aligned position, no-load, non-excited ($I_{\text{dc}} = 0$)

3 A (enhancing). Field winding will increase flux densities in teeth-2 group and at the same time reduce ones in teeth-1 group due to counter-effective flux as discussed in 2.4.2.1.

2.4.3.1 PM demagnetization examination

Even though this DESM prototype belongs to parallel type since the main effective flux (flux to intentionally adjust air-gap flux) from field winding does not pass though PMs leading to a general statement that a parallel configuration could avoid a risk of demagnetization. However,

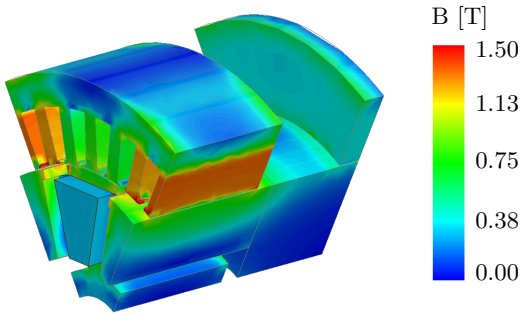

Fig. 2.41: Flux density distribution at aligned position, no-load, $I_{dc} = 3$ A

in this case demagnetization still occurs due to the counter-effect flux paths created by field windings (discussed in 2.4.2.1), passing through PMs in demagnetizing direction in the flux enhancing mode. This could be considered as an "unintentional demagnetization". This is more risky when the magnetic paths of the main flux are saturated, all further increased flux will become counter-effective and make demagnetization worse.

This could be partly observed in Fig. 2.40 and Fig. 2.41 when field current increases from zero to 3 A in the flux enhancing mode. The teeth facing the unconcentrated area approach saturation and at the same time, flux densities in teeth-1 group are reduced. In order to more elaborately examine the demagnetization effect, the flux densities in both side and azimuth PMs will be computed at their centers according to a wide range of field current as seen in Fig. 2.42. As seen, because side and azimuth PMs have same thickness (6 mm) so flux density for two kinds of PM are almost the same. Fig. 2.42 also reveals that counter-effect flux from field windings becomes stronger when increasing field current i.e. the slope increases. This is due to more and more counter-effect flux from field windings passing through PMs as explained above.

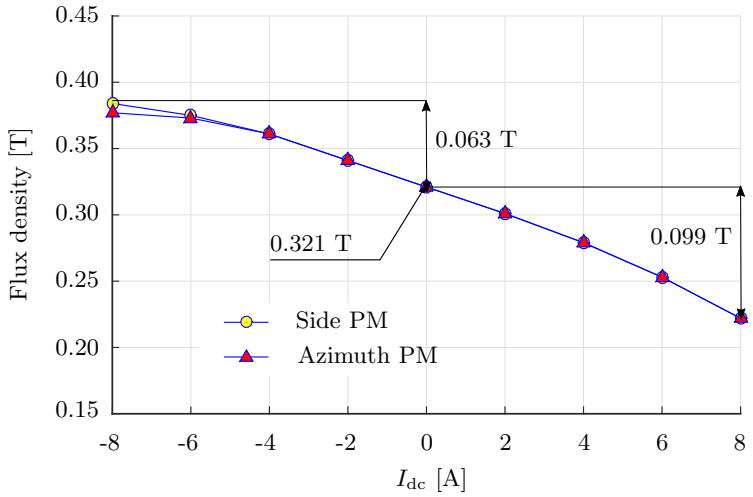

Fig. 2.42: PM demagnetization due to field winding at aligned position, no-load

At a field current of 8 A, flux densities of PMs reduce to 0.222 T which is generally higher than the knee point of commonly used ferrite PMs [39]; therefore, no big danger appears. Also for

the prototype being studied, field current is not expected to be higher than values around 7 A due to the thermal limit. However in cases when PM thickness is reduced, demagnetization risk will increase and hence a careful consideration should be made accordingly.

2.4.3.2 Flux control range examination

This part discusses air-gap flux regulation of the studied prototype in both flux weakening and enhancing modes. An example is shown in Fig. 2.43 for flux linkage and back EMF of a phase. Here back EMF is calculated by taking derivative of flux linkage with respect to time. For a good motor deisgn, back EMF waveform must be well estimated [40]. Harmonic content of a back EMF waveform at no-load, $i_{\mathrm{dc}} = 0$ A is demonstrated in Fig. 2.44. As reported, 5^{th} accounts for a big portion of harmonic content, this would result in a big torque pulsation, iron loss. However, discussion about this influence is currently not an objective.

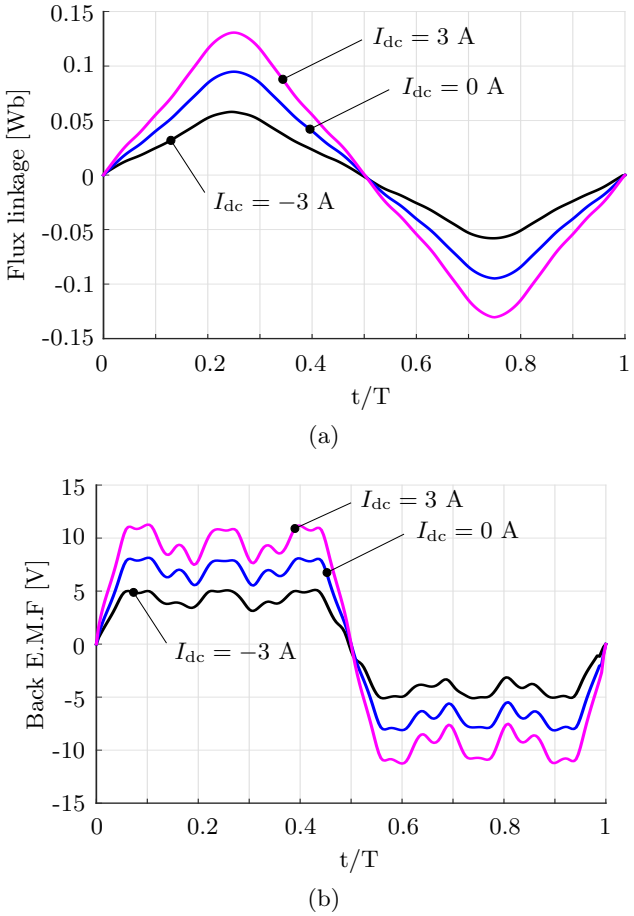

Fig. 2.43: Air-gap flux control at no-load due to field current variation. a) Phase flux linkage. b) Phase back EMF at a speed of 170 rpm

Obviously, due to a certain change in field current, the linked flux will alter accordingly and hence its back EMF. With a change of 3 A corresponding to 900 AT (two field windings and 150 turns per each), the maximum flux changes by 36 mWb. In order to further explore flux control capability, a wide range of field current will be utilized. For this purpose, the maximum flux

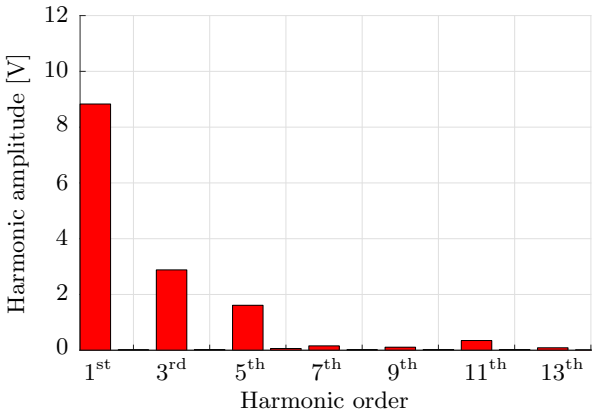

Fig. 2.44: Back EMF harmonic content at no-load, $i_{dc} = 0$ A

per turn will be computed as illustrated in Fig. 2.45. As it will be seen, three regions appear. The first region corresponds to a very negative field current, this causes end-shield saturated as in Fig. 2.46a) as all homopolar flux paths going in the same direction through end-shield and add up together leading to no change in both main and counter-effect flux from field windings and global flux would stay unchanged.

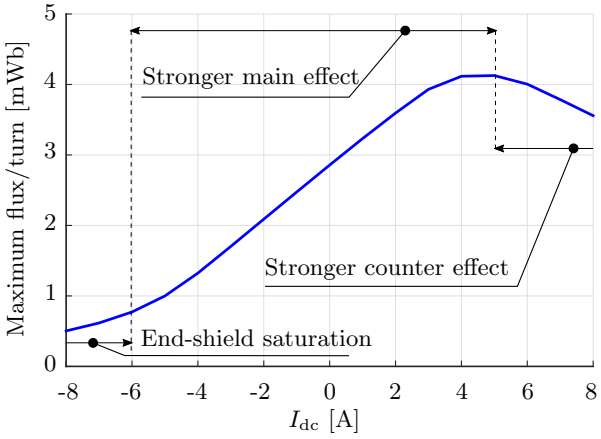

Fig. 2.45: Maximum flux at no-load according to field current variation

The second region corresponds to the linear range as in Fig. 2.40 or Fig. 2.41 where the trend follows the change in the main flux from field winding. The last region corresponds to highly positive field current, this causes saturation of magnetic paths for main flux from field winding as in Fig. 2.46b) hence no increase for that. Any increase in field current will increase counter-effect flux and hence, global flux decreases. This counter-effective flux seems to be a drawback. However, this is not a big problem since the points beyond the maximum are not of interest.

2.4.3.3 Torque calculation

Maxwell Stress Tensor (MST) and virtual work principle are two most common methods used to compute electromagnetic torque. MST method calculates torque acting on a rigid body

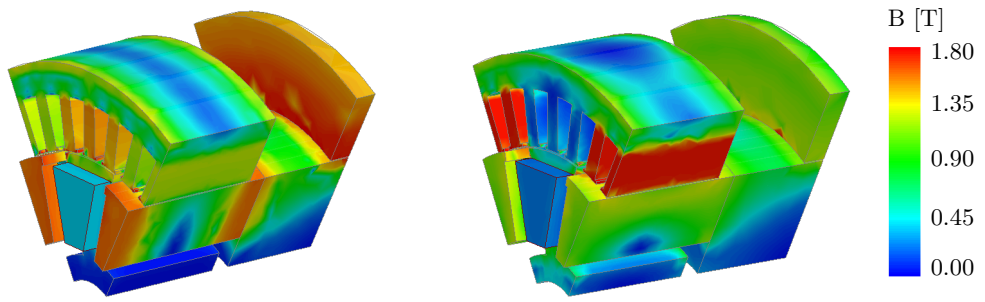

(a) (b)

Fig. 2.46: Induction distribution at aligned position, no-load (B-H magnetization curve saturates at 1.8 T). a) Field current I_{dc} = -8 A. b) Field current I_{dc} = 8 A

expressed as (2.5) [41, 42]

$$T_e = \oint_S r \times \sigma dS = \oint_S r \left\{ \frac{1}{\mu_0}(B.n)B - \frac{1}{2\mu_0}B^2 n \right\} dS \tag{2.5}$$

with r is the radius of the surface S, σ is the stress tensor, B is the magnetic flux density, n is the unit normal vector of the integration surface and μ_0 is permeability of the air. A closed integration surface that surrounds the rotor in free space must be chosen. For a two dimensional electromagnetic field models (for a majority of motors), the surface integral is reduced to a line integral along the air-gap, (2.5) then becomes (2.6)

$$T_e = \frac{L}{\mu_0} \int_0^{2\pi} r^2 B_r B_\theta d\theta \tag{2.6}$$

with L is the active length of the motor, B_r and B_θ are the radial and tangential components of flux density B.

From (2.6), it may be noted that only the flux densities on the integration contour are employed which allows for simple and quick calculations. As remarked in [41], MST method owns several advantages such as the field computation is required once, the choice of the surface S is arbitrary, provided that no medium other than empty space is crossed (a good practice is that the surface S should pass through nodes in the region where the mesh does not change). However, MST method is prone to the mesh discretisation [43–45]. In order to achieve a good accuracy, an appropriate meshe is importantly required. For the studied DESM prototype, handling a very fine 3-D mesh in the air-gap is quite a challenge as the number of elements is limited due to time and computer resources.

The virtual work method is based on the stored magnetic co-energy change or the virtual work with a small displacement. By this method, electromagnetic torque is calculated as the derivative of the magnetic co-energy W_{co} with respect to angular position θ at a constant current expressed as (2.7):

$$T_e = \left. \frac{\partial W_{co}}{\partial \theta} \right|_{i=\mathrm{const}} \tag{2.7}$$

Basically, this method requires calculations at two successive rotor angular positions and hence computation time is doubled. Moreover, it may be necessary a trial-end-error procedure to select a suitable value of the position increment, $\Delta\theta$. If $\Delta\theta$ is too small the co-energy variation will be insufficient to overcome round off error. If $\Delta\theta$ is too large, the calculated torque will no longer be accurate for the specified position [46]. But it gains an advantage due to the global information used which could avoid errors due to localised inaccuracy associated with the discretisation as with MST method.

Using the virtual work principle, the flux-MMF diagram is a generalized version of the flux-linkage versus current ($\psi - i$) diagram used commonly for analyzing switched reluctance motors [47–50]. It plots the variation of instantaneous effective flux linking a particular phase against the instantaneous MMF of that phase. This plot is a closed trajectory over one electrical cycle indicating the average torque produced over one electrical cycle for any one phase as (2.8) [49]. The total area consists of a number of incremental areas bound by the magnetization curves at successive rotor positions and each of these areas indicates the instantaneous torque at a particular rotor position for any one phase [49].

$$T_e = mp\frac{\Delta W_{co}}{2\pi} \tag{2.8}$$

where m is the number of phases, p is the number of pole pairs and ΔW_{co} is the co-energy converted per phase over an electrical cycle. Fig. 2.47 demonstrates average and instantaneous torque calculations. In this illustrative example, four flux-MMF diagram are plotted corresponding to currents of $i = 0$, i_1, i_2 and i_3. The average torque at i_3 is reflected by the area enclosed by the biggest ellipse (yellow). Two magnetization curves are presented, $A_1A_2A_3A_4$ for position θ_k and $B_1B_2B_3B_4$ for position θ_{k+1}. With an assumption that due to a very small angular difference, A_4 and B_4 are vertically the same. Therefore, the instantaneous torque at (θ_k, i_3) is reflected by the area bound by these two magnetization curves (the blue area) i.e. $S_{A_1A_2A_3A_4B_4B_3B_2B_1}$.

Important features of the flux-MMF diagram are summarized as follows [49]:

- Ability to represent many performance characteristics of a machine graphically including torque capability and torque smoothness
- Area enclosed indicates torque capability
- Shape indicates nature of excitation (ideally ellipsoidal for sinewave and rectangular for squarewave)
- Deviation from ideal shape and uneven spacing of magnetization curves indicates torque ripple and saturation

For the DESM prototype being studied, flux-MMF diagrams at different armature currents are sketched in Fig. 2.48. The torque angle is set to zero.

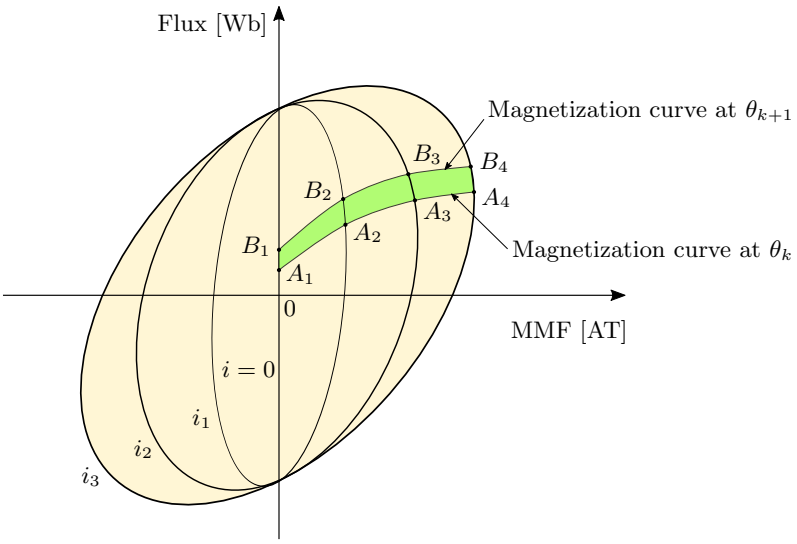

Fig. 2.47: An illustrative flux-MMF diagram

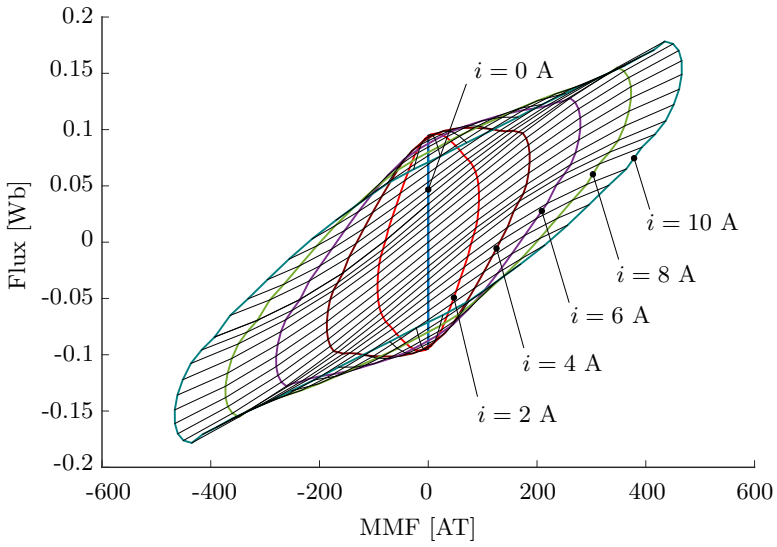

Fig. 2.48: Flux-MMF diagram at various armature currents, non-excited ($I_{\text{dc}} = 0$)

From this flux-MMF diagram, big torque ripple is predicted due to the uneven spacing of magnetization curves.

Average torques at different armature currents are displayed in Fig. 2.49 at zero field current and Fig. 2.50 is average torque according to variations of both armature and field currents. Thanks to the contribution of field windings, a certain torque value could be achieved by various combinations of armature and field currents; therefore, providing a solution with the best combination yielding the minimum copper loss.

Fig. 2.51 displays instantaneous torques at various armature currents with respect to rotor position. For the instantaneous torque calculation, firstly instantaneous torque is calculated for one phase by computing the incremental areas in the flux-MMF diagram bound by the magne-

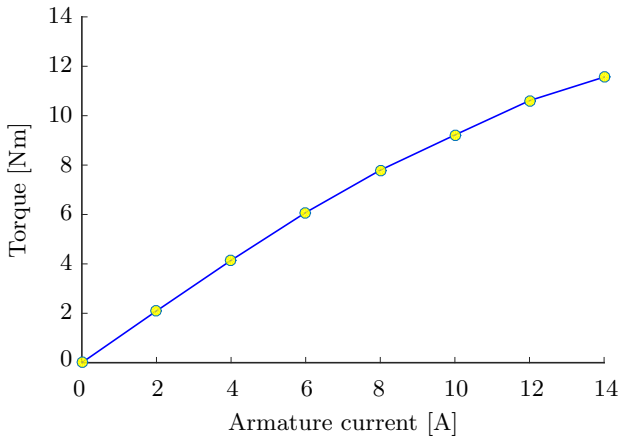

Fig. 2.49: Generated torque at various armature currents, non-excited ($I_{\mathrm{dc}} = 0$)

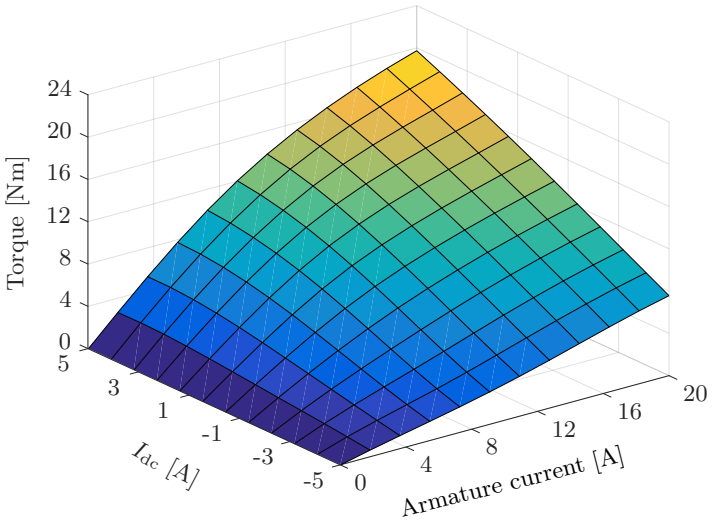

(a)

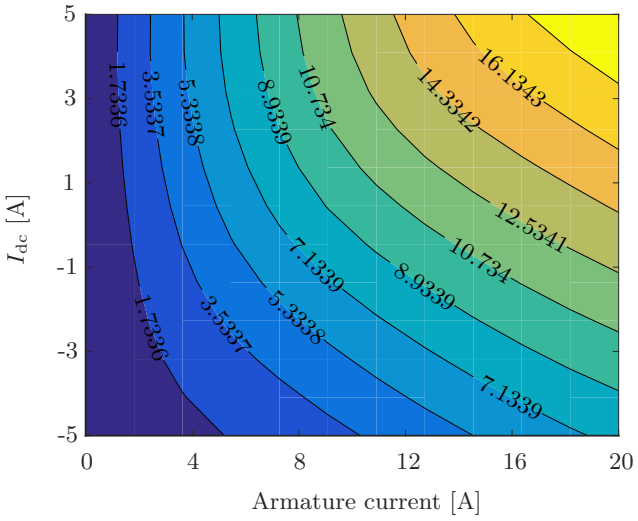

(b)

Fig. 2.50: Average torque at various armature and field currents. a) Torque map. b) Torque contour

tization curves (the black lines inside the closed trajectories in Fig. 2.48). Then interpolations are made for two other phases by shifting angles of $\pm 2\pi/3$. The instantaneous torque is the sum of individual ones. From these torque waveform, torque ripples are calculated ranging between 30% and 40% which confirm the torque ripple prediction from flux-MMF diagram. This big torque ripple would be undesirable for low speed applications. For railway traction, this problem would be mitigated due to very high train inertia. Torque ripple could be reduced by using some geometry modification techniques such as slot opening adjustment, skewing, tooth tip shaping, etc. Moreover, it could be handled with current controlling approaches either armature or excitation currents. Despite that fact, torque ripple minimization is not the target of this research.

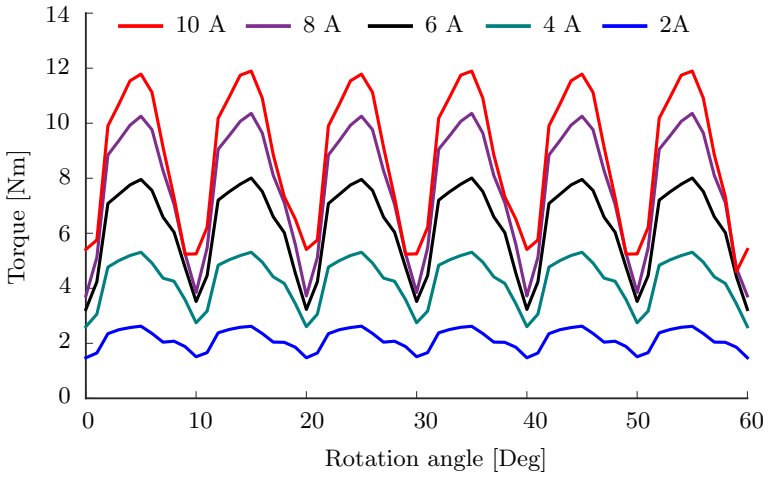

Fig. 2.51: Instantaneous torque at different armature currents, ($I_{\mathrm{dc}} = 0$)

Conclusion

This chapter has reviewed a basis on DESMs with a number of topologies were developed. Advantages of DESMs were highlighted in terms of both flux control flexibility and energy efficiency. A prototype realized in SATIE was chosen for further study in this thesis according to its dominance in air-gap flux regulation over others. Owing to a 3-D flux path characteristic, a 3-D FEM package is required for highly accurate performance predictions. This results in a long computation time. In this specific machine simulated by 3-D Maxwell FEM package, computation time at one point takes about 58 seconds (with about 60000 tetrahedron elements). However in the early design stage, there is usually a need of a numerous model's evaluations; therefore, this process will be incredibly time consuming if 3-D FEM analyses are used. In order to handle this task, next chapter will present a fast model for the 3-D FEM replacement.

Chapter 3

Modeling with Equivalent Magnetic Circuit Network (EMCN)

In the previous section, a DESM prototype was analyzed by using the 3-D FEM. Using this high fidelity model can yield accurate results; however the long computation time is the inherited problem with FEM (especially with the 3-D case) [51]. In the design phase, an enormous number of evaluations are often needed. An optimization process is an example. Therefore, a model with acceptable accuracy but is fast to evaluate is obviously prioritized to mitigate the computation time. In contrast to FEM, equivalent magnetic circuit network (EMCN) provides a noticeable compromise between the computation time and accuracy. This chapter is dedicated to the EMCN modeling the studied DESM prototype. The result accuracy and computation time will be elaborated by comparing with ones obtained by the 3-D.

3.1 Equivalent Magnetic Circuit Network

EMCN method has long been proven as an effective alternative tool for motor analyses with a much shorter computation time while maintaining the result accuracy close to ones performed by FEM [52–56]. The EMCN model has been used for electrical machine analyses, such as switched reluctance motors [55], asynchronous motors [52], and permanent magnet motors [56]. Using the EMCN is also advantageous over the FEM when there is a need to couple with other analyses such as thermal or acoustic ones [57]. In the EMCN method, two important circuit laws guiding equation system formulation namely the Kirchhoff's current law and the Kirchhoff's voltage law, leading to the nodal-based and mesh-based equations, respectively [58]. In this thesis, the Kirchhoff's current law, which is the more common method due to the ease of establishing and extending equation system compared to the latter one.

3.1.1 Nodal based EMCN formulation

To begin, some basic components of an EMCN model will be shortly recalled. Conventionally, two methods could be used with the EMCN are the tooth contour [59] and flux tube [60]. In this work, the flux tube method, which is the most popular implementation of the EMCN will

be employed. The flux is considered constant inside the tube and two ends of the tube are assumed equipotential planes as displayed in Fig. 3.1.

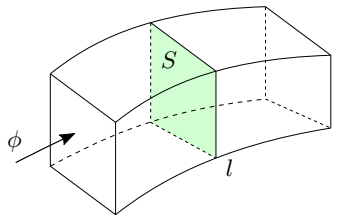

Fig. 3.1: Flux tube idea for the reluctance calculation

The basic expression for reluctance and permeance of the flux tube are given by (3.1):

$$R = \int_0^L \frac{dl}{\mu_0 \mu_r S(l)} \tag{3.1a}$$

$$P = \frac{1}{R} \tag{3.1b}$$

where L is the length of the tube, S is the cross section of the tube at position l, μ_r is the relative permeability of the tube material, and μ_0 is the permeability of the air. With a tube of length L and constant cross section S over the tube, (3.1a) becomes (3.2):

$$R = \frac{L}{\mu_0 \mu_r S} \tag{3.2}$$

Another important component in the EMCN is the source, which is either the magneto-motive force source (MMF) or flux source. In fact these two sources are interchangeable, i.e. a MMF with an internal reluctance R in series could be replaced by an equivalent flux source ϕ connected in parallel with that reluctance as illustrated in Fig. 3.2 with $\phi = \frac{F}{R}$.

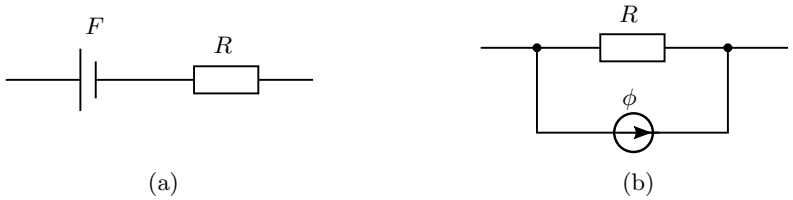

Fig. 3.2: Source in EMCN. a) MMF source. b) Flux source

In electrical machines, an MMF sources is usually the representation of a permanent magnet or carrying-current coils. A permanent magnet can be modeled by a reluctance connected in series with an equivalent MMF (shown in Fig. 3.2a)) as (3.3):

$$F_{\text{pm}} = \frac{B_r h_m}{\mu_0} \tag{3.3}$$

where B_r and h_m are PM thickness and residual magnetic flux density, respectively.

A coil consisting of N turns carrying a current i is equivalent to an MMF expressed by (3.4):

$$F_{\text{coil}} = Ni \tag{3.4}$$

With these basic components, the formulation for the nodal-based network can be explained by a circuit having n nodes (u_i) $(i = 1 \div n)$ demonstrated in Fig. 3.3. F_{ij} is an MMF source placed between the node i and node j, R_{ij} is reluctance between the node i and the node j, hence its permeance $P_{ij} = \dfrac{1}{R_{ij}}$

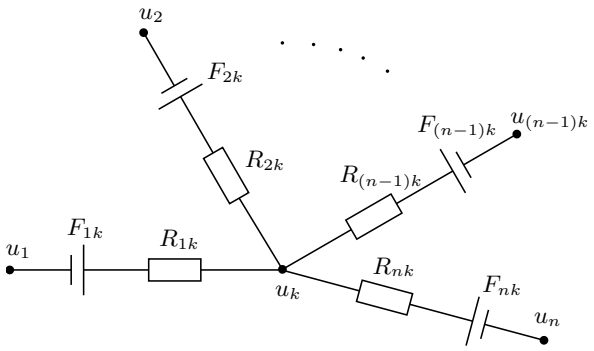

Fig. 3.3: A simple nodal based circuit

Applying the Kirchhoff's current law to the magnetic circuit, i.e. the flux conservation law (3.5) at node k.

$$\sum_k \phi_k = 0 \tag{3.5}$$

One could be obtained (3.6):

$$\sum_{\substack{i=1 \\ i\neq k}}^{n} \frac{(u_i - u_k - F_{ik})}{R_{ik}} = 0 \tag{3.6a}$$

$$\sum_{\substack{i=1 \\ i\neq k}}^{n} (u_i - u_k - F_{ik})\, P_{ik} = 0 \tag{3.6b}$$

$$u_k \sum_{\substack{i=1 \\ i\neq k}}^{n} P_{ik} - \sum_{\substack{i=1 \\ i\neq k}}^{n} u_i P_{ik} = \sum_{\substack{i=1 \\ i\neq k}}^{n} F_{ik} P_{ik} \tag{3.6c}$$

Similarly applying for all other nodes, (3.6c) is generalized as (3.7).

$$\begin{bmatrix} P_{11} & P_{12} & \cdots & P_{1n} \\ P_{21} & P_{22} & \cdots & P_{2n} \\ \cdots & & & \\ \cdots & & & \\ P_{n1} & P_{n2} & \cdots & P_{nn} \end{bmatrix} \begin{bmatrix} u_1 \\ u_2 \\ \cdots \\ \cdots \\ u_n \end{bmatrix} = \begin{bmatrix} \phi_1 \\ \phi_2 \\ \cdots \\ \cdots \\ \phi_n \end{bmatrix} \tag{3.7}$$

where ϕ_k is the sum of flux sources connected to node k expressed as the right hand side of (3.6c) and $[P]$ is the permeance matrix defined by (3.8).

$$P_{ij} = \begin{cases} -p_{ij} & \text{if } i \neq j \\ \displaystyle\sum_{\substack{k=1 \\ k\neq i}}^{n} p_{ik} & \text{if } i = j \end{cases} \tag{3.8}$$

Finally the nodal-based system formulation can be expressed as (3.7). By solving this equation, the scalar nodal magnetic potentials are obtained. The further iterative process dealing with the nonlinear characteristic will be discussed later when applying with the DESM prototype.

3.2 EMCN model of the DESM

Regarding the reluctance mesh formulation, two alternatives are proposed: a lumped parameter model as in [53, 61, 62], and a generalized model [63–65]. Basically, with a lumped parameter model, a small number of reluctances are presented based on main pre-assumed flux paths. This requires a prior knowledge of the machine's critical flux paths. Fig. 3.4 is an example of a lumped parameter model for a stator doubly fed doubly salient machine [53].

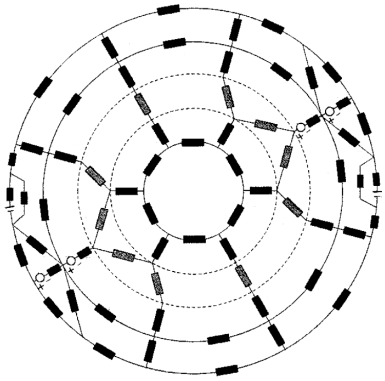

Fig. 3.4: An EMCN model by lumped parameter

Whereas, by mean of generalization as will be presented, each part of the machine is divided into a mesh of elements, each mesh is then characterized by a number of rows and columns.

3.2.1 Basic block element

On the contrary to the lumped parameter reluctance network, the basic element of the generalized model is a reluctance block, which is bi-directional. It means that flux paths are assumed to flow in two orthogonal directions. In this case, they are radial and tangential directions. One block consists of four reluctances in two directions and/or an MMF depending on the magnetization exists or not in the block's area. The block center is considered as a node. Fig. 3.5 shows a basic block having width w, height h and length l

Reluctance calculations for individual components in a block are given by (3.9):

$$\begin{aligned} R_{x1} = R_{x2} = R_x = \frac{w}{2hl\mu_0\mu_r} \\ R_{y1} = R_{y2} = R_y = \frac{h}{2wl\mu_0\mu_r} \end{aligned} \tag{3.9}$$

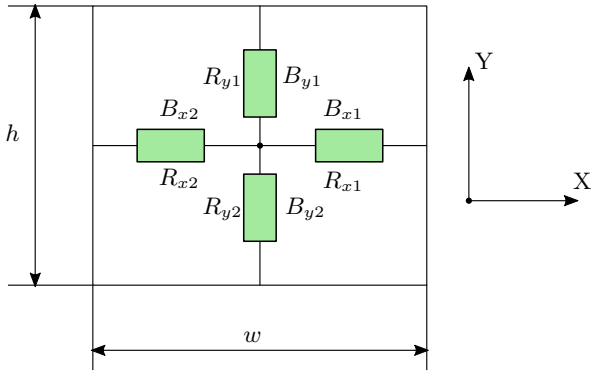

Fig. 3.5: A bi-directional block

where μ_r is the relative permeability of the block material (air, core or PM). This value is given to all individual reluctances in the block.

There are four reluctances included in one block and hence four flux density values. So that there is a need to calculate an equivalent flux density B_{eq} of the block. As it will be discussed later, this flux density will facilitate the calculation of block's permeability by using the B-H magnetization curve. B_{eq} is obtained from flux density components by using the energy conservation law.

The energy stored in a reluctance of a volume V is expressed as (3.10):

$$E = \int_V \int_0^B HdBdV \tag{3.10}$$

In the linear case with a rectangular shape, (3.10) is simplified as (3.11).

$$E_R = \frac{B^2}{2\mu_0\mu_r} V_{\mathrm{R}} \tag{3.11}$$

where V_{R} is the volume of the reluctance R.

The energy stored in the block in Fig. 3.5:

$$E = \frac{B_{x1}^2}{2\mu_0\mu_r} V_{\mathrm{Rx1}} + \frac{B_{x2}^2}{2\mu_0\mu_r} V_{\mathrm{Rx2}} + \frac{B_{y1}^2}{2\mu_0\mu_r} V_{\mathrm{Ry1}} + \frac{B_{y2}^2}{2\mu_0\mu_r} V_{\mathrm{Ry2}} \tag{3.12a}$$

$$E = \frac{1}{2\mu_0\mu_r} \frac{wh}{2} \left(B_{x1}^2 + B_{x2}^2 + B_{y1}^2 + B_{y2}^2\right) \tag{3.12b}$$

$$E = \frac{wh}{4\mu_0\mu_r} \left(B_{x1}^2 + B_{x2}^2 + B_{y1}^2 + B_{y2}^2\right) \tag{3.12c}$$

The energy stored in the block calculated with B_{eq}:

$$E = \frac{B_{eq}^2}{2\mu_0\mu_r} whl \tag{3.13}$$

From (3.12c) and (3.13), the equivalent flux density amplitude B_{eq} can be derived as (3.14):

$$B_{eq} = \sqrt{\frac{B_{x1}^2 + B_{x2}^2 + B_{y1}^2 + B_{y2}^2}{2}} \tag{3.14}$$

The equivalent flux density amplitude components in x and y directions could be derived as (3.15a) and (3.15b), respectively.

$$B_x = \sqrt{\frac{B_{x1}^2 + B_{x2}^2}{2}} \tag{3.15a}$$

$$B_y = \sqrt{\frac{B_{y1}^2 + B_{y2}^2}{2}} \tag{3.15b}$$

3.2.2 Meshing principle

Although the flux paths in the motor are truly 3-D in certain positions, in order to simplify the calculations with a smaller number of nodes and reluctances, the whole model will be disassembled into several parts as displayed in Fig. 3.6. In short, three meshes (part 1, 3, and 5) are presented in X-Y plane, which are 2-D and reluctances in Z-direction (part 2 and 4) are added to account for the third dimensional flux direction. In these reluctance meshes, the part 3's mesh is the most complicated one due to complex and different geometries and material zones. In fact, several layers should be considered for this part to improve accuracy but the total element number and the computation time will significantly increase.

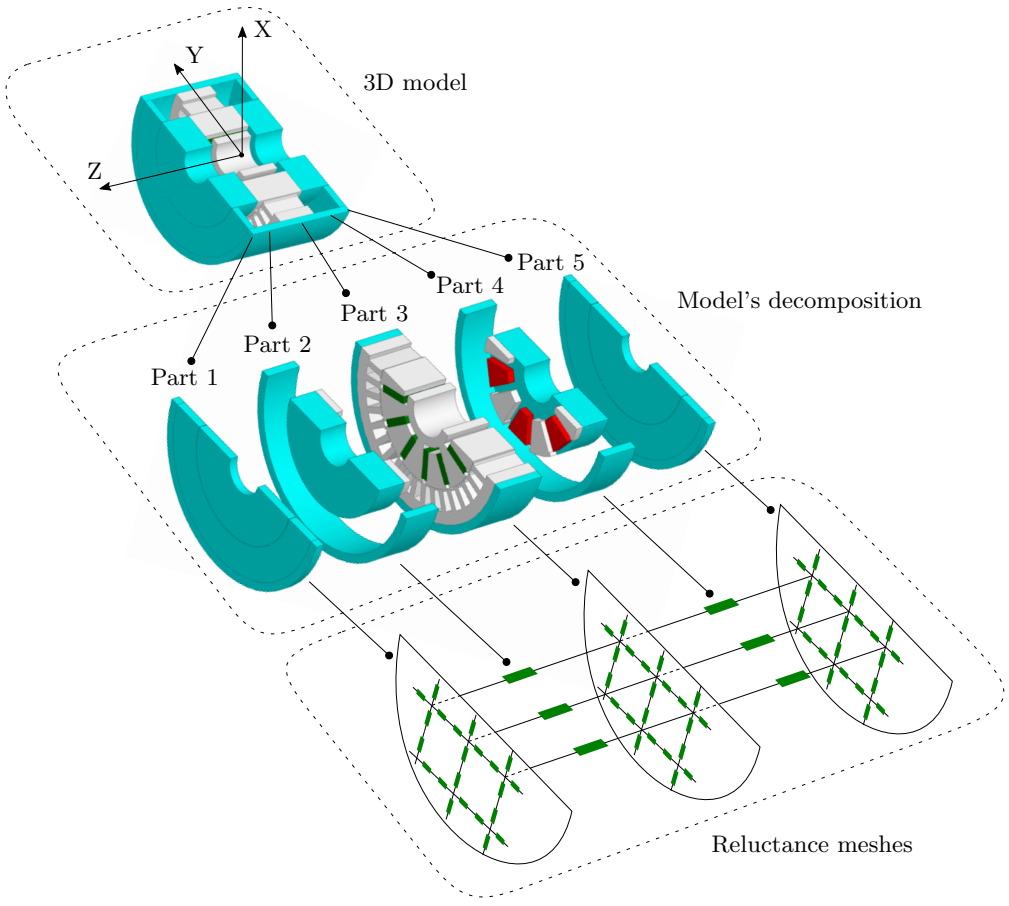

Fig. 3.6: DESM model disassembling for reluctance network

The basic principle for mesh divisions follow the same general guide as applied to the FEM, i.e. there are more elements in the critical parts, for example the air-gap region. Meshes used in this generalized model is characterized by a number of rows and columns (radially and tangentially). Row and column divisions are based on the material region. One should be noted that the basic block element is rectangular; therefore, shape approximations should be accomplished since rotary machines basically use cylindrical coordinate where rectangular shapes are rarely presented (except for regions such as PMs). Meshings for each part of the machine will be detailed in the following.

3.2.2.1 Main stator meshing

This meshing process is for the main stator, which is the part 3 in Fig. 3.6. the row and column division principles in Fig. 3.7 are based on various material regions as follows:

- Three regions in radial direction shown in Fig. 3.7a): the stator yoke, stator tooth, and stator tooth tip. Each region is then divided into rows. All rows in each region has a same height.
- Three types of region in tangential direction in Fig. 3.7b): the slot opening, tooth tip beyond the stator tooth, and stator tooth. Each region is then divided into columns. All collumns in each region has a same width.

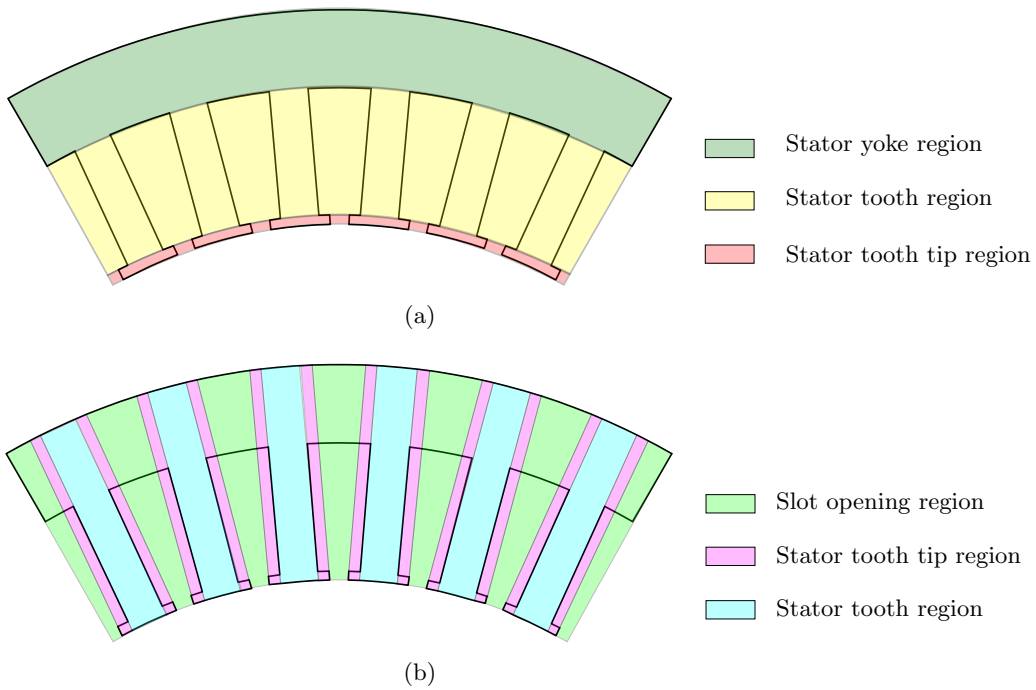

Fig. 3.7: Radial and tangential regions in the stator. a) Radial regions. b) Tangential regions

It is noted that the numbers of rows and columns in each region are adjustable. Details are given in Table. 3.1. The number of blocks in stator is 150 (5 rows and 30 columns in total). The

derived stator mesh is shown in Fig. 3.8 with each small cell is a basic block of four reluctances.

Table 3.1: Numbers of rows and columns in each stator region

Radial region			Tangential region		
Yoke	Tooth	Tooth tip	Slot opening	Tooth tip	Tooth
2	2	1	2	1	1

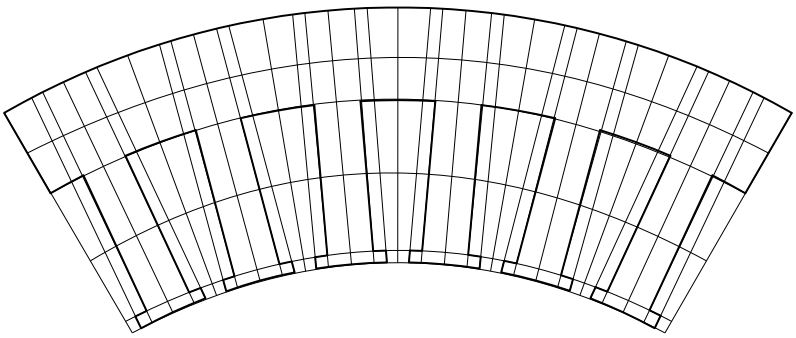

Fig. 3.8: Block mesh of the stator

As it can be seen in Fig. 3.8, each cell is not perfectly rectangular; therefore, an approximation should be made. To this end, an equivalent height and width of each block need to be calculated. The height of each block could be easily derived based on the height of each radial region and the number of rows in that radial region. For example in Fig. 3.9, the height h_s of each block in the slot opening region equals half of the stator tooth height since there are 2 rows in this region.

For the block width, even though there are three different types of tangential region presented but regarding the block width calculation, there are two regions type: type 1 is the region with parallel edges (tooth tip and tooth regions), and type 2 is the slot opening region. With type 1, the width w_1 is given by (3.16)

$$w_1 = \frac{\text{Region width}}{n_1} \tag{3.16}$$

where n_1 is the number of columns in that region.

An example as shown in Fig. 3.9, the width of block B_1 (type 1) is the width of the stator tooth tip w_{tt}.

With block in the region type 2, the width is approximated as the width of an equivalent rectangular with same block height and area given by (3.17)

$$w_2 = \frac{S_s}{h_2} \tag{3.17}$$

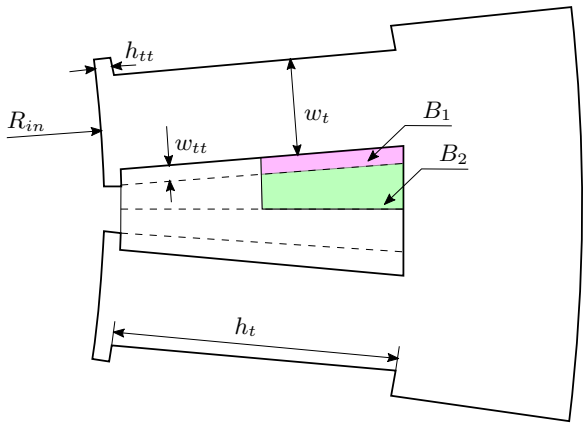

Fig. 3.9: Configuration to calculate block width

where S_s is the area of one block being considered, and h_2 is the block height. S_s is calculated by (3.18).

$$S_s = \frac{1}{n_2}\left[\frac{\pi\left(R_{\text{up}}^2 - R_{\text{low}}^2\right)}{n_s} - \frac{h_t}{n_v}\left(w_t + 2w_{tt}\right)\right] \tag{3.18}$$

where n_s is the number of stator teeth (36 in this study), w_t is the stator tooth width, n_2 is the number of columns in the slot opening, n_v is the number of rows in the radial stator tooth region in Fig. 3.7a. R_{up} and R_{low} are upper and lower bound radii of the block. For instance, with the block B_2 in Fig. 3.9, these radii are calculated as (3.19)

$$\begin{aligned} R_{\text{up}} &= R_{in} + h_{tt} + h_t \\ R_{\text{low}} &= R_{in} + h_{tt} + 0.5h_t \end{aligned} \tag{3.19}$$

where R_{in} is the stator's inner radius, h_{tt} and h_t are heights of the stator tooth tip and stator tooth.

3.2.2.2 Rotor meshing

Rotor meshing principle and block dimension calculations follow the ones as with the stator part. Regions for the rotor mesh shown in Fig. 3.10 are:

- Four regions in the radial direction: The rotor pole tip, PM, leg, and base regions,
- Three region types in the tangential direction: The rotor core, rotor pole tip, and gap area between two poles,

The numbers of rows and columns in each region are given in Table. 3.2. The number of blocks in the rotor is 96 (6 rows and 16 columns in total). The derived rotor mesh is shown in Fig. 3.11.

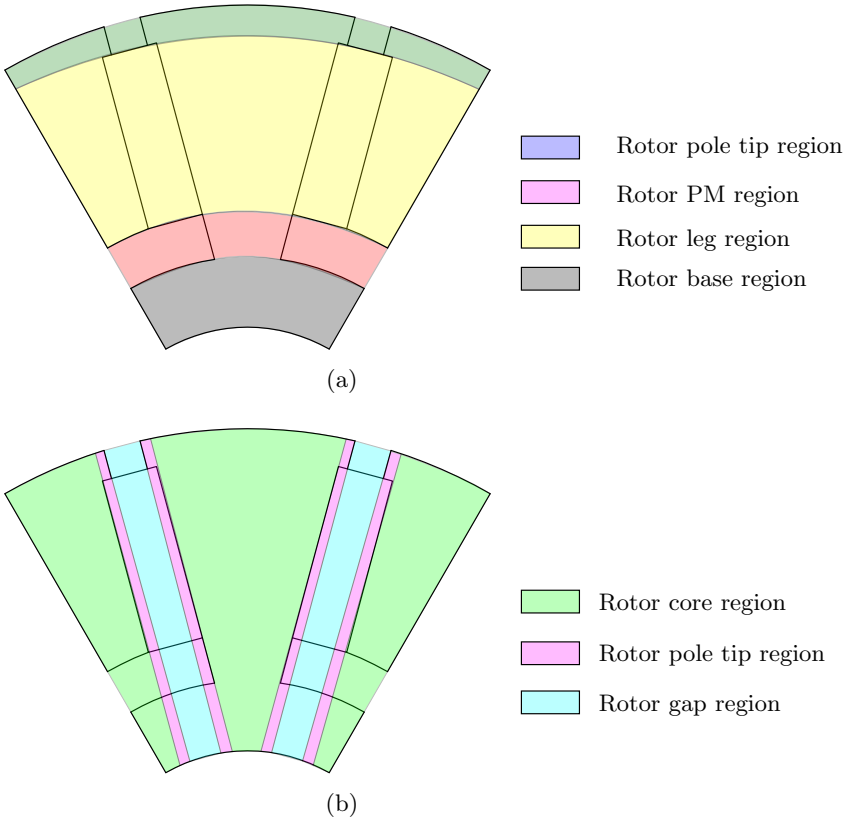

Fig. 3.10: Radial and tangential regions in the rotor (colors are not related). a) Radial regions. b) Tangential regions

Table 3.2: Numbers of rows and columns in each rotor region

Radial region				Tangential region		
Pole tip	PM	Leg	Base	Core	Pole tip	Gap
2	2	1	1	4	1	2

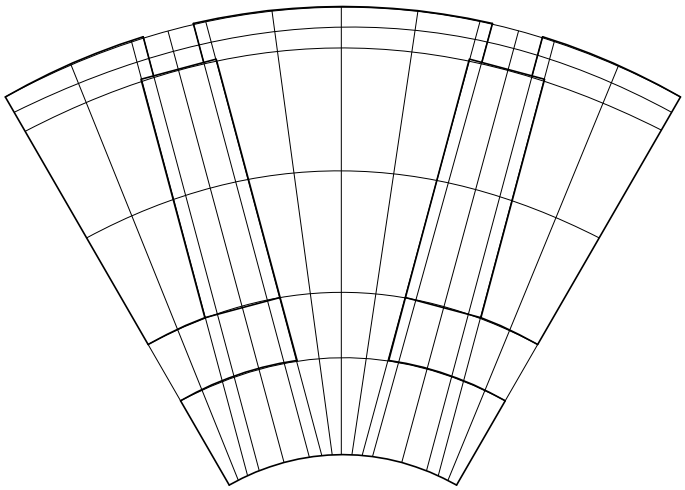

Fig. 3.11: Block mesh of the rotor

3.2.2.3 Air-gap meshing

The air-gap mesh is rather different compared to the stator and rotor meshes. It is still based on bi-directional elements; however, the creation is derived from stator and rotor meshes in a manner that: edges of elements of the stator and rotor (contiguous with the air-gap) define element edges in the air-gap as shown in Fig. 3.12. Air-gap mesh will be redefined for each rotor position, i.e. taking into account the rotation.

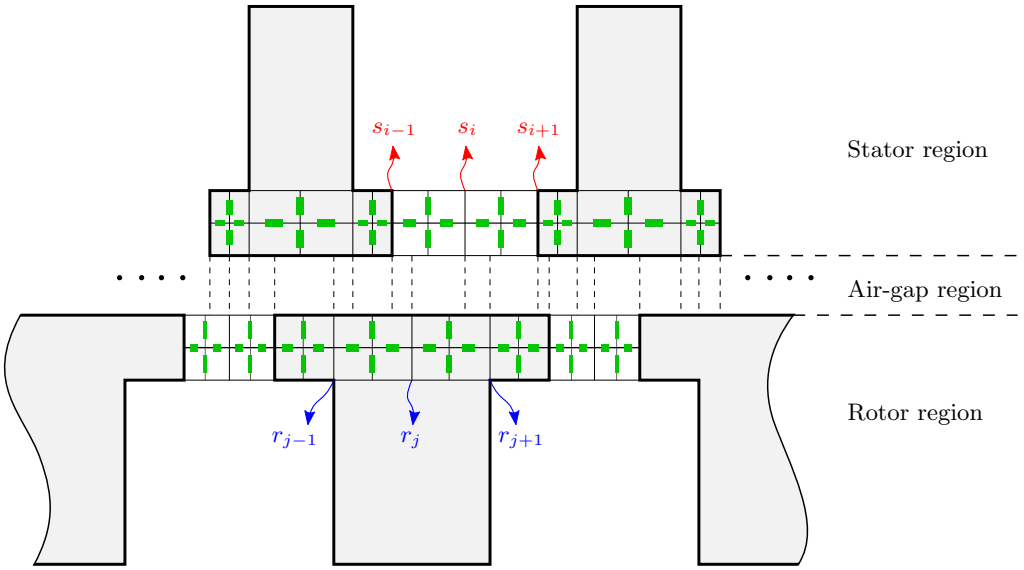

Fig. 3.12: Air-gap meshing principle

Fig. 3.12 shows the air-gap meshing principle based on meshes on the boundaries stator-airgap and rotor - airgap. Let's assume all the elements on the stator-air-gap boundary define their edge positions as (3.20).

$$\boldsymbol{E}_{\mathrm{S}} = [s_1, s_2, ..., s_n] \tag{3.20}$$

Similarly, elements on the rotor-air-gap boundary defines corresponding edge positions as (3.21).

$$\boldsymbol{E}_{\mathrm{R}} = [r_1, r_2, ..., r_m] \tag{3.21}$$

All edges of two groups $\boldsymbol{E}_{\mathrm{S}}$ and $\boldsymbol{E}_{\mathrm{R}}$ are then mixed and sorted in the ascending order. The derived new coordinates group define edges $\boldsymbol{E}_{\mathrm{A}}$ of elements in the air-gap mesh. For example, if the edge coordinates in $\boldsymbol{E}_{\mathrm{S}}$ are [0 2 4 6] and edge coordinates in $\boldsymbol{E}_{\mathrm{R}}$ are [1 5 7 9], then coordinates of air-gap element edges are stored in $\boldsymbol{E}_{\mathrm{A}}$ = [0 1 2 4 5 6 7 9]. It should be noted that, depending on the stator and rotor geometries and specific rotor positions, some edges of rotor's elements may coincide with ones of stator's element, the redundant edges will be removed. Air-gap elements are all bi-directional with the height being the air-gap length g, depth being the machine's active length, and width calculated as (3.22).

$$w = r_a(a_{i+1} - a_i) \tag{3.22}$$

where a_i and a_{i+1} are two edges defining the element being calculated and r_a is the radius right at the middle of the air-gap. So that an air-gap element takes the average length, which is at the middle of the element. This is plausible because in a small deviation (air-gap length), air-gap radius is large and two edges are close in tangential direction). Because of that, air-gap elements are assumed to be rectangular as the all other basic elements.

Having meshes of stator, rotor and air-gap defined, the derived mesh of the part 3 is visualized as Fig. 3.13 with 150 blocks for the stator, 96 blocks for the rotor, and 48 blocks for the air-gap.

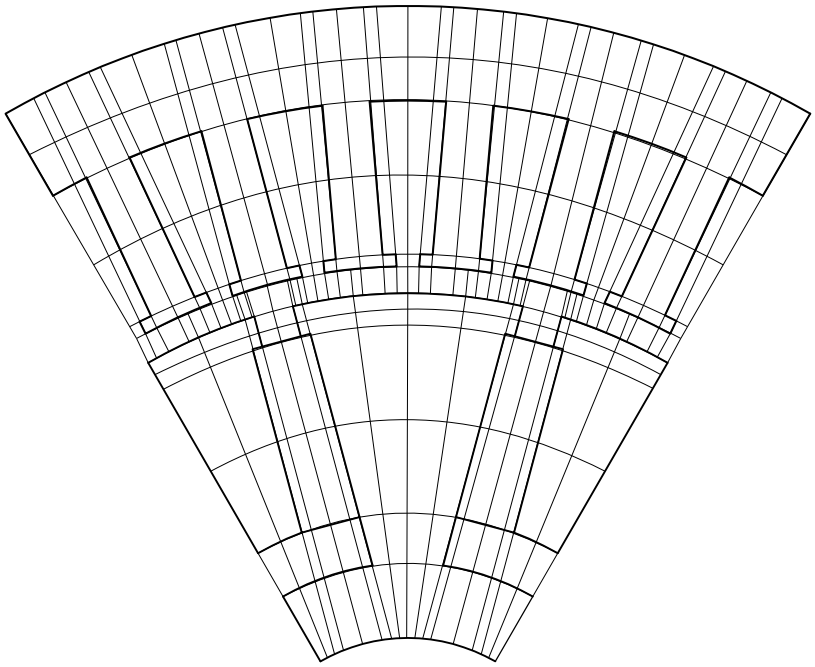

Fig. 3.13: Block mesh of part 3

3.2.2.4 Outer part meshing

Due to the simple structures, meshes for parts 1 and 5 (Fig. 3.6) are the same and much simpler compared to the one of the part 3. Part 1 and part 5 are referred to "outer part". There are three region types in the radial direction (the rotoric flux collector, outer air-gap, and end-shield) and only one type in the tangential direction. In order to make a good connection between the outer parts and part 3, especially in the rotor region, the number of rows in the rotoric part equals to one in the rotor of the part 3, which is 10. On top of the end-shield, one row is dedicated to act as the outer stator core. The same mesh for the part 1 and 5 is shown in Fig. 3.14 with 120 blocks in total (10 rows and 12 columns).

It is advised to carefully pay attention to the air-gap permeance calculation due to fringing flux paths demonstrated in Fig. 3.15. The fringing flux paths exist in both main air-gap and outer air-gap regions. The fringing flux paths in the main air-gap region could be neglected since the axial length is much bigger compared to the air-gap length, i.e. contribution of the fringing path

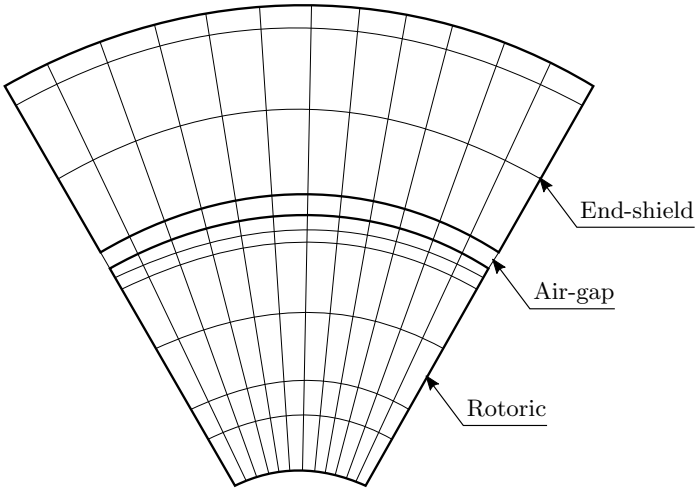

Fig. 3.14: Block mesh of the outer part

permeance to the total air-gap permeance is neglected. It is, however, not the case for the outer air-gap since the axial length of this air-gap (equals end-shield thickness) is much shorter. In addition, the cross section of the flux tube representing this outer air-gap fringing is significant.

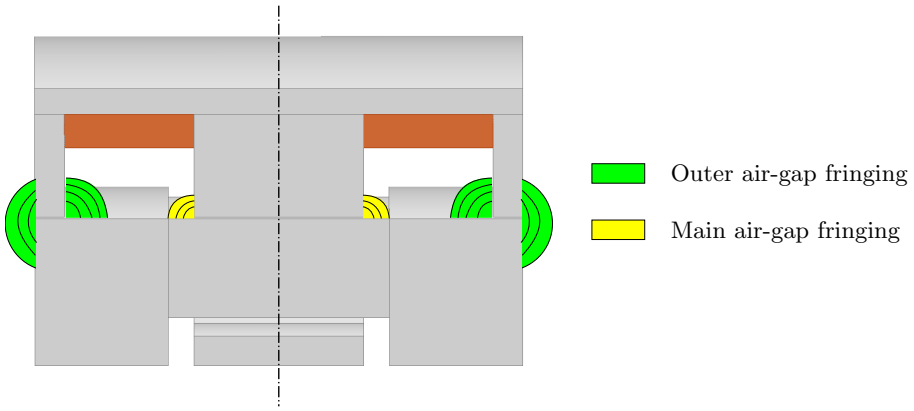

Fig. 3.15: Fringing flux in the air-gaps

The basic shape of the fringing flux is shown in Fig. 3.16.

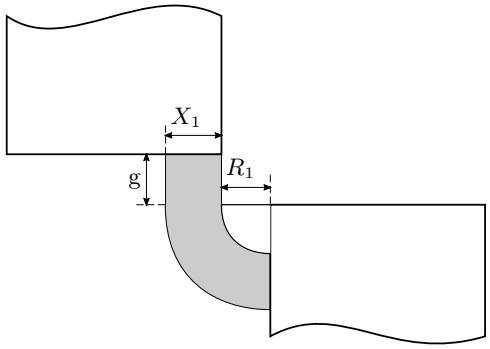

Fig. 3.16: Fringing flux shape for permeance calculation

The fringing permeances with quarter-ring and half-ring shapes are expressed by (3.23).

$$\begin{aligned} P_{\text{quater-circle}} &= \frac{2\mu_0 L_a}{\pi} \ln\left(1 + \frac{\pi X_1}{\pi R_1 + 2g}\right) \\ P_{\text{half-circle}} &= \frac{\mu_0 L_a}{\pi} \ln\left(1 + \frac{\pi X_1}{\pi R_1 + g}\right) \end{aligned} \tag{3.23}$$

In case of the fringing flux shown in Fig. 3.15, $R_1 = 0$. These permeances are then put in parallel to the permeance of the air-gap under the end-shield. It is shown that by considering these fringing flux paths, the outer air-gap reluctance reduces by 20%

3.2.3 Block connection

After having a mesh of elementary blocks with the nodes located at theirs centers, the next task is to make connections to establish reluctances and MMF sources between nodes. Two types of connection are possible, namely **one-to-one** (one block faces one another in a certain direction) and one-to-several connections (one block faces several blocks). The first one-to-one type is illustrated in Fig. 3.17. In this case, it is straightforward to calculate the reluctance between the node i and node j, which is the sum of individual reluctances of each block in the connection as (3.24).

$$R_{ij} = R_i + R_j \tag{3.24}$$

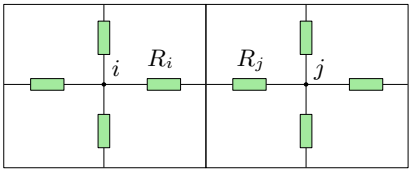

Fig. 3.17: One-to-one block connection

This kind of connection appears quite a lot in the meshes of stator or rotor where they are mostly row-by-column meshes. However, on the boundaries between the stator and air-gap or the rotor and air-gap, it is different since one block in the stator/rotor possibly faces several blocks in the air-gap as already shown in Fig. 3.12. This introduces **one-to-several** block connection. Fig. 3.18a) is for an example of a block, where the node i is facing three blocks $j1$, $j2$ and $j3$. In the EMCN, it is compulsory to have connection between every two nodes either zero permeance (not connected) or by a certain value. In Fig. 3.18a), physically there must be a certain flux passing between the node i and node $j1$. Therefore a non-zero permeance P_{ij1} between these two nodes must be presented. To this end, the block i could be assumed to be divided into three blocks $i1$, $i2$, and $i3$ with a same magnetic potential for each note (Fig. 3.18b)).

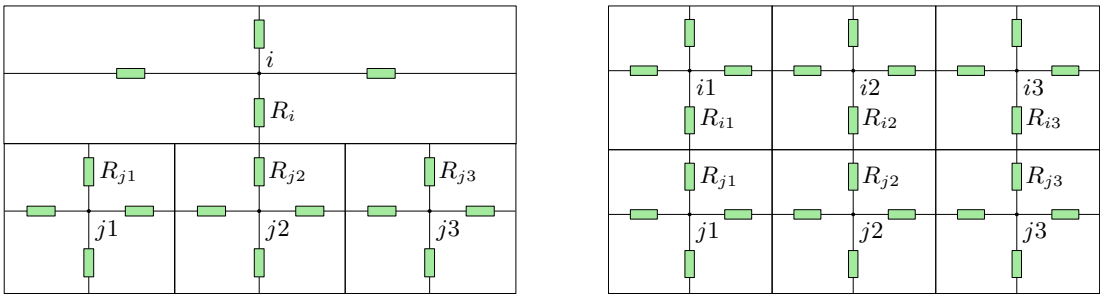

Fig. 3.18: One-to-several block connection. a) Blocks example. b) Equivalent connection

By transforming one-to-several connection into several one-to-one connections, the connection can be established, for instance as (3.25):

$$R_{ij1} = R_{i1j1} = R_{i1} + R_{j1} = 3R_i + R_{j1} \tag{3.25}$$

with the note that due to the equal division, $R_{i1} = R_{i2} = R_{i3} = 3R_i$.

3.2.4 EMCN model completeness

In the previous section, using two types of block connection (one-to-one and one-to-several), networks are defined for parts 1, 3 and 5 in Fig. 3.6. Permeance connection matrices $[P]$ as in (3.7) for these three parts will be computed individually. In order to have a single permeance matrix for the machine, it is necessary to combine these individual matrices and also interconnections between matrices, i.e. the connection in Z-direction (machine axial direction) should be made. The idea is visualized in Fig. 3.19.

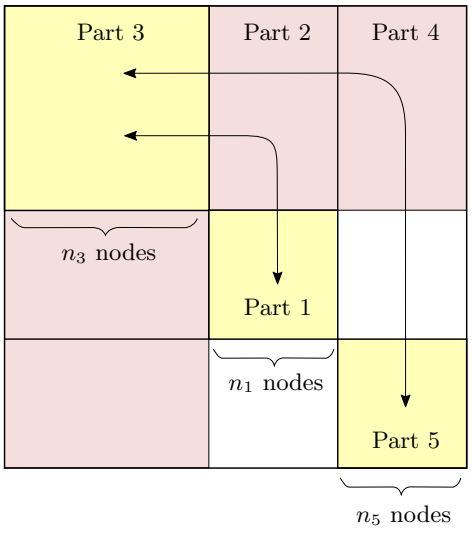

Fig. 3.19: Matrix combination and interconnection

Parts 1, 3 and 5 are firstly combined together without interconnections, i.e. permeance between

any node of a part and one of the other is set to zero. Matrices for parts 2 and 4 are then added to modify interconnections. Main points for Fig. 3.19 based on Fig. 3.6 are summarized as follows:

- Matrices for parts 1, 3 and 5 are all square and symmetric over their diagonals.
- Matrices for parts 1 and 5 are the same (due to the same geometries), i.e. $n_1 = n_5$.
- All nodes in the model are already presented in parts 1, 3 and 5, i.e. the total number of nodes: $n = n_3 + n_1 + n_5 = n_3 + 2n_1$.
- Arrow represents an interconnection existed between parts.
- Part 2 and 4 matrices are the same, the part 2 is for interconnection between part 1 and 3. Part 4 is for interconnection between part 5 and 3.
- The resultant matrix is symmetric over its diagonal.

These connecting parts (2 and 4) carry the outer stator yoke (reluctances and MMF sources from field windings), side PM (reluctances and MMF sources), rotor solid parts (in Z-direction), and leakage in Z-direction due to side PMs. In order to be more accurate, these connections are distributed along the tangential paths.

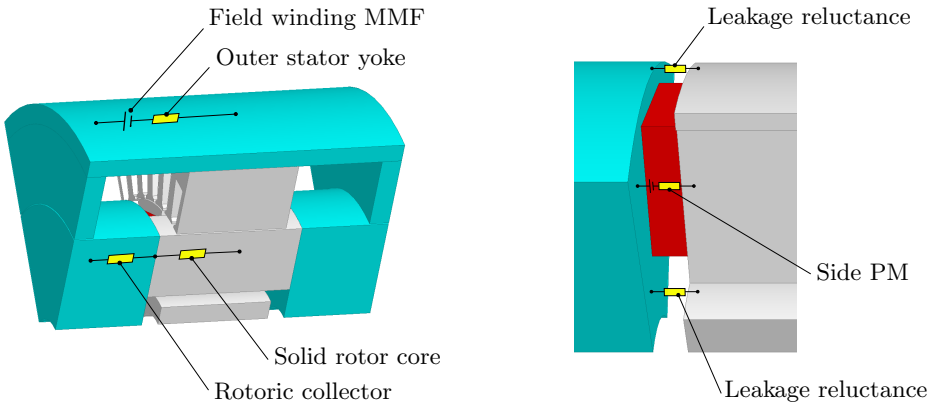

Fig. 3.20: Reluctances in axial direction. a) Due to core b) Due to side PM and leakage

Defining and computing these components will update connections between nodes, which were initially set to zero.

The flux source (the right hand side of (3.7)) will also be updated similarly as with the permeance matrix. The MMF sources due to armature windings are placed in the stator teeth with the net value is given by (3.26)

$$F_{\text{armature}} = N_t(i_1 - i_2) \tag{3.26}$$

where N_t is the number of armature turns, i_1 and i_2 are armature currents flowing in the winding accommodated two adjacent slots of the tooth. (3.26) is with an assumption that i_1 and i_2 are axially flowing in the same direction.

3.2.5 Magnetic saturation consideration

Having permeance and flux source matrices defined, scalar magnetic potentials are obtained by solving (3.7). This equation is simply rewritten as (3.27). In order to solve this equation, it would firstly come up with the nonlinear characteristic of the core material, which is represented by a magnetization curve.

$$\boldsymbol{PU} = \boldsymbol{\phi} \tag{3.27}$$

It is noted that most of elements in the permeance matrix $\boldsymbol{P}$ are zero. For example at aligned position, the number of nodes in the whole network is 533 resulting in a $533^2 = 284089$ element matrix $\boldsymbol{P}$. However, there are only 2837 non-zero elements as illustrated in Fig. 3.21, i.e. 1% of the total element number.

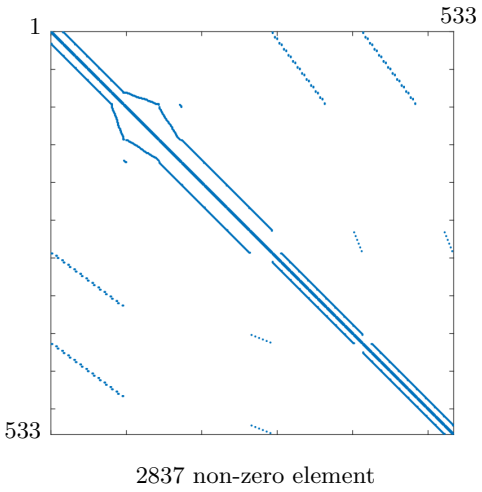

Fig. 3.21: Non-zero elements distribution in the permeance matrix $\boldsymbol{P}$

3.2.5.1 B-H magnetization curve approximation

For the electromagnetic modeling, there is often a need to analytically approximate the B-H magnetization curve. This will ensure a fast and smooth calculation compared to a direct lookup table using interpolated from the measured data. Although several functions could be used to represent the magnetization but if possible, a single function should present the whole range from the origin to the saturation region. This single function can make an easy application and simplify the process from the programming point of view. The choice of an approximation function depends mainly on the range, in which the approximation should be valid. For the linear range, the approximation function could be straightforward to handle. However, this becomes more complicated when extending to the saturated region that includes the knee point [66].

A simple approximation with power series either given by a single term as (3.28a) or by series

formula as (3.28b) [66].

$$B = aH^n \tag{3.28a}$$

$$H = a_0 + a_1 B + a_n B^n + a_m B^m \tag{3.28b}$$

where a_i, n and m are fitting coefficientsss.

Another possibility is to replace the curve by hyperbolas using Frölich's equation given by (3.29) [66]:

$$|B| = \frac{|H|}{a + b|H|} \tag{3.29}$$

Constants a and b can be determined from a plot of $1/|B|$ against $1/|H|$. The slope gives the coefficient a and the intercept gives b. However, this approximation is valid only for a maximum value of $B = 1/b$, and it often becomes necessary to subdivide the magnetization curve in several regions in order to obtain a good fit in the saturation range.

In a more complex manner, aiming to describe the magnetic properties of materials, one must know the flux density B, magnetic field strength H, and the intensity of magnetization M, which are correlated by (3.30) [60].

$$B = \mu_0(H + M) \tag{3.30}$$

With nonlinear magnetic materials, M is a complicated function of H, which can be approximated by a second order rational fraction given by (3.31) [67].

$$M = \frac{a_0 + a_1 H + a_2 H^2}{1 + b_1 H + b_2 H^2} \tag{3.31}$$

where a_i and b_i are coefficients, which can be generally determined by curve fitting technique given by (3.32).

$$\begin{cases} a_0 = 0 & a_1 = \chi & a_2 = \dfrac{\lambda M_s + \chi^2}{M_s + \alpha\chi} \\ b_1 = \dfrac{\alpha\lambda + \chi}{M_S - \alpha\chi} & b_2 = \dfrac{\lambda M_s + \chi^2}{M_s\,(M_s - \alpha\chi)} \end{cases} \tag{3.32}$$

where χ is the initial magnetic susceptibility, λ is the Rayleigh material constant [68], M_s is the saturation magnetization, and α is the Néel constant [69]. From (3.31) and (3.32), it can be observed that at weak fields ($H \to 0$), M approaches the initial magnetic susceptibility χ, and ($H \to +\infty$) M approaches zero at high fields.

In some magnetism problems, for example EMCN which will be discussed later on, an equation for the permeability is given by (3.33) [67].

$$\mu_r = \frac{B}{\mu_0 H} = 1 + \frac{a_1 + a_2 H}{1 + b_1 H + b_2 H^2} \tag{3.33}$$

From (3.33), at high fields, i.e. strong saturation, μ_r approaches 1 (air medium). However, in order to obtain this relation, some complex coefficients such as χ, M_S and α are needed making it more complex.

In [70], the permeability function can be more conveniently determined by using a fitting curve only from the measurement data. Firstly, the relation between the magnetization intensity and field strength is given by (3.34)which differs from (3.31).

$$M = \frac{\alpha H}{1 + \beta H} \tag{3.34}$$

where α/β equals to the saturation magnetization, M_s. In order to provide additional degrees of freedom in capturing the magnetization characteristic, (3.34) is modified to be (3.35):

$$M = \text{sig}(H) \sum_{k=1}^{K} \frac{m_k \left(|H|/b_k\right)^{n_k}}{1 + \left(|H|/b_k\right)^{n_k}} \tag{3.35}$$

where sig(.) function is to incorporate $H < 0$. Parameter m_k, b_k and n_k are then obtained by minimizing the error between the prediction and the measurement.

[70] defines permeability function $\mu_r(B)$ as (3.36)

$$\mu_r(B) = \frac{\frac{1}{K} \sum_{k=1}^{K} \left(\left| \frac{B}{m_k} \right|^{n_k} + a_k^{n_k} \right)^{\frac{1}{n_k}}}{\frac{1}{K} \sum_{k=1}^{K} \left(\left| \frac{B}{m_k} \right|^{n_k} + a_k^{n_k} \right)^{\frac{1}{n_k}} - 1} \tag{3.36}$$

where K is the approximation order, a_k, m_k and n_k are fitting coefficients. For strong fields ($H \to +\infty$ and hence $B \to +\infty$), $\mu_r \to 1$. Any optimization technique can be used to obtain coefficients in (3.36). Although this permeability function proposes a somewhat complex procedure to handle, but it is indeed flexible and applicable to a wide variety of materials with an unique closed expression in the whole range of magnetization region.

Coefficients obtained with a fifth order ($K = 5$) approximation are shown in Table. 3.3, where b_k is defined such that: $a_k = b_k/(b_k - 1)$.

Table 3.3: Fitting coefficients for the permeability function ($K = 5$)

k	1	2	3	4	5
b_k	1e10	3e6	694.32	722.95	111.25
n_k	6.68	11.82	7.05	12.61	39.97
m_k	19.91	1.85	49.99	21.46	17.55

Fitting curve (3.36) is sketched in Fig. 3.22.

The fitting curve is displayed in Fig. 3.23 in comparison with the original magnetization curve, a good fitting is observed.

3.2.5.2 Method to solve nonlinear EMCN equations

Newton Raphson (NR) method is often an efficient method when dealing with nonlinear equations. The basic form of this method is recalled shortly as follows: For an n-dimensional set of

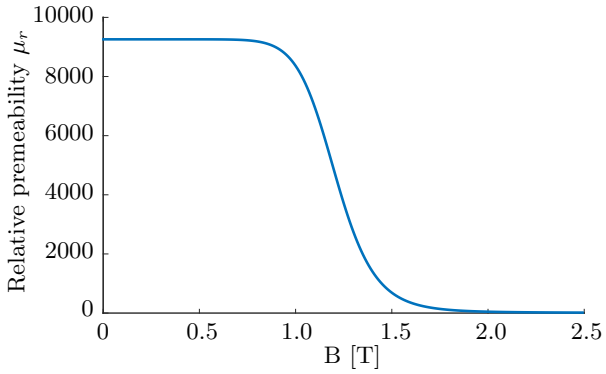

Fig. 3.22: Relative permeability as function of flux density

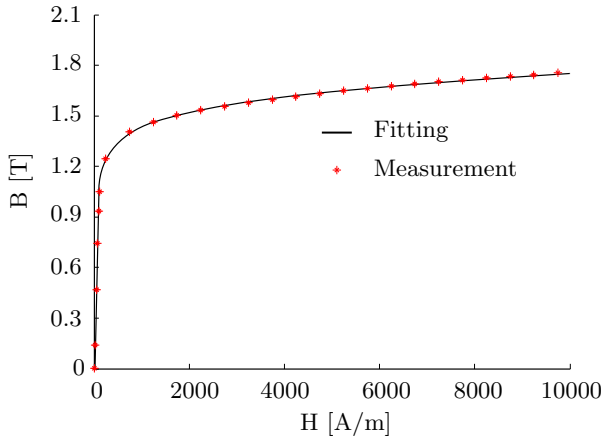

Fig. 3.23: Magnetization curve of the core material

nonlinear equations:

$$\boldsymbol{f}(\boldsymbol{x}) = 0 \tag{3.37}$$

where $\boldsymbol{f} = [f_1(x)\ f_2(x)\ ...\ f_n(x)]^{\mathrm{T}}$ and $\boldsymbol{x} = [x_1\ x_2\ ...\ x_n]^{\mathrm{T}}$

Supposing that $\boldsymbol{f}(\boldsymbol{x})$ is differentiable and an iterative process for solving (3.37) by the NR method can be defined at iteration $(k+1)$ as (3.38) [71]:

$$\boldsymbol{x}^{(k+1)} = \boldsymbol{x}^{(k)} - \left[\boldsymbol{J}\left(\boldsymbol{x}^{(k)}\right)\right]^{-1} \boldsymbol{f}\left(\boldsymbol{x}^{(k)}\right) \tag{3.38}$$

where $\boldsymbol{x}^{(k)}$ is the solution at the kth iteration. For the first iteration, an initial guess should be given. For an EMCN model, a constant permeability is often given to all reluctance blocks. $\boldsymbol{J}$ is the Jacobian matrix of $\boldsymbol{f}$ defined as (3.39):

$$\boldsymbol{J} = \frac{\delta \boldsymbol{f}}{\delta \boldsymbol{x}} = \begin{bmatrix} J_{11} & J_{12} & \cdots & J_{1n} \\ J_{21} & J_{22} & \cdots & J_{2n} \\ \cdots & & & \\ \cdots & & & \\ J_{n1} & J_{n2} & .. & J_{nn} \end{bmatrix} \tag{3.39}$$

where $J_{ij} = \dfrac{\delta f_i}{\delta x_j}$

Usually, the NR method requires more computations due to the differentiating process. Applying this method to EMCN, (3.27) is rephrased as (3.40)

$$\boldsymbol{f}(\boldsymbol{U}) = \boldsymbol{P}\boldsymbol{U} - \boldsymbol{\phi} = 0 \tag{3.40}$$

Taking derivative of $\boldsymbol{f}(\boldsymbol{U})$ with respect to $\boldsymbol{U}$ raises another difficulty since the permeance matrix $\boldsymbol{P}$ and source matrix $\boldsymbol{\phi}$ are unknown and are implicit functions of $\boldsymbol{U}$ as in (3.6c). So that instead of using NR method, another method, which is considered as a form of fixed point (FP) method will be used. Even though the drawback of this method is a slow convergence speed generally compared to the NR one.

The original form of the FP method is given by (3.41):

$$\boldsymbol{f}(\boldsymbol{x}) = \boldsymbol{x} \tag{3.41}$$

Solution at $(k+1)$th iteration is expressed as (3.42):

$$\boldsymbol{x}^{(k+1)} = \boldsymbol{f}(\boldsymbol{x}^{(k)}) \tag{3.42}$$

The iterative process (3.42) is converged at kth iteration if (3.43) is satisfied.

$$\left\| \frac{\boldsymbol{x}^{(k+1)} - \boldsymbol{x}^{(k)}}{\boldsymbol{x}^{(k)}} \right\|_{\infty} \leq \varepsilon \tag{3.43}$$

(3.43) means that the maximum local error between two consecutive iterations is not bigger than a predefined tolerance ε.

Although the objective of (3.27) is to find potential at n nodes of the network but it can be turned into finding permeabilites of n blocks. Initially, a constant permeability $\mu^{(0)}$ is given to all blocks. At kth iteration, having known permeabilities $\boldsymbol{\mu}^{(k)}$, node potential $\boldsymbol{U}^{(k)}$ is obtained by (3.44):

$$\boldsymbol{U}^{(k)} = \left(\boldsymbol{P}^{(k)}\right)^{-1} \boldsymbol{\phi}^{(k)} \tag{3.44}$$

From the newly solved $\boldsymbol{U}^{(k)}$, the flux density between nodes i and j is calculated as (3.45).

$$B_{ij}^{(k)} = \frac{\left(U_i^{(k)} - U_j^{(k)} - F_{ij}\right) P_{ij}^{(k)}}{S_{ij}} \tag{3.45}$$

with quantities between nodes i and j: F_{ij} is a MMF which might be presented, $P_{ij}^{(k)}$ is the permeance at kth iteration and S_{ij} is cross section of the reluctance path. F_{ij} and S_{ij} are unchanged throughout iterations.

From (3.14) and (3.45), flux densities of all blocks will be easily obtained and permeabilites of all blocks $\boldsymbol{\mu}^{(k*)}$ can be recalculated by using the permeability function (3.36).

The stopping criterion is given by (3.46).

$$\left\| \frac{\boldsymbol{\mu}^{(k*)} - \boldsymbol{\mu}^{(k)}}{\boldsymbol{\mu}^{(k)}} \right\|_{\infty} \leq \varepsilon \tag{3.46}$$

To summarize, Fig. 3.24 displays the block diagram for the EMCN model formulation and solving. There are some main points should be remarked as follows:

- Only the air-gap mesh and armature winding's MMFs are rotor-position dependent, so all meshes and PM's MMFs are defined at the beginning.
- In order to save computational time, reluctance calculations of linear reluctances (PM, air elements in the slots) are accomplished right after the preliminary meshes are defined, and elements in the air-gap right after air-gap mesh is defined.
- Even though the stopping criterion is set as (3.46), but the maximum number of iterations could be added as a supplementary criterion to prevent an infinite iteration loop when no converged solution found according to (3.46).

3.2.5.3 Examination of the proposed method with a simple case

In this part, a simple 2-D electromagnetic field will be used to examine the proposed algorithm. The model to be analyzed will be a C-core being excited by a DC field winding (wrapped inside the C-core). The excitation current variation is large so as to examine the saturation. The quantity to be calculated is the flux flowing in the core.

Fig. 3.25a) shows the dimension of the C-core model and Fig. 3.25b) is for the meshing idea. Accounting for the fringing flux of the air-gap, the model is bound by an air volume with a dimension of 20 mm beyond each side. The meshing will be tried with a huge number of elements to examine the performance of the proposed algorithm with the induction map in comparison with one obtained by FEM. The result will be the flux passing through the red line in Fig. 3.25b).

In detail, the air-gap length g is set to 2 mm. The induction map, shown in Fig. 3.26 at highly saturated zone, reveals a good accordance between two analyses.

The comparisons between the EMCN and FEM are displayed in Fig. 3.27. As it can be seen, a good accordance between two analyses even at very high saturation level.

3.3 Results and comparisons with 3-D FEM

Firstly, Fig. 3.28 compares the flux linkage at no-load according to field currents in both the flux weakening (I_{dc} = -3 A) and flux reinforcing (I_{dc} = 3 A) modes. As it can be seen, the EMCN model reveals very close results versus ones retrieved by FEM. This can be explained by the

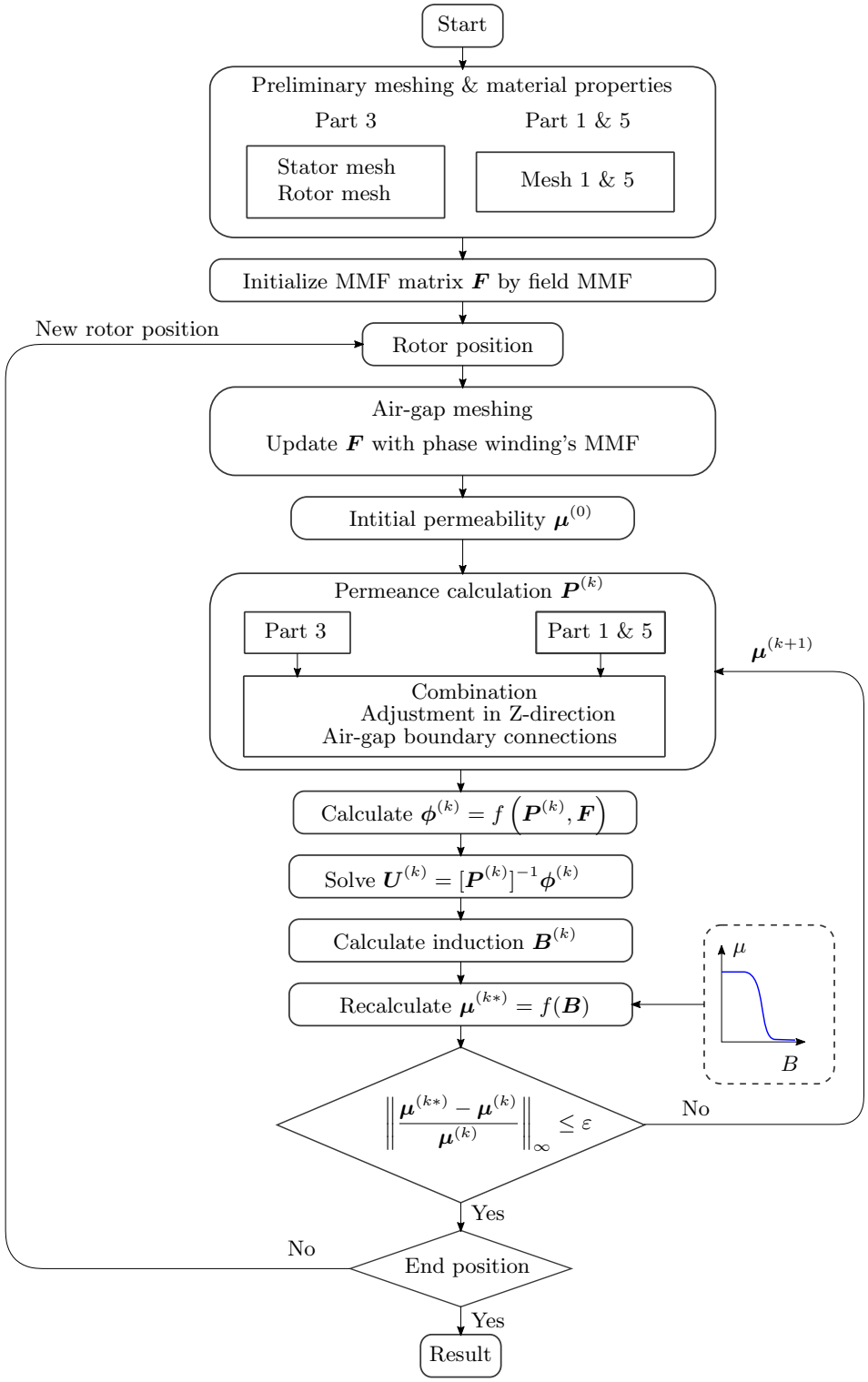

Fig. 3.24: EMCN algorithm block diagram

difficulty of a perfect machine's modeling in the 3-D configuration. When the field current is injected (either positive or negative), this adds more influences in the axial direction and other directions rather than just tangential and radial ones.

The flux control capability over a wide range of the field current is demonstrated in Fig. 3.29.

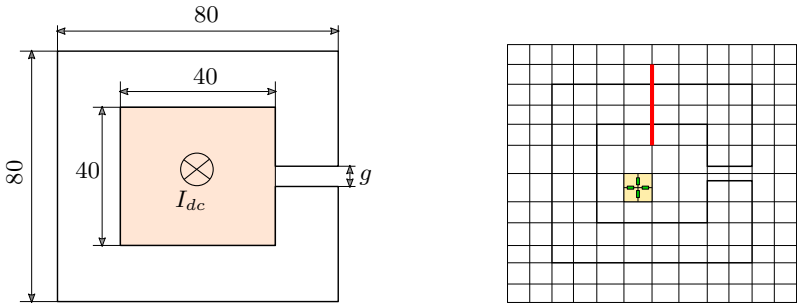

Fig. 3.25: A C-core sample. a) Dimension [mm]. b) Meshing strategy

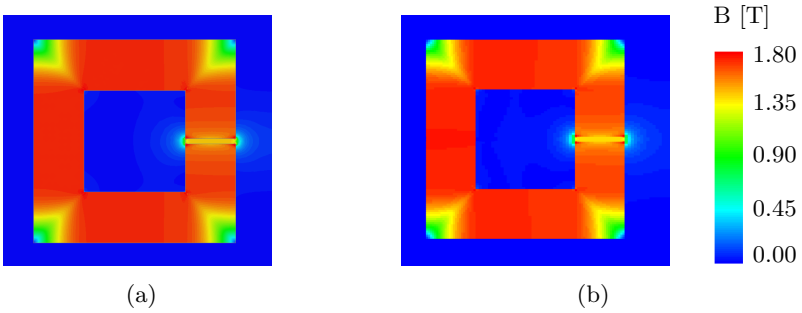

Fig. 3.26: Flux density distribution comparison at MMF = 5000 AT. a) 2D FEM. b) EMCN

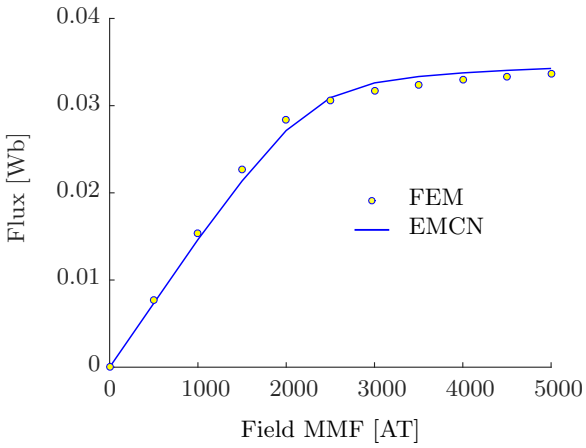

Fig. 3.27: Calculated flux comparison

The non-linearity examination is also performed with good agreement except for a very high saturation situation due to the modeling imperfection as explained above.

The tangential and radial components of the air-gap flux density distribution for one pole pair at aligned position, no-load and field current are set to zero ($I_{dc} = 0$ A) are displayed in Fig. 3.30

A good comparison agreement is seen for radial air-gap flux density; however, a bigger difference is seen with the tangential components, this can be explained as the tangential flux density is very prone to the mesh around the air-gap region. The FEM analysis for DESM in this research is 3-D, so that a very fine mesh is prohibited due to the computer's memory. As observed in

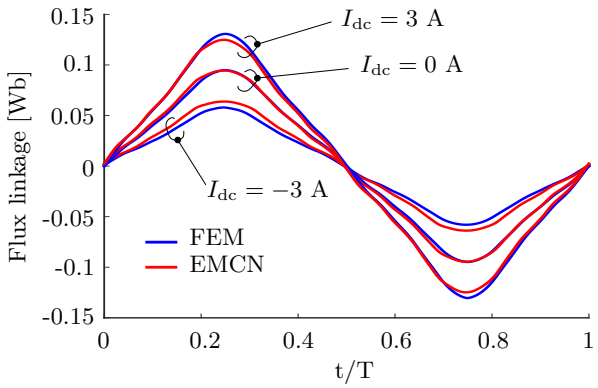

Fig. 3.28: Flux linkage comparison at no-load due to field current variation

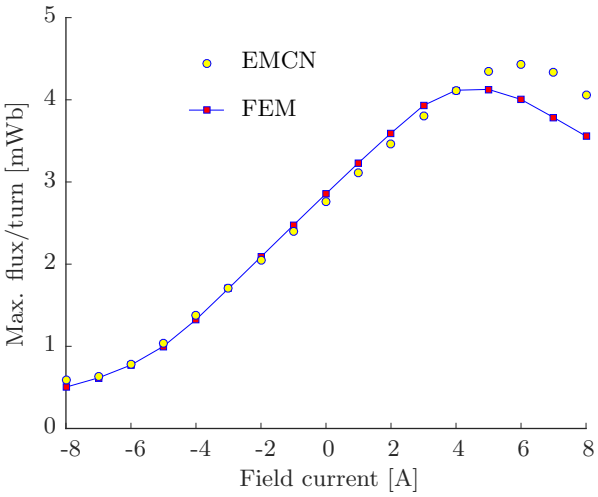

Fig. 3.29: Maximum flux at no-load according to field current variation

Fig. 3.30a), the radial flux density is asymmetric between the first half and second half of one pole pair. This happens owing to the homopolar topology of the studied DESM as explained in 2.4.2.1, in which when the field current is set to zero, air-gap flux densities in the concentrated area are reported to be almost double compared to ones in the unconcentrated region. Also, the flux densities below the slots are substantially reduced.

The electromagnetic torque is again computed by using the flux MMF method (calculated with flux-MMF method presented in chapter 2). The instantaneous torque for an armature current is shown in Fig. 3.31 and Fig. 3.32 is for average torque according to the armature current variation. It is noted that the rated armature current is 10 A. Good agreements between the EMCN and FEM methods are reported in these comparisons. The torque comparison is also shown together with the linear torque computed by EMCN to visualize the saturation impact.

The accuracy and computation time for the torque comparison between the EMCN and FEM analyses are summarized in Table. 3.4.

As it can be seen, the relative maximum error is about 2.2% revealing a very good EMCN modeling result. The mesh generation by the FEM consists of about 58000 tetrahedral elements,

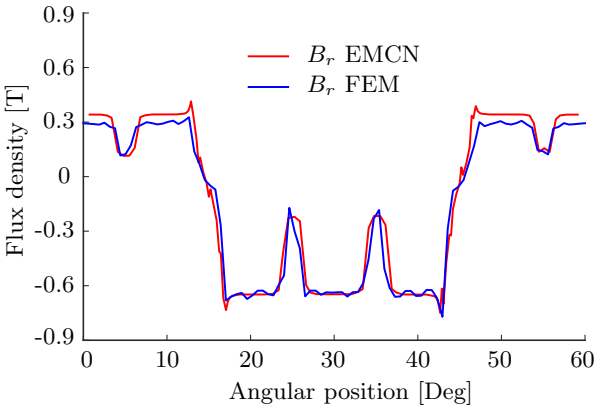

(a)

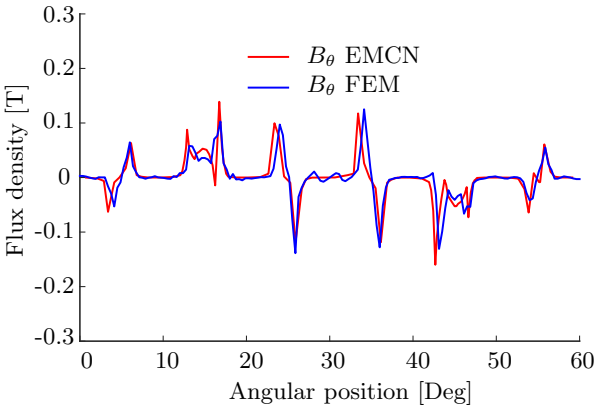

(b)

Fig. 3.30: Air-gap flux density distribution at no-load, $I_{dc} = 0$ A, aligned position. a) Radial component. b) Tangential component

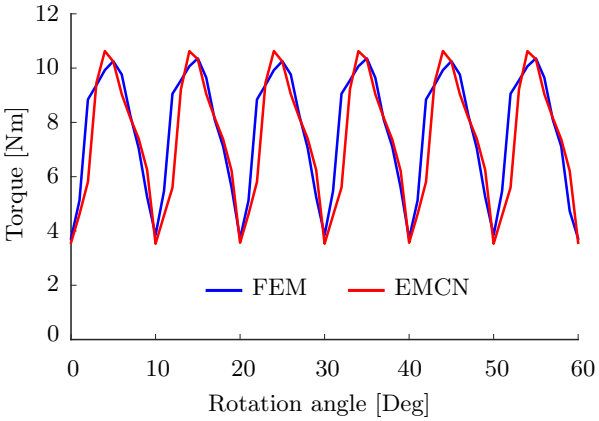

Fig. 3.31: Instantaneous electromagnetic torque at the armature current of 8 A, $I_{dc} = 0$ A

while the number of nodes for EMCN is about 530, which is 110 times smaller. The computation time per rotor position for the EMCN is 300 times as fast as the one with the FEM, which is 0.2 s compared to 58 s. From these points, the aforementioned advantage of the EMCN method is confirmed: accurate enough but much less time consuming compared to the FEM method.

The mean torque comparison at a wider range of the armature and excitation currents are

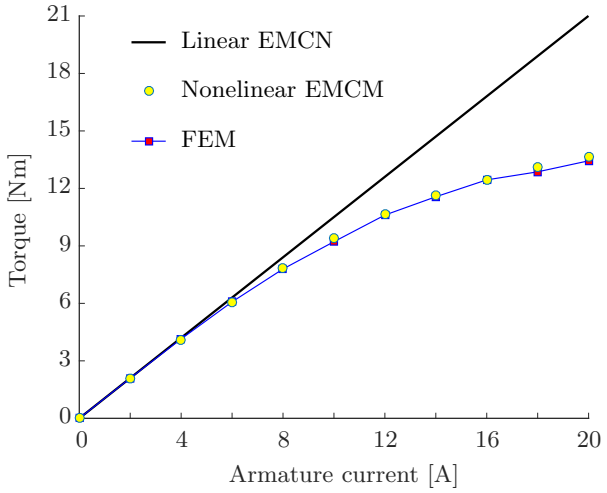

Fig. 3.32: Generated torque according to armature currents, $I_{dc} = 0$ A

Table 3.4: Comparison between the EMCN and FEM methods based on torque calculation

Accuracy											
Armature current [A]	0	2	4	6	8	10	12	14	16	18	20
Error [%]	NaN	1.8	1.3	0.5	0.9	2.2	0.6	0.6	0.2	1.8	1.7

Mesh & Average time		
	Mesh generation	Computation time/point
EMCN	530 nodes	0.2 s
FEM	58000 elements	58 s

shown in Fig. 3.33. A good accordance between two results.

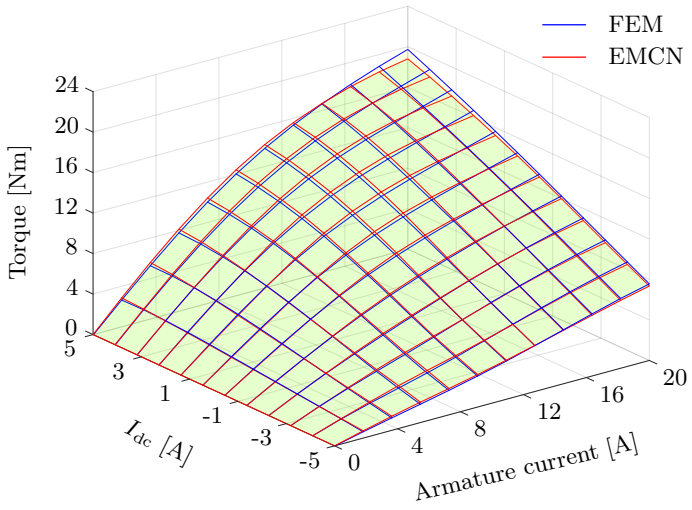

Fig. 3.33: Average torque comparison

3.4 Iron loss calculation

In order to improve machine's efficiency, the very first step has to accomplish is the losses determination. Different losses exist in the machine including core losses, copper losses of the both armature and field windings, mechanical losses, and stray load losses. Among these losses, mechanical and stray load losses are not calculated by the electromagnetic analysis. This part focuses on the iron loss calculation since copper loss is straightforwardly calculated as (3.47):

$$P_{\mathrm{Cu}} = \sum_{i=1}^{n} I_i^2 R_i \tag{3.47}$$

where I_i and R_i is current and resistance of the ith winding (either the armature or field windings), respectively. The winding resistance can be obtained easily based on the winding geometry.

3.4.1 Iron losses models

The iron loss calculation is the subject of numerous researches. An accurate computation of core loss must require detail information on microscopic scale behavior of the magnetic domain structure. This task is usually too challenging. Therefore, core losses formulations based on the sample experimental data with assumptions are normally utilized.

A simple and common formulation that characterizes core losses is the power equation by Steinmetz [72] given by (3.48).

$$P_{\mathrm{Fe}} = k f^{\alpha} \hat{B}^{\beta} \tag{3.48}$$

where $\hat{B}$ is the peak flux density of a sinusoidal waveform with frequency f and k, α and β are material dependent coefficients.

This equation is only valid for a limited frequency and flux density ranges. Another limitation is that the flux density in (3.48) must be sinusoidal, which is not applicable for almost the cases, where harmonics are usually presented. Authors of [73] tried to overcome this limitation by taking into account the fact that the loss due to the domain wall motion has a direct dependency of dB/dt. The modified Steinmetz equation given by (3.49) introduces a dependence of core loss on the flux density variation, i.e. it is able to deal with distorted waveforms.

$$P_{\mathrm{Fe}} = \frac{1}{T} \int_0^T k_i \left| \frac{dB}{dt} \right|^{\alpha} \left(\hat{B} \right)^{\beta - \alpha} dt \tag{3.49}$$

where k_i, α and β are material dependent coefficients. It should be noted that coefficients α and β are the same as ones in (3.48).

The advantages of (3.49) is that it considers multiple peaks occurring in the flux density waveform.

Model proposed by Bertotti [74] expressed as (3.50) is one of the most common model. In this model, the core loss formulation is separated into three terms namely the hysteresis (P_h), eddy current (P_e), and anomalous (P_a) losses.

$$\begin{aligned} P_{\text{Fe}} &= P_h + P_e + P_a \\ &= k_h f \hat{B}^{\alpha} + k_e f^2 \hat{B}^2 + k_a f^{1.5} \hat{B}^{1.5} \end{aligned} \tag{3.50}$$

It should be noted that (3.50) cannot estimate accurately eddy current and anomalous losses since it only handles the peak flux densities. (3.51) [75] below presented in time domain is a solution.

$$P_{\text{Fe}} = k_h f \hat{B}^{\alpha} + \frac{k_e}{2\pi^2 T} \int_0^T \left(\frac{dB}{dt} \right)^2 dt + \frac{k_a}{8.763T} \int_0^T \left| \frac{dB}{dt} \right|^{1.5} dt \tag{3.51}$$

where α, k_h, k_e and k_a are material dependent coefficients, respectively. f is the frequency of the flux density with peak $\hat{B}$, and B is the instantaneous flux density. T is the flux flux density wave form period.

The eddy current loss coefficient k_e depends onthe material's conductivity σ and its thickness d as (3.52).

$$k_e = \frac{\sigma d^2 \pi^2}{6} \tag{3.52}$$

In some cases, the anomalous loss can be merged into the eddy current loss, and therefore the eddy current loss coefficient k_e will be adjusted accordingly. In fact, all of these loss coefficients are conveniently determined by using measurement fitting based on the sinusoidal flux densities. However, the formulation (3.50) is also valid for non-sinusoidal flux densities. This features an advantage over the formulation (3.48). The core loss formulation based on (3.50) with two components: hysteresis and eddy current losses will be used since it is the most widely applied one.

Another formulation, which is slightly different from (3.50), was proposed in [76], author agreed to separate the core loss into the hysteresis and eddy current components, the eddy current loss calculation is the same as in (3.50), but a new formulation for the hysteresis loss is proposed as (3.53).

$$P_h = f(k_{h1} \Delta B + k_{h2} \Delta B^2) \tag{3.53}$$

where k_{h1} and k_{h2} are hysteresis loss coefficients, ΔB is peak-to-peak flux density.

In the following parts, details about the eddy current and hysteresis losses based on formulation (3.50) will be discussed especially considering flux density waveforms other than sinusoidal ones.

3.4.2 Iron loss with non-sinusoidal flux densities

Core materials is rarely exposed to purely sinusoidal flux density, harmonic contents usually present. This section investigates on how non-sinusoidal flux densities affect the iron loss computation method. Firstly, (3.51) is recalled as (3.54) with a form of two components, where

the anomalous loss is merged into the eddy current loss. Coefficients are determined by the measurement fitting.

$$P_{\text{Fe}} = k_h f \hat{B}^{\alpha} + \frac{k_e}{2\pi^2 T} \int_0^T \left(\frac{dB}{dt} \right)^2 dt \tag{3.54}$$

The very common approach to handle a distorted signal is to decompose it into harmonics. The distorted waveform causes no change calculation for the eddy current loss since it directly works on the time domain. Indeed, the eddy current loss resulted from a distorted waveform equals to the sum of eddy current losses caused by its individual harmonic components.

However, the summing-up approach is not valid for the hysteresis loss because of the fact that this kind of loss simulate the B-H hysteresis loop due to the applied flux density. Depending on the magnitude and phase of the flux density harmonics, the resultant waveform may contain minor loops (flux density reversals). As an example shown in Fig. 3.34, a flux density containing a significant third harmonic causing flux reversals. If the hysteresis loss is calculated based on the peak value $\hat{B}$ only as $P_h = k_h f \hat{B}^2$, the result is inaccurate. The loss calculation must contain additional components characterized by the area bound by these minor loops. The areas of these loops are again proportional to the all components ΔB_i.

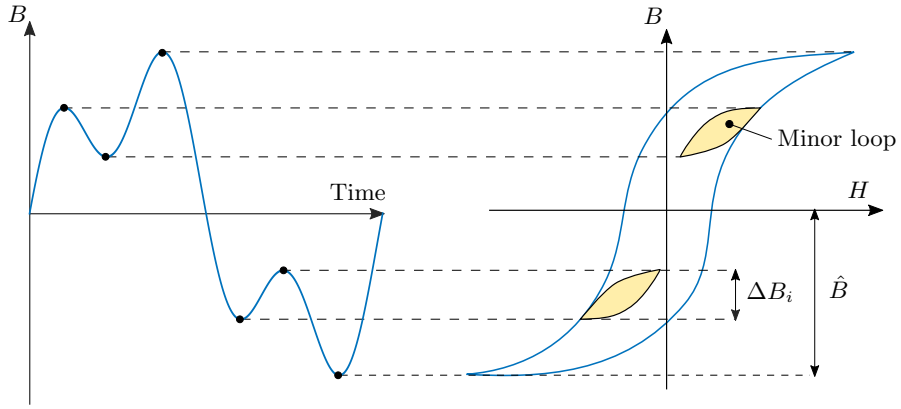

Fig. 3.34: Hysteresis loop with minor loops

Given that the total loss depends on the magnitude of every local minor loops and their positions. An exact correction may result in a complicated function of these factors. Author of [77] proposed a simplified process assuming that the correction can be correlated with the unweighted algebraic sum the minor loops. According to that, the hysteresis loss caused by a non-sinusoidal flux density is adjusted as (3.55).

$$P_{h,\text{dist}} = P_{h,\text{sine}}(\hat{B}) \cdot CF \tag{3.55}$$

where $P_{h,\text{sine}}(\hat{B})$ is the hysteresis loss caused by a sinusoidal waveform with the same peak flux density $\hat{B}$, and CF is a correction factor defined as (3.56).

$$CF = 1 + \frac{k}{\hat{B}} \sum_1^n \Delta B_i \tag{3.56}$$

where k is a coefficient in the range 0.6 to 0.7. ΔB_i is the magnitude of ith minor loop, and n is the number of minor loops. ΔB_i are calculated by working on all the local maximum and minimum points in the flux density waveforms.

An example to demonstrate the proposed approach for correction factor is shown below. A flux density waveform is assumed to have only third harmonic component.

$$B(t) = \sin(\omega t) + B_3 \sin(3\omega t + \varphi) \tag{3.57}$$

The amplitude ranges from 20% to 100% of the first harmonic amplitude, and the phase angle φ varies between 0 and 180 electrical degree. Fig. 3.35 gives effects of the third harmonic's phase angle on ΔB_i for the case 40%, and the correction factors are shown in Fig. 3.34 according to different cases (coefficient k is chosen as 0.65). As it will be observed, when the third harmonic is in phase with the fundamental one, the correction factor gets biggest. At a low value of third harmonic's amplitude and a big phase angle, the correction is unity, i.e. no correction is made. This is because of no minor loop presented even though the flux density waveform is not sinusoidal. The hysteresis loss is computed based on the peak flux density only. A maximum value of about 65% correction when the third harmonic has the same amplitude order as the fundamental one and two components are in phase.

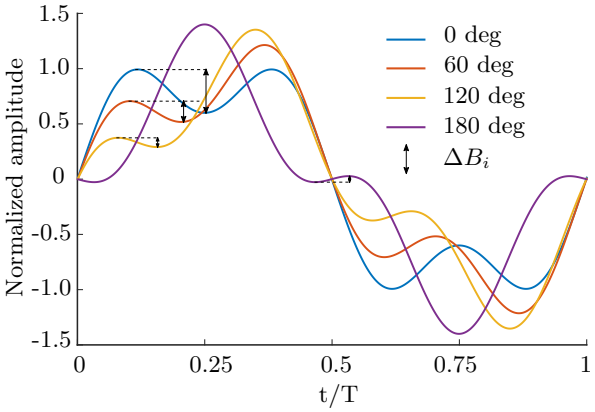

Fig. 3.35: Effect of third harmonic's phase angle on minor loop

Fig. 3.37 shows flux densities in the stator tooth due to the field current variation. As it will be seen, in the field weakening mode, the minor loop amplitude tends to increase although the one of the major loop decreases globally. The corrections for minor loops are small.

The core loss formulation according to (3.54) is adaptive to flux densities flowing in a single direction (1-D). In electrical machine, there exists some regions, where fields are essentially rotational. A FEM software package usually provides an option to calculate flux densities in orthogonal X and Y components (radial and tangential components are then deduced from orthogonal ones by a proper transformation based on the angular information). The resultant iron loss is commonly calculated by summing up separate loss components as in [78]. With a formation of elementary block in EMCN consisting of four branches, which are actually in

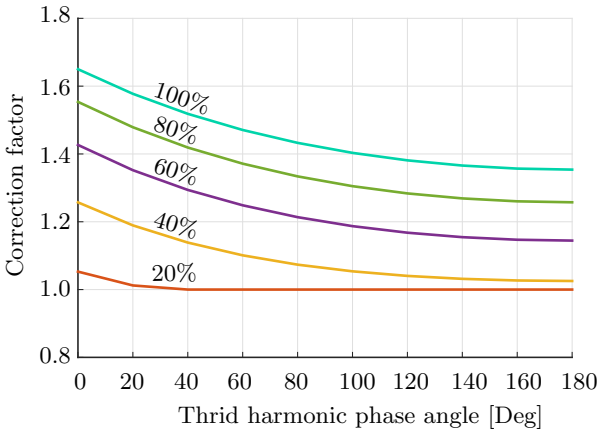

Fig. 3.36: Correction factor according to amplitude and phase angle of third harmonic

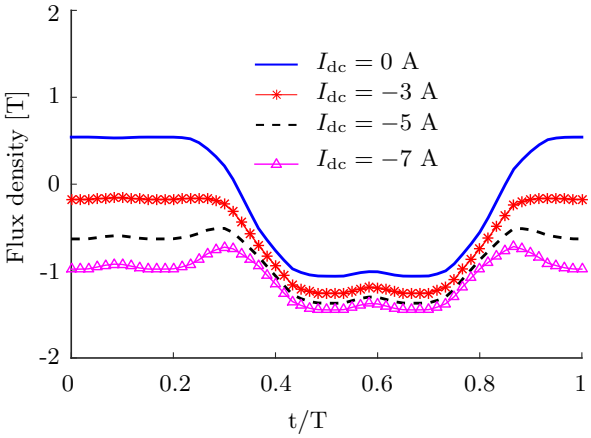

Fig. 3.37: Flux density in the middle of stator tooth at no-load according to various I_{dc}

tangential and radial directions. The iron loss of a block is the sum of loss components in all branches, and the total iron loss of the machine equals the sum of ones in all individual blocks. Flux density loci of some sample points, which are marked in Fig. 3.38, are shown in Fig. 3.39.

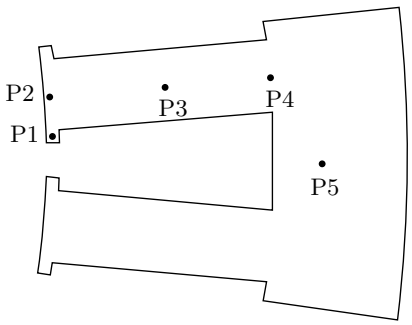

Fig. 3.38: Sample points in the stator. P1 - Tooth tip side, P2 - Tooth tip middle, P3 - Tooth middle, P4 - Tooth junction, P5 - Yoke middle

One should be pointed out that, due to the homopolar flux paths, most of flux density variations consist of DC components as in Fig. 3.37. This actually changes hysteresis loop as demonstrated

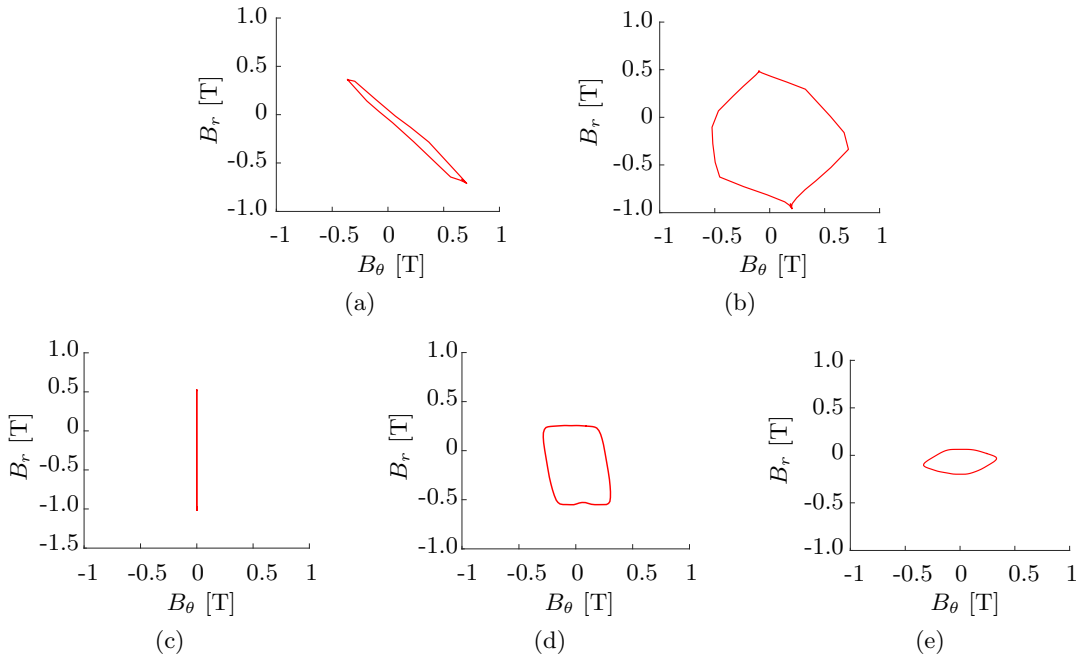

Fig. 3.39: Flux density loci at no-load, $I_{\mathrm{dc}} = 0$. a). P1 - Tooth tip side. b) P2 - Tooth tip middle. c) P3 - Tooth middle. (d) P4 - Tooth junction. (e) P5 - Yoke middle

in Fig. 3.40 and increases the hysteresis loss as in [79].

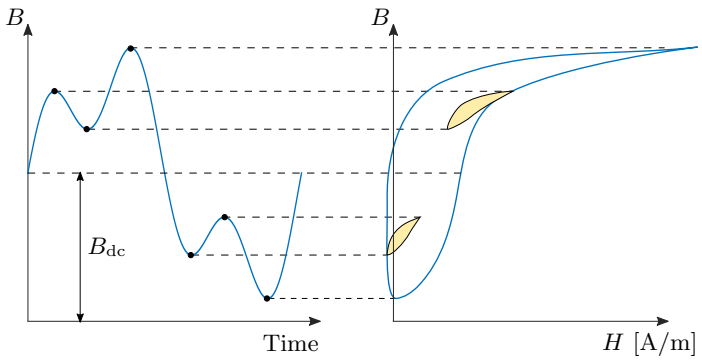

Fig. 3.40: DC-biased flux density

A factor, defined as (3.58) [79], is introduced in order to account for this hysteresis loss increase.

$$\varepsilon(B_{\mathrm{dc}}) = 1 + k_{\mathrm{dc}} B_{\mathrm{dc}}^{\gamma} \tag{3.58}$$

where B_{dc} is DC-biased flux density, k_{dc} and γ are coefficients determined from experiments. In [79], $k_{\mathrm{dc}} = 0.65$ and $\gamma = 2.1$ are expected to approximately applicable to some cases without causing a big difference. Considering the case with $B_{\mathrm{dc}} = 0.3$, ε equals 1.052, i.e. 5.2% increase in the hysteresis loss.

3.4.3 Losses in permanent magnets

Since PM has its own electrical resistivity, flux density variations in PMs will produce losses including the eddy current loss and probably the hysteresis loss. The present of the hysteresis loss depends on whether or not the magnet's polarization is reversed. If the field strength variation is large enough and varies between a positive and a negative values, a hysteresis loop may be similar as that of a soft magnetic material. Fortunately, in the DESM prototype being considered, the PM demagnetization does not strongly occur as mentioned in 2.4.3.1. The flux density in the azimuth PM is shown in Fig. 3.41 (This pattern for side PMs is quite similar).

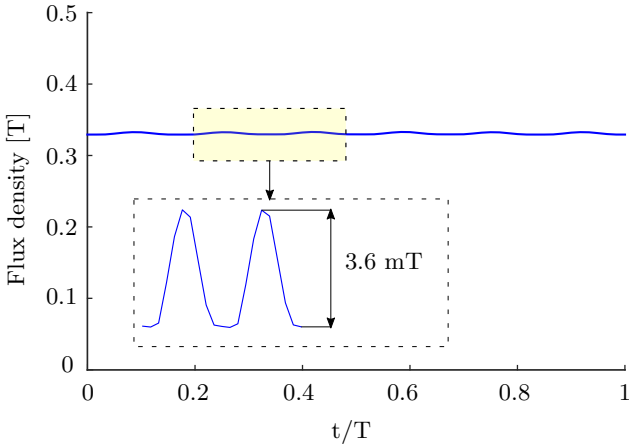

Fig. 3.41: Flux density in a azimuth PM at no-load, $I_{\mathrm{dc}} = 0$

With a very small flux density variation with unchanged magnet polarization, it can be properly assumed that hysteresis losses in PMs are negligible. This shows an advantage of interior PM machines versus surface mounted PM ones in term of the low PM loss. In case of surface mounted PM machines, PM may be exposed to a large air-gap flux density variation and the PM losses, therefore, increase.

Regarding the eddy current loss, the most general calculation for a rectangular core with a constant permeability developed by Mukerji *et al.* [80] will be used. As shown in Fig. 3.42, a basis rectangular model with the thickness d, width W being excited by a surface current density:

$$J_0 = NIe^{j2\pi ft} \tag{3.59}$$

where N is number of coil turns, I is current amplitude, and f is applied frequency.

The magnetic field with a density B will be created perpendicularly to the sample's surface, which is the X-Y plane in Fig. 3.42. Results are based on solving linear Maxwell's equations applied to the linear material of PM ($\mu_r = 1$).

The unit volume eddy current loss is given by (3.60) (refer to [80] for more details)

$$p_c = \frac{16B_m^2 f}{\mu\pi} \sum_{p=1}^{\infty} \frac{1}{(2p-1)^2} \left(\frac{A}{d} + \frac{B}{W} \right) \tag{3.60}$$

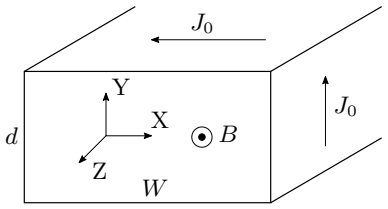

Fig. 3.42: A rectangular core with surface current density J_0

where:

$$A = \frac{\alpha_{mi}\sinh(\alpha_{mr}d) - \alpha_{mr}\sin(\alpha_{mi}d)}{\left(\alpha_{mr}^2 + \alpha_{mi}^2\right)\left[\cosh(\alpha_{mr}d) + \cos(\alpha_{mi}d)\right]}$$

$$B = \frac{\beta_{mi}\sinh(\beta_{mr}W) - \beta_{mr}\sin(\beta_{mi}W)}{\left(\beta_{mr}^2 + \beta_{mi}^2\right)\left[\cosh(\beta_{mr}W) + \cos(\beta_{mi}W)\right]}$$

$$\alpha_{mr} = \frac{1}{\sqrt{2}}\left[\sqrt{\left\{\left(\frac{m\pi}{W}\right) - \omega^2\mu\epsilon\right\}^2 + \omega^2\mu^2\sigma^2} + \left\{\left(\frac{m\pi}{W}\right) - \omega^2\mu\epsilon\right\}\right]^{\frac{1}{2}}$$

$$\alpha_{mi} = \frac{1}{\sqrt{2}}\left[\sqrt{\left\{\left(\frac{m\pi}{W}\right) - \omega^2\mu\epsilon\right\}^2 + \omega^2\mu^2\sigma^2} - \left\{\left(\frac{m\pi}{W}\right) - \omega^2\mu\epsilon\right\}\right]^{\frac{1}{2}}$$

$$\beta_{nr} = \frac{1}{\sqrt{2}}\left[\sqrt{\left\{\left(\frac{m\pi}{d}\right) - \omega^2\mu\epsilon\right\}^2 + \omega^2\mu^2\sigma^2} + \left\{\left(\frac{m\pi}{d}\right) - \omega^2\mu\epsilon\right\}\right]^{\frac{1}{2}}$$

$$\beta_{ni} = \frac{1}{\sqrt{2}}\left[\sqrt{\left\{\left(\frac{m\pi}{d}\right) - \omega^2\mu\epsilon\right\}^2 + \omega^2\mu^2\sigma^2} - \left\{\left(\frac{m\pi}{d}\right) - \omega^2\mu\epsilon\right\}\right]^{\frac{1}{2}}$$

where B_m is maximum induction (at the surface), $m = 2p - 1$, σ is material conductivity, and ϵ is material permittivity.

This solution can handle the case where the field inside the core is not uniform, for instance, the lamination case). If considering skin depth given by (3.61).

$$\delta = \sqrt{\frac{2}{\omega\sigma\mu}} \tag{3.61}$$

It can be suggested that if one of three factors: the frequency - ω, the conductivity - σ, and the permeability - μ becomes small such that the skin depth effect is relatively large compared to the core thickness, the conventional coefficient $k_e = \dfrac{\sigma d^2\pi^2}{6}$ used in the eddy current loss formulation is still valid, even with the case where d is not in order of a lamination thickness. Moreover, (3.60) is interesting since it treats the width and thickness of the sample equally.

(3.60) can be applied to ferrite PMs (the electrical conductivity of about $\sigma = 10^{-2}$ S/m) in the DESM model. This low conductivity makes PM eddy current losses approximately zero. In cases when rare earth magnets are used the eddy current loss will much increases. This is due to the electrical conductivity the rare earth PM is about $\sigma = 6.25 \times 10^5$ S/m, which is much higher compared to ferrite PMs.

Note that, in the DESM model, several parts are solid, the hysteresis loss calculations for these parts similar, but the eddy current losses are different. The same approach to calculate the

eddy current loss in PM above can be used. However, the difficulty is that the core material is nonlinear, and the core shape is not rectangular. Even though the flux density fluctuation in these parts are small but due to the solid core, the eddy current loss is hardly predicted. So as to verify this prediction, the core loss due to eddy current will be computed by using the FEM in next part.

3.4.4 Core loss calculation validations

3.4.4.1 Eddy current loss calculated by FEM

Eddy current loss computations in the solid cores by using the FEM is conducted for a wide range of field currents. By using the FEM, these computations are performed by giving the solid cores a conductivity of 10^7 S/m. Table. 3.5 shows eddy current losses for solid core parts (refer to Fig. 2.25 in chapter 2) at 1000 rpm, no-load according to field currents.

Table 3.5: Eddy current losses for solid parts at 1000 rpm, no-load condition

Field current [A]	-7	-5	-3	0	3	5	7
Eddy current loss [W]	0.052	0.223	0.001	0.003	0.009	0.107	1.373

Despite the fact that, in order to have an accurate and reliable result by dynamic eddy current loss calculation, a very fine mesh should be adopted, this is quite challenging to the 3-D FEM due to limits of time and computer resources. But from Table. 3.5, it could arrive at the negligibility of eddy current losses due to solid parts.

3.4.4.2 Core loss comparisons

For the core loss model in (3.54) to be accomplished, core loss coefficients must be determined. These coefficient can be derived from calibrations with sample measurements as shown in Fig. 3.43. Loss coefficients are detailed in Table. 3.6.

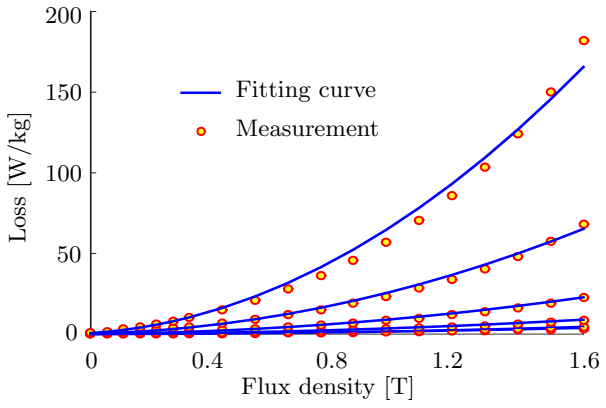

Fig. 3.43: Curve fitting for the specific loss measurement

Table 3.6: Loss coefficients derived from measurement fitting

Coefficient	k_h	α	k_e
Value	199	2	0.752

The core loss contribution done by EMCN of the stator and rotor is shown in Fig. 3.44.

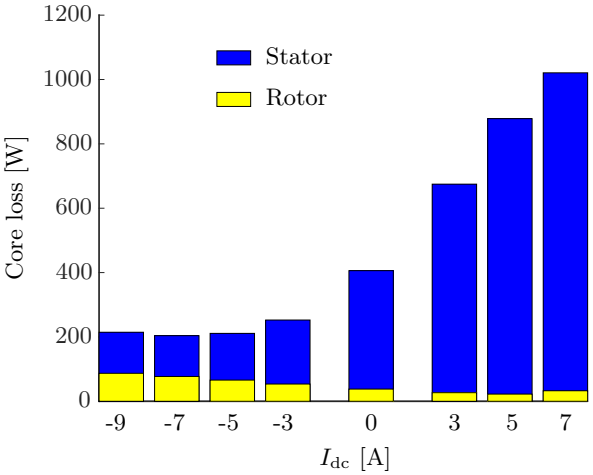

Fig. 3.44: Core loss by EMCN at 6000 rpm, no-load condition according to the field current

As seen, the rotor's core loss takes a very small portion of the total loss, except the flux weakening area, where the stator loss decreases and the rotor loss increases. This is due to flux densities in the stator tooth is much reduced, and flux densities in rotor increase as displayed in Fig. 3.45 for a point in the middle of the solid rotor core.

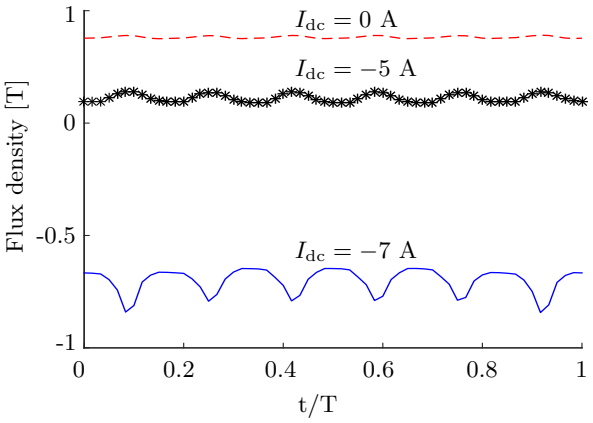

Fig. 3.45: Flux density of a point in the rotor according to field current changes

As it will be seen, a good accordance between FEM and EMCN results for a wide range of the field current as displayed in Fig. 3.46, and between EMCN and experiments demonstrated in Fig. 3.47.

The core loss comparison according to the load variation shown in Fig. 3.48, when the field

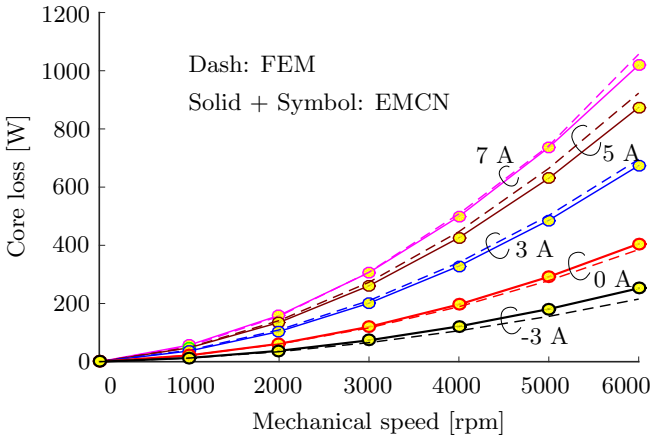

Fig. 3.46: Core loss comparison according to field current variation at no-load

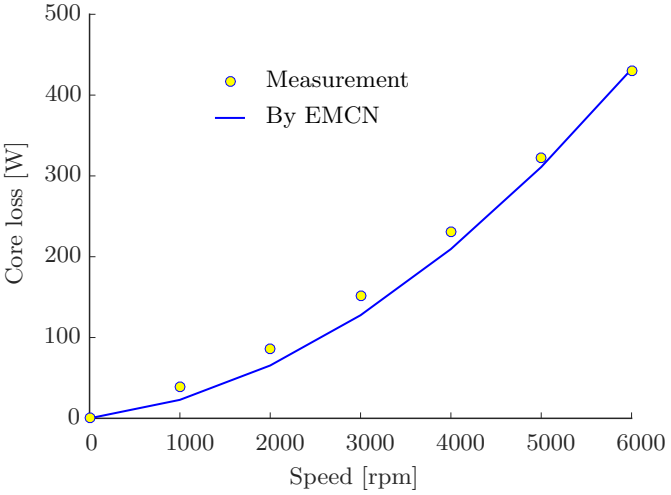

Fig. 3.47: Core loss comparison with measurement at no-load, $I_{\mathrm{dc}} = 0$ A

windings are not excited. As it will be observed, EMCN results agree well with ones obtained by the FEM, and due to the armature reaction, flux densities change their amplitudes as well as harmonics, therefore the core loss increases.

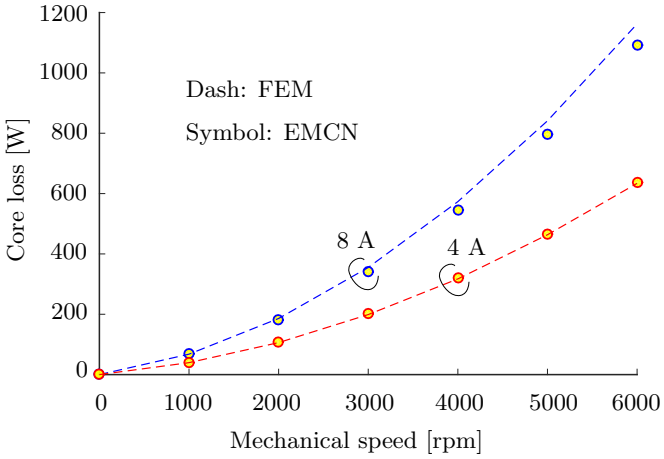

Fig. 3.48: Core loss according to load variation, $I_{\mathrm{dc}} = 0$ A

3.4.5 Core loss calculation using symmetry option

As discussed in chapter 2, using the symmetry option can save the computation time for the torque calculation, i.e. the torque can be faster calculated by using only one sixth of the electrical period without any accuracy sacrifice. In this section, a same idea is examined for the core loss calculation. The difference is that for the torque calculation using the flux MMF diagram, the symmetry is based on the phase flux linkages and currents. But for the core loss calculation, the symmetry will be based on the similarities between flux density patterns at different positions. This approach promises a huge advantage with a gain of 6 times faster, while considering a long optimization process. However an accuracy examination must be performed.

It is important to remind some of the key characteristics of the machine:

- Symmetry three phase machine.
- 6 slots per pole per phase.
- Flux density patterns in the rotor repeat six times in one period.
- Core loss in the end-shield, rotoric flux collector, and outer stator parts are negligible.

Therefore, the idea is to use only one sixth of the electrical period of one pole pair in the stator, and the main rotor to retrieve core losses. The flux densities at points $A_1 \div A_6$ (the radial component in the stator teeth) and $B_1 \div B_6$ (tangential component in the stator yoke) are shown in Fig. 3.49. It is obvious that the flux densities of all other one sixth electrical periods can be derived from the first one sixth ones as shown in Fig. 3.50.

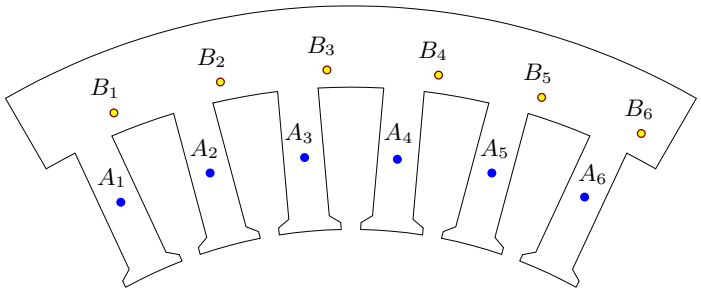

Fig. 3.49: Testing points for flux densities calculation

The core loss comparisons between one obtained from the full electrical period model and the symmetry approach are displayed in Fig. 3.51 at the armature current of 8 A and different field currents and rotational speeds. As it will be seen, two result are well matched.

Conclusion

This chapter has discussed about the application of EMCN in the modelling of a DESM prototype. The flexible network was introduced to control the detail level of the mesh. The

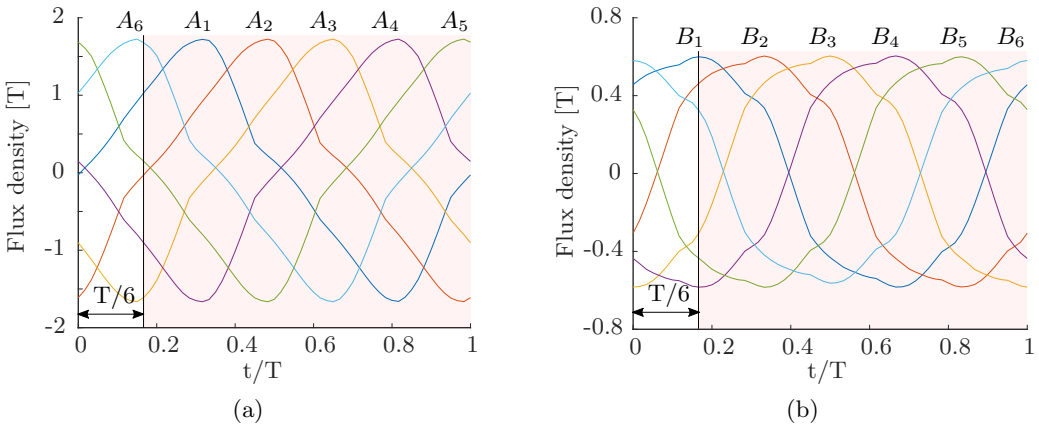

Fig. 3.50: Flux density symmetry characteristic. a) Radial flux density in stator teeth. b) Tangential flux density in stator yoke

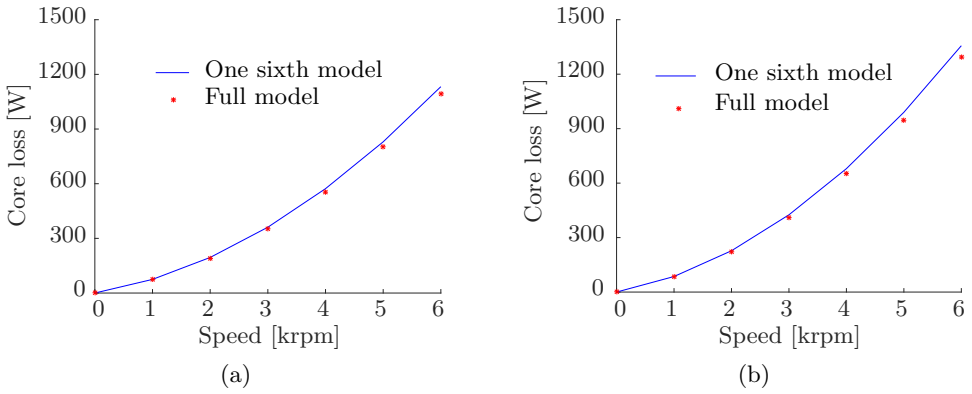

Fig. 3.51: Core loss comparison between models using full and one sixth electrical period. Armature current 8 A, phase angle is zero. a) $I_{\mathrm{dc}} = 0$ A. b) $I_{\mathrm{dc}} = 4$ A.

non-linearity of the magnetization curve is taken into consideration by iteratively solving the system nodal equation. The iron loss model has been focused to carefully consider addition losses due to harmonics and DC component flux densities. The good accordance between results obtained by the EMCN method and ones from the FEM has validated the accuracy of the EMCN. Moreover, EMCN also reveals its advantageous feature over the FEM candidate in term of computation time. With all things presented, the EMCN method applied to the DESM prototype prepares a readiness for a good design stage such as an optimization, where model's parameters are expected to change and certainly connections with other parts such as an inverter, converter, etc.

Chapter 4

Thermal model of the DESMs

The power of an electrical machine is normally limited by the thermal aspects. Overheating will cause the insulation deterioration and consequently reduce the machine's life span. Recently, attentions to thermal designs has been rewarded by major improvements in the overall performance. In comparison with classical machines, a DESM has additional excitation windings, i.e. extra heat sources from these windings' copper losses. In one hand, this requires a careful attention to the machine's efficiency. On the other hand, it causes the thermal performance of the machine worse. The main aim of this chapter is to develop a thermal model in transient regime for the studied DESM. This chapter is organized as follows: first, mechanical loss calculations are briefed since these losses are parts of thermal model. Second, individual lumped thermal resistances and their calculations are addressed. Third, a lumped parameter thermal network and solving technique in transient mode are introduced. Finally, thermal coefficients calibration by experiments will be presented. The final step is of importance since most of thermal equations are empirical, meaning that they are subject to specific structures, assembly process, etc.

4.1 Thermal analysis approach

The heat transfer process can be modeled by using a thermal network analogous to an electrical network composing of resistances and capacitors. Thermal resistances in a thermal network consists of conductive, convective, and radiative resistances for different parts of the machine. Machine's thermal analyses can be categorized into two basic types: lumped parameter circuit and numerical methods. No matter what type of method used, a big challenge to a thermal analysis is thermal resistances determination, which often requires empirical formulations. Those values usually have significant impacts on the analysis result.

With the numerical method, two available options are FEM method and computational fluid dynamics (CFD). CFD has an advantage that it can be used to predict flow in complex regions, such as ones around end-winding regions. The FEM can only be used to model conductive heat

transfer in solid components [81]. The FEM method usually provides more accurate results with detailed local temperature distribution. However, its long computation time makes it less effective in the design optimization process. In addition, only temperatures at few machine's positions are sometimes sufficient to the thermal design (for instance, the winding temperature to manage insulation deterioration, the permanent magnet temperature to predict the demagnetization risk). Moreover, as mentioned above, a thermal analysis requires a lot of empirical formulations. This means that using FEM analysis has no big advantage in determining critical model's parameters.

In this work, the lumped parameter thermal method will be utilized. By mean of lumped parameter, each component of the machine is presented by one or several thermal resistances, a thermal capacitor representing its heat storage and/or a heat source. A network for transient analysis will be developed, i.e. both thermal resistances and thermal capacitors are presented. The system equation is solved by using an iterative method. Aiming at evaluating motor's performance at a wide range of operation range, a coupling between thermal and electromagnetic models are necessarily provided. This is mainly due to the losses dependence on the temperature and vice-versa. The losses from electromagnetic model are important inputs to the thermal model. Copper losses of armature and field windings can be easily calculated based on their geometries. In chapter 3, iron losses has been computed. Mechanical losses, which include windage and bearing friction losses, will be shortly addressed in the following section.

Fig. 4.1 illustrates the mechanical structure of the studied DESM. This consideration is supportive for the thermal analysis. The thermal processes consider all three types conduction, radiation and convection processes. However, due to a complex surface geometries inside the machine, and also temperatures are not quite different between these surfaces and the air around, radiations are neglected inside the machine.

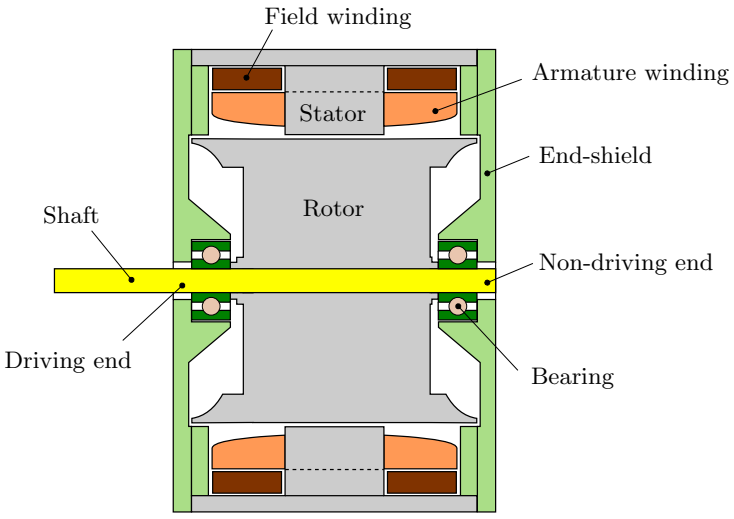

Fig. 4.1: Overall mechanical structure of the studied DESM

4.2 Mechanical losses

Two principal mechanical losses presented in an electrical machine are windage loss in the air-gap due to rotor's rotation and friction losses in the bearings. Proper calculations of these losses not only help designers better determine machine's efficiency but also provide a good heat source input to the thermal model. At a glance, these losses are predicted to be small due to two reasons: first, the machine size is relatively small resulting in a small air-gap diameter and hence roughly small windage loss and light rotor (acting on the bearing) leading to a small bearing friction load as well. Second, the speed of the machine is not high (the rated speed is about 2000 rpm).

Fig. 4.2: Mechanical losses to be considered. a) Windage. b) Bearing friction

4.2.1 Windage loss

The windage loss in a rotating machine is the power absorbed by the air-gap between the rotor and the stator. A conventional approach for the windage loss calculation is to compare a proposed machine to a similar machine with a known windage loss [82]. However, in the design phase, an analytical calculation approach is useful when various parameters might vary and hence the windage loss is conveniently derived. Also, extrapolating the windage loss from available commercial machine data is not an easy task. As presented in [82], empirical equations are developed for a cylindrical rotor and an adjustment factor is considered account for the saliency effect.

4.2.1.1 Windage loss in a cylindrical rotor machine

According to [82], the windage loss of a cylinder rotating in a concentric cylinder is determined based on following assumptions:

- No axial flow exists.
- The air-gap length is small compared to the air-gap radius and axial length.
- The air in the gap is homogeneous.

With those assumptions, the windage loss is expressed as (4.1).

$$W_{\text{windage}} = \pi C_d \rho R^4 \omega^3 L \qquad [\text{W}] \tag{4.1}$$

where ρ is the air-gap density [kg/m^3], R is the average air-gap diameter [m], ω is the rotor angle speed [rad/s], L is the axial length [m], and C_d is the skin friction coefficient.

This friction coefficient depends on the air flow state in the gap, i.e. the laminar, transition or turbulence state, which is characterized by the Reynold number given by (4.2).

$$R_e = \frac{\omega R D}{\nu} \tag{4.2}$$

where D is the air-gap length [m], and ν is the kinematic viscosity of the air [m^2/s].

- If $R_e \leqslant 2300$: air flow is laminar.
- If $2300 < R_e \leqslant 4000$: air flow is transition.
- If $4000 < R_e$: air flow is turbulence.

The friction coefficient C_d is defined as (4.3a) for the laminar flow and (4.3b) for the transition and turbulence cases.

$$C_d = \frac{2}{R_e} \tag{4.3a}$$

$$\frac{1}{\sqrt{C_d}} = 2.04 + 1.768 \cdot \ln\left(R_e \sqrt{C_d}\right) \tag{4.3b}$$

4.2.1.2 Windage loss in a salient machine

(4.1) is developed for the cylinder rotor case. In order to take into account the saliency aspect, which additionally increases the windage loss due to its obstacle to the rotation, the loss calculated by (4.1) will be multiplied with a factor empirically given by (4.4) [82].

$$K = 8.5\left(\frac{H}{R}\right) + 2.2 \tag{4.4}$$

where H is the pole depth.

As generally stated in [82] that (4.4) is not applicable for the case where $H/R < 0.06$. This factor will be examined later with the studied DESM.

Taking the studied DESM's dimensions, with the air-gap temperature is 50℃. At the speed of 2000 rpm, the windage loss is estimated to be 0.2 W if the rotor is assumed cylinderical. This loss is quite negligible even if applying the saliency factor.

The windage loss is, therefore, neglected in the next analysis.

4.2.2 Bearing friction loss

In a rotating machine, two bearings are usually located at the driving and non-driving ends. The friction loss is subject to the rotating speed and rotor's mass and bearing's properties (the bearing size and friction coefficient). With a bearing using the lubricant oil, after a certain time in use, the friction coefficient usually increases due to the deterioration of the lubricant oil. Therefore, it is complicated to obtain an accurate calculation of this friction loss. According to SKF bearing manufacturing [83], the bearing friction can be computed by (4.5).

$$W_{\text{bearing}} = 0.525 \cdot 10^{-4} \mu P d n \qquad [\text{W}] \tag{4.5}$$

where μ is the friction coefficient, P is the equivalent dynamic bearing load [N], d is the bearing diameter [mm], and n is the rotating speed [rpm].

Considering the studied DESM, the bearing loss is approximately 1 W, which is substantially small and will be neglected.

With all mechanical losses considered, it would be concluded as expected the beginning that the mechanical losses are negligible (1.2 W at 2000 rpm) due to the small machine size and low/medium speed. Note that, in practice, additional mechanical losses would occur due to mechanical tolerance from the manufacturing process or one resulted from vibration due to machine's asymmetry, etc.

4.3 Thermal resistances calculation

Thermal resistance, thermal capacitor and heat source are three component categories of a thermal network. Fig. 4.3 displays a typical node in a thermal network.

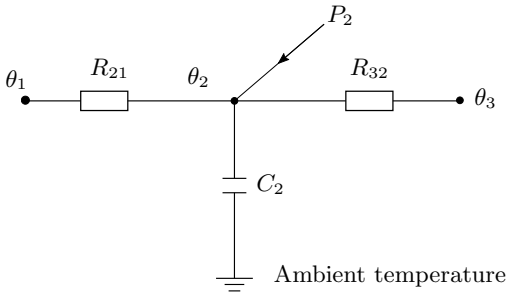

Fig. 4.3: A typical node in a thermal network

where P is the heat source, θ is the node temperature, C is the heat storage capacitor, and R is the thermal resistance.

Heat sources are derived from electromagnetic and mechanical analyses, heat storage capacitors are determined by (4.6).

$$C = mc_p \tag{4.6}$$

where m and c_p are mass [kg] and specific heat capacity [J/kg ℃] of the component, respectively.

However, it is not straightforward for thermal resistance calculations, which normally requires empirical thermal coefficients. In next part, different types of thermal resistance computation will be discussed in detail.

4.3.1 Basic cylindrical component

In a rotating machine, many components are fully or partly shaped as cylindrical: the stator yoke, stator teeth, rotor core, etc. Therefore, a cylindrical component would be considered as the basic shape for the conductive thermal resistance calculation. The basic form for the conductive thermal resistance is given by (4.7).

$$R = \int_0^L \frac{dl}{kS(l)} \tag{4.7}$$

where k and L are the thermal conductivity and length of the object, respectively, and $S(l)$ is the cross section at length l.

In [84], a sufficiently complex model was presented as shown in Fig. 4.4.

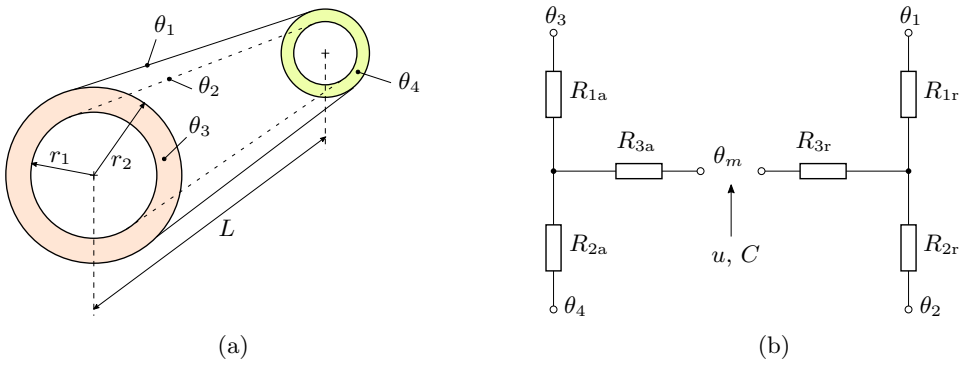

Fig. 4.4: Cylindrical component. a) Physical shape. b) Equivalent thermal model

Where θ_1, θ_2, θ_3 and θ_4 are temperatures at the inner, outer surface and two sides of the cylinder, respectively. Index "a" and "r" represent the thermal conduction in the axial and radial directions. The central node of each network gives the mean temperature θ_m of the component. u is the internal heat generation and C is heat storage capacitor.

This configuration would give a quite accurate result. However, it increases the calculation complexity and the number of nodes in the network as pointed out in [85]. Authors of [85] had simplified the configuration while maintaining a good result accuracy by neglecting the axial thermal flux and also R_3 resistance since it is always neglected from a practical point of view [86]. The simplified model is demonstrated in Fig. 4.5. As it will be seen, two nodes for one component has been removed.

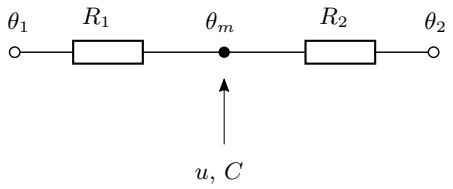

Fig. 4.5: Simplified model for a cylindrical component

Resistance components are expressed as (4.8) [85].

$$R_1 = \frac{1}{2\pi kL} \ln \frac{r_m}{r_1} \tag{4.8a}$$

$$R_2 = \frac{1}{2\pi kL} \ln \frac{r_2}{r_m} \tag{4.8b}$$

where

$$r_m = \frac{r_1 + r_2}{2} \tag{4.9}$$

where r_1, r_2 and L are the inner, outer surface radii and axial length of the cylinder, respectively. k is the thermal conductivity of the cylinder's material.

The total thermal capacitance of the cylinder is found from material density ρ, the specific heat capacitance c_p and the cylinder's dimensions as (4.10)

$$C = \rho\pi \left(r_2^2 - r_1^2\right) L c_p \tag{4.10}$$

4.3.2 Outer frame heat transfer

The heat transfer from the frame's surface to the ambient is one of the most important elements in thermal analysis since it is the way to evacuate generated heat from the machine. With a relatively low power (the rated power of about 2 kW), the studied DESM uses natural air cooling causing convective coefficient h_c small, ranging from 5 to 100 w/℃/m^2. In this case, a portion from radiative heat transfer will be significant.

4.3.2.1 Convective heat transfer coefficient

The convection process depends on the surface area, type of surface (i.e, horizontal or vertical) and the ambient air temperature θ_a. The typical outer frame of a horizontal electrical machine can be depicted in Fig. 4.6.

In the next calculations, following assumptions are made:

- Surface temperatures θ_s are uniform.
- Two vertical plates are identical.
- Average surface emissivity are used.

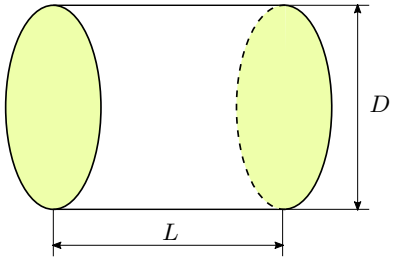

Fig. 4.6: Outer frame configuration

The convective heat transfer is derived from a series of calculations expressed in (4.11) [87].

$$\begin{aligned} h_c &= \frac{kN_u}{L_c} \\ N_u &= \left\{ A + \frac{0.387 \cdot R_a^{1/6}}{\left[1 + (B/Pr)^{9/16}\right]^{8/27}} \right\}^2 \\ R_a &= \frac{\beta \cdot g \cdot (T_s - T_a) \cdot L_c^3}{\nu \cdot \alpha} \end{aligned} \tag{4.11}$$

where N_u, R_a and Pr are Nusselt, Rayleigh and Prandt numbers of the ambient air, respectively. β, ν and α are expansion, viscosity and diffusivity coefficients of the ambient air. L_c is the characteristic length of the surface determined by (4.12).

$$L_c = \begin{cases} D & \text{With a horizontal cylinder of diamter} D \\ \dfrac{D\sqrt{\pi}}{2} & \text{With a vertical circle plate of diameter D} \end{cases} \tag{4.12}$$

A and B are surface dependent coefficients determined by (4.13).

$$[A, B] = \begin{cases} [0.6 \quad 0.559] & \text{With horizontal surface} \\ [0.825 \quad 0.492] & \text{With vertical plate} \end{cases} \tag{4.13}$$

The convective resistance in case of a horizontal cylinder surface S_1:

$$R_1 = \frac{1}{h_1 S_1} \tag{4.14}$$

The convective resistance in case of a vertical plate surface S_2:

$$R_2 = \frac{1}{h_2 S_2} \tag{4.15}$$

where h_1 and h_2 are convective coefficients of the vertical plate and horizontal surfaces, respectively. The equivalent convective resistance resulted from a parallel connection of individual convective resistances:

$$\begin{aligned} \frac{1}{R_c} &= \frac{1}{R_1} + \frac{2}{R_2} = h_1 S_1 + 2h_2 S_2 \\ R_c &= \frac{1}{h_1 S_1 + 2h_2 S_2} = \frac{1}{h_{\text{ceq}} S} \end{aligned} \tag{4.16}$$

where h_{ceq} is the equivalent convective coefficient and S is the total surface area.

From (4.16), h_{ceq} could be computed as (4.17):

$$\begin{aligned} h_{ceq} &= \frac{h_1 S_1 + 2h_2 S_2}{S_1 + 2S_2} \\ &= \frac{h_1 \pi \frac{D^2}{4} + h_2 \pi D L}{\pi \frac{D^2}{4} + \pi D L} \\ &= \frac{h_1 D + 2h_2 L}{D + 2L} \end{aligned} \tag{4.17}$$

4.3.2.2 Radiative heat transfer coefficient

The radiative heat transfer facilitates the heat evacuation from the machine especially in case of natural air convection circumstances. The radiative heat transfer strongly depends not only on the temperature difference between the surface and the ambient but also on the surface property characterized by an emissivity coefficient ϵ. The surface heat density q_r evacuated from a body surface is given by (4.18) [87]

$$q_r = \epsilon \sigma_c \left(\theta_s^4 - \theta_a^4\right) \tag{4.18}$$

where σ_c is the Stefan-Boltzmann constant ($5.67{\cdot}10^{-8}$ W/m^2/K^4).

The emissivity coefficient of a real surface is not a constant, it rather varies with the temperature, color and material of the surface as well as the wave length and the direction of the emitted radiation [87]. That will make the heat transfer quite complex. Therefore, the emissivity is practically assumed to be constant all over the surface.

The surface heat density exchange in (4.18) can be also written in the form of radiative heat transfer coefficient h_r as (4.19).

$$q_r = h_r \left(\theta_s - \theta_a\right) \tag{4.19}$$

From (4.18) and (4.19), h_r is obtained as (4.20).

$$h_r = \frac{\epsilon \sigma_c \left(\theta_s^4 - \theta_a^4\right)}{\theta_s - \theta_a} = \epsilon \sigma_c \left(\theta_s + \theta_a\right)\left(\theta_s^2 + \theta_a^2\right) \tag{4.20}$$

And thermal resistance due to radiative heat transfer:

$$R_r = \frac{1}{h_r S} \tag{4.21}$$

4.3.2.3 Equivalent surface heat transfer coefficient

With corresponding convective and radiative heat transfer coefficients being determined, the equivalent heat transfer coefficient h_e is derived. The thermal resistance between the machine surface and the ambient (due to both convection and radiation processes):

$$R_s = \frac{1}{\frac{1}{R_c} + \frac{1}{R_r}} = \frac{1}{\left(h_c + h_r\right) S} \tag{4.22}$$

And h_e can be derived as (4.23).

$$h_e = \frac{1}{R_s S} = h_c + h_r \tag{4.23}$$

Therefore, the equivalent coefficient is simply the sum of individuals. In practice, it is impossible to separately measure each coefficient but the equivalent coefficient instead. However, with (4.23) the contribution of each process can be evaluated. As it will be seen, with natural air convection, the radiation portion is significant.

A case study with different outer surface temperatures will be shown below to calculate the surface heat transfer coefficient.

Table 4.1: Case study parameter

Parameter	**Value**
Emissivity	0.5*
Total axial length	115 mm
Outer diameter	185 mm
Ambient temperature	22℃
Outer surface temperature	20 ÷ 100℃

* An average value between 0 and 1 is chosen

The coefficients according to the surface's temperature variation are demonstrated in Fig. 4.7. As it will be seen, both coefficients (due to convection and radiation) increase as the surface temperature goes up. This is explained by (4.20) for the radiative coefficient. For convective coefficient, it is due to the fact that increasing the temperature difference between the surface and ambient temperature makes the Rayleigh number increases. As the result, the Nuselt number increases and the radiative coefficient increases as well. The individual contributions of each coefficient are very close for this case with the natural air convection. However, in cases of forced air convection or water cooling systems, the convective coefficient would be few hundreds. In those cases, radiative heat transfer is negligible.

4.3.3 Air-gap heat transfer

The convective heat transfer in the air-gap is different from one on the surface since it is confined in a narrow gap between the stator and rotor instead of a large open space between the outer surface and the ambient environment. For the studied DESM, there is no internal forced air ventilation, this heat transfer process is affected by the temperature, dimensions of the air-gap as well as surface speed of the rotor. As pointed out in [88] which is demonstrated in Fig. 4.8, at low speed, only one steady state flow is established. However, a secondary state flow will be formed as speed increases, this introduces a turbulence state in the air-gap and hence increases transferred heat.

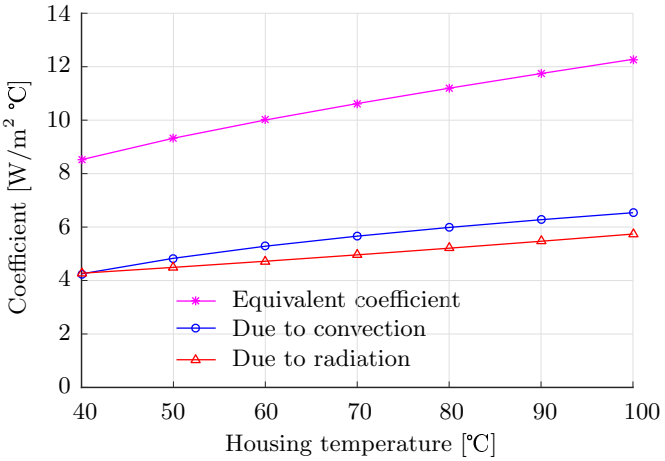

Fig. 4.7: Heat transfer coefficient according to surface temperature

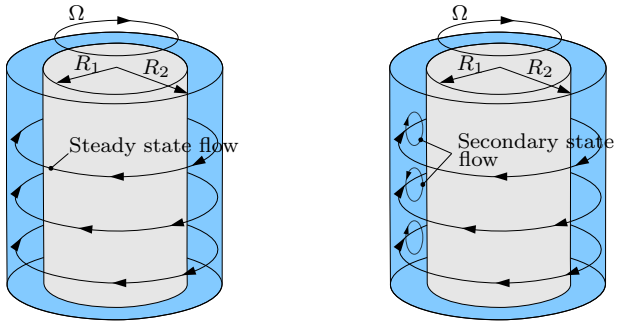

Fig. 4.8: Disturbance in the air-gap according to rotor speed. a) Low speed. b) High speed

In order to judge whether the flow in the air-gap is laminar, vortex or turbulent, the Taylor number T_a is used given by (4.24).

$$T_a = \frac{\Omega \cdot r_m^{0.5} \cdot d^{0.5}}{\nu} \tag{4.24}$$

where Ω is the motor's angular speed [rad/s], r_m is the average air-gap diameter [m], and d is the air-gap length [m].

Depending on T_a, the Nusselt number and air-gap state will be determined as (4.25).

$$N_u = \begin{cases} 2 & T_a \leqslant 41 \text{ (laminar)} \\ 0.212 \cdot \theta_a^{0.63} \cdot P_r^{0.27} & 41 < T_a \leqslant 100 \text{ (vortex)} \\ 0.386 \cdot \theta_a^{0.5} \cdot P_r^{0.27} & 100 < T_a \text{ (turbulent)} \end{cases} \tag{4.25}$$

The convective coefficient in the air-gap is then defined as (4.26) with 10% increased to take into account the slotting effect as discussed in [89].

$$h_{ca} = \frac{1.1 N_u k}{d} \tag{4.26}$$

The air-gap thermal resistance is then defined as (4.27)

$$R_{\text{air-gap}} = \frac{1}{h_{ca} S_{\text{air-gap}}} \tag{4.27}$$

where $S_{\text{air-gap}}$ is the cylindrical surface of the air-gap.

The air-gap thermal resistance according to the rotor speed and air-gap temperature is displayed in Fig. 4.9.

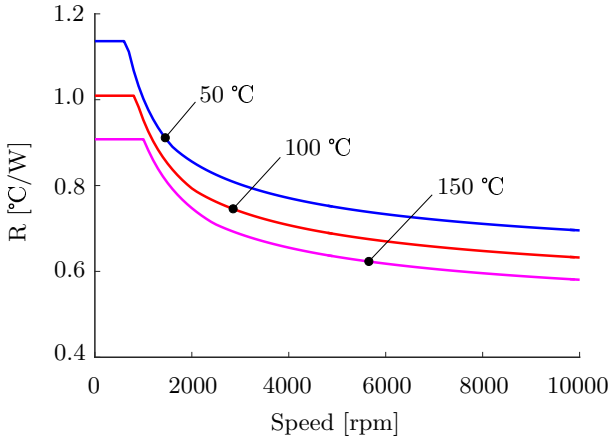

Fig. 4.9: Air-gap thermal resistance variation according to rotor speed and air-gap temperature

As observed in Fig. 4.9, at the low speed the Taylor number is small and the Nusselt number stays constant. Therefore, the air-gap thermal resistance does not change as the rotor speed varies. Increasing the rotor speed will creates vortex, turbulence air flow in the air-gap help facilitate the heat transfer. As the result, the corresponding thermal resistance decreases. The dependence of the air-gap thermal resistance on its temperature is also clear that the thermal conductivity (strong impact on the thermal resistance) of the air increases along with its temperature. Fig. 4.9 also reveals the fact that having a completely passive rotor has an obvious advantage of the heat evacuation since the heat from the rotor has to pass through air-gap thermal resistance, which is pretty big. Considering an energy loss of 200 W located in the rotor, with an air-gap thermal resistance of 0.5℃/W would make a temperature of roughly 100℃ of rotor higher than that of the stator. Therefore, from the thermal point of view, heat sources of the machine should be located close to the machine's surface as much as possible. The studied DESM's topology only has PMs embedded in the rotor, while all the windings are on the stator side. As analyzed in chapter 3, PMs losses are quite negligible leading to the rotor could be considered passive.

4.3.4 Thermal resistances between windings and core

4.3.4.1 Thermal resistance between armature active winding and stator core

The thermal resistance between the armature copper and core is of importance because this big resistance is on the main path of the heat evacuation. In the thermal domain, the armature

winding usually presents a complex structure to accurately calculate thermal resistance since various layers exist as demonstrated in Fig. 4.10.

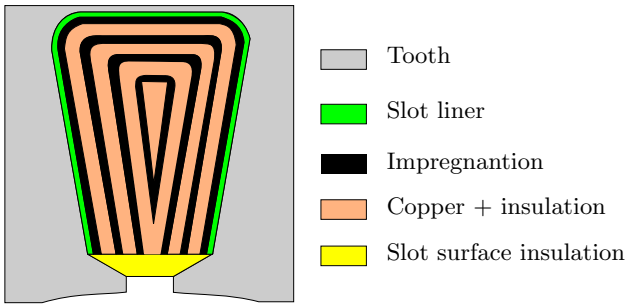

Fig. 4.10: Winding insulation in the slot

Authors of [90] proposed an equivalent thermal conductivity $k_{\text{cu,ir}}$ of the air and insulation material in the slots. This equivalent conductivity depends on many factors such as the material, quality of the impregnation, filling factor, etc. A linear regression from series of tests to determine this equivalent value as function of filling factor k_f is given by (4.28). The filling factors for those tests were in range $0.35 \div 0.45$, which is close to the one of studied DESM (0.35). Therefor, the regression model can be applicable.

$$k_{\text{Cu,ir}} = 0.1076 \cdot k_f + 0.029967 \tag{4.28}$$

Noted that, in case of no copper presented ($k_f = 0$), $k_{\text{cu,ir}}$ is 0.029967, which is the thermal conductivity of the air at 80°C.

The thermal resistance between the copper and the iron core is determined as (4.29).

$$R_{\text{Cu,ir}} = \frac{S_{\text{slot}}(1 - k_f)}{k_{\text{Cu,ir}} l_{\text{sp}}^2 L_{\text{s}}} \tag{4.29}$$

where l_{sp} is the stator slot perimeter, L_{s} is the active stack length, and S_{slot} is the stator slot surface.

From (4.28) and (4.29), it is concluded that improving the filling factor will lower the thermal resistance between the copper and the core not only by increasing equivalent thermal conductivity but also decreasing insulation layer thickness. The studied DESM has the filling factor of 0.35 leading to the equivalent thermal conductivity of 0.0676, which is 2.25 times as high as that of the air at 80°C.

4.3.4.2 Thermal resistance between ending and active parts of armature winding

The heat evacuation from the active part (inside stator slots) of the armature winding can be done conveniently through an insulation contact with the stator teeth. However, the end-windings faces difficulties since this process must be principally done in axial direction though active winding and then to the stator teeth. With the presence of the global excitation windings,

an additional path is provided though this winding via small air gap between these windings as shown in Fig. 4.11. Thermal resistances in these two paths are generally large. Therefore, the end-winding temperature is predicted to be higher compared to that of the active winding. With an assumption of uniform temperature distribution in each of end-winding and active winding parts, the thermal resistance between the end-winding and active winding can be expressed as (4.30):

$$R_{\text{end-active}} = \frac{l_{\text{end}}}{S_{\text{slot}} k_f} \alpha_{\text{ea}} \tag{4.30}$$

where l_{end} is the length of the end-winding and α_{ea} is a coefficient characterizing the heat transfer between the end-winding and active winding, this coefficient will be determined by experiments.

4.3.4.3 Thermal resistance between field windings and stator core

The double excitation principle presents additional field windings, this makes the machine complicated not only from the electromagnetic point of view but also from thermal one. The main reason is due to the "non-standard" assembly of these windings. Unlike armature windings, where manufacturing and assembly processes would have a standardization and hence the formulation for its thermal resistance is available, no similar researches have been done for that of the toroidal field winding in the studied DESM. A close look at one field winding of the DESM is shown in Fig. 4.11. As it can be seen, the contact surface between the winding and core is smaller than that of a winding located in the slot. Moreover, this contact is not so tight, i.e. a big air space is presented between the windings and stator core. These explain why the heat evacuation for the field windings of the prototype is more difficult than the one of the armature windings.

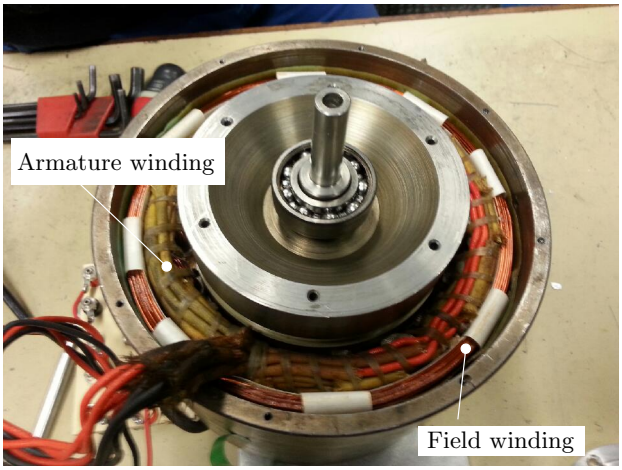

Fig. 4.11: Field winding of the studied DESM

The residual air and contact surface between the field windings and core (especially to the end-shield side) is difficulty to determine. Despite of these difficulties, formula (4.29) corrected

by a factor α_f will be applied. Therefore, an experiment is required in order to determine this correction factor.

4.3.4.4 Thermal resistance between armature end-winding and field winding

The thermal resistance between the armature end-winding and field windings shown in Fig. 4.11 consists of thermal resistance of the end-winding's insulation and one of a small air-gap between these two parts. With the DESM prototype, parameters of these types are not constant along the air gap and complicated in shape. Therefore, an equivalent air-gap will be considered to calculate this thermal resistance. With this assumption, formulas from (4.24) to (4.27) can be applied. The air-gap length will be determined experimentally.

4.3.5 Thermal contact resistance

In electrical machines, there exists different types of contact, such as between laminations, between the stator core and frame, mechanical bearing area, etc. Due to rough surfaces, it cannot be assumed that a thermal short circuit exists between them. Instead, some air presented in the contact area resulting in a thermal resistance. In this section, lamination contacts are neglected since axial heat flows in the core are not considered as mentioned earlier.

The rotor in fact consists of the rotor's iron core and PMs, therefore, thermal contacts appear between them. However, due to a small loss on rotor, the rotor will be considered as a cylindrical component discussed in 4.3.1.

Ball bearing thermal contact resistance calculation also present a difficulty since the balls are in contact with the inner and outer rings just in a very small mechanical spot. Additionally, inside the bearing the presence of lubricant oil introduces factors of uncertainty for thermal resistance determination. A simple solution is to consider this thermal resistance as an equivalent air-gap of about 0.3 mm [90].

The thermal contact resistance coefficient between the inner (laminated) and outer (solid) stator yokes is a function of the surface's roughnesses and the pressure, which is created during the machine's assembly. An example of the frame contact coefficient as a function of the contact pressure is shown in Fig. 4.12 [84].

Unfortunately, information on pressure and surface's roughnesses are usually unavailable. However, as discussed in [84], even a large variation of this value has surprisingly little effect on the estimates of winding temperatures. Therefore in this thesis, an arbitrary coefficient of 1000 $W/m^2{}^\circ C$ (a value in the middle of ranges shown in Fig. 4.12 will be adopted).

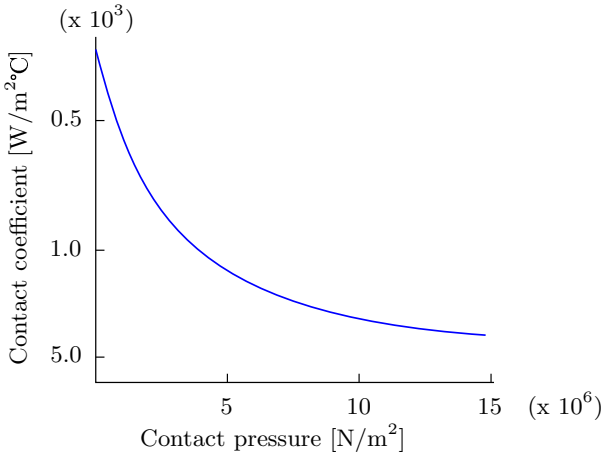

Fig. 4.12: Frame-core contact coefficient according to contact pressure

4.4 Transient thermal network

The complete lumped parameter thermal network of the studied DESM is displayed in Fig. 4.13 for the transient analysis with notes as follows:

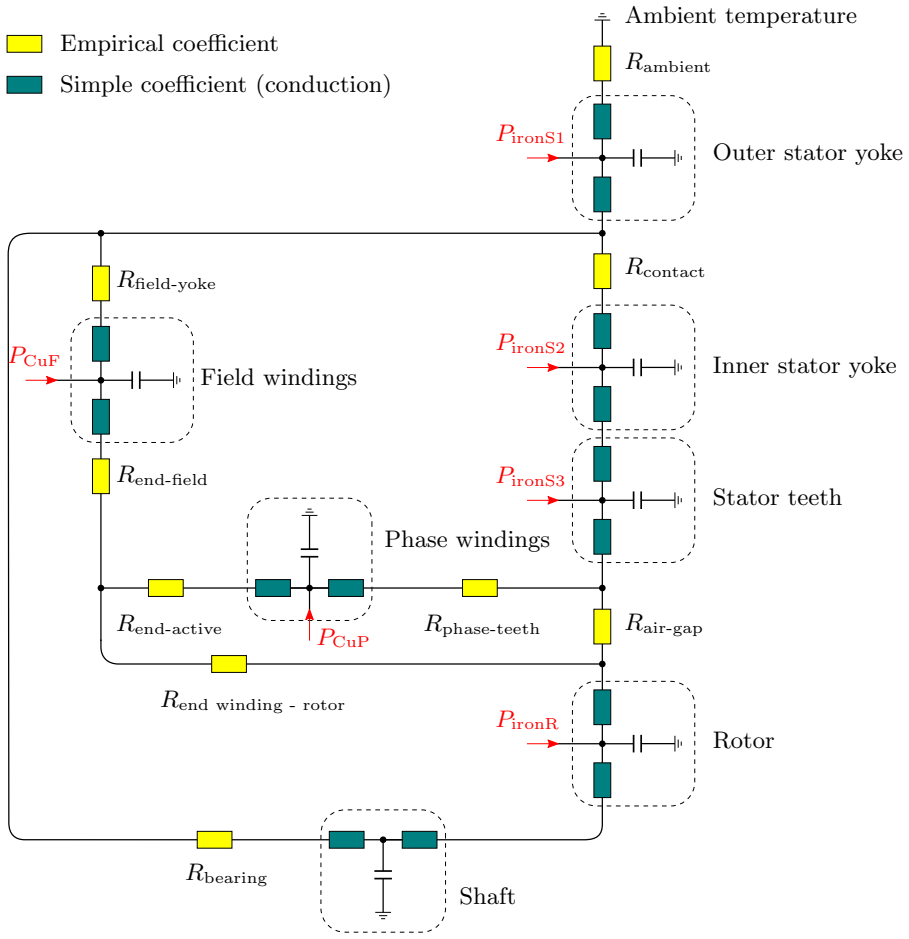

Fig. 4.13: Thermal network of the studied DESM

- Two groups of thermal resistance are presented: one using empirical formulations (yellow) and the other can be simply calculated based on object's geometry.
- R_{ambient}, $R_{\text{air-gap}}$ and $R_{\text{end winding - rotor}}$ are temperature dependent. Therefore, they will be updated iteratively.
- Only copper losses are temperature-dependent loss (the iron losses are assumed to be constant).
- Mechanical losses (bearing friction and windage) are neglected as discussed in section 4.2.
- Residual flux densities of PMs are assumed to be temperature independent since during the transient analysis, numerous iterations will be performed. If these flux densities are subject to the temperature, electromagnetic analysis has to be run at the same number of iterations, that will significantly increase the computation time.
- P_{ironS1}, P_{ironS1}, P_{ironS1} are the iron losses in the outer stator yoke, inner stator yoke and stator teeth, respectively. P_{ironR} is the iron loss of the rotor. P_{cuF} and P_{cuP} are copper losses of the field and phase windings

4.4.1 Approach with constant heat sources

Before going with the transient process, where the heat sources are temperature dependent, a solution to the process with constant heat sources will be carried out as an easy and basic step. The thermal network can be quite easily solved with MATLAB Simulink, however this will lead to a time consuming process due to the coupling between the Simulink and Matalb. Therefore, an analytical method can be much more practical.

Firstly, a typical node as in Fig. 4.3 is recalled as Fig. 4.14 with thermal resistances are replaced by thermal conductances ($G = \frac{1}{R}$).

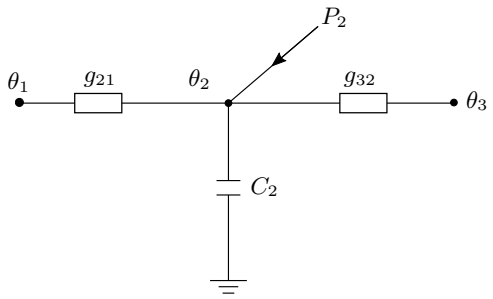

Fig. 4.14: A typical node in transient mode

Applying the Kirchhoff's circuit law on node 2:

$$\begin{aligned} -C_2\frac{d\theta_2}{dt} + (\theta_1 - \theta_2)\, g_{21} + (\theta_3 - \theta_2)\, g_{23} + P_2 = 0 \\ C_2\frac{d\theta_2}{dt} + \theta_1 G_{21} + \theta_2 G_{22} + \theta_3 G_{23} = P_2 \end{aligned} \tag{4.31}$$

where $G_{21} = -g_{21}$, $G_{23} = -g_{23}$, $G_{22} = g_{21} + g_{23}$

Nodal equation for any node $\boldsymbol{i}$ in a system of $\boldsymbol{n}$ nodes.

$$C_i \frac{d\theta_2}{dt} + \theta_1 G_{i1} + \theta_2 G_{i2} + ... + \theta_i G_{ii} + ... + \theta_n G_{in} = P_i \tag{4.32}$$

where $G_{ii} = \sum_{\substack{j=1 \\ j \neq i}}^{n} g_{ij}, \quad G_{ij} = -g_{ij}\ (i \neq j)$

The system formulation can be expressed as (4.33).

$$[\boldsymbol{C}] \cdot \frac{d[\boldsymbol{\theta}]}{dt} + [\boldsymbol{G}] \cdot [\boldsymbol{\theta}] = [\boldsymbol{P}] \tag{4.33}$$

where $[\boldsymbol{C}]$, $[\boldsymbol{\theta}]$, $[\boldsymbol{G}]$ and $[\boldsymbol{P}]$ are matrices for the nodal capacitors, nodal temperatures, thermal conductances, and nodal heat sources, respectively. It should be remarked that the establishment of the thermal conductance matrix $[\boldsymbol{P}]$ is exactly the same as one performed for magnetic permeance matrix in chapter 3.

It should be noted that the capacitor matrix essentially consists of zero elements as no thermal storage capacitors are considered at certain nodes as shown in Fig. 4.13; therefore, (4.33) includes both linear differential and linear equations. As a matter of fact, the solving approach to these two equation types are different. Therefore, system equations (4.33) should be divided into two sub-system equations given by (4.34): one includes n_1 nodes, where thermal capacitors are presented (**subsystem 1**), and the other for those without thermal capacitor (**subsystem 2**)

$$\begin{cases} [\boldsymbol{C_1}] \cdot \dfrac{d[\boldsymbol{\theta_1}]}{dt} + [\boldsymbol{G_1}] \cdot [\boldsymbol{\theta_1}] & = [\boldsymbol{P_1}] - [\boldsymbol{G_3}] \cdot [\boldsymbol{\theta_2}] \\ [\boldsymbol{G_2}] \cdot [\boldsymbol{\theta_2}] & = [\boldsymbol{P_2}] - [\boldsymbol{G_3}]^T \cdot [\boldsymbol{\theta_1}] \end{cases} \tag{4.34}$$

$[\boldsymbol{C_1}], [\boldsymbol{\theta_1}], [\boldsymbol{P_1}]$: thermal capacitors, temperatures, and heat sources at nodes of the subsystem 1.

$[\boldsymbol{\theta_2}], [\boldsymbol{P_2}]$: Capacitors, temperatures, and heat sources at nodes of the subsystem 2.

Thermal conductance matrices $[\boldsymbol{G_1}], [\boldsymbol{G_2}]$ and $[\boldsymbol{G_2}]$ are derived from system matrix $[\boldsymbol{G}]$ as in Fig. 4.15.

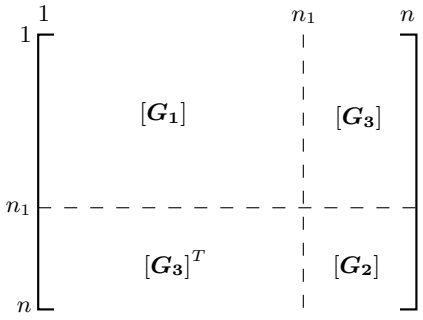

Fig. 4.15: Sub - thermal conductance matrix determination

4.4.1.1 Iterative method for differential equations solving

The system equations (4.34) can be rewritten in the differential form given by (4.35).

$$\begin{cases} [\boldsymbol{C_1}] \cdot \dfrac{\Delta[\boldsymbol{\theta_1}]}{\Delta t} + [\boldsymbol{G_1}] \cdot [\boldsymbol{\theta_1}] & = [\boldsymbol{P_1}] - [\boldsymbol{G_3}] \cdot [\boldsymbol{\theta_2}] \\ [\boldsymbol{G_2}] \cdot [\boldsymbol{\theta_2}] & = [\boldsymbol{P_2}] - [\boldsymbol{G_3}]^T \cdot [\boldsymbol{\theta_1}] \end{cases} \tag{4.35}$$

where Δt is sufficiently small.

The solution to (4.35) is found by the iterative method, where differential equations are solved by updates from the previous solution, and the rest (linear equations) is directly solved from newly updated differential equations. The solution at iteration $(k+1)$ is given by (4.36) with the assumption that thermal conductance matrices are unchanged for this basic step (with constant heat sources).

$$\begin{cases} [\boldsymbol{\theta_1}]^{(k+1)} & = [\boldsymbol{\theta_1}]^{(k)} + \Delta t \cdot [\boldsymbol{C_1}]^{-1} \left([\boldsymbol{P_1}] - [\boldsymbol{G_3}] \cdot [\boldsymbol{\theta_2}]^{(k)} - [\boldsymbol{G_1}] \cdot [\boldsymbol{\theta_1}]^{(k)} \right) \\ [\boldsymbol{\theta_2}]^{(k+1)} & = [\boldsymbol{G_2}]^{-1} \cdot \left([\boldsymbol{P_2}] - [\boldsymbol{G_3}]^T \cdot [\boldsymbol{\theta_1}]^{(k+1)} \right) \end{cases} \tag{4.36}$$

Note that, the solution (4.36) is applicable to any transient $R-C$ circuit (with C are all grounded) with constant current sources.

4.4.1.2 $R-C$ network example

In order to examine the accuracy, effectiveness and general use of this approach as a basic step, a randomly-created $R-C$ network will be used as displayed in Fig. 4.16. Values are given as follows:

$R_1 = 16, R_2 = 25, R_3 = 4, R_4 = 12, R_5 = 6, R_6 = 5, R_7 = 8$ $[\Omega]$

$C_1 = 200, C_2 = 60, C_4 = 47, C_5 = 100$ $[\mu F]$

$i_1 = 5, i_5 = 10$ $[A]$

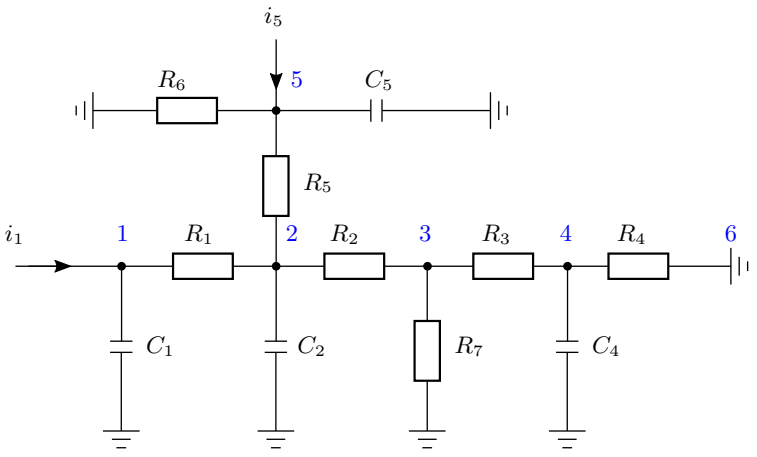

Fig. 4.16: A randomly-created $R-C$ circuit with grounded capacitors

All nodal voltages are to be calculated by using (4.36) and compared to MATLAB Simulink. The conditions for analysis are:

- All capacitors are completely discharged.
- $\Delta t = 0.1$ ms.

The result comparison is shown in Fig. 4.17. As it will be seen, two models reveals exactly same results but the analytical is much faster with only 26 ms compared to that of 2.37 s for the Simulink model (mainly due to interacting time between the Simulink and script environment).

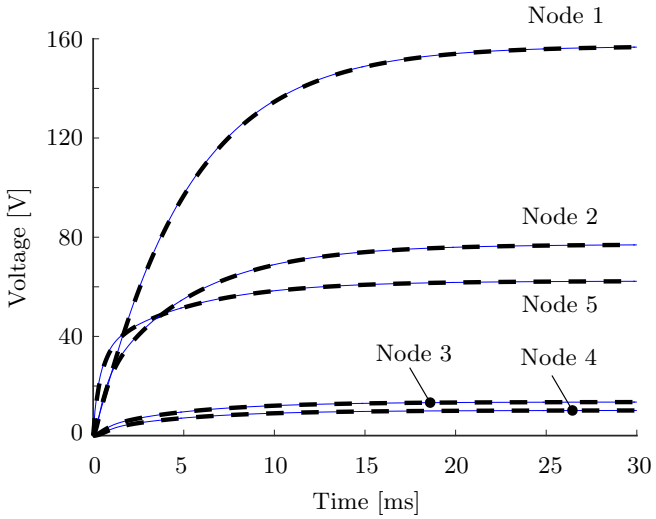

Fig. 4.17: Comparison between analytical and Simulink. Solid - Analytical, dash - Simulink

4.4.2 Coupling between thermal and electromagnetic models

The thermal and electromagnetic analyses are hard to reveal accurate results if the are performed separately since losses are temperature dependent. Therefore, two systems should be coupled to each other, where computed losses from the electromagnetic model are input to thermal model and in return, the temperature result from the thermal analysis are input to the electromagnetic one. The coupling is shown in Fig. 4.18.

The working principle of the coupled system in Fig. 4.18 is explained as follows:

- The electromagnetic model is only run whenever there is a change in any of three following variables: the rotor peed, field current, and armature current (***Condition 1***).
- Losses (copper and iron losses) from the electromagnetic model and initial temperatures (at the beginning, the ambient temperature is taken for every nodes) are input to the thermal modal.
- The thermal analysis is run with an iterative process, as presented in 4.4.1, with a predefined time period for one iteration. During this time period, heat sources (losses) and the

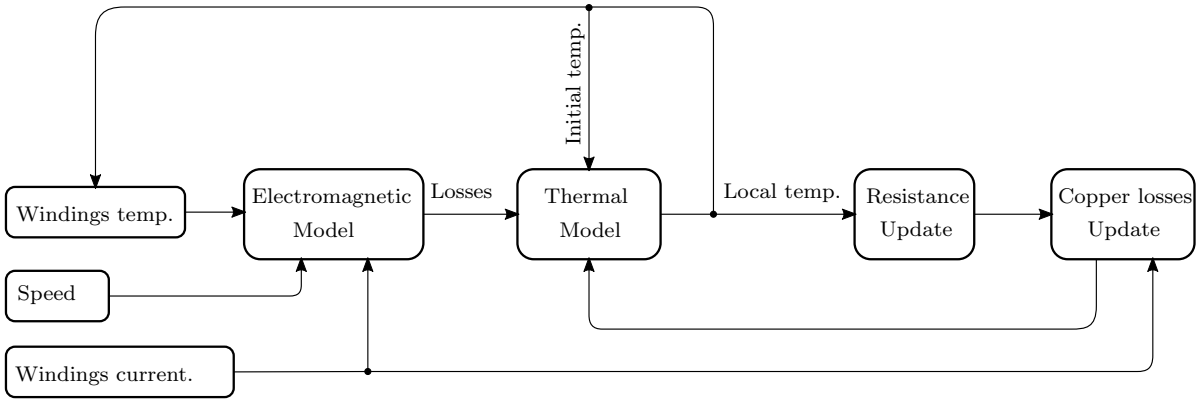

Fig. 4.18: Coupling between thermal and electromagnetic model

surface's heat transfer coefficient are assumed constant. This analysis will output node temperatures.

- These newly updated temperatures will be used for initial temperatures and to re-calculate copper losses in the next iteration of the thermal analysis.
- The iterative process for the thermal analysis continues until the predefined stop time or ***condition 1*** is met.
- If ***condition 1*** is met, the electromagnetic model will be run with newest updates of windings temperatures

4.5 Thermal coefficient re-determination by experiments

As shown in Fig. 4.13, many thermal resistance calculations require empirical equations and even that kind of equations does not exist for some, for instance, the thermal resistance between field windings and the outer stator yoke. Therefore, coefficients verification and re-determination by measurements are necessary.

4.5.1 Experiment approach

In order to more accurately determine thermal coefficients, various experiments to separately evaluate contributions of different heat sources will be conducted. The copper loss and core loss are two main heat sources of the machine since the mechanical losses are neglected, however the core loss is mainly located in the stator core and is evacuated to the surface by a conductive thermal resistance, which does not require empirical equations. Therefore, static (i.e. no rotation and hence no core loss occurred) experiments with copper losses (by field and armarture windings) will be carried out.

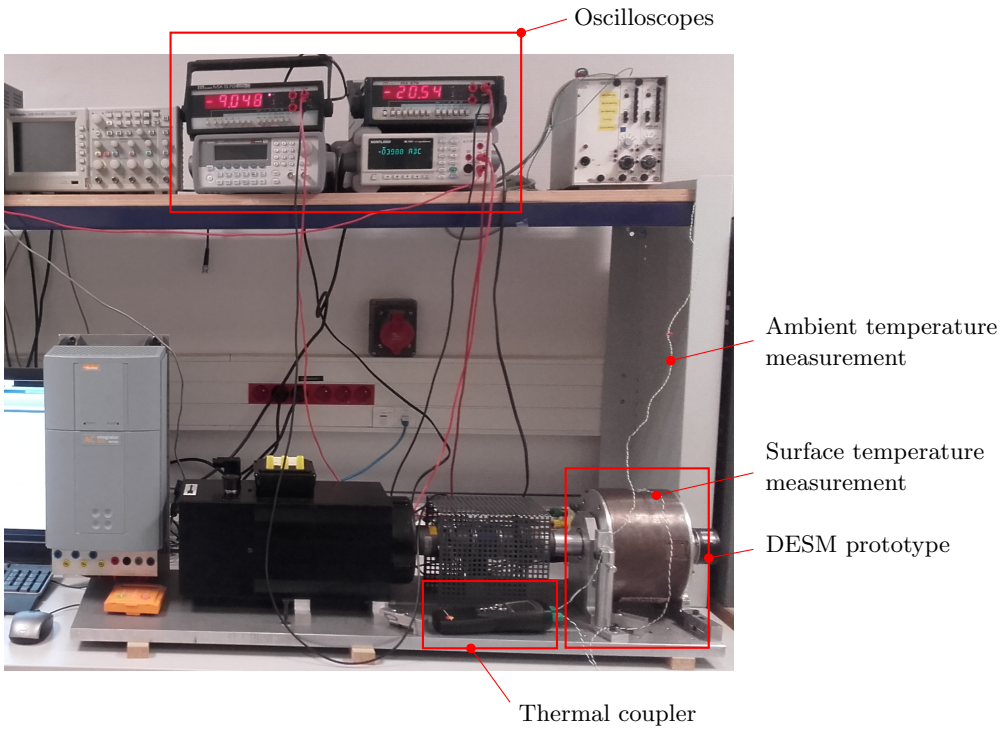

Fig. 4.19: Thermal measurement set up

As shown in Fig. 4.19, a thermal coupler is used to measure the surface temperature, the average temperature of windings are calculated by (4.37)

$$\theta_{\text{winding}} = \theta_0 + \frac{1}{\alpha}\left(\frac{R}{R_0} - 1\right) \tag{4.37}$$

where θ_0 and R_0 are the initial temperature and winding electrical resistance at that temperature. α is the winding temperature coefficient at θ_0 ($\approx 0.004/℃$ at 20℃). R is the winding electrical resistance, which is simply derived from measured current and voltage of the winding.

Three static measurements will be conducted as follows:

- Case 1: Two field windings (group 1) are connected in series and excited with a DC current of 4 A. Armature windings (group 2) are not excited.
- Case 2: Two field windings are not excited. Three armature windings are connected in series and excited with a DC current of 4 A.
- Case 3: Two field windings and three armature windings are all connected in series and excited with a DC current of 4 A.

For each measurement, following procedures will be taken:

- The voltage U and current I of each winding group (field and armature windings) will be recorded.
- The surface temperature θ_s is recorded.

- The recording time interval is 30 mins (decided after several trials based on the thermal transient process).

For each measurement, following data can be retrieved:

- The surface temperature (directly measured).
- The winding temperatures as (4.37)
- The surface coefficient is calculated by (4.38).

$$h = \frac{\sum_{i=1}^{n} U_i I_i}{\Delta\theta \cdot S} \tag{4.38}$$

where U_i and I_i are the final voltage and current of winding group ith, $\Delta\theta$ is the final temperature difference between the surface and ambient, and S is the outer surface area of the machine.

In order to verify predicted coefficients with measurement, the equivalent thermal network for the experiment can be simplified as Fig. 4.20. In this simplified network, the thermal network for the air-gap and rotor part are neglected due to the heat loss from the field and armature windings are almost evacuated through the stator core to the surface. As it will be seen in Fig. 4.20, there are two paths for the heat evacuation: through the field or armature windings. In comparison with a conventional machine, where there is no presence of windings like the global field windings in this machine, the heat evacuation for the armature windings will hardly pass through the air space in the end-winding area to the surface, i.e. only the right-hand-side path in Fig. 4.20.

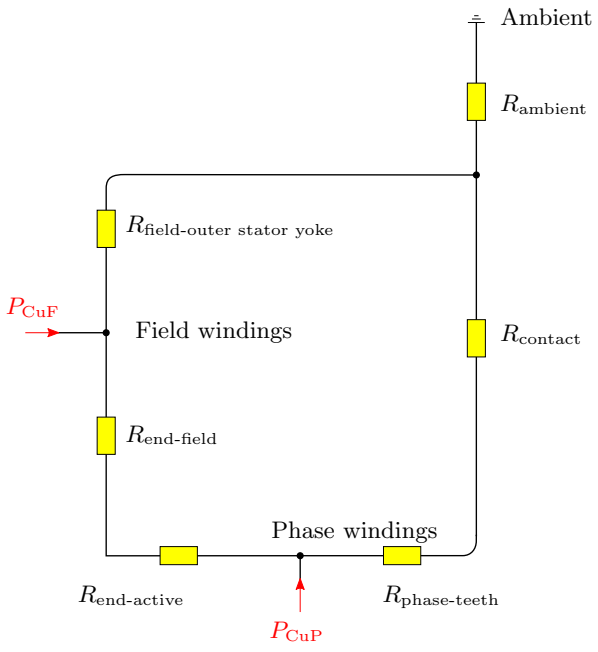

Fig. 4.20: Simplified thermal network for the static measurement

4.5.2 Measurement result and thermal coefficient determination

The thermal transient processes for the three cases mentioned above are shown in Fig. 4.21. As shown, the transient time is approximately 6 hours. This is because of the low surface thermal coefficient causing a high thermal resistance and hence a big thermal time constant.

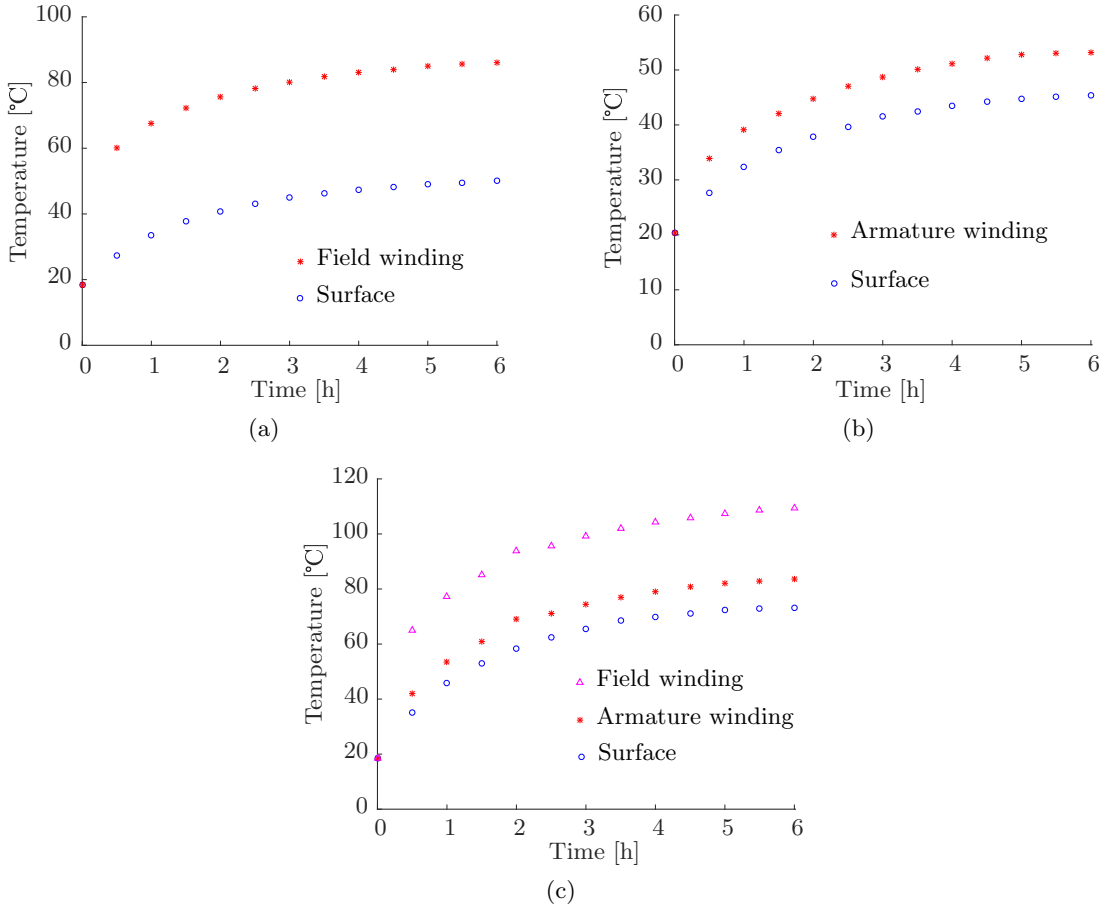

Fig. 4.21: Temperature measurements. a) Case 1. b) Case 2. c) Case 3

The final values of the transient process, which can be considered as steady-state values, are reported in Table. 4.2.

Table 4.2: Static measurement results

Case	Surface temp.	Field winding temp.	Armature winding temp.	Field winding power	Armature winding power
1	50	86	N/A	53.04	N/A
2	44.3	N/A	53.2	N/A	39.4
3	73.2	109.5	83.7	58.0	44.3

Even though the applied current is rather low and at the static condition, the recorded temperature is high due to the natural air cooling. From these measurement results, following

coefficients (Fig. 4.20) will be determined:

- The surface heat coefficient.
- The coefficient corresponding to thermal resistance between the field windings and the outer stator yoke: α_f.
- The coefficient related to the thermal resistance between the end-winding and active parts of the armature winding: α_{ea}.
- The equivalent air-gap length between the armature end-windings and field windings: l_e

It should be noted that thermal resistance between active parts of the armature windings and the stator core follows (4.29), and the thermal contact resistance between the inner and outer stator cores is calculated with a fixed contact coefficient of 1000 W/m^2 ℃ as mentioned in 4.3.5.

4.5.2.1 Surface heat coefficient determination

The first and easy-to-determine thermal coefficient is the surface heat coefficient, which consists of convective and radiative ones. Having accepted that all heat sources will be evacuated through the surface of the machine, the surface heat coefficient h_s is calculated by (4.38) according to different surface temperatures and copper losses. These values are listed in Table. 4.3 in comparison with ones calculated by equations from (4.17) to (4.23).

Table 4.3: Surface heat coefficient at 20℃ ambient temperature

Case	Surface temp. [℃]	Measured h_s [W/℃/m^2]	Calculated h_s [W/℃/m^2]
1	50	13.34	10.96
2	44.3	12.15	10.51
3	73.2	14.83	12.57

From Table. 4.3, it is obvious that at higher surface temperature, the coefficient increases, this is due to the increases in the convection and as well as the radiation. However, there are differences between measured and calculated ones. This can be explained by different surface emissivities. In addition, the machine in the experiment is coupled with some components, which certainly increases the equivalent surface are of the machine and hence coefficient derived from (4.38) will be higher. Therefore, a correction factor of 1.2 is applied to this coefficient. The measured, calculated coefficient in Table. 4.3 together with the corrected one are displayed in Fig. 4.22.

4.5.2.2 Coefficients associated with windings

Coefficients associated with the armature and field windings as mentioned above namely α_f, α_{ea}, and l_e will be determined by a simple optimization to minimize the norm $\|\cdot\|_\infty$ between

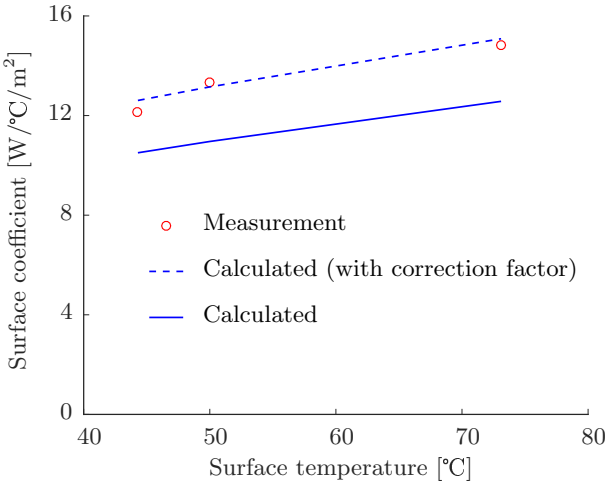

Fig. 4.22: Surface coefficient according to surface temperature at 20℃ ambient temperature

steady-state temperatures of calculation and measurement in three cases. A coefficient set chosen is reported in Table. 4.4. The accuracy of these values will be concluded by validations with experiments.

Table 4.4: Coefficient fitting

α_f	α_{ea} [W/m/℃]	l_e [mm]
2.5	8.0610^{-5}	3.3

The value of α_f means that the thermal resistance between the global field windings and stator core is 2.5 times as high as that of a classical armature winding located in a slot. It clearly shows the low heat transfer capability of global field windings.

4.5.2.3 Coefficient verification

With all coefficients determined, the whole system will be verified with experimental results displayed in Fig. 4.21. The comparison is shown in Fig. 4.23.

A good accordance is reported in Fig. 4.23 for both the final values and transient process. Note that, in this comparison, the calculated temperature of the armature winding is uniformed between ending and active parts (derived from the total armature winding resistance). Separated temperatures for these two parts are shown in Fig. 4.24. At the steady state, the temperature of the end-winding is 87.8℃, which is 3℃ higher than that of the active part. The calculated average temperature of armature winding is 85.5℃ which is very close to the measured one (83.7℃)

In order to further investigate the accuracy of the fitting coefficients, an additional measurement is conducted with a higher armature current of 6 A and the field current is set to zero. The

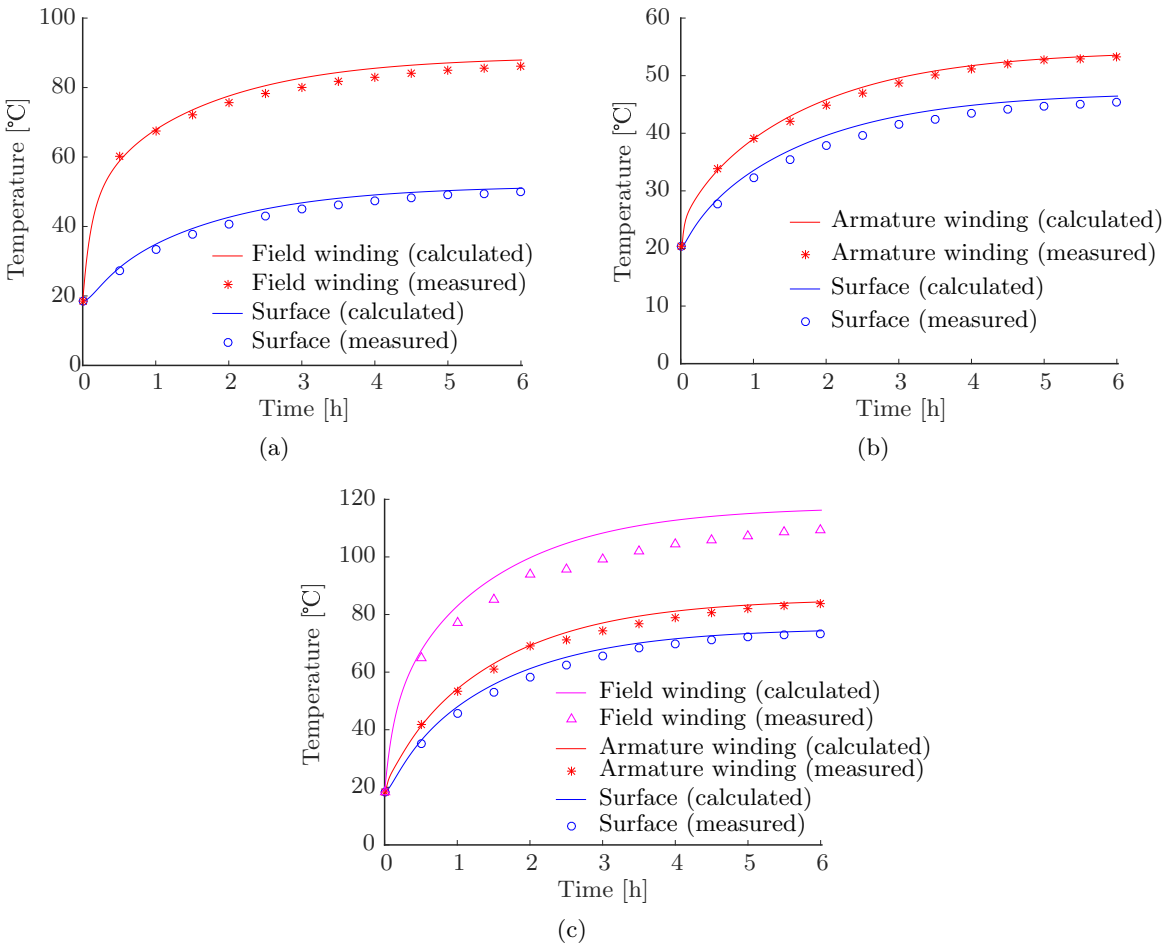

Fig. 4.23: Temperature measurement. a) Case 1. b) Case 2. c) Case 3

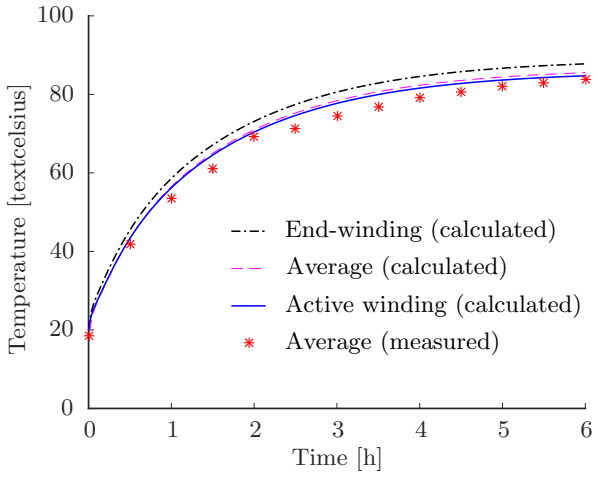

Fig. 4.24: Temperature of armature winding

comparison between predicted temperatures and measurement is shown in Fig. 4.25.

As it can be seen, the good accordance verified the determined coefficients and accuracy of the thermal model.

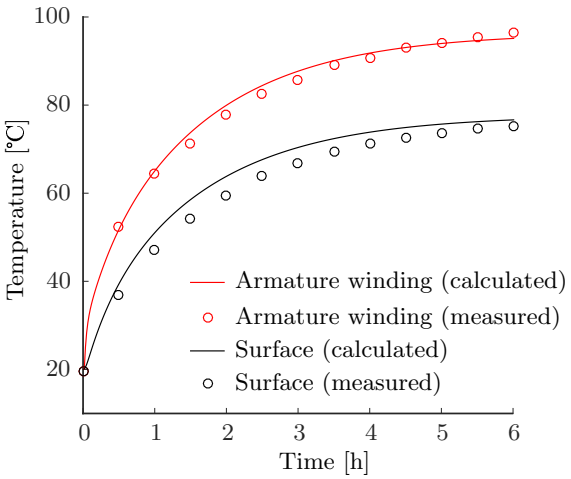

Fig. 4.25: Measurement with phase current 6 A, field current 0 A

4.5.2.4 Thermal analysis of model in dynamic regime

With the thermal model has been verified experimentally, an analysis will be tested in the dynamic regime, i.e. with rotation. Four cases will be considered:

- The phase current of 10 A (rated current), the field current of 0 A, and the speed of 1000 rpm.
- The phase current of 10 A (rated current), the field current of 4 A, and the speed of 1000 rpm.
- The phase current of 10 A (rated current), the field current of 0 A, and the speed of 2000 rpm (rated speed).
- The phase current of 10 A (rated current), the field current of 4 A, and the speed of 2000 rpm (rated speed).

The temperatures in the steady-state at different parts of the machine are reported in Table. 4.5. As it will be observed, the temperatures of windings go beyond 180℃ ,i.e. the H insulation class. The natural air cooling method appears to be unsuitable. Therefore a new surface heat coefficient h_s of 100 W
textcelsius /m^2. This is the upper limit for the natural air convection. Temperatures are re-calculated with the new surface heat coefficient shown in Table. 4.6, the new temperatures fall below class F (155℃), which will be set as the temperature limit of the windings in design.

Conclusion

This chapter has focused on the thermal aspect of the studied DESM. A lumped parameter analytical model has been developed with the objective to determine overall temperatures of

Table 4.5: Predicted temperatures at various parts of the machine

Case	End-winding	Active winding	Field winding	Stator	Rotor	Surface
1	305	289	225	233	246	206
2	341	322	313	260	274	231
3	359	342	265	280	298	244
4	394	374	358	306	325	267

Table 4.6: Predicted temperatures with the new surface heat coefficient

Case	End-winding	Active winding	Field winding	Stator	Rotor	Surface
1	119	109	65	72	82	53
2	130	118	111	79	89	59
3	145	134	82	95	109	68
4	158	146	132	104	117	74

the windings, which are accurate enough for the optimization process. The main advantage of this approach is the fast computation time, which is about 86 ns for one iteration in solving the linear differential equation system. A well-known feature of a thermal analysis is that a lot of empirical equations was used; therefore, measurements are necessarily required to determine heat coefficients and verify that thermal model. Due to the fact that there is no winding presented in the rotor part while losses due to permanent magnet are quite small, the main heat is evacuated from the windings (in the stator part) though the stator core to the surface without passing air-gap area between stator and rotor.

Due to the difficulties of the natural air cooling, which was considered for the DESM prototype), a new surface heat coefficient is assumed. This assumption only changes heat evacuation on the surface, all determined heat coefficients inside the machine are kept unchanged. In next chapter, the multi-physics model coupling between electromagnetic and thermal one will be used for the design optimization of the machine based on a driving cycle.

This page intentionally left blank

Chapter 5

Machine Optimization on a Train Driving Cycle

The multi-physics model for the DESM prototype developed in previous chapters will be utilized in this chapter for the design optimization taking into account a train driving cycle. As it will be shown later, performing an optimization considering a huge number of operating points in the driving cycle is a challenging task. This is because of considering the model's nonlinearity, even though a very fast model (compared to FEM) was used. A set of representative points will be chosen. These points must represent the region, where the machine most frequently works on. The objectives of the optimization are to minimize the cost and total losses on the driving cycle. The number of objectives would be higher in reality, however in the first phase of design, these two classical objectives, which are strongly related to the economy aspect would be acceptable. This chapter will firstly study the performance of the DESM prototype on the driving cycle. Then optimizations based on a single operating point will be examined. The most important part to be conducted is to compared the DESM with a classical permanent magnet machine based on the driving cycle. Finally, a conclusion and ranges to use DESM machines will be discussed.

5.1 Train driving cycle and design methodology

5.1.1 Train driving cycle

In the transportation domain, vehicles are required to operate at different speeds at given times along their trips. This leads to the requirement of machine's torque to accelerate/decelerate accordingly. This operation defines a load cycle for specific cases (urban, rural, motor way, railway, etc.). A load cycle is basically torques - speeds combination. There are a couple factors influencing a load cycle:

- Required speed/acceleration (driving cycle) as a function of time. As mentioned above, this depends on the vehicle types.
- Route profile, i.e. road characteristic.

These factors help to determine necessary torques to achieve the required speeds/accelerations. The driving cycle is a benchmark for the machine testing, however, the driving cycle would vary significantly on account of real conditions of the route profile, weather, driving behavior, etc.

The train driving cycle is illustrated in Fig. 5.1 [91]. As it will be seen, the machine are required to be able to operate in both the motor and generator modes. The operating points in the torque vs. speed space does not distribute in the whole space but instead, are clustered in some regions. This clustering distribution will be considered in the design approach. Generally there are 1000 operating points at specific times but some points are repeated several times and the number of discrete points is in fact 639.

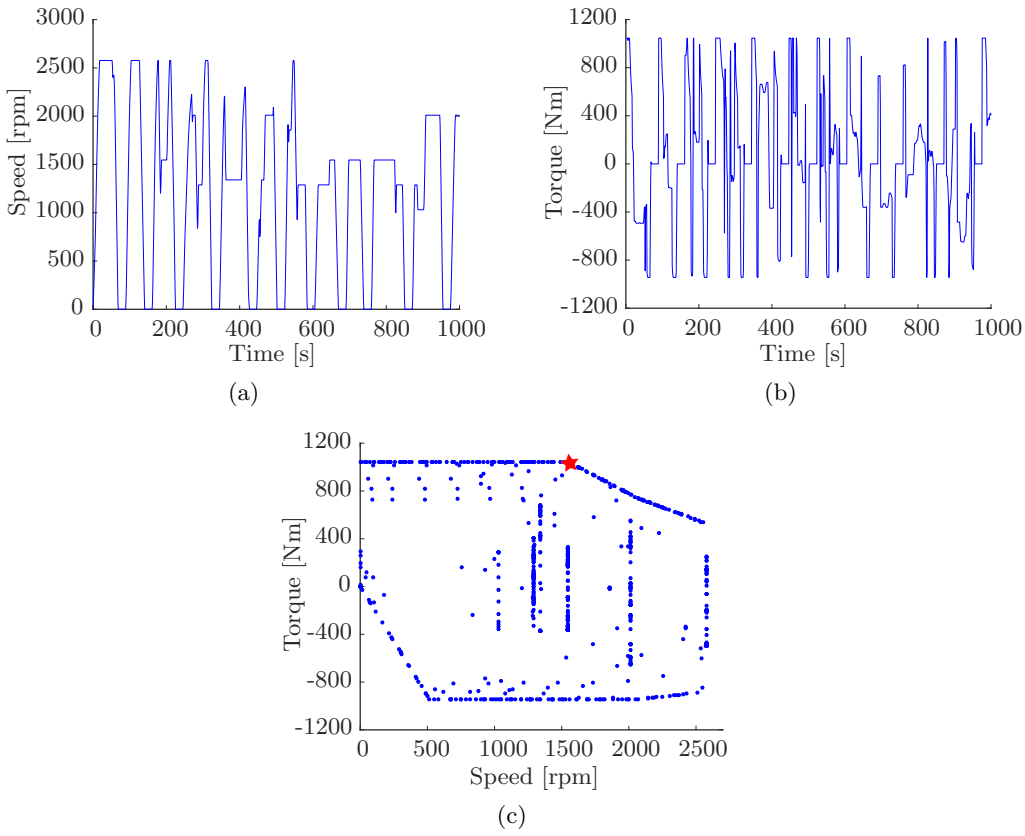

Fig. 5.1: A train driving cycle. a) Speed profile. b) Torque profile. c) Torque vs. speed characteristic

Another point worth mentioning in the torque - speed characteristic is that the ratio between the maximum and base speed. The base speed is the transition point between constant torque and constant power regions, red star marked. On this driving cycle this ratio is 2533/1547 $\approx$ 1.7, which is relatively small. It means that at high speed operation, the requirement of flux weakening control might be easy to achieved. This will certainly affect the optimal design. The influence of this ratio will be also examined later on in this chapter.

5.1.2 Design methodology

This chapter deals with a number of optimizations considering the given driving cycle; therefore, discussions for both the model usages and driving cycle will be given below.

5.1.2.1 Scale-down load cycle

As shown in the Fig. 5.1, the maximum required torque is about 1000 Nm. However, the prototype was designed with the nominal torque of 10 Nm. Two approaches would be considered: A theoretical redesign process considered for the real train application or a modified load cycle with a scale-down factor for torque of 1/100 as shown in Fig. 5.2 (the speed range is kept unchanged). The first approach will face difficulty of lacking experimental verifications for the modelings. More importantly, the main objective of the research is to examine the double excitation principle and compare with a classical electrical machine; therefore, having machines with validated modeling accuracy will be more preferable. The scale-down approach is, therefore, adopted.

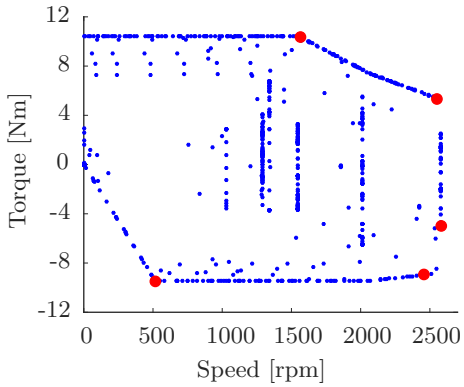

Fig. 5.2: Torque speed characteristic of the driving cycle with torque is scaled down 100 times

5.1.2.2 Sinusoidal armature current assumption

In the motor mode, the machine is practically supplied from a three phase pulse width modulation (PWM) inverter, and the armature current is assumed to be sinusoidal. At a high speed, this assumption works since high harmonic orders are filtered out by the armature winding inductance. But this will be less accurate at low speed, these harmonics may stay at large amplitudes causing the armature current waveform distorted. Equation solving with nonlinear analysis model will much increase the complexity and more importantly making the optimization on driving cycle become impractical. Therefore, the armature currents are assumed to be sinusoidal in all cases.

5.1.2.3 Steady state or transient thermal analysis

Even though a transient thermal analysis were well developed in chapter 4; however, this transient model is only applicable if all operating points on the driving cycle are considered in sequence in the time domain. If optimal controls are to be found for all of these points, i.e. 1000 optimization loops incurred (each loop may take hundreds model evaluations, several driving cycles needed for the stable temperatures and about 5 seconds for one evaluation), the computation would last about few weeks to evaluate one single machine on a computer with a core (4) i7, 2.93 Ghz processor. Another option is to build surface approximations with the input is control variable set including the armature current amplitude and its phase angle, field current, speed and several temperature values from previous points. These will make the problem unfeasible. Due to these reasons, the steady state thermal analysis will be used. Note that using the steady state approach for the temperature calculation will overestimate temperatures since the thermal time constant is much higher than operating time at each point.

5.1.2.4 Optimization algorithm

The Non-dominated Sorting Genetic Algorithm (NSGA)-II belonging to Mutltiobjective Evolutionary Algorithm (MOEA) is a popular algorithm solving multi-objective optimization problems. The Multi-objective Particle Swarm Optimization (MOPSO) is widely applied as well. Within the scope of this thesis, the MOPSO algorithm will be used. The reason is that it is firstly hard to generally decide which algorithm is overwhelming. Second, MOPSO algorithm was developed in SATIE [92, 93] and used conveniently in the laboratory. It would be interesting to examine results by comparisons between these two algorithms. However, this comparison is not considered since the optimization needs to run twice and it would take too much time. Instead, quick comparisons between MOPSO and NSGA-II algorithms with mathematical functions are demonstrated in B.

5.1.2.5 Machine requirement

In this research, machine requirements only focus on the given driving cycle, i.e. the machine should satisfy only points presented in the driving cycle. In the motor mode, the machine must satisfy constraints for the voltage and temperature limits. In the generator mode, the input mechanical power should overcome all the losses, thermal and voltage limit as well. Basically, the machine must satisfy 5 corner points bounding the driving cycle (red circle marked in Fig. 5.2): 2 points in the motor modes including the base (maximum torque and hence high current required) and maximum speed (due to voltage limit) points, and 3 points in the generator mode with high torque and low speed, i.e. small mechanical input must overcome the copper loss incurred by a high current. Two other points in the generator mode are at high torques and

high speeds, i.e. the thermal limit might be reached. These two points are in fact quite close in performance.

5.2 Performance of the DESM prototype on the driving cycle

Before going to optimize the machine regarding the driving cycle, the discussed DESM prototype will be examined on this cycle. With dimensions of the machine are fixed, the objective is to find the optimal control to minimize losses at each operating point. It could be a good reference for comparisons later on.

5.2.1 Optimization problem formulation

The objective of finding the optimal control set is to minimize the total losses with respect to constraints. With the double excitation principle, the control set consists of three variables: the armature current I_{arm}, phase angle between the armature current and no-load back EMF ψ ,and the excitation current I_{dc}. The optimization problem is expressed as (5.1):

$$\begin{aligned} \underset{X=\{I_{arm},\psi,I_{dc}\}}{\text{minimize}} \quad & f(X) = P_{\mathrm{Cu}} + P_{\mathrm{Fe}} + P_{\mathrm{PE}} \text{ [W]} \\ \text{s.t.} \quad & V_{\max} \leqslant 150 \text{ [V]} \\ & \theta_{\max} \leqslant 155 \text{ [°C]} \\ & T = T^* \text{ [Nm]} \\ & \Omega = \Omega^* \text{ [rpm]} \end{aligned} \tag{5.1}$$

where P_{Cu}, P_{Fe}, P_{PE} are the total copper losses of both the armature and excitation windings, core loss and total losses in the power electronic module, $V_{\max}$ is the peak of the first harmonic of the phase voltage, $\theta_{\max}$ is the maximum temperature of both the windings, T is the shaft torque, and T^* is the torque requirement. Ω and Ω^* are the speed and speed requirement, respectively. With the mechanical loss neglected as proved in chapter 4 and taking into account the core loss, the shaft torque is different from the electromagnetic torque expressed by (5.2):

$$T = T_e - \frac{P_{\mathrm{Fe}}}{\Omega} \tag{5.2}$$

where T_e is the electromagnetic torque and Ω is the mechanical speed. At the standstill position, the shaft torque is the same as the electromagnetic torque and the second term in right hand side of (5.2) are neglected. Therefore, regarding the convenience of numerical computations, the minimum speed is set to 1 rpm without causing any difference since core loss at this speed is almost zero.

For the torque equality constraint $T = T^*$, it is quite challenging to deal with, so this constraint is relaxed by 5% as (5.3).

$$|T - T^*| \leqslant 0.05|T^*| \tag{5.3}$$

In the motor mode, the machine is supplied from a DC link voltage of 300 V, the inverter is set to work in the linear modulation range to avoid more sideband harmonics centered around the harmonics of the switching frequency. As the result, the peak phase voltage can be delivered is $300/2 = 150$ V.

5.2.2 Strategy for optimal control finding

Dealing with a task of finding optimal controls at a large number of operating points, two strategies would be considered:

1. Strategy directly using nonlinear model evaluation:
   At each operating point, the input is the 3 variable control set, this control set is evaluated with objective functions and verified against constraints by the optimization process. The optimal set will be searched and the computation time is proportional to the number of operating points.

2. Strategy using meta-model:
   A large set of control variables is used to generate approximated response surfaces. The optimization to search for the optimal control will be performed based on these surfaces. The optimal control set at each point is then validated against the high fidelity model (in this case is the multi-physics model developed in previous chapters). If a big errors exist, this control set will be added to the surface and the process repeats. This approach is useful when dealing with a huge number of points and when there is a need to quickly discover performances of any point in the search region. For the case being studied, in order to generate response surfaces including the core loss calculation the input variable set should include 5 variables (three for current variables, one for speed and one for operating mode). This large set of variable does not only require much computation time but also actually causes numerical bugs for the post processing with interpolation process.

.

The first approach will, therefore, be studied in the following.

As mentioned above, this approach uses the multi-physics model as functions to evaluate the input variables. With the mono-objective optimization to find the optimal control, it would be suggested to use the Sequential Quadratic Programming (SQP) method. Usually, with a classical machine, where there are only two control variables (for the armature current only), the objective or constraint surfaces are expected to be smooth. Therefore, using the gradient method might work effectively. However, in case of 3 variable control set as with double excitation machines, multiple objectives and constraint surfaces exist (each surface for one value of excitation current), it means that multiple local optimum points present. As a consequent, the gradient method may make result likely to be trapped into local minimums. This point could be illustrated as examples shown in Fig. 5.3 for the shaft torque and total loss response

surfaces with field currents are -3 A and 3 A. The surfaces are given according to $d-$ and $q-$ axis currents.

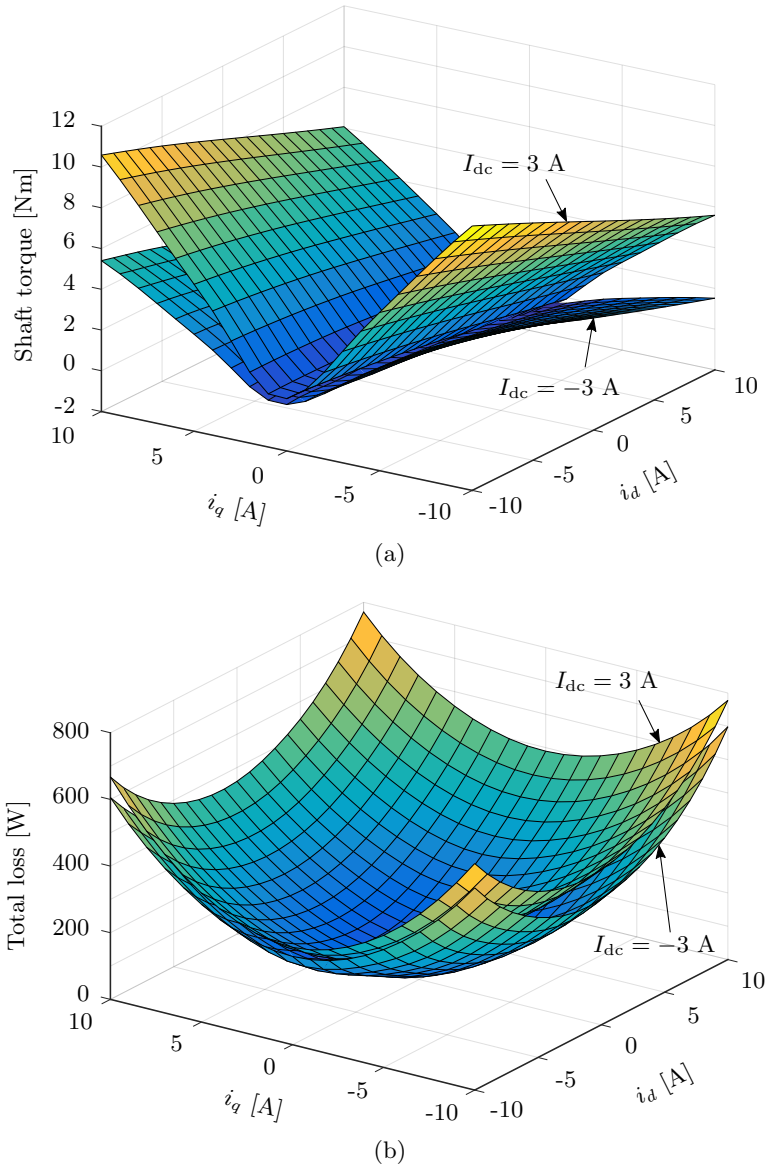

Fig. 5.3: Response surfaces at the speed 2000 rpm, motor mode. a) Shaft torque. b) Total loss

For this purpose, the MOPSO algorithm will be applied. The interesting point with MOPSO is that it certainly could handle mono-objective problems by simply fixing one objective constant. Two important parameters for the MOPSO are the numbers of particles n_p and iterations n_{iter}, since they directly affect the result accuracy and computation time. For a large number of optimizations it is desirable to reduce the computation time. Having large numbers will improve the optimality but time consuming and vice versa. These numbers depend on both the number of input variables and problem complexity. There is, in fact, no rule of thumb to choose these numbers. In this part, several combinations between the number of particles and iterations will be tested with repetitions. The reason for the repetition is due to the heuristic nature of the algorithm; therefore, by doing this, it can ensure the good result retrieved. The

chosen combination set will be applied later on for all cases to find the optimal control sets.

The test will be applied for the rated operating point with 7 combinations sets $\{n_p, n_{\text{iter}}\} = \{5, 5\}; \{5, 10\}; \{10, 5\}; \{10, 10\}; \{20, 10\}; \{10, 20\}$ and $\{20, 20\}$. These combinations will be repeated 5 times and results will be compared with the case $\{50, 50\}$, which is expected to have the true optimum.

The results and comparison are summarized in Table. 5.1. With the armature current quantities (rms value I and phase angle ψ) are converted into $d-$axis and $q-$axis ones expressed by (5.4).

$$\begin{aligned} i_d &= \sqrt{3} I \sin\psi \\ i_q &= \sqrt{3} I \cos\psi \end{aligned} \tag{5.4}$$

The "N/A" note means no solutions were found, this is due to a very small number of particles/iterations used. The expected true optimum $\{i_d^*, i_q^*, i_{dc}^*\}$ = {-4.48, 12.38, 3.48} [A] leads to the optimum total loss of 397 W. This result is done with 50 particles and 50 iterations, which is considered big enough to make sure a convergence, and in fact from results summarized in Table. 5.1, losses through cases and iterations converge to this value. The results shows that same combinations of n_p and n_{iter} repeats several times does not reveal same results due to the heuristic characteristic of the optimization algorithm as mentioned. However, if the more number of particle or iteration used, the results become less deviated. Keeping in mind the evaluation of one control set takes about 5 seconds and the total computation should be at least $5 \times n_p \times n_{\text{iter}}$ seconds. Summarized in Fig. 5.4, having a good stability and accuracy (about 2% deviated from the optimum), the case {10, 10} is a good compromise between the accuracy as shown in Fig. 5.4 and computation time. It should be noted that about 100 functions evaluations for optimization is a very promising number for example a guide for SQP usages in MATLAB, at least few hundred function evaluations should be set as a stopping criteria. Therefore, this combination will be chosen and referred to the name 10-by-10 approach.

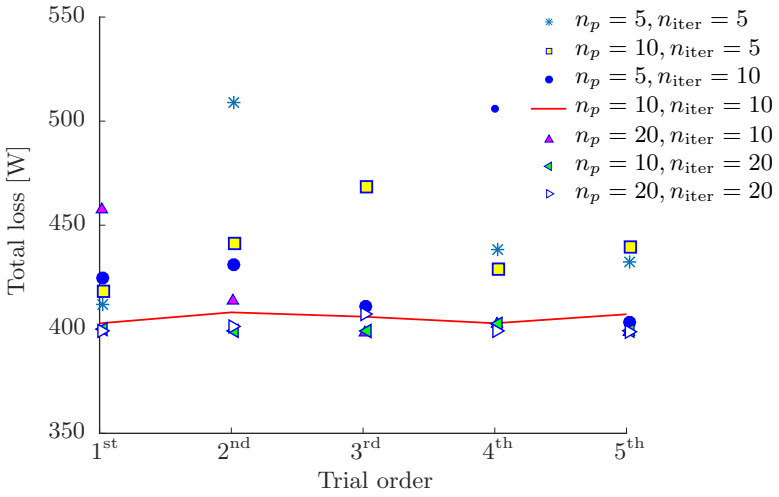

Fig. 5.4: Accuracy comparison between difference $\{n_p, n_{\text{iter}}\}$ combinations

Table 5.1: Different combinations of $\{n_p, n_{\text{iter}}\}$ comparison

Quantity	{5, 5}	{10, 5}	{5, 10}	{10, 10}	{20, 10}	{10, 20}	{20, 20}
			1^{st} trial				
i_d [A]	-6.18	-5.58	-3.73	-4.89	-7.69	-5.36	-4.40
i_q [A]	12.82	12.16	13.72	12.14	13.65	12.25	12.37
i_{dc} [A]	2.55	2.34	2.68	1.75	2.73	2.95	3.39
Total loss [W]	411	417	423	402	457	399	398
			2^{nd} trial				
i_d [A]	-0.90	-5.29	-4.16	-4.79	-6.48	-5.16	-5.00
i_q [A]	14.70	11.67	11.81	12.52	12.36	12.23	12.01
i_{dc} [A]	4.13	5.00	4.94	3.64	3.26	3.57	3.93
Total loss [W]	508	439	430	408	413	397	400
			3^{rd} trial				
i_d [A]	N/A	-8.79	-2.35	-5.46	-4.41	-4.94	-4.89
i_q [A]	N/A	12.42	12.82	12.39	12.47	12.30	11.85
i_{dc} [A]	N/A	3.32	3.84	3.48	3.52	3.54	4.27
Total loss [W]	N/A	467	410	406	397	397	406
			4^{th} trial				
i_d [A]	-4.85	-6.00	-9.05	-5.66	-3.58	-6.16	-4.51
i_q [A]	13.40	13.28	14.12	12.41	12.67	11.91	12.32
i_{dc} [A]	3.28	2.31	0.97	3.27	3.59	3.65	3.67
Total loss [W]	437	427	506	403	402	401	397
			5^{th} trial				
i_d [A]	-4.69	-8.85	-5.33	-5.97	-5.26	-4.65	-4.43
i_q [A]	11.63	11.67	12.68	12.48	12.18	12.24	12.37
i_{dc} [A]	5.00	3.44	3.00	3.16	3.59	2.35	3.62
Total loss [W]	431	438	402	407	398	398	398

Table 5.2: Computation time for difference combinations $\{n_p, n_{\text{iter}}\}$

Cases	{5, 5}	{10, 5}	{5, 10}	{10, 10}	{20, 10}	{10, 20}	{20, 20}
Computation time [mins]*	2.08	4.16	4.16	8.32	16.64	16.64	33.28

* Based on a single thread computation

5.2.3 Result analysis

As mentioned above, the equality torque constraint is relaxed as an inequality constraint as (5.3) to facilitate the searching process of the optimal control; therefore, the comparison between the

real torque and required torque is examined as in Fig. 5.5

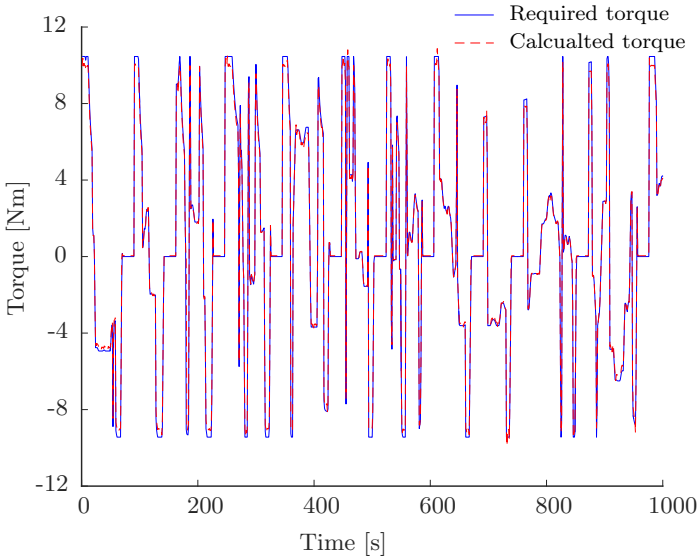

Fig. 5.5: Comparison between real torque and required torque on the driving cycle

Generally two torque profiles should match as set in the optimization constraint. However the continuousness of the real torque profile means that the optimization algorithm with 10-by-10 approach by MOPSO is able to find an optimal control set at every operating point (if no solution found the controls are set as N/A).

The total copper loss along the driving cycle displayed together with the torque profile is shown in Fig. 5.6. The copper loss is large when a high torque is required. Core losses along the driving cycle are shown in Fig. 5.7. Generally, high speed operating points yield big core loss but the core loss also depends on the maximum induction, which is a consequence of the current control adjustment.

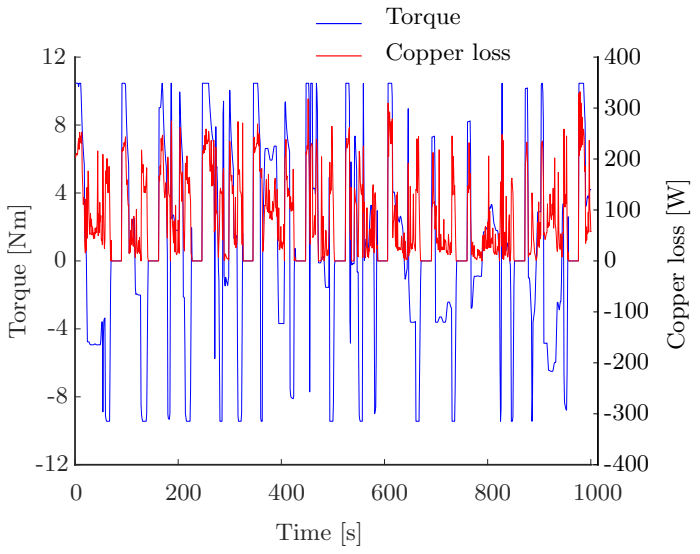

Fig. 5.6: Total copper losses along the driving cycle

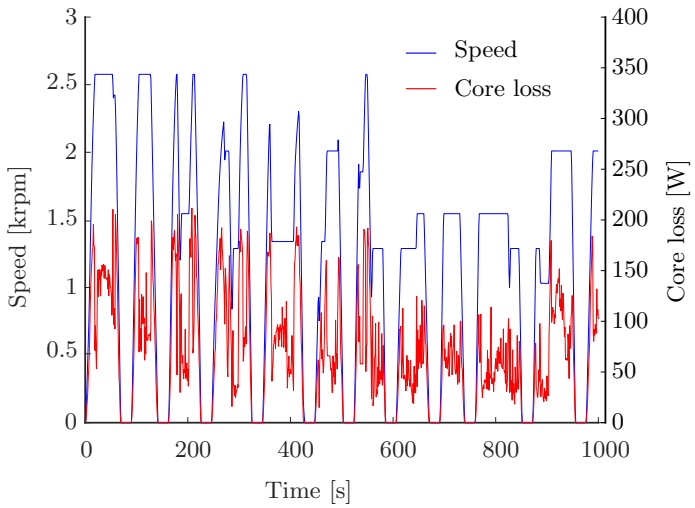

Fig. 5.7: Core loss along the driving cycle

Fig. 5.8 shows current evolutions with respect to time along the driving cycle. It is generally claimed that the contribution of the excitation winding provides one more degree for the controlling the air-gap flux and hence it provides more possibilities to optimize the machine's performance. Therefore, at the same time, it makes the controlling strategy more complex to perceive, especially in the context of minimizing total losses with respecting torque, voltage and thermal limits constraints. Additionally, issues with local minimal trapping and multi-optimum points may exist for a certain cases also contribute to the control complexity. As it will be seen in Fig. 5.8, $q-$axis current roughly follows the trend of the torque profile but for $d-$axis and excitation currents are more complex to have a clear dependence. Individual losses of the prototype on the driving cycle is summarized in Table. 5.3.

Table 5.3: Individual losses of the prototype on the driving cycle

	Excitation windings	Armature windings	Iron core	Power electronics	Total
Loss [kW]	10.64	68.01	64.12	20.97	163.74

5.3 Single point optimization

In this section, optimizations of the DESM machine will be carried out based on one single operating point. The optimization objective, which is shown in (5.5), is to minimize both the cost and total losses. The cost considered here only accounts for the raw materials. This cost actually varies regarding suppliers, time and also material quantities. Therefore, in order to accomplish fair comparisons between structures, a normalized cost will be used in which the per-kg iron cost is assigned to 1, values for the copper and ferrite PM are 7 and 6, respectively [94]. Note that the unit cost for ferrite PM is less than copper meaning that regarding the

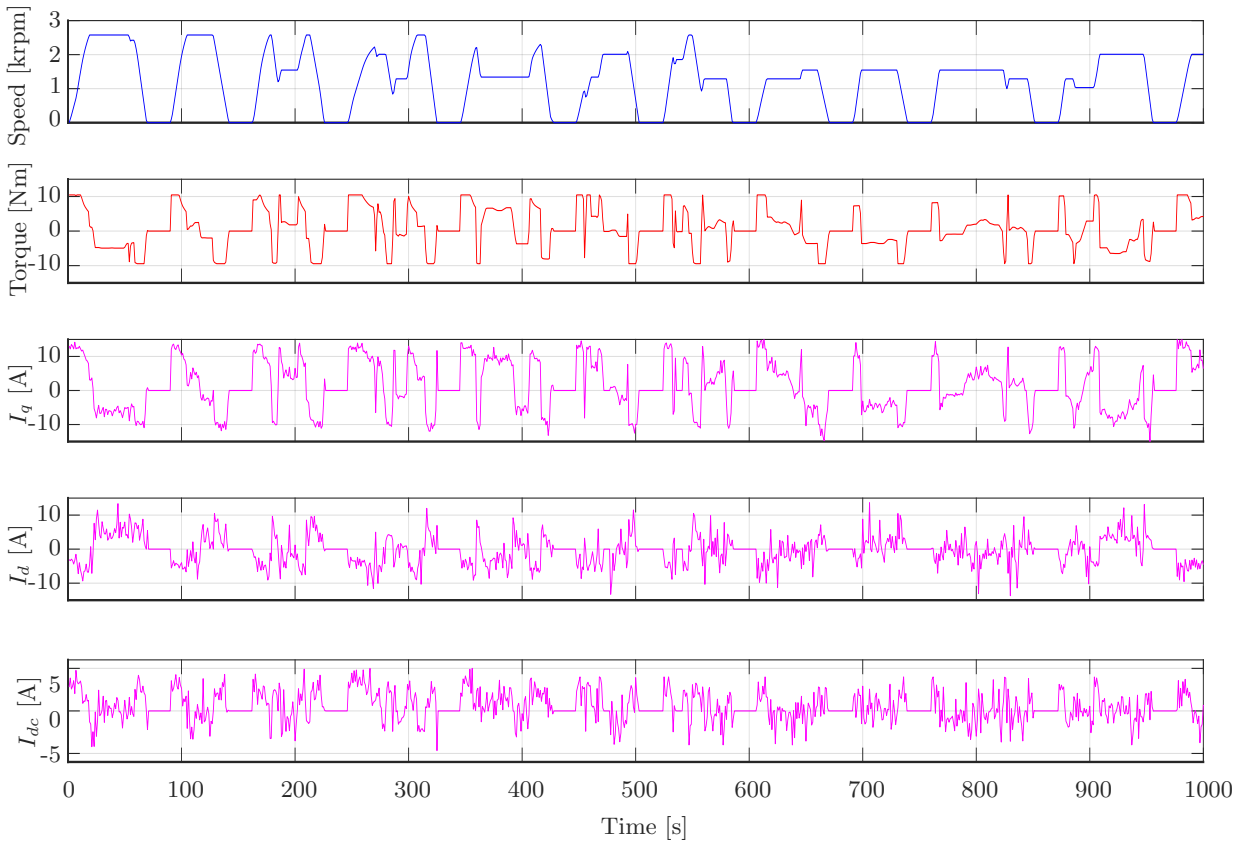

Fig. 5.8: Control strategies along the driving cycle

objectives (the loss and cost minimization), using ferrite PM might gain some advantages over the excitation winding; however, detailed comparisons should be investigated.

$$\begin{aligned} \underset{X=\{X_g,X_c\}}{\text{minimize}} \quad & f(X) = \begin{cases} P_{\text{Cu}} + P_{\text{Fe}} + P_{\text{PE}} \text{ [W]} \\ C(X_g) \end{cases} \\ \text{s.t.} \quad & V_{\max} \leqslant 150 \text{ [V]} \\ & \theta_{\max} \leqslant 155 \text{ [°C]} \\ & T = T^* \text{ [Nm]} \\ & \Omega = \Omega^* \text{ [rpm]} \end{aligned} \tag{5.5}$$

where X_g and X_c are the geometry and control variables, respectively. $C(X_g)$ is the machine cost, and Ω^* is the operating speed.

The formulation (5.5) is generally applicable to either single point or multiple points optimization, i.e. T^* (Ω^*) can be a set of required torques (speeds).

5.3.1 Bi-level optimization approach

The optimization problem formulated as (5.5) leads to two possible solutions:

- One level optimization approach:
  This approach is exactly shown as (5.5), where all geometry and control variables are input variable set. This approach requires a large number of machines to be evaluated. However, the biggest challenges is that when dealing with multiple-point optimization, the number of constraints will proportionally increase. For instance, if 3 operating points to be optimized at the same time, the number of constraints are 9 including 3 equality constraints and the number of variables are 9 (3 for each point). This will make the optimization problem infeasible (mainly due to the number of constraints)

- Bi-level optimization approach:
  In this approach the variable set is divided into 2 variable sub-set X_g and X_c as in (5.5). The meaning of bi-level is that for each machine, one or several (as the same number of operating points to be optimized) mono-objective sub-optimizations (lower level) are performed to search for the optimal control set, all constraints are handled at this level. At the upper optimization level, the objective is to minimize cost and optimal losses newly found at the lower level. This level does not deal with any constraint since they are all handled in the lower level, only two objectives are considered. With this bi-level approach, the computation time actually increases proportionally with the number of operating points, but it effectively overcomes the infeasibility problem with one level optimization approach above since at a time, only 3 constraints are to be handled. (5.5) is reformulated with the bi-level approach as (5.6).

Upper level:

$$\underset{X=\{X_g\}}{\text{minimize}} \quad f_1(X) = \begin{cases} \hat{P}_{\text{Loss}} \\ C(X_g) \end{cases}$$

Lower level:

$$\begin{aligned} \underset{X=\{X_c\}}{\text{minimize}} \quad & f_2(X) = P_{\text{Loss}} \\ \text{s.t.} \quad & V_{\max} \leqslant 150 \text{ [V]} \\ & \theta_{\max} \leqslant 155 \text{ [°C]} \\ & T = T^* \text{ [Nm]} \\ & \Omega = \Omega^* \text{ [rpm]} \end{aligned} \tag{5.6}$$

where $\hat{P}_{\text{loss}}$ is the optimal loss (minimum loss found in the lower level) and P_{loss} is the total losses.

The lower level uses optimization strategy for the optimal control as presented in 5.2.2. In order not to stop the optimization process when no solution found in the lower level, the 3 control variables are all set to zero and optimal loss is set to infinity so is to be dominated by any feasible solutions in the upper level. Therefore, the temporarily assigned values will not be kept in the final result.

5.3.2 Geometry variable set

Nine geometry variables are chosen for the upper optimization level as marked in Fig. 5.9

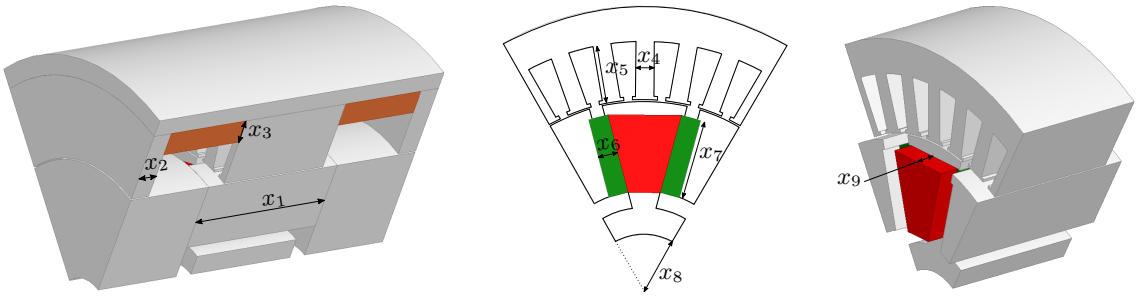

(a) (b) (c)

Fig. 5.9: Geometry variables

This set of variable allows machines to change their sizes in both radial and axial directions. The excitation winding's window is fixed in size, and excitation windings are allowed to only change its height (x_3). In case the optimal solution does not want to use excitation windings, x_3 approaches zero but to avoid computation error, the lower limit of this variable is set to 0.05 mm. Due to the model complexity, the number of pole pairs is kept unchanged, i.e. 6. Variable ranges in detail are summarized in Table. 5.4.

Table 5.4: Geometry variable ranges

Variable	Description	Range [mm]	Prototype [mm]
x_1	Stack length	30 ÷ 60	40
x_2	Bridge thickness	3 ÷ 12	7
x_3	Field winding height	0.05 ÷ 9	9
x_4	Tooth width	3 ÷ 6.5	5.5
x_5	Tooth length	10 ÷ 25	16.5
x_6	Azimuth PM thickness	4.5 ÷ 10	6
x_7	Azimuth PM length	10 ÷ 32	24
x_8	Shaft radius	10 ÷ 20	17
x_9	Side PM thickness	3 ÷ 10	6

Normally the values for the prototype fall in the middle of their corresponding ranges except for the x_3. The reason is after several trials, 9 mm even seem to be large for the upper limit of this variable so this limit is just kept the same as the prototype. Putting the upper bound unnecessarily large will reduce the change of finding the optimal set from the optimization point of view.

In order to verify the model's accuracy when geometry varies, torque surface comparison between

EMCN and FEM methods are performed for a wide range of excitation and armature currents. Two extreme models derived from Table. 5.4 as shown in Fig. 5.10: one model with all geometry variables stay at their lower bounds (lower-bound machine), and the other for the upper bounds (upper-bound machine). As it will be seen, the lower-bound machine is much smaller in size compared to the upper-bound one.

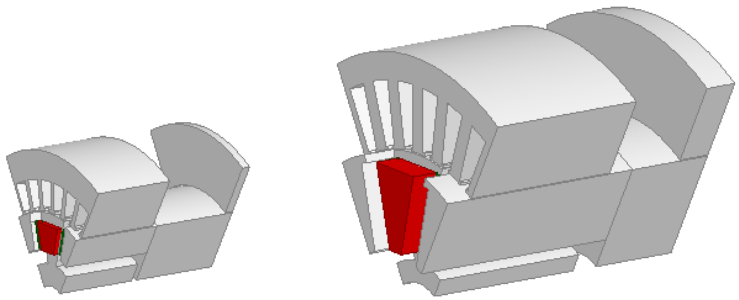

Lower bound machine Upper bound machine

Fig. 5.10: Two extreme machines with lower bounds (exterior radius of 60.8 mm) and upper bound (exterior radius of 115.8 mm)

Result comparison displayed in Fig. 5.11 shows a good accordance between results obtained by EMCN and FEM methods, meaning that within the specified range of geometry variables in Table. 5.4, results are reliable.

For the validity of the thermal analysis model, it should be reliable since equations used in the thermal network are empirical meaning that it is validated through various measurements with different machine's dimensions. Moreover, there is no forced fluid (either air or water) for the cooling, this make the heat evacuation process stable with heat coefficients are almost constant.

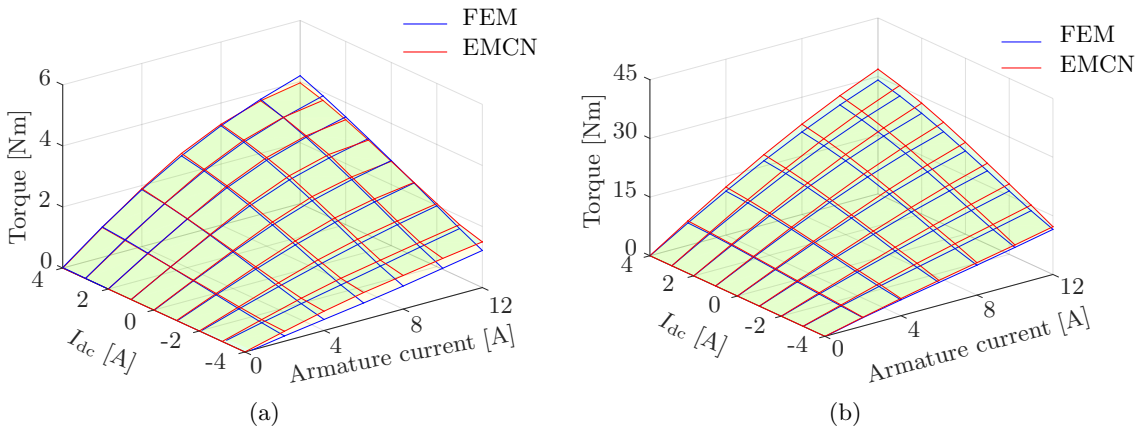

Fig. 5.11: Mean torques of the two extreme geometries. a) Lower bound. b) Upper bound

5.3.3 Case study

For the single-point optimization, two cases will be examined including the rated operating point which is classically considered and the another is the maximum speed operating point in the motor mode which is also commonly focused. These two points are marked in red in Fig. 5.2 (two upper points). The reasons for this are not just analyze machine design by using single point optimization but more importantly to see how designs change by different design target (i.e. at different single operating points). Detailed information of these two points are listed in Table. 5.5.

Table 5.5: Two single operating points for the case study

Point	Torque [Nm]	Speed [rpm]
Rated	10.45	1547
Max. speed	5.39	2553

Running MOPSO with a choice of 50 particles and 50 iterations (2500 machine evaluations), the pareto front results are shown in Fig. 5.12. The result shows the pareto fronts tends to converge to the final curves after about 20 iterations, further running tries to improve the diversity of the pareto front.

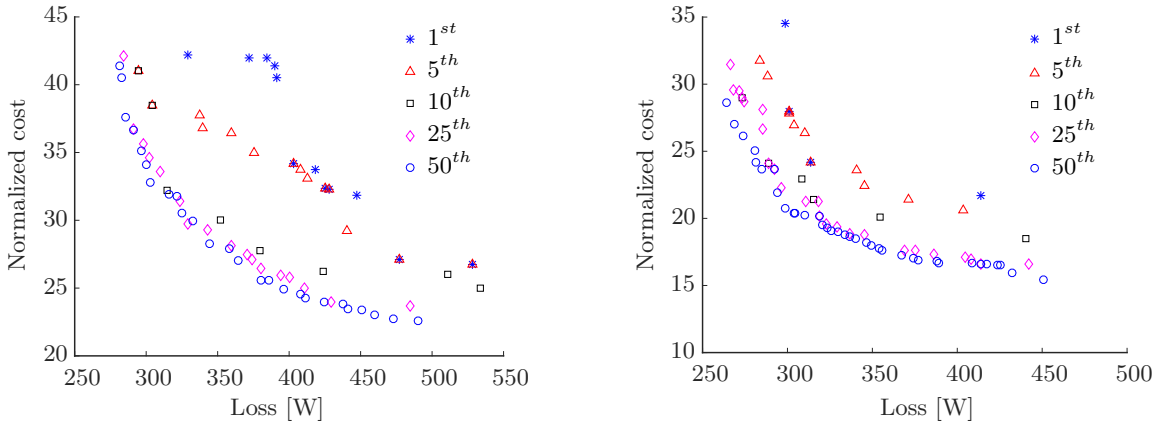

Fig. 5.12: Pareto front convergences through iterations. a) Rated. b) Max. speed

Result comparison between two cases are displayed in Fig. 5.13. There are some points on the top left of the pareto fronts (3 points for the maximum speed case and 6 points for rated speed case) can be removed since there is a very little gain for the loss saving but a big sacrifices for cost. As will be seen, rated operating points require bigger machines with more losses, this is due to the higher torque requirement, which is almost twice as big as the one for the maximum speed point. The result shows that, in order to have relatively same losses, an optimal machine operating at the rated point is about 1.5 times more expensive than the one for maximum speed

point.

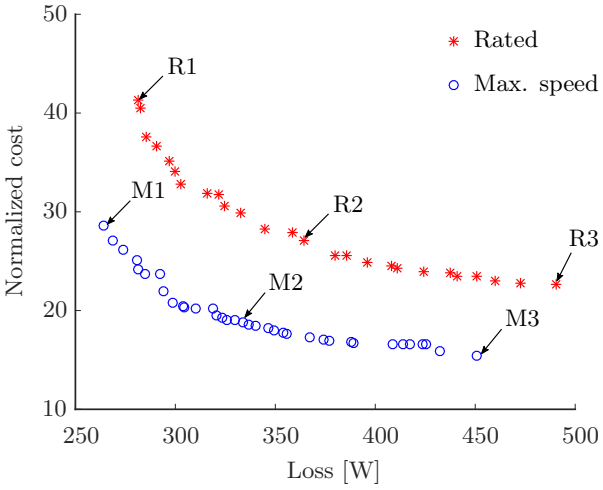

Fig. 5.13: Pareto front comparison between rated and max. speed points

In order to see how the excitation winding varies, the thicknesses of this windings are examined through solutions along the pareto fronts as seen in Fig. 5.14

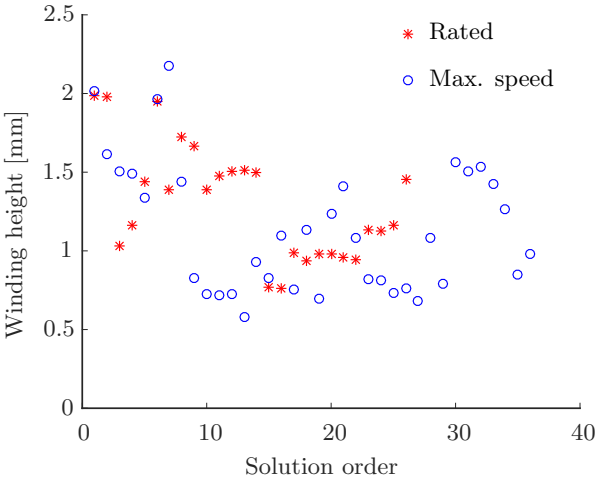

Fig. 5.14: Excitation winding height through solutions on the pareto front (From left to right in Fig. 5.13)

Results for two cases reveal that the use of excitation windings are very limited with the winding's height of about 2 mm (the one for the prototype is 9.2 mm), which is shown in Fig. 5.15 for a couple of machines marked in Fig. 5.13, this point was mentioned earlier in this section with the reason that PM are more preferable to used compared to the excitation windings. It is hard to say operating at the maximum speed requires more contribution of excitation winding since the difference are not noticeable.

Detailed dimensions of these six machines are reported in Table. 5.6. As it will be seen, due to the little use of the excitation windings, the bridge thickness acting as bridge to conduct flux created by this winding tend to stay at the minimum (lower bound) of 3.0 mm.

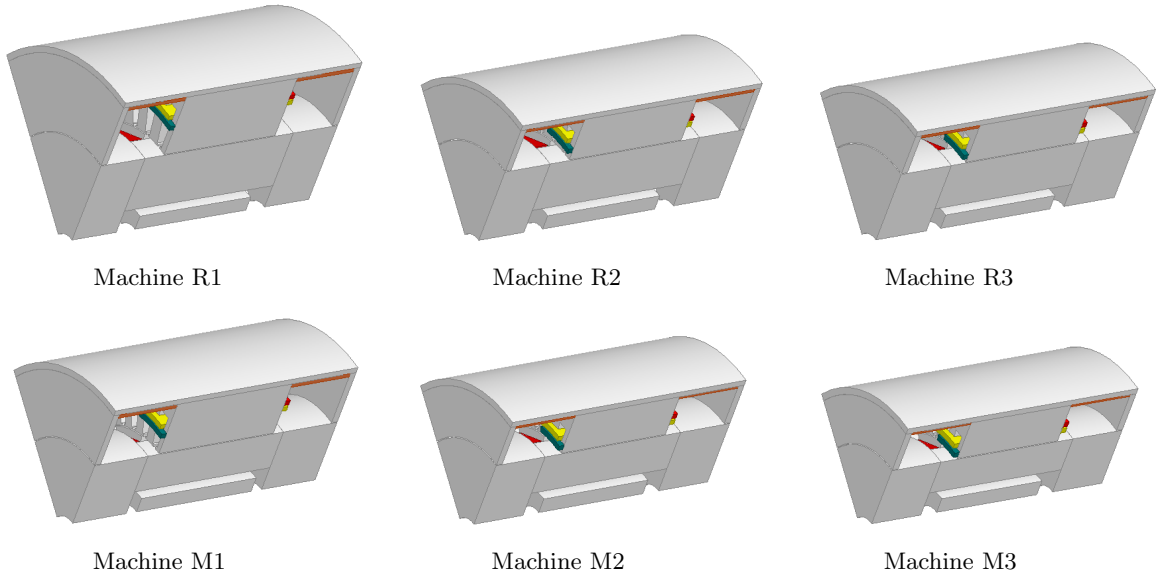

Fig. 5.15: Machine geometries in the pareto fronts comparison

Table 5.6: Detailed dimensions of extracted machines on the pareto fronts

Variable	Description	Rated point			Max. speed point		
		R1	R2	R3	M1	M2	M3
x_1	Stack length	58.9	58.7	56.9	60.0	53.9	51.6
x_2	Bridge thickness	3.0	3.0	3.1	3.0	3	3.0
x_3	Field winding height	2.0	1.5	1.5	2.0	1.1	1.0
x_4	Tooth width	6.4	6.0	5.9	4.9	4.8	4.2
x_5	Tooth length	24.7	13.8	11.6	19.1	11.7	10.4
x_6	Azimuth PM thickness	5.8	7.5	7.3	5.9	5.8	5.3
x_7	Azimuth PM length	29.4	25.2	23.2	18.6	18.7	15.3
x_8	Shaft radius	10.2	10.6	10.3	12.3	10.1	10.1
x_9	Side PM thickness	10.0	9.8	7.4	5.5	8.1	8.2

5.4 Multiple points optimization and comparisons with a PM machine

In this section, the machine optimization at multiple points will be addressed. The main objective is to take into account the practical requirement when the machine must deal with the driving cycle, where multiple operating points are needed to be considered simultaneously. Dealing with multiple operating points at various speeds will effectively compromise machine designs. For instance, at the low speed region, to minimize the losses, machines prefer to use more PMs instead of copper winding, but when working at the high speed region, this will

cause much more core loss, and the overvoltage problem might occur. Several multiple point cases will be considered. But note that the computation time increases proportionally with the number of points. Therefore, handling a big number of points is impractical. In addition, the DESM will be compared with a classical PMSM machine (derived from the DESM with some parts removed).

5.4.1 Corresponding PMSM model and comparison with DESM

In order to evaluate the contribution of the double excitation principle on the driving cycle, a PMSM model is built. For a good comparison, this PMSM model is derived from the DESM one with some parts are removed as shown in Fig. 5.16. Two excitation windings, side PMs, and rotoric flux collectors are removed. The outer stator and end-shield parts act as the machine housing. In this model the end-shield thickness are kept the same as one of the DESM prototype.

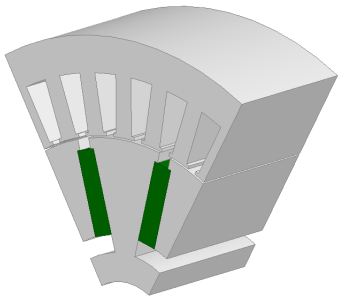

Fig. 5.16: PMSM model derived from DESM

In order to observe differences in performance between the PMSM and DESM machines, the comparison of these two machines with the parameters corresponding to the prototype will be investigated. This will help further explain the analysis result on the driving cycle. Based on the prototype configuration, the DESM model is obviously more costly compared to the PMSM counterpart due to the excitation windings and side PMs costs but the most important difference regarding the performance is the homopolar flux paths (analyzed in chapter 2) together with leakage flux of the DESM machine reduce its performances. Therefore, the flux in PMSM model will be more focused and increased, leading to a higher torque generation and at the same time, more core loss will be generated but it might benefit from lower copper loss as well.

The comparison between two machines will be performed for the torque and loss calculations. Compared to the PMSM model, the DESM model has two more additional flux sources, which are side PMs and excitation windings. Therefore, the comparisons shown in Fig. 5.17 will consider various excitation currents (7 values equally distributed between 0 A and 6 A), and side PM thicknesses. Note that all other parameters of two machines are kept the same particularly the azimuth PM dimensions.

As it was predicted before, due to the leakage flux in the DESM machine, in order to have same

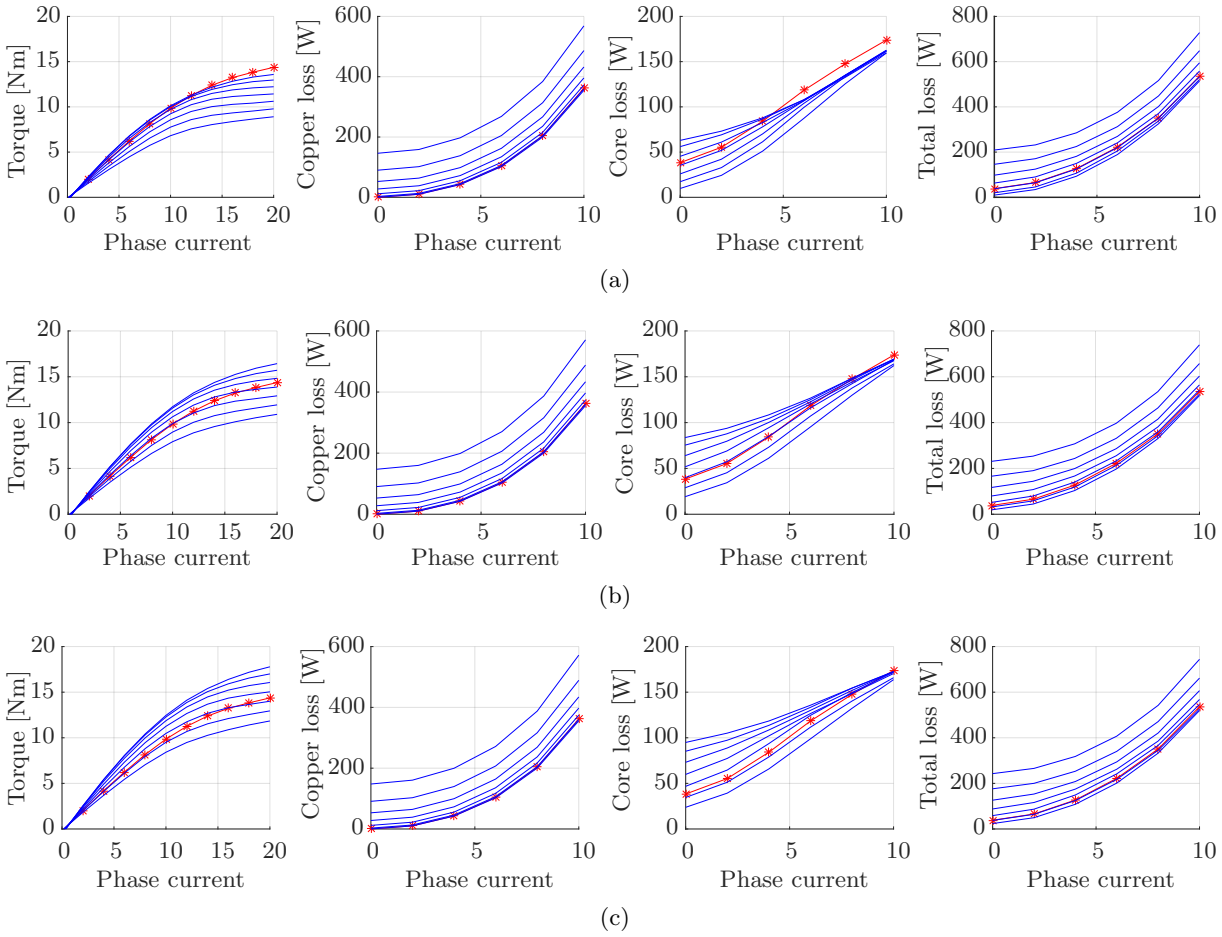

Fig. 5.17: Comparison between PMSM and DESM according to side PM thickness. Solid - DESM. Solid + star - PMSM. For DESM, $I_{\text{dc}} = 0 \div 6$A from bottom to top curves: a) 2 mm. b) 4 mm. c) 6 mm

torque as with the PMSM model, the DESM need more either the excitation current or side PM. As a result, the copper and core losses increase. If the total losses are intended to keep the same as with the PMSM, more price should pay for side PMs in the DESM model. For example in Fig. 5.17a), with the side PM thickness of 2 mm, in order to obtain same a torque as with PMSM, I_{dc} should be around 6 A, leading to a must higher total losses. In order to reduce the excitation current to lower copper loss at the same level as with PMSM model and in Fig. 5.17c), the side PM thickness should increase (as 6 mm) and the total losses stay quite the same between these two machines in this case.

From this quick comparison based on the prototype's dimensions, the PMSM machine seem to gain some advantages over the DESM model in term of cost and losses savings. However, when operating at the high speed region, where a strong field weakening might be required, the PMSM machine has no solution other than using negative $d-$axis currents. It might, therefore, result in a high copper and overheating problems. The comparison for the maximum torque envelop between two machines is displayed in Fig. 5.18a, the corresponding total losses are shown in Fig. 5.18b.

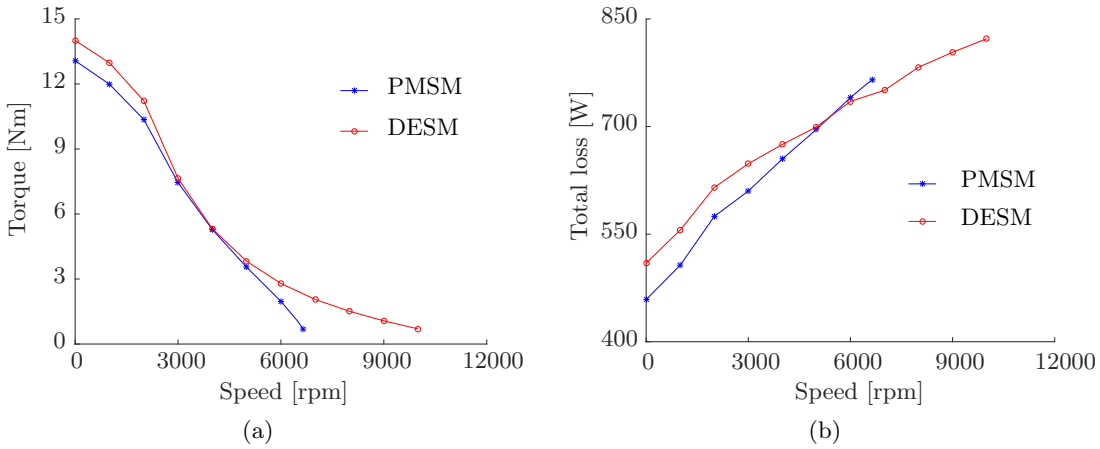

Fig. 5.18: Torque envelop and losses comparisons between DESM and corresponding PMSM models

As seen in Fig. 5.18a, double excitation principle allows the machine to operate at a higher speed compared to PMSM machine (aboutt 11000 rpm compared to 6500 rpm). The effectiveness of excitation windings are highlighted in this high speed region. Since it together with the $d-$axis current helps conveniently reduce the air-gap flux, copper losses are shared between these two windings. But in the low speed region (less than few thousands rpm), the PMSM model seem to be more advantageous due to a lower loss.

5.4.2 Multiple points optimization on the driving cycle

This part focuses on the machine design with two objectives are to minimize the total losses on the driving cycle and machine cost. It would be a perfect solution if all operating points are considered, because the calculated losses are exact which matches correctly the optimization objective. However, the computation time will be impractical. The roughly estimated computation time for each point is 60 hours making the consideration of all points impossible, even taking into account a dozen of points are impractical. In the following, an alternative approach will be presented to shorten the computation time.

5.4.2.1 Representative points

In this research, a set of representative points will be chosen. These points should represent the most frequently operated regions of the machine. They could be chosen by the most solicited points i.e. points with maximum energy on the driving cycle as 3 points shown in Fig. 5.19. This approach is rational since the designs pay attention to the important operating points in term of energy usage.

However this approach does not account for the clustering effect meaning that there are always points closed to each other, energy at each point are not significant but that group of points

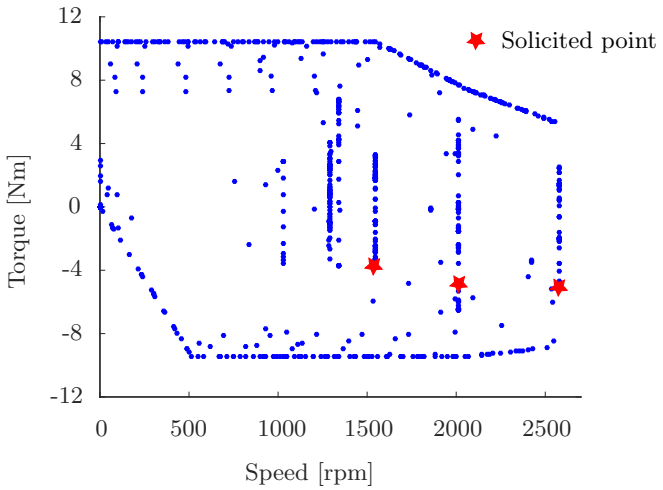

Fig. 5.19: Solicited operating points on the driving cycle

forms a big energy portion on the driving cycle. A more appropriate alternative is to combine "solicited points" idea with a technique so called "energy center of gravity" [3]. This technique simply divides the whole driving cycle space into groups and the clustering effect is, therefore, considered. In this research, the operating space is equally divided with 9 divisions in each dimension (torque and speed) as illustrated in Fig. 5.20. Therefore, 81 groups are presented. It is obvious that another numbers of divisions and even another splitting techniques should be considered to see the influence on the optimal designs but the time consuming issue currently limits that interesting idea.

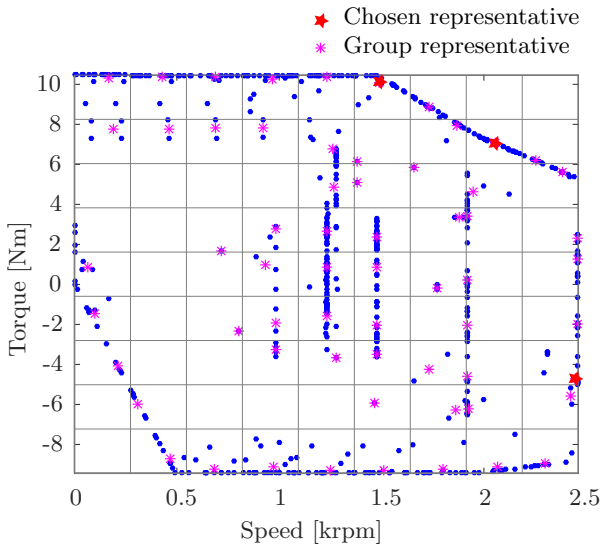

Fig. 5.20: Group division on the driving cycle space

A representative is then picked for each group with the energy equals total the energy of all points

in that group. The equivalent torque and speed are given by (5.7a) and (5.7b), respectively:

$$T_{eq}^{i} = \frac{1}{\sum_{j=1}^{n_i} E_j} \sum_{j=1}^{n_i} T_j E_j \tag{5.7a}$$

$$\Omega_{eq}^{i} = \frac{1}{\sum_{j=1}^{n_i} E_j} \sum_{j=1}^{n_i} \Omega_j E_j \tag{5.7b}$$

where n_i is the number of points in the cell "i", E_j, T_j, Ω_j are energy, torque, and speed of point j in the cell "i"

The equivalent energy loss based on these representatives are given by (5.8).

$$E_{eq} = \sum_{i=1}^{N} T_{eq}^{i} \Omega_{eq}^{i} \Delta t_i \tag{5.8}$$

where N is the number of representative points, Δt_i is the working time duration of the representative point i as the sum of all operating points in the cell containing that representative point.

After having groups, representative points with the maximum energy will be chosen as marked in Fig. 5.20. Due to the limit of the computation time, a strategy with 3 representative points are currently used and detailed in Table. 5.7.

Table 5.7: Three representative point characteristics

	Point 1	Point 2	Point 3
Torque [Nm]	10.07	7.06	-4.72
Speed [rpm]	1559	2150	2563
Operating mode	Motor	Motor	Generator

5.4.2.2 Optimization based on representative points

Due to the removal of the excitation windings and side PMs, three associated geometry variables will be removed from the optimization variable set for the PMSM model including: the end-shield thickness x_2, excitation winding height x_3, and side PM thickness x_9. Moreover, the excitation current variable is also not considered making the optimal control finding is easier compared to one for the DESM model.

As mentioned in 5.1.2.5, machines should additionally satisfy constraints at 5 corner operating points. However, incorporating these points into the lower-level optimization would significantly increase the computation time. In order to tackle this issue, the optimization will not take into consideration these points in the lower-level but after the pareto front derived. This approach

may reduce the accuracy of the optimal pareto front. Therefore, a compromise between the computation time and diversity (due to removals of several solutions on the pareto front) is actually presented here.

The pareto front comparison between two types of machine is shown in Fig. 5.21a. The comparison generally shows that on the basis of a set of 3 specified representative points, PMSM model gains advantages over the DESM counterpart.

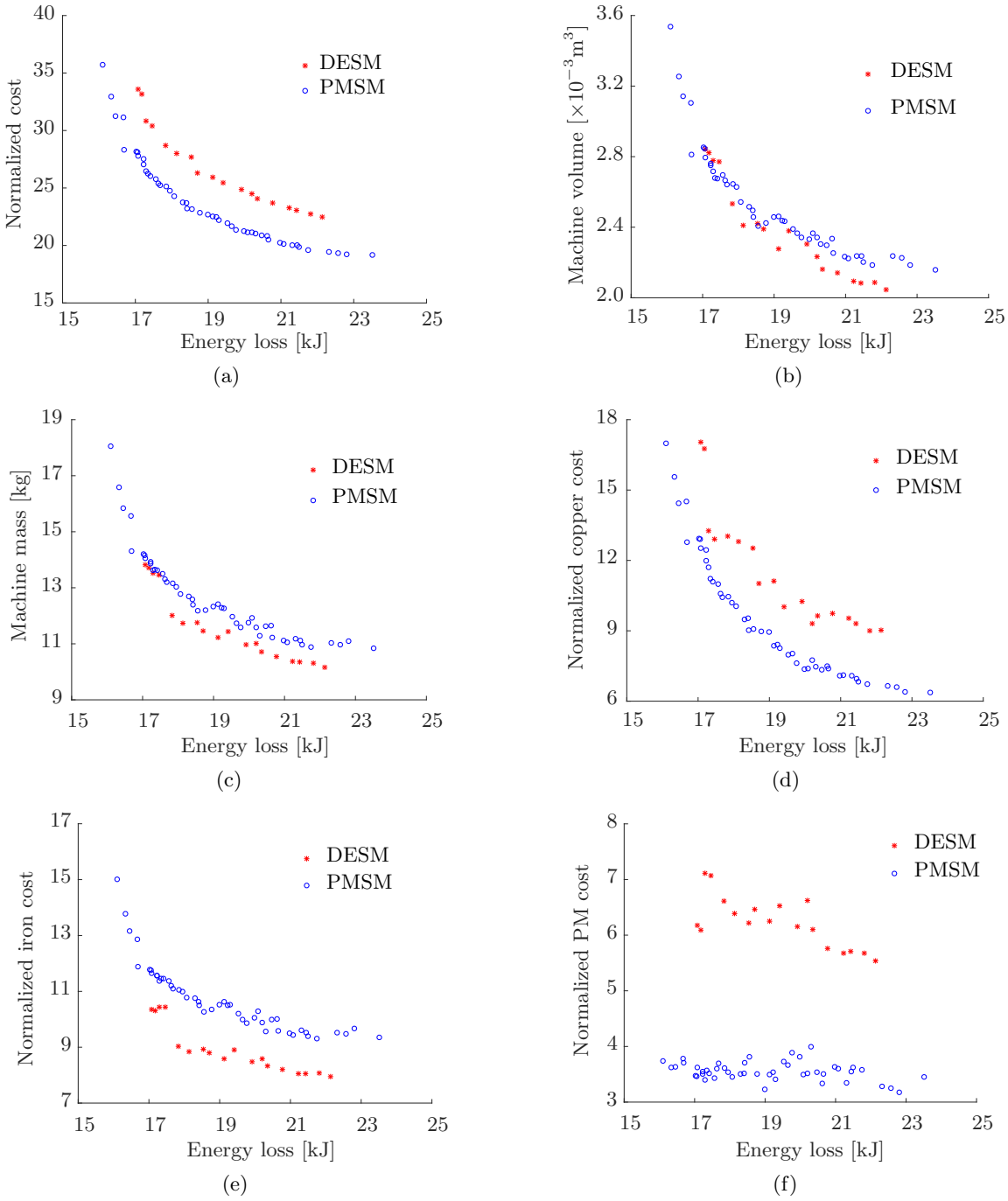

Fig. 5.21: Detail comparisons for solutions along the pareto front. a) Volume. b) Mass. c) Copper cost. d) Iron cost. e) PM cost

Fig. 5.21b-f also show an investigation in detail for other quantities including the total volume, mass and individual costs (costs of copper, iron, and PMs) along solutions on the pareto front in Fig. 5.21a. It is interesting to realize that even PMSM models are better than DESM ones in term of the cost and losses minimization objective but for that same machines, two types of machine are very close regarding both the volume and total mass (DESM models, in fact, seem to be a little bit better than PMSM). This is explained by the fact that due to flux leakages in DESM compared to PMSM model, DESM machine needs to use more PMs and copper to compensate that flux to sustain torque capability. More PM and copper materials in DESM model are seen in Fig. 5.21d. and Fig. 5.21e.

The solutions presented in Fig. 5.21a. are for energy losses due to 3 representative operating points. These machines satisfy all constraints for this set of representatives. However, this does not ensure that the machine is able to work at all the points in the driving cycle as mentioned in 5.1.2.5. The feasibility examinations at 5 operating points (marked in Fig. 5.2) are performed. Verifying against those points would make some solutions Fig. 5.21a unfeasible and filtered out as shown in Fig. 5.22. It is noticed that points with lower cost, i.e. probably small in size are removed, this is due to the thermal limits are reached.

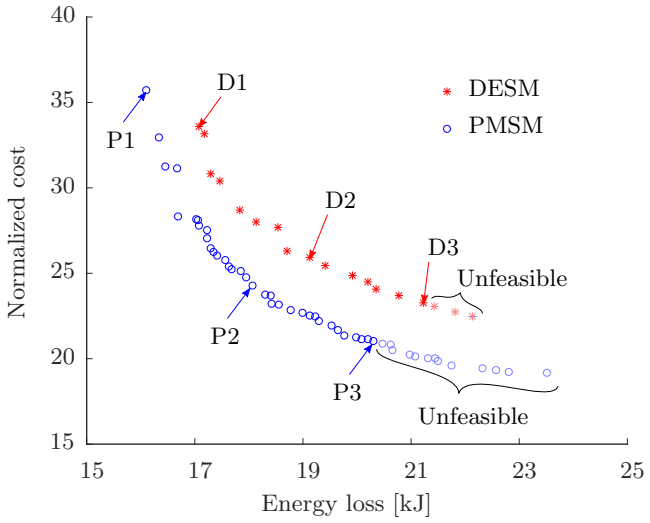

Fig. 5.22: Pareto front comparison after verifying against corner operating points

5.4.2.3 Result analysis

The ultimate purpose is to minimize the total losses in all operating points. To this end, some machines will be extracted from the pareto front and examined their losses on many other operating points as well. Three specific machines (marked in Fig. 5.22) are selected for each type of model (DESM and PMSM): D1, D2 and D3 for the DESM type, and E1, E2 and E3 for the PMSM type. These machines are illustrated in Fig. 5.23 with dimensions are detailed in Table. 5.8. As can be observed, the excitation winding thicknesses are pretty small guessing that the excitation winding usage are not preferable.

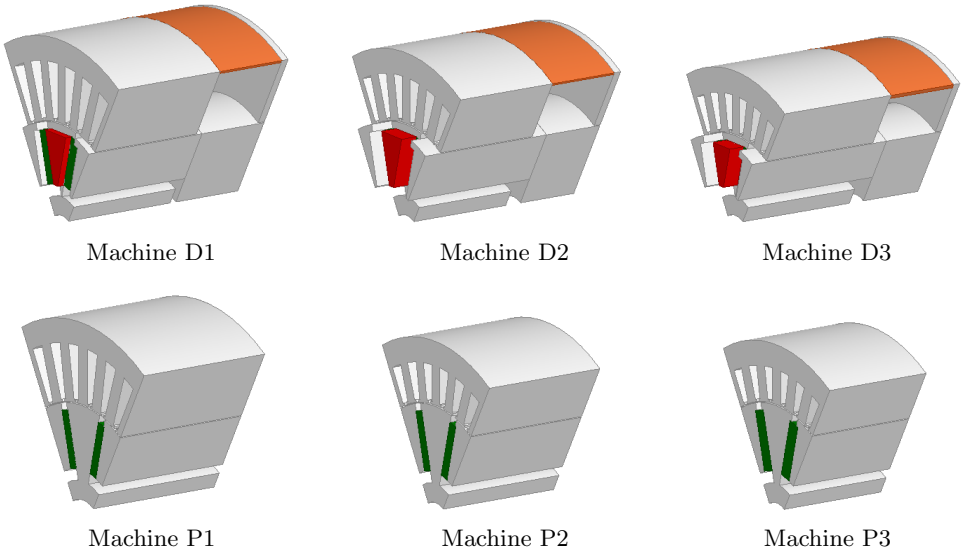

Fig. 5.23: Specific machines for each model. Upper row is for DESM type and lower row is for PMSM type

Table 5.8: Dimensions of extracted machines in Fig. 5.23. [Unit: mm]

Variable	Description	Prototype		Optimal DESM			Optimal PMSM		
		DESM	PMSM	D1	D2	D3	P1	P2	P3
x_1	Stack length	40.0	40.0	50.2	45.2	52.0	60.0	54.6	47.2
x_2	Bridge thickness	7.0	7.0	3.0	3.0	3.0	3.0	3.0	3.0
x_3	Field winding height	9.0	N/A	1.2	0.9	1.8	N/A	N/A	N/A
x_4	Tooth width	5.5	5.5	5.3	5.7	5.1	6.5	5.4	5.9
x_5	Tooth length	17.5	17.5	25	19.5	16.3	24.6	16.6	14.9
x_6	Azimuth PM thickness	6	6	9.0	9.9	9.9	4.5	4.5	5.9
x_7	Azimuth PM length	24.0	24.0	22.8	22.6	17.8	24.5	24.9	25.2
x_8	Shaft radius	10	10.0	10	10.2	10.8	15.1	10.1	10.0
x_9	Side PM thickness	6.0	N/A	2.9	7.3	6.9	N/A	N/A	N/A

The optimization result shows that the bridge thicknesses of the DESM machine type try to approach the lower bound, which is 3.0 mm (3.0 mm thickness is fixed for the thickness of the PMSM type). The reason is mainly due to the fact that increasing the bridge thickness will increase the machine's outmost radius resulting in a much increase of the iron material.

Machines presented in Fig. 5.23 are then verified against all points in the driving cycle to calculate exactly the total losses in the driving cycles, which are values of interest. Machines have to be able to reach required torques at given speeds. Fig. 5.24 compares generated torques (with optimal control set found) and required torques for 6 extracted machines. A very good accordance is seen, it means that all machines are able to work at all operating points.

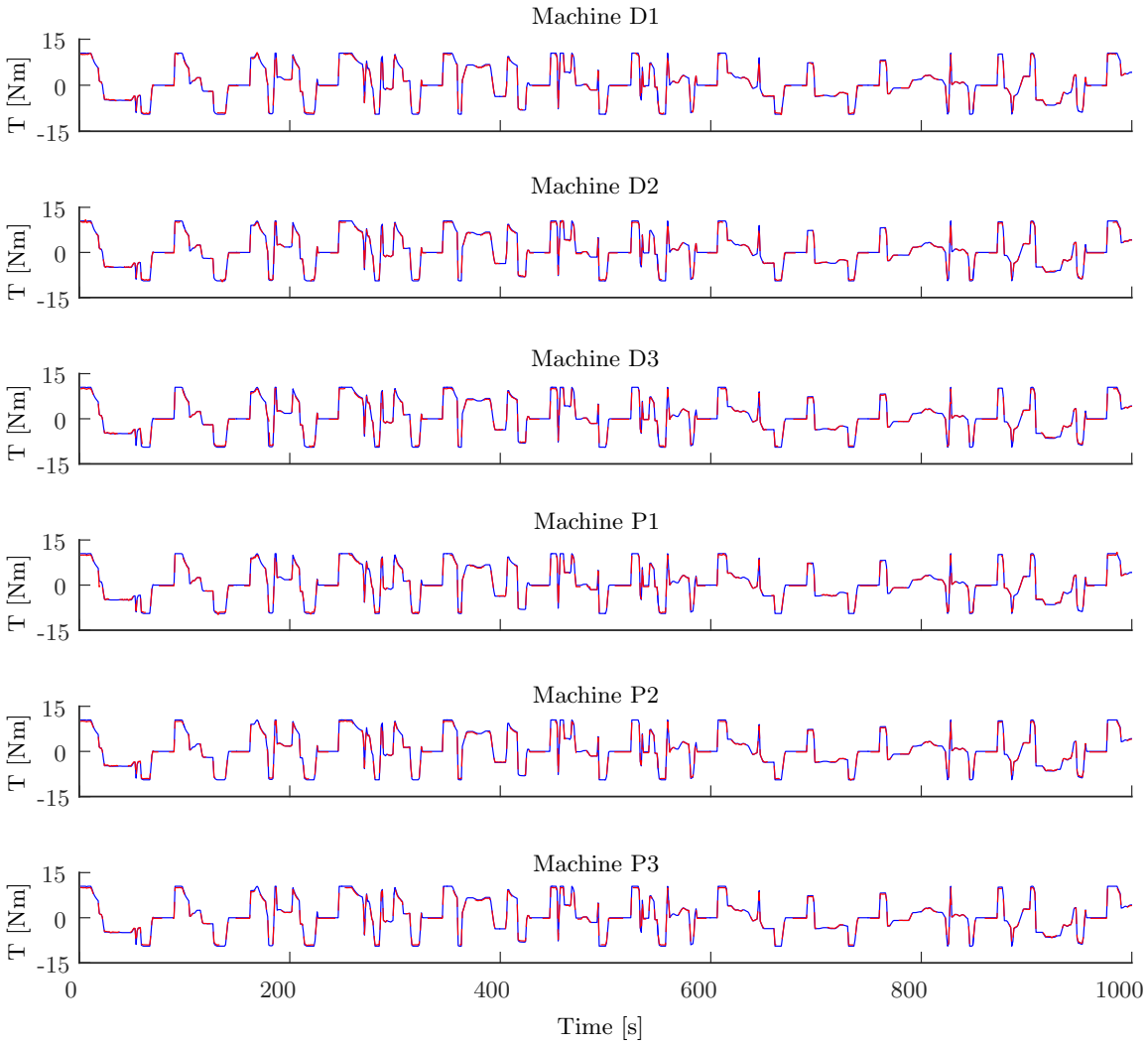

Fig. 5.24: Torque verifications. Solid - required torque, dash - generated torque

Three extracted DESM machines are quickly verified against result obtained by FEM by flux control examination as shown in Fig. 5.25. As will be seen, a good accordance between two analysis methods (EMCN and FEM). The result also shows that the flux controlling by the excitation current are not quite effective, this is due to the bridge thickness stay at its minimum level making magnetic reluctance for flux path from excitation winding significant.

The total energy losses comparison over the given driving cycle of 1000 seconds between extracted machines together with the prototypes are displayed in Fig. 5.26. It is interesting to see that the points extracted from pareto front in Fig. 5.22 still form sets of non-dominated solutions for both model types (DESM and PMSM) and improvements are made compared to the prototypes, which are considered as initial designs. This result also supports the idea of the energy center of gravity center principle because this principle only works on representative points and there is no thorough foundation for the optimality when verifying against all operating points on the driving cycle (i.e better machines derived from representatives may become worse when working on the whole driving cycle).

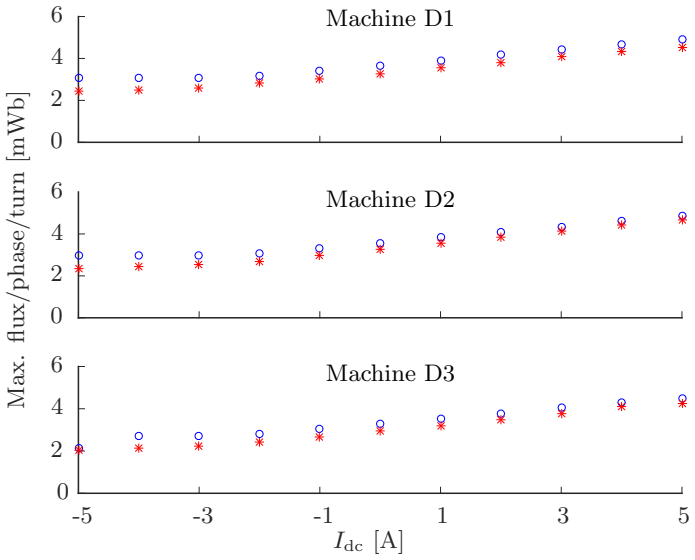

Fig. 5.25: Flux control verification for DESM machines. Circle - by EMCN, star - by FEM

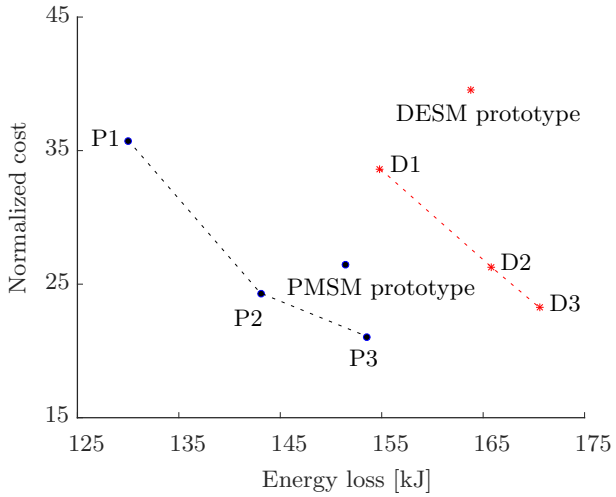

Fig. 5.26: Cost and total losses comparisons between various machines of two models

Individual losses, i.e. copper, core and power electronics losses of each machine are illustrated in Fig. 5.27. The results shows that the copper loss portion increases when the machine gets smaller.

Details for the costs and losses of machines in Fig. 5.26 are reported in Table. 5.9. Taking average over the three optimal machines, PMSM configuration has a cost of 27.01, which is almost indifferent from 27.71 for the DESM model but it could save about 13% of total energy losses (142.21 kJ compared to 163.7 kJ) and the PMSM model gains advantages over the DESM one.

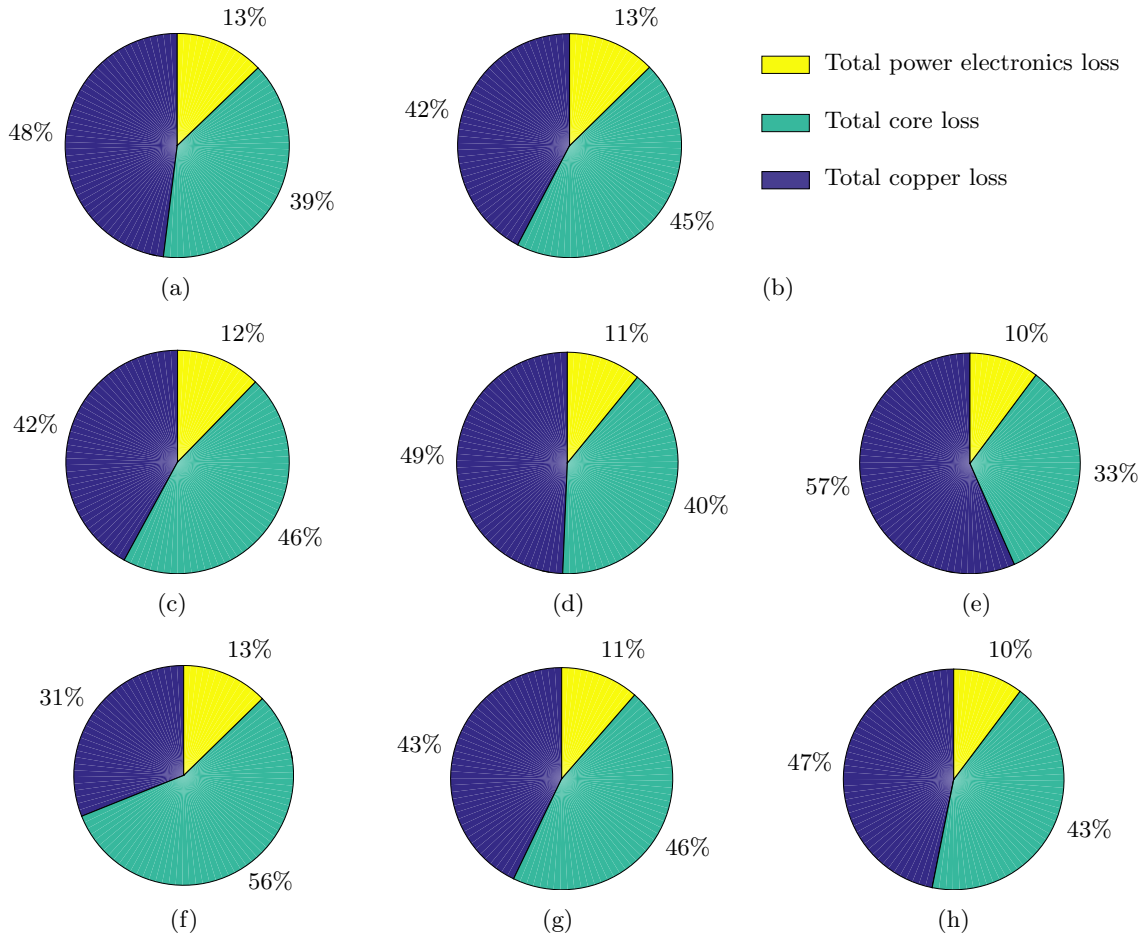

Fig. 5.27: Individual total losses on the driving cycle of various machines for two models. a) DESM prototype. b) PMSM prototype. c) Machine D1. d) Machine D2. e) Machine D3. f) Machine P1. g) Machine P2. h) Machine P3.

Table 5.9: Costs and individual losses comparison of different machines

Machine	Normalized cost	Copper loss	Core loss	PE* loss	Total loss
DESM prototype	**39.52**	78.65	64.12	20.97	**163.74**
PMSM prototype	**26.44**	64.11	68.14	19.15	**151.40**
Machine D1	**33.58**	65.14	70.68	19.00	**154.82**
Machine D2	**26.28**	81.80	65.94	18.06	**165.80**
Machine D3	**23.27**	96.56	56.62	17.41	**170.59**
Machine P1	**35.74**	40.39	73.11	16.49	**129.98**
Machine P2	**24.26**	61.36	65.43	16.31	**143.10**
Machine P3	**21.02**	71.98	65.79	15.77	**153.54**

* Power Electronics
Loss unit: kJ
Driving cycle period: 1001 s

5.4.2.4 Optimization with 6 representative points

In order to examine the influence of the number of representative points on optimal designs, this part present the design optimization case with 6 representative points. The methodology is exactly the same as done with the case of 3 representative points already discussed above, just more points are considered. Therefore, only some main results will be pointed out for the discussion. Fig. 5.28 shows 6 star-marked representatives chosen among representative point of 81 groups. The detailed torque-speed characteristics of these points are listed in Table. 5.10.

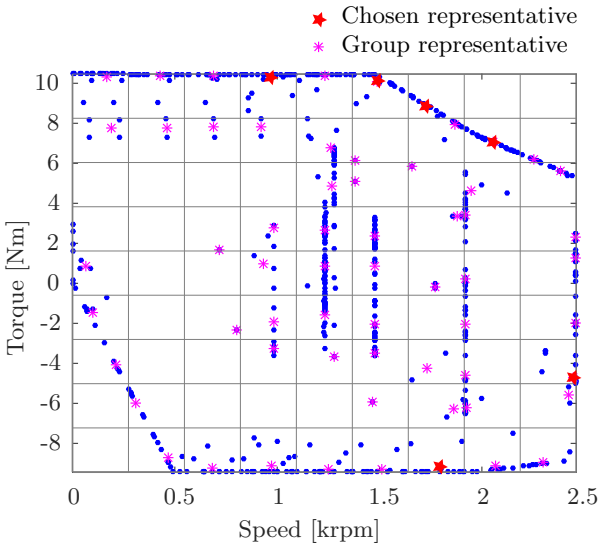

Fig. 5.28: Group division and 6 representative points

Table 5.10: Six representative point characteristics

	Point 1	Point 2	Point 3	Point 4	Point 5	Point 6
Torque [Nm]	10.07	7.06	-4.72	10.27	8.87	-9.25
Speed [rpm]	1559	2150	2563	1013	1821	1883
Operating mode	Motor	Motor	Generator	Motor	Motor	Generator

The pareto front comparison between the DESM and PMSM models after verifying against corner points is shown in Fig. 5.29 with several machines illustrated in Fig. 5.30 will be extracted for a more detailed analysis. It is noted that the energy losses much increase compared to ones shown in Fig. 5.22 as there are 3 more points considered. The result yields that the PMSM gains advantages over the DESM as shown in the case with 3 representative points.

In order to roughly examine influence of having more points on the optimal design, all machines shown in Fig. 5.29 will be recalculated with objectives as for the case of 3 representative points (costs are unchanged but energy loss will reduce since they are for 3 points only) and compared with pareto fronts displayed in Fig. 5.22. This comparison is reported in Fig. 5.31. In this figure, “DESM 6 point” in the legend means DESM machine topologies derived from using 6

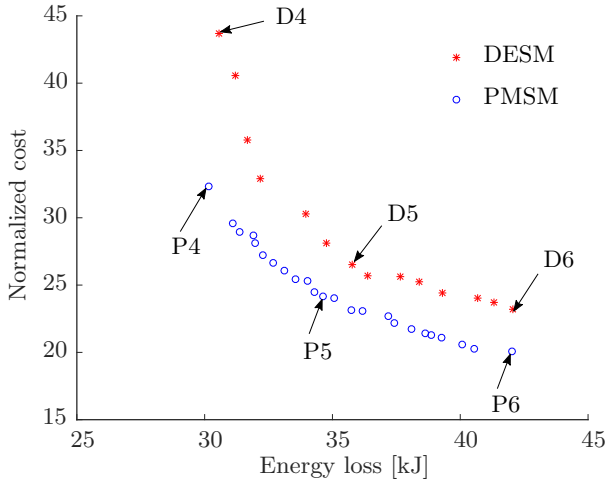

Fig. 5.29: Pareto front comparison between DESM and PMSM

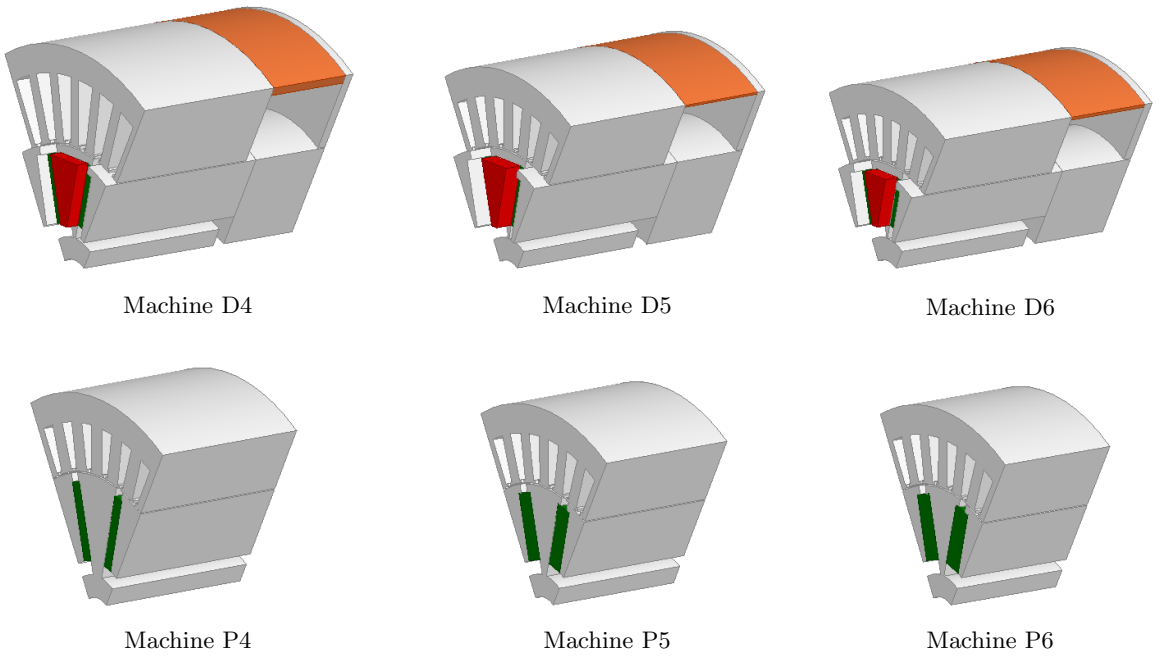

Fig. 5.30: Specific machines for each model. Upper row is for DESM type and lower row is for PMSM type

representative points.

It is clearly seen in Fig. 5.31 that no point in a "6 point" pareto front dominates any point on the corresponding "3 point" curve since the "3 point" curves are the pareto fronts of its objectives. Generally, there is no noticeable difference between 2 cases with the same machine type. Therefore, it can state that the number of representative points will not largely matter the optimal designs. Only some differences for the DESM case in the low loss area. It could be due to the fact the DESM case (in Fig. 5.29) did not well converge. It is plausible since in the case of DESM, more optimization variables presented. Rerunning this optimization could improve but in order to get the DESM curve presented in Fig. 5.29, it takes almost 2 months

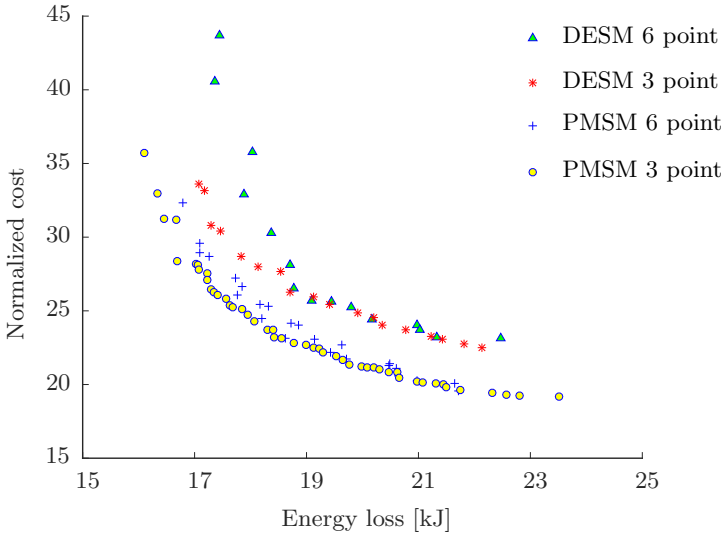

Fig. 5.31: Comparison between 6 and 3 representative points with the objectives are for 3 points

with a core (4) i7, 2.93 Ghz processor computer.

Energy losses calculations for extracted machines in Fig. 5.30 over the driving cycle are displayed in Fig. 5.32 in comparison with extracted machines in the case with 3 representative points (D1, D2, D3, P1, P2, and P3).

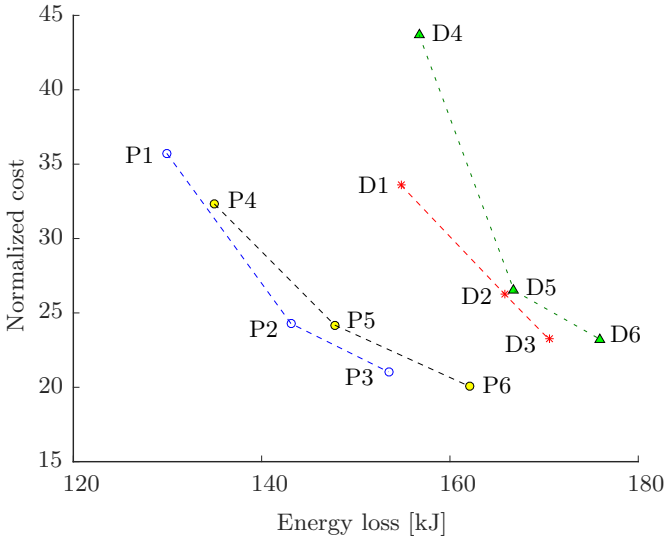

Fig. 5.32: Comparison between various machines in both 6 and 3 representative point cases

As seen, the relative comparisons in Fig. 5.32 are similar to those presented in Fig. 5.31. Therefore, it can be generally stated that the influence of having more representative points consideration mainly makes it harder to converge, i.e. more particles or generations in the optimization should be required at the expense of a longer computation time. This could be due to the fact that additional points have less contribution to the total energy and also representative points are not quite different regarding the operating speed.

5.4.3 DESM and PMSM comparison with extended speed range

As discussed in 5.4, DESM machines cannot gain advantages over the PMSM ones with objectives to minimized both material cost and total losses on the driving cycle. This is mainly due to the ratio γ between the maximum and base speed are not sufficiently high. In this section, further comparisons between the DESM and PMSM models are performed on the extended speed range with γ are similar to that of vehicle applications. Same objectives (cost and losses minimization) are applied to this case with 2 points as shown in Fig. 5.33. Machines are obliged to reach the rated operating point and the point at the maximum speed (no torque constraint considered at the maximum speed, however it should approach zero to attain minimum losses).

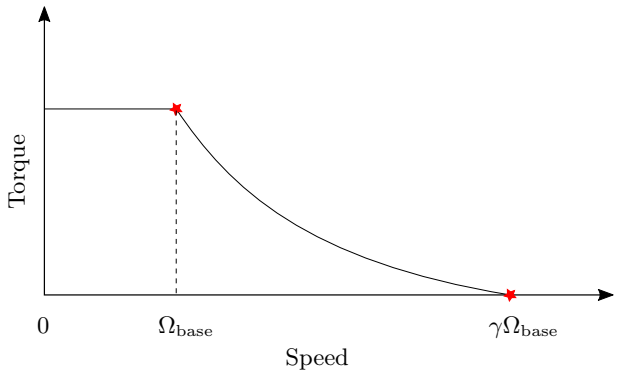

Fig. 5.33: Two operating points with extended speed range

Two cases will be considered with the maximum speeds are 4 and 5 times as high as the base speed ($\gamma = 4; 5$). The loss is calculated as the sum of losses at the base and maximum speeds. The pareto front comparisons are given in Fig. 5.34 with some extreme machines extracted displayed in Fig. 5.35. Dimensions of these machines are detailed in Table. 5.11.

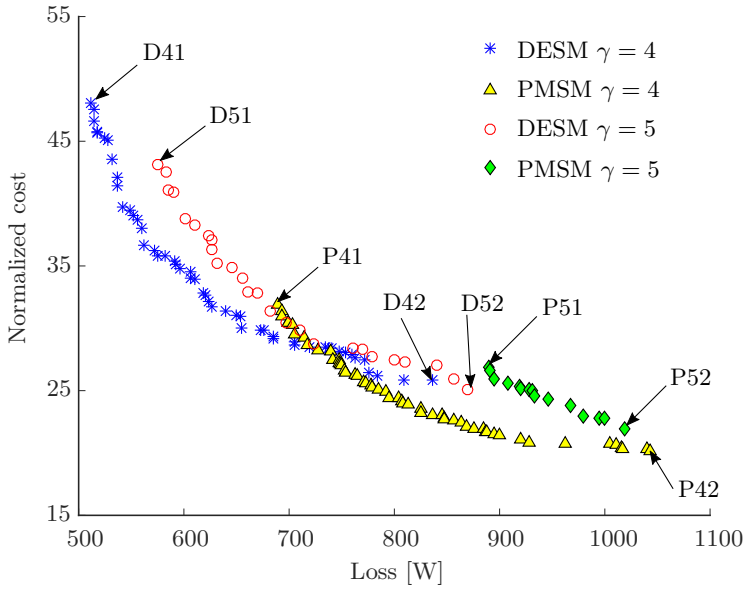

Fig. 5.34: Comparison between DESM and PMSM machines considering extended speed range

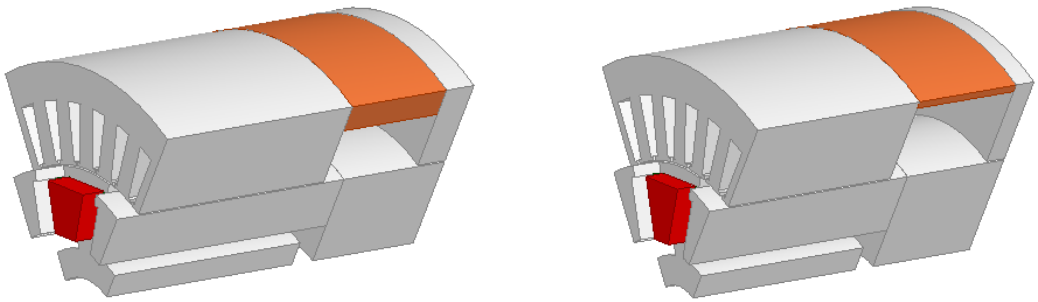

Machine D41 Machine D42

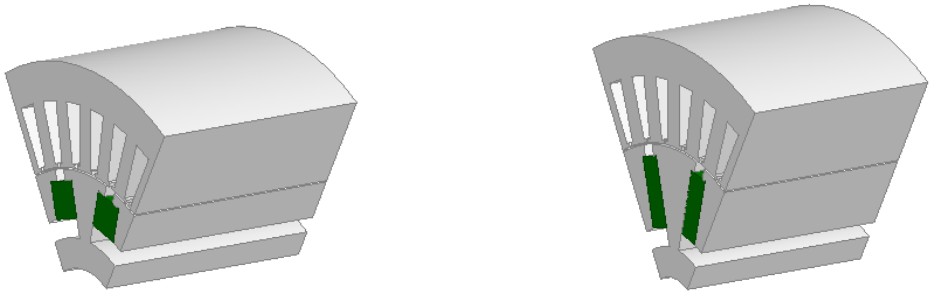

Machine P41 Machine P42

(a)

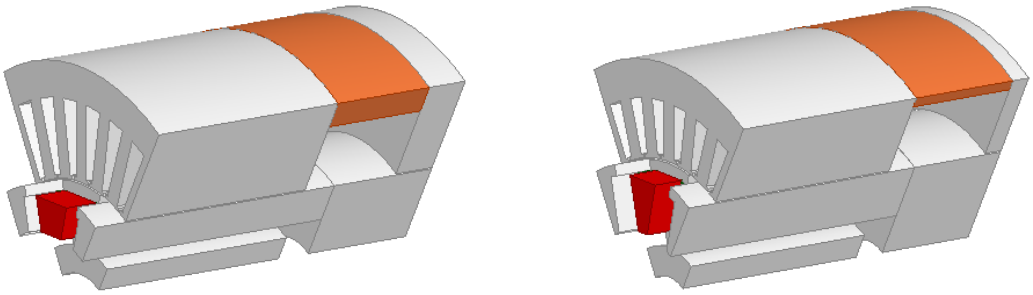

Machine D51 Machine D52

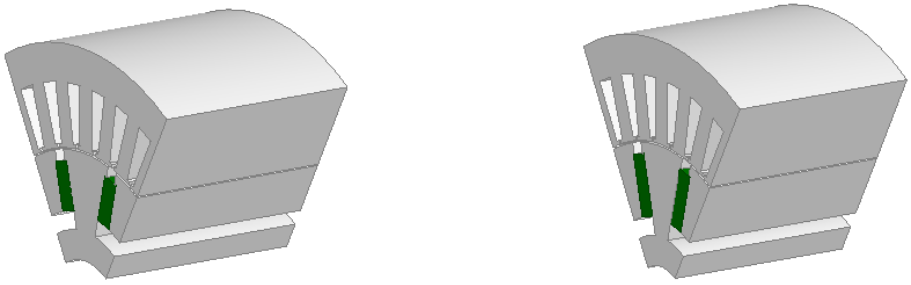

Machine P51 Machine P52

(b)

Fig. 5.35: Specific machines for each model according to γ. a) $\gamma = 4$. b) $\gamma = 5$

The speed range characteristic and machine type clearly reveal compromises on the machine designs and performances. The following could be observed:

- The higher speed range requirement ($\gamma = 5$) leads to a more total loss and introduces

Table 5.11: Dimensions of extracted machines in Fig. 5.34. [Unit: mm]

Variable	Description	D41	D42	P41	P42	D51	D52	P51	P52
x_1	Stack length	60.0	51.2	6.0	54.0	60.0	54.8	57.1	52.5
x_2	Bridge thickness	8.8	5.6	3.0	3.0	12.0	5.0	3.0	3.0
x_3	Field winding height	9.0	2.4	N/A	N/A	9.0	3.2	N/A	N/A
x_4	Tooth width	6.0	5.0	4.9	5.7	5.1	5.0	5.5	5.4
x_5	Tooth length	25.0	17.3	25.0	14.8	22.7	15.9	21.3	19.2
x_6	Azimuth PM thickness	7.5	7.2	9.8	6.4	6.4	9.7	5.4	5.0
x_7	Azimuth PM length	14.3	16.6	10.0	18.9	10.0	14.9	13.3	16.5
x_8	Shaft radius	20.0	12.9	20.0	12.4	18.4	12.9	19.1	12.8
x_9	Side PM thickness	6.7	5.7	N/A	N/A	10.0	8.3	N/A	N/A

difficulties for machine design.
This is due to the fact that operating at high speed, machines are normally required to have less excitation source to handle both voltage and thermal limit, but this will cause high copper loss at based speed. In fact, trial was made to extend maximum speed with $\gamma = 6$, the PMSM model are unable to find machines.

- The optimal DESM design can handle higher speed range without sacrificing much losses compared to the PMSM model.
  This fact can be explained by the copper loss shared between the excitation and armature windings. For example, the lack of excitation source at low speed due to the small amount of PMs can be compensated by a positive excitation current and hence reduce the burden for the armature current to satisfy the high torque at the low speed. But that is not the case with the PMSM type since the excitation source comes only from the PM and stays almost constant.

- The DESM model is able to have a much lower loss compared to the PMSM one.
  The same reason with the shared copper loss between two types of windings in the DESM make this machine able to reduce losses.

The influence of γ can be also observed based on the variation of the field winding's height along the pareto fronts as shown in Fig. 5.36.

It is clear that field winding heights are much bigger compared to ones obtained in the optimizations in the previous section over the driving cycle with $\gamma \approx 1.7$ and heights with $\gamma = 5$ are bigger than ones with $\gamma = 4$, in overall. It means that he field windings are more preferred when the DESM operates at very high speed regions.

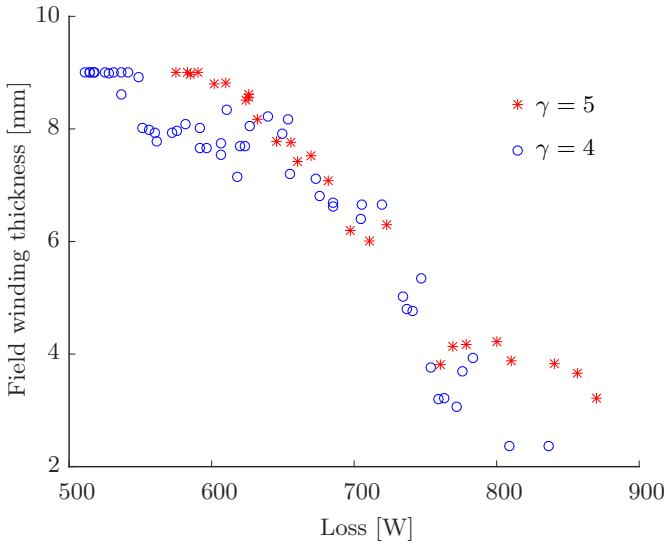

Fig. 5.36: Field winding heights variation according to γ

Conclusion

This chapter has been presented using the multi-physics model for design optimization of the DESM machine on the driving cycle with the objectives are to minimize both the total energy losses and material cost. In order to make the optimization practical regarding the computation time, a set of representative points was suggested based on the energy center of gravity principle. Some interesting machines was extracted and examined on all the operating points of the driving cycle. The comparison between the DESM type and the corresponding permanent magnet machine was made. Results revealed that under the small range of operating speed ($\gamma = \frac{\Omega_{\text{max}}}{\Omega_{\text{base}}} = 1.7$), the PMSM model yields better performances due to no strong flux weakening required and PMSM machines tend perform better the DESM ones due to a lot of flux leakage presented in DESM model. However, in circumstances where the speed range is extended (higher γ), the DESM model is expected to be able to overwhelm the PMSM counterpart, especially regarding the total losses minimization.

Conclusion and Perspectives

Conclusion

The thesis is dedicated to the design optimization of a double excitation synchronous machine (DESM) in railway traction. Overall, the multi-physics model with saturation consideration was used in order to attain more accurate results. Five chapters were included and conclusions for each chapters were given. In this final part, a general conclusion linking separate chapters and also future work will be addressed.

Chapter 1 briefly introduced railway traction history and importantly covered several types of electrical machine available in this application domain. Mainly due to the mature development, induction machines are currently the most popular choice. Beside that, permanent magnet synchronous motors (PMSMs) through years appear as a very promising candidate with advantages of PMs such as high energy and high power density. In addition, the PM cost is being reduced making PMSMs more attractive. A common problem with PMSMs is that the air-gap flux is hard to controlled. Therefore, the idea is to maintain advantages of PMSM machines but the air-gap flux capability is improved. This introduces the idea of the double excitation principle by using excitation windings similarly to ones in would field synchronous machines. With that approach, the main focus is to answer the question whether double excitation synchronous machines (DESMs) could provide better performances compared to PMSMs regarding the railway traction application.

Chapter 2 reviewed a basis of DESMs with a number of topologies in literature. Advantages of DESMs were highlighted in terms of both flux control flexibility and energy efficiency. A prototype realized in SATIE was chosen for further study, it is mainly due to the effective flux control curve, i.e. the maximum flux versus the excitation current. A more detailed analysis of the prototype was given. For the prototype being studied, the topology is truly three dimensional requiring the use of the 3-D finite element method (FEM), and it leads to a very time consuming process for the early design stage. Therefore, a much faster alternative

analysis method is needed.

Chapter 3 was dedicated to the electromagnetic modeling of the DESM using the equivalent magnetic circuit network (EMCN) method. Unlike analytical methods, this semi-numerical method is able to consider saturation effect. The fast computation time is the main advantages of this method while a good accuracy is still maintained. The 3-D topology with complex magnetic flux paths and different core material (solid and laminated) increases the modeling's complication. The generalized approach with basic elements of 4 reluctances was used. This enables it to calculate local flux densities; therefore, the core loss can be computed. The torque and losses and main outputs of this electromagnetic model, which are important for the calculations considering a driving cycle. Losses are also prerequisite to the thermal analysis model for the temperature calculations and moreover recalculate the losses, i.e. the coupling process. Therefore, a thermal analysis modeling was followed.

Chapter 4 focused on the thermal aspect and its coupling with the electromagnetic model for the studied DESM. A lumped parameter thermal resistance network model has been developed with the objective is to determine the overall temperatures of the windings, which should be accurate enough for the optimization process. Generally, two global excitation windings and the natural air convection on the surface of the prototype contribute more to the heat evacuation's difficulty. Since all windings placed in the stator side and losses from the rotor are substantially small, the overheating issue for PMs is mitigated. The big challenge of the thermal analysis is that many empirical equations are used; therefore, some heat coefficients were necessarily determined by experiments. Due to the difficulties of the natural air cooling (applied to the DESM prototype), a new surface heat coefficient was assumed.

Chapter 5 has been presented using the multiphysics model developed in the previous chapters. The objectives are to minimize both the total energy losses and material cost. A full consideration of 1000 operating points and transient thermal model make the design process impractical due to the long computation time. Instead, a set of representative points was selected and the steady state thermal model was used. The DESM model was compared with a PMSM one having a similar configuration. The results showed that for the train driving cycle with a small range of operating speed, the PMSM type yields better performances due to no strong flux weakening required and a lot of flux leakage presented in the DESM model. However, several trials with extended speed ranges, the DESM model seemed to overwhelm the PMSM counterpart, especially regarding to loss minimization.

Perspectives

The optimization was performed with a DESM prototype on a few representative points. In order to more comprehensively analyze performance of the DESM, more work needed to be done:

- Consider various sets of representative points either more points or different cell divisions

(it was 9-by-9 grid in the thesis) to see influences on the optimal design.

- Develop controlling algorithm for the machines of interest to figure out exactly control variable set (the control set was found by setting generated torque in the range of 5% deviated from required one). Moreover, considering the driving cycle with respect to time, this controlling algorithm is wished to incorporate with transient thermal analysis to have results reflecting the real time operation.
- It is interesting to consider other DESM topologies and compared with the PMSMs. The considered DESM topology might not be perfect to support the advantages of the double excitation principle.

This page intentionally left blank

Appendix A

Losses in power electronics modules

In a variable speed drive system, a motor is usually driven by power electronics modules to control the voltage and frequency. With a double excitation motor, a DC-DC converter is also necessarily to provide the field current, which can be regulated in both magnitude and direction (for weakening and enhancing modes). The inverter supply to armature winding is displayed in Fig. A.1

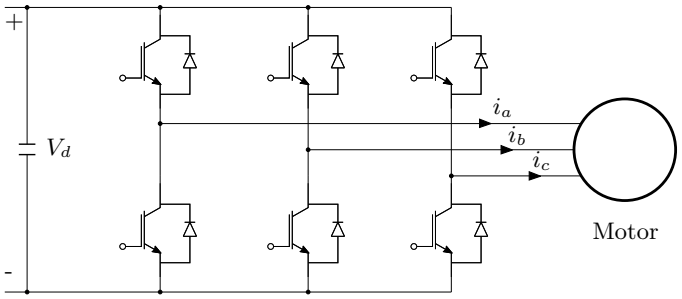

Fig. A.1: Three phase inverter topology

where V_d is the DC link voltage, which is usually fixed depending on available power supply (batteries, electric line, etc.)

The operation of power electronics modules cause some losses including switching and conduction losses (leakage loss is usually negligible). Basically, the switching loss is subject to the switching frequency and turn-on and turn-off energies, which is associated with the rising and falling time). Meanwhile, the conduction loss can be simply understood as the joule loss as load current passes through the on-resistance of the power semiconductors (either IGBT, MOSFET or Diode).

A.1 Inverter losses

Calculations of inverter losses are fundamentally based on the sinusoidal load current assumption. Moreover, a linearised loss model is assumed. The switching loss energy E_s is linearised

given by (A.1a) and the conduction loss P_c for a single semiconductor is calculated by (A.1b) [95].

$$E_s = E_{sr} \cdot \frac{V_v}{V_{ref}} \cdot \frac{i_v}{i_{ref}} \tag{A.1a}$$

$$P_c = V_0 \cdot i_v + r \cdot i_v^2 \tag{A.1b}$$

where:
E_{sr} is the rated switching loss energy given for the reference commutation voltage and current V_{ref} and i_{ref}.
V_v and i_v indicate the actual commutation voltage and current, respectively.
V_0 and r are semiconductors threshold voltage and differential resistance, respectively.

A.1.1 Conduction loss

The conduction loss on each IGBT switch and on each free-wheeling Diode are expressed by (A.2a) and (A.2b), respectively.

$$P_{\text{con,I}} = \frac{V_{\text{CE,0}} \cdot \hat{i}_L}{2\pi}\left(1 + \frac{\pi M}{4}\cos\phi\right) + \frac{r_{\text{CE}} \cdot \hat{i}_L^2}{2\pi}\left(\frac{\pi}{4} + \frac{2M}{3}\cos\phi\right) \tag{A.2a}$$

$$P_{\text{con,D}} = \frac{V_{\text{F,0}} \cdot \hat{i}_L}{2\pi}\left(1 - \frac{\pi M}{4}\cos\phi\right) + \frac{r_{\text{F}} \cdot \hat{i}_L^2}{2\pi}\left(\frac{\pi}{4} - \frac{2M}{3}\cos\phi\right) \tag{A.2b}$$

where:
$\hat{i}_L$: peak load current (sinusoidally assumed)
M: modulation index
ϕ: displacement angle between load current and the fundamental of phase voltage
V, r: threshold voltage and differential resistance of IGBT (Diode)

The total conduction loss for 6 pairs (IGBT and free-wheeling diode) is given by (A.3).

$$P_{\text{con}} = 6(P_{\text{con,I}} + P_{\text{con,D}}) \tag{A.3}$$

where the sinusoidal PWM where control signal is generated by comparing a sinusoidal signal (peak $\hat{V}_{\text{sin}}$) with a triangle one (peak $\hat{V}_{\text{tri}}$) (shown in Fig. A.2, modulation index M is defined as (A.4)

$$M = \frac{\hat{V}_{\text{sin}}}{\hat{V}_{\text{tri}}} \tag{A.4}$$

where the constant DC link voltage, the output voltage will be controlled by changing the modulation index demonstrated in Fig. A.3 [96].

As seen in Fig. A.3, if the required fundamental output phase voltage is above the maximum available value, i.e. $2V_d/\pi$, then the PWM fails to supply.

The threshold voltage and differential resistance of the IGBT and Diode in (A.2a) and (A.2b) can be determined from datasheets as guided in [97].

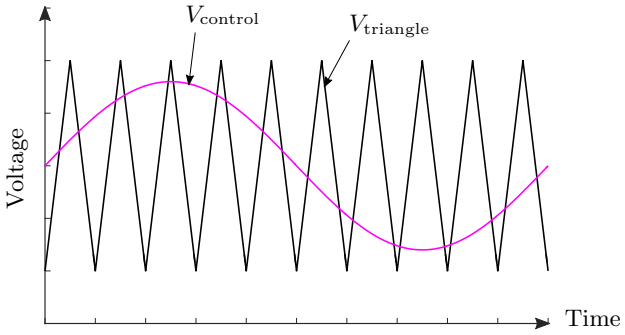

Fig. A.2: Sinusoidal and triangle signals used for sinusoidal PWM

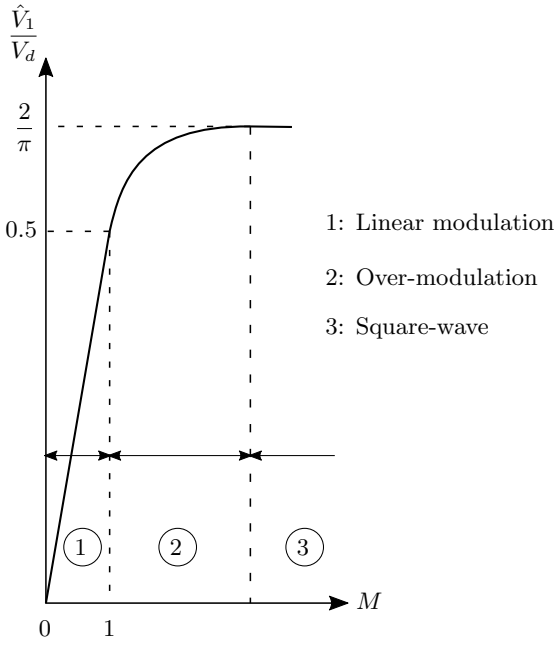

Fig. A.3: Normalized peak of fundamental output phase voltage

A.1.2 Switching loss

The switching loss can be obtained by multiplying the sum of turn-on and turn-off energies for one switching event with the number of switching times (proportional to the switching frequency). A switching loss formulation is introduced in [95] as (A.5). However, this formulation is only correct for the linear modulation range ($M \leq 1$), where the sinusoidal signal cuts all edges of the triangle signal. Therefore, the number of turn-on, turn-off pairs is essentially the switching frequency f_s.

$$P_{\text{sw}} = \frac{6}{\pi} \cdot f_s \cdot (E_{\text{On,I}} + E_{\text{Off,I}} + E_{\text{Off,D}}) \frac{V_d}{V_{\text{ref}}} \cdot \frac{\hat{i}_L}{i_{\text{ref}}} \tag{A.5}$$

where:

$E_{\text{On,I}}, E_{\text{Off,I}}$: turn-on and turn-off switching energies associated with the IGBT

$E_{\text{Off,D}}$: turn-off energy in the Diode due to reverse recovery current

Accounting for the over-modulation ($M > 1$), where the number of switching event pairs (turn-on and turn-off) is actually less than the switching frequency, (A.5) is modified as (A.6).

$$P_{\text{sw}} = \frac{6}{\pi} \cdot n_c \cdot (E_{\text{On,I}} + E_{\text{Off,I}} + E_{\text{Off,D}}) \frac{V_d}{V_{\text{ref}}} \cdot \frac{\hat{i}_L}{i_{\text{ref}}} \tag{A.6}$$

where n_c is the actual number of switching event pairs

A.2 DC-DC converter loss

The double excitation principle with a capability of having both the flux weakening and flux enhancing modes. The field current should be, therefore, capable of changing either its magnitude or its direction. To this end, a bidirectional DC power circuit is demonstrated in Fig. A.4.

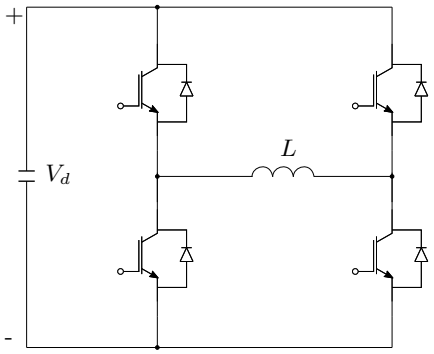

Fig. A.4: Bidirectional power circuit for excitation windings

A.2.1 Conduction losses

The conduction loss on a single Mosfet and Diode are given by (A.7a) and (A.7b) respectively [98]

$$P_{\text{con,S}} = r_{\text{CE}} \cdot I_{S,\text{rms}}^2 \tag{A.7a}$$

$$P_{\text{con,D}} = r_{\text{F}} \cdot I_{D,\text{rms}}^2 + V_{F,0} \cdot (1 - D)\hat{i}_{\text{load}} \tag{A.7b}$$

where RMS currents through the Mosfet and diode are calculated by (A.8a) and (A.8b), correspondingly.

$$I_{S,\text{rms}} = \sqrt{D \left[I_{L,\text{min}}^2 + I_{L,\text{min}} \Delta I_L + \frac{\Delta I_L^2}{3} \right]} \tag{A.8a}$$

$$I_{D,\text{rms}} = \sqrt{(1 - D) \left[I_{L,\text{max}}^2 - I_{L,\text{max}} \Delta I_L + \frac{\Delta I_L^2}{3} \right]} \tag{A.8b}$$

where $I_{L,\text{min}} = \hat{i}_{\text{load}} - \frac{\Delta I_L}{2}$, $I_{L,\text{max}} = \hat{i}_{\text{load}} + \frac{\Delta I_L}{2}$
ΔI_L is the current ripple through the inductor
D is the duty cycle

A.2.2 Switching losses

Switching losses on a single Mosfet and Diode are given by (A.9a) and (A.9b), respectively.

$$P_{sw,S} = (E_{\mathrm{On,M}} + E_{\mathrm{Off,M}}) \cdot f_{sb} \tag{A.9a}$$

$$P_{sw,D} = E_{\mathrm{Off,D}} \cdot f_{sb} \tag{A.9b}$$

where $E_{\mathrm{On,M}}$ and $E_{\mathrm{Off,M}}$ are turn-on and turn-off energies of the Mosfet
$E_{\mathrm{Off,D}}$ is the turn-off energy of the Diode.
f_{sb} is the switching frequency of the Mosfet.

It should be noted that when the data for the turn-off energy in the Diode is not available in the Diode's datasheet, this energy can be calculated according to (A.10).

$$E_{\mathrm{Off,D}} = Q_{rr} \cdot V_d \tag{A.10}$$

where Q_{rr} are reversible recovery charge of the diode

This page intentionally left blank

Appendix B

Multi-objective optimization algorithm

The intention of this part is not to go in detail about multi-objective optimizaiton algorithms but focuses on a comparison between the Multi-objective Particle Swarm (MOPSO), which has been used in the thesis, and the Non-dominated Sorting Genetic Algorithm (NSGA) - II, which is the most common algorithm for multi-objective optimizations.

A mono-objective optimization problem, which either minimize or maximize an objective, is a very classical form of optimization. The formulation is given by (B.1) with a set of m inequality constraints (g) and a set of p equality constraints (h). It should be noted that maximizing $f(x)$ is equivalent to minimizing $-f(x)$ and $g(x) \geqslant 0$ is equivalent to $-g(x) \leqslant 0$. Therefore, all optimization problems can be expressed as minimizing optimization cases without any loss of generality.

$$\begin{aligned} \min_{X} \quad & f(X) \\ \text{s.t.} \quad & g_i(X) \leqslant 0 \quad (i = 1 \div m) \\ & h_j(X) = 0 \quad (j = 1 \div p) \end{aligned} \tag{B.1}$$

where $X = [x_1, x_2, ..., x_n]$ is the design vector.

This kind of optimization will lead to only one single best (optimal) solution with an unique design set (it might be sometimes challenging to find any feasible solutions if difficult constraints are considered). The designer will then work on that single solution. However, in the real world, designers will find many cases, where there are n ($n \geqslant 2$) objectives (multi-objective) needed to be handled. The multi-objective optimization is generally formulated as (B.2).

$$\begin{aligned} \min_{X} \quad & F(X) = \{f_k(X)\} \quad (k = 1 \div n) \\ \text{s.t.} \quad & g_i(X) \leqslant 0 \quad (i = 1 \div m) \\ & h_j(X) = 0 \quad (j = 1 \div p) \end{aligned} \tag{B.2}$$

In this multi-objective problem, two solutions are compared to each other to decide whether a solution dominates the other. A solution F_1 dominates a solution F_2 (denoted as $F_1 \preceq F_2$) when both following conditions are satisfied (minimizing goals is being considered):

1. F_1 is smaller than or equal F_2 in all objectives.

2. F_1 is greater than F_2 in at least one objective.

If any of two above conditions is violated, solution F_1 is said not to dominate F_2. A set of solutions that there is no solution is dominated by any other one is called non-dominated pareto front. An example of dominance relationship and pareto front is demonstrated in Fig. B.1. In this example, a problem to minimize $F(X) = \{f_1(X), f_2(X)\}$ is considered. As it will be seen, point A dominates points E, D, C, and point B dominates only points E and D. Points A and B form the non-dominated pareto front even though points B and C are non-dominated solultions compared to each other but C is dominated by A, so it is removed from the pareto front.

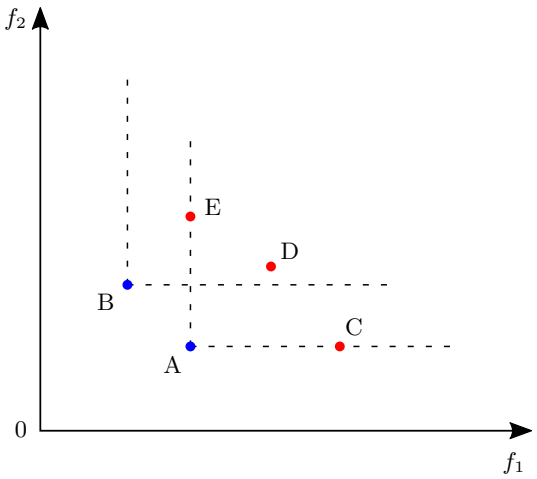

Fig. B.1: Non-dominated pareto front illustration

B.1 Non-dominated Sorting Genetic Algorithm (NSGA)-II

The NSGA-II proposed by authors of [99], this algorithm belongs to the evolutionary algorithm concept. It has been the most common algorithm to deal with multi-objective optimizations. This algorithm uses the elitism and crowded tournament selection. A non-dominated sorting approach with $O(mN^2)$ computational complexity is introduced, where m is the number of objectives and N is the population size.

Once the population is created, the non-dominated pareto front is extracted. This front will be replaced by individuals of the next generation. Each individual in each front are assigned with rank fitness values and the crowding distance between the individual and its neighbors. The crowding distance help to improve diversity in the population. The parents are selected from the population through the binary tournament. Only individual with better crowding distance are chosen to generate off-spring from crossover and mutation. The off-spring and current population are then combined for the next selection based on the rank and crowding

distance.

B.2 Multi-Objective Particle Swarm Optimization (MOPSO)

This optimization algorithm originated from the Particle Swarm Optimization (PSO), which was inspired on the choreography of a bird flock [100]. This algorithm is similar to a genetic algorithm in a manner that systems are initiated with a population of random solutions. Each individual is assigned its own velocity and location in each dimension. In search of the optimal solution through iterations, velocities, and locations of each individual are stochastically updated using the best solution it has achieved so far called p_{best} and the best global solution found by all individuals called g_{best}. The approach uses the concept of population and a measure of he performance similar to the fitness value used in the evolutionary algorithm. Also, the adjustments of individuals are analogous to the use of the crossover mutation. PSO algorithm allows individuals to benefit from their past experiences and also experiences of other individuals; therefore, this algorithm promotes a cooperative model rather than a competitive model as in the evolutionary algorithm.

B.3 Mathematical comparisons

Three bi-objective optimization problems will be tested to compare performance between the NSGA-II (codes from MATLAB central) and the MOPSO (codes by Judicael [92])

Problem 1: KUR:

$$\text{Minimize} = \begin{cases} f_1(x) = \sum_{i=1}^{2} \left[-10e^{\left(-0.2\sqrt{x_i^2+x_{i+1}^2}\right)} \right] \\ f_2(x) = \sum_{i=1}^{3} \left[|x_i|^{0.8} + 5\sin(x_i^3) \right] \end{cases} \tag{B.3}$$

with $-5 \leqslant x_i \leqslant 5$, $i = 1 \div 3$

Problem 2: ZDT3

$$\text{Minimize} = \begin{cases} f_1(x) = x_1 \\ f_2(x) = g(x) h\left(f_1(x), g(x)\right) \\ g(x) = 1 + \frac{9}{29} \sum_{i=2}^{30} x_i \\ h\left(f_1(x), g(x)\right) = 1 - \sqrt{\frac{f_1(x)}{g(x)}} - \frac{f_1(x)}{g(x)} \sin\left(10\pi f_1(x)\right) \end{cases} \tag{B.4}$$

with $0 \leqslant x_i \leqslant 1$, $i = 1 \div 30$

Problem 3: Binh and Korn function

$$\begin{aligned} \text{Minimize} &= \begin{cases} f_1(x) = 4x_1^2 + 4x_2^2 \\ f_2(x) = (x_1 - 5)^2 + (x_2 - 5)^2 \end{cases} \\ \text{s.t.} &\begin{cases} g_1(x) = (x_1 - 5)^2 + x_2^2 \leqslant 25 \\ g_2(x) = (x_1 - 8)^2 + (x_2 + 3)^2 \geqslant 7.7 \end{cases} \end{aligned} \tag{B.5}$$

with $0 \leqslant x_1 \leqslant 5$, $0 \leqslant x_2 \leqslant 3$

Problem 1 is straightforward since there is no constraint and the pareto front is continuous, problem 2 also does not have constraints but the number of variables much increases up to 30, also the pareto front is presented with several discontinuous regions. Problem 3 introduces constraints and the pareto front with a small region seems to be difficult to find solutions. These characteristics are observed in Fig. B.2.

Optimality and diversity are of two important criteria to evaluate the quality of a pareto front. The opimality is to indicate whether the pareto front converge to the true optimal pareto front. Meanwhile, the diversity is to evaluate the distribution of non-dominated solutions along the pareto front. A diversity quality examination was proposed by [101], which is pretty simple but useful to measure the distance variance of neighboring solutions in the pareto front defined as (B.6) with almost the same convergence quality even though there is explicit criterion for the proof.

$$\begin{aligned} SP &= \sqrt{\frac{1}{n-1}\sum_{i=1}^{n}\left(\bar{d} - d_i\right)^2} \\ \text{With:} \quad d_i &= \min_{i,j \neq i}\left(\sum_{k=1}^{K}|f_i^k - f_j^k|\right) \end{aligned} \tag{B.6}$$

where n is the number of solutions of the pareto front, K is the number of objectives, $\bar{d}$ is mean of all distance d_i, a small value of SP indicates better diversity of the pareto front. The comparison between the MOPSO and NSGA-II for three mentioned problems are shown in Table. B.1. Due to the stochastic nature of the algorithms, the optimizations are repeated 5 times for each algorithm. Also, different combinations of numbers of generations (n_g) and particles (individuals)(n_p) are tested. In the table, due to limited spaces, the MOPSO is shorted as PS (particle swarm) and NSGA-II is shorted as GA (genetic algorithm). The pareto front comparisons for a case of 50 generations and 50 particles are shown in Fig. B.2.

The average values of SP through runs are reported in Table. B.2

Several remarks on the diversity could be noted as follows:

- The MOPSO technique appears to be better when dealing with continuous pareto fronts as with the problem 1.

Table B.1: Pareto front diversity comparison with SP index for various cases

n_g & n_p	Problem	Run 1		Run 2		Run 3		Run 4		Run 5	
		PS	GA	PS	GA	PS	GA	PS	GA	PS	GA
20 & 20	1	0.40	1.48	0.38	2.34	0.35	1.86	0.43	1.53	0.55	1.71
	2	0.28	0.32	0.86	0.32	1.62	0.32	0.80	0.37	0.85	0.35
	3	0.14	0.04	0.13	0.09	0.06	0.06	0.10	0.08	0.06	0.15
50 & 20	1	0.35	2.07	0.39	1.90	0.21	1.53	0.35	1.72	0.19	1.43
	2	0.20	0.31	0.27	0.30	0.22	0.46	0.30	0.30	0.21	0.37
	3	0.11	0.06	0.11	0.06	0.06	0.06	0.08	0.06	0.03	0.04
20 & 50	1	0.27	0.34	0.26	0.44	0.25	0.52	0.25	0.53	0.24	0.51
	2	0.29	0.14	0.29	0.11	0.45	0.16	0.34	0.19	0.25	0.13
	3	0.07	0.04	0.07	0.06	0.06	0.04	0.05	0.04	0.10	0.08
50 & 50	1	0.16	0.43	0.16	0.42	0.16	0.47	0.15	0.42	0.18	0.47
	2	0.21	0.15	0.25	0.13	0.26	0.19	0.22	0.14	0.20	0.14
	3	0.07	0.01	0.05	0.01	0.06	0.01	0.05	0.01	0.09	0.01

Red color indications emphasize smaller values of PS compared to GA

Table B.2: Pareto front diversity comparison with mean SP index for various cases

n_g & n_p	Problem 1		Problem 2		Problem 3	
	PS	GA	PS	GA	PS	GA
20 & 20	0.42	1.78	0.88	0.34	0.10	0.08
50 & 20	0.30	1.73	0.24	0.35	0.08	0.06
20 & 50	0.25	0.47	0.32	0.15	0.07	0.05
50 & 50	0.16	0.44	0.23	0.15	0.07	0.01

- It is obvious that increasing numbers of iterations or particles make results more reliable, as seen with less variations of SP through runs. Through many other cases, a combination 50 generations and 50 particles are adopted as personal experience.
- With same numbers of function evaluations (same product $n_g \cdot n_p$), having more particles (number of generations decreases as the result) seems to bring better result since it is able to better explore the space.

These are some simple comparisons between two algorithms, in order to explore more obvious strength of one over the other, intensive comparisons should be accomplished. However, it goes far beyond the subject of this thesis. It is hard to explicitly conclude which one is better than the other even though the NSGA-II is generally accepted as the most common algorithm to handle muti-objective optimizations. Using any of them in engineering optimization problems could just be a matter of the designer's habit. That explains why MOPSO is used in this thesis as MOPSO was developed in SATIE.

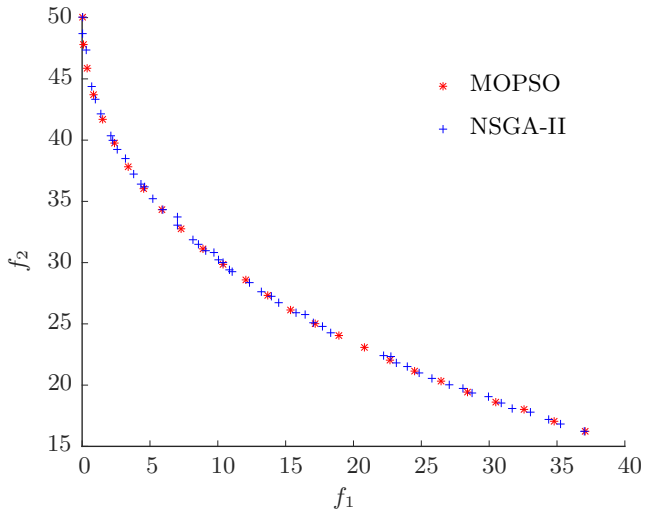

(a)

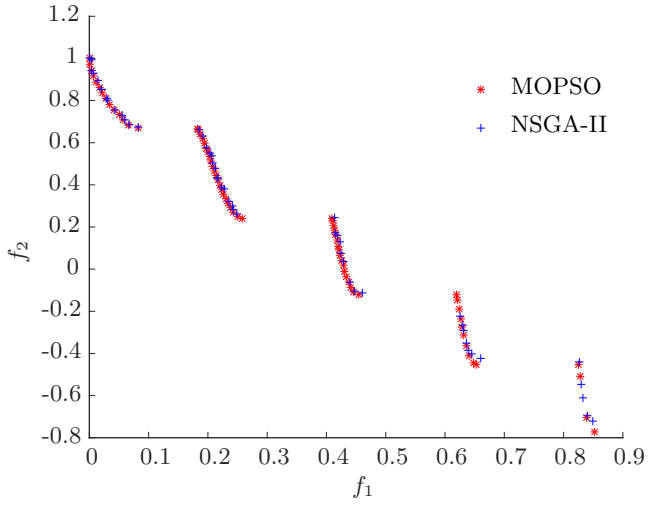

(b)

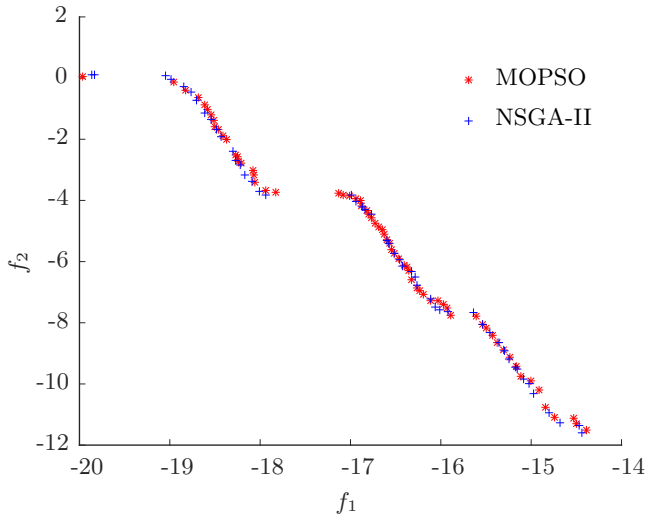

(c)

Fig. B.2: Optimal pareto front comparison between MOPSO and NSGA-II. a) Problem 1. b) Problem 2. c) Problem 3

References

[1] S. Kreuawan, F. Gillon, and P. Brochet, "Optimal design of permanent magnet motor using multidisciplinary design optimization," in *Electrical Machines, 2008. ICEM 2008. 18th International Conference on*, pp. 1–6, Sept 2008.

[2] E. Hoang, M. Lecrivain, S. Hlioui, and M. Gabsi, "Hybrid excitation synchronous permanent magnets synchronous machines optimally designed for hybrid and full electrical vehicle," in *Power Electronics and ECCE Asia (ICPE ECCE), 2011 IEEE 8th International Conference on*, pp. 153–160, May 2011.

[3] P. Lazari, J. Wang, and L. Chen, "A computationally efficient design technique for electric-vehicle traction machines," *IEEE Transactions on Industry Applications*, vol. 50, pp. 3203–3213, Sept 2014.

[4] A. J. Gillespie and H. lan Hayes, *Practical guide to railway engineering.* Arema, 2003.

[5] J. Rhodes, "Steam vs. diesel: A comparison of modern steam and diesel in the class I railroad environment." http://www.internationalsteam.co.uk/trains/newsteam/modern50.htm.

[6] J. Ghetiya, A. Paul, and G. R. Selokar, "Experimental studies on emission and performance of c.i engine with biodiesel and its blends," *Int. Journal of Computational Engineering Research*, vol. 2, pp. 106–113, Jan-Feb 2012.

[7] M. Kumar, B. Signh, and V. Jain, "Friction analysis and reduction in single sylinder four stroke diesel engine," *Int. journal of Emerging Research in Management & Technology*, vol. 2, pp. 1–8, Oct. 2013.

[8] H. I. Andrew, *Railway traction: the principle of mechanical and electrical railway traction.* Elsevier, 1986.

[9] Y. Bak, E. Lee, and K.-B. Lee, "Indirect matrix converter for hybrid electric vehicle application with three-phase and single-phase outputs," *Energies*, vol. 8, no. 5, p. 3849, 2015.

[10] J. Wang, Z. Yang, F. Lin, and J. Cao, "Harmonic loss analysis of the traction transformer of high-speed trains considering pantograph-ocs electrical contact properties," *Energies*, vol. 6, no. 11, p. 5826, 2013.

[11] S. Frey, *Railway electrification system and engineering.* White Word Publications, 2012.

[12] M. Zeraoulia, M. Benbouzid, and D. Diallo, "Electric motor drive selection issues for hev propulsion systems: A comparative study," *Vehicular Technology, IEEE Transactions on*, vol. 55, pp. 1756–1764, Nov 2006.

[13] R. Hill, "Electric railway traction. ii. traction drives with three-phase induction motors," *Power Engineering Journal*, vol. 8, pp. 143–152, June 1994.

[14] N. Hashemnia and B. Asaei, "Comparative study of using different electric motors in the electric vehicles," in *Electrical Machines, 2008. ICEM 2008. 18th International Conference on*, pp. 1–5, Sept 2008.

[15] R. Hill, "Dc and ac traction motors," in *Electric Traction Systems, 2006. The 9th Institution of Engineering and Technology Professional Development Course on*, pp. 33–52, Nov 2006.

[16] Y. Amara, L. Vido, M. Gabsi, E. Hoang, A. Hamid Ben Ahmed, and M. Lecrivain, "Hybrid excitation synchronous machines: Energy-efficient solution for vehicles propulsion," *Vehicular Technology, IEEE Transactions on*, vol. 58, pp. 2137–2149, Jun 2009.

[17] L. Vido, *Étude d'actionneurs électriques à double excitation destinés au transport, dimensionnement de structures synchrones.* Thèse, École normale supérieure de Cachan - ENS Cachan, 2004.

[18] Y. Amara, *Contribution à la conception et à la commande des machines synchrones à double excitation application au véhicule hybride.* Thèse, École normale supérieure de Cachan - ENS Cachan, Dec. 2001.

[19] L. Vido, Y. Amara, and M. Gabsi, "Machines synchrones à double excitation msde," *Techniques de l'ingénieur*, Février 2011.

[20] C. Syverson, "Hybrid alternator," Mar. 14 1995. US Patent 5,397,975.

[21] Y. Amara, J. Lucidarme, M. Gabsi, M. Lecrivain, A. Almed, and A. Akemakou, "A new topology of hybrid synchronous machine," *Industry Applications, IEEE Transactions on*, vol. 37, pp. 1273–1281, Sep 2001.

[22] J. Tapia, F. Leonardi, and T. Lipo, "Consequent-pole permanent-magnet machine with extended field-weakening capability," *Industry Applications, IEEE Transactions on*, vol. 39, pp. 1704–1709, Nov 2003.

[23] T. Radomski, "Alternating current generator," Sept. 25 1990. US Patent 4,959,577.

[24] D. Akemakou, "Dual excitation electrical machine, and especially motor vehicle alternator," Mar. 14 2000. US Patent 6,037,691.

[25] X. Luo and T. Lipo, "A synchronous/permanent magnet hybrid ac machine," *Energy Conversion, IEEE Transactions on*, vol. 15, pp. 203–210, Jun 2000.

[26] F. Liang and J. Miller, "Permanent magnet electric machine with flux control," Apr. 16 2002. US Patent 6,373,162.

[27] W. Geng, Z. Zhang, K. Jiang, and Y. Yan, "A new parallel hybrid excitation machine: Permanent-magnet/variable-reluctance machine with bidirectional field-regulating capability," *Industrial Electronics, IEEE Transactions on*, vol. 62, pp. 1372–1381, March 2015.

[28] D. Fodorean, A. Djerdir, I. A. Viorel, and A. Miraoui, "A double excited synchronous machine for direct drive application: Design and prototype tests," *Energy Conversion, IEEE Transactions on*, vol. 22, pp. 656–665, Sept 2007.

[29] E. Hoang, M. Lecrivain, and M. Gabsi, "A new structure of a switching flux synchronous polyphased machine with hybrid excitation," in *European Conference on Power Electronics and Applications*, pp. pp.1–8, Sept. 2007.

[30] L. Vido, M. Gabsi, M. Lecrivain, Y. Amara, and F. Chabot, "Homopolar and bipolar hybrid excitation synchronous machines," in *Electric Machines and Drives, 2005 IEEE International Conference on*, pp. 1212–1218, May 2005.

[31] B. Nedjar, S. Hlioui, Y. Amara, L. Vido, M. Gabsi, and M. Lecrivain, "A new parallel double excitation synchronous machine," *Magnetics, IEEE Transactions on*, vol. 47, pp. 2252–2260, Sept 2011.

[32] S. Jacobs, D. Hectors, F. Henrotte, M. Hafner, M. Herranz Gracia, K. Hameyer, P. Goes, D. R. Romera, E. Attrazic, and S. Paolinelli, "Magnetic material optimization for hybrid vehicle PMSM drives," in *International conference for inductive and electromagnetic components, INDUCTICA*, (Berlin, Germany), May 2009.

[33] S. Lukic and A. Emado, "Modeling of electric machines for automotive applications using efficiency maps," in *Electrical Insulation Conference and Electrical Manufacturing amp; Coil Winding Technology Conference, 2003. Proceedings*, pp. 543–550, Sept 2003.

[34] C. Chan, K. Chau, J. Jiang, W. Xia, M. Zhu, and R. Zhang, "Novel permanent magnet motor drives for electric vehicles," *Industrial Electronics, IEEE Transactions on*, vol. 43, pp. 331–339, Apr 1996.

[35] D. Fodorean, I.-A. Viorel, A. Djerdir, and A. Miraoui, "Performances for a synchronous machine with optimised efficiency while wide speed domain is attempted," *Electric Power Applications, IET*, vol. 2, pp. 64–70, Jan 2008.

[36] F. Biais and P. Langry, "Optimization of permanent magnet traction motor for electric vehicle," in *15th EVS*, Oct. 1998.

[37] Y. Amara, E. Hoang, M. Gabsi, M. Lecrivain, A. H. B. Ahmed, and S. Derou, "Measured performances of a new hybrid synchronous machine," *EPE Journal*, vol. 12, no. 4, pp. 42–50, 2002.

[38] Y. Amara, E. Hoang, M. Gabsi, M. Lecrivain, and A. H. B. Ahmed, "3d finite elements analysis of a hybrid synchronous machine," in *Proceeding of Electromotion*, vol. 2, pp. 385–390, June 2001.

[39] I. Hussain, *Electric and hybrid Vehicle design fundamentals*. CRC Press, 2011.

[40] J. R. H. Jr and T. J. E. Miller, *Design of brushless permanent magnet motors*. Oxford, U. K, 1994.

[41] J. Coulomb, "A methodology for the determination of global electromechanical quantities from a finite element analysis and its application to the evaluation of magnetic forces, torques and stiffness," *Magnetics, IEEE Transactions on*, vol. 19, pp. 2514–2519, Nov 1983.

[42] N. Sadowski, Y. Lefevre, M. Lajoie-Mazenc, and J. Cros, "Finite element torque calculation in electrical machines while considering the movement," *Magnetics, IEEE Transactions on*, vol. 28, pp. 1410–1413, Mar 1992.

[43] D. Howe and Z. Zhu, "The influence of finite element discretisation on the prediction of cogging torque in permanent magnet excited motors," *Magnetics, IEEE Transactions on*, vol. 28, pp. 1080–1083, Mar 1992.

[44] S. Salon, S. Bhatia, and D. Burow, "The convergence of flux density in the air gap of induction motors," *Magnetics, IEEE Transactions on*, vol. 32, pp. 4284–4286, Sep 1996.

[45] J. Zhang, M. Cheng, and W. Hua, "Calculation of cogging torque for stator interior permanent magnet machine," in *Electromagnetic Field Computation (CEFC), 2010 14th Biennial IEEE Conference on*, pp. 1–1, May 2010.

[46] M. Popescu, D. Dorrell, and M. McGilp, "Instantaneous electromagnetic torque/force estimation in electrical motors using the finite element method- a review," in *ICEM*, 2006.

[47] R. Deodhar, D. Staton, T. Jahns, and T. Miller, "Prediction of cogging torque using the flux-mmf diagram technique," in *Industry Applications Conference, 1995. Thirtieth IAS*

Annual Meeting, IAS '95., Conference Record of the 1995 IEEE, vol. 1, pp. 693–700 vol.1, Oct 1995.

[48] D. Staton, W. Soong, and T. Miller, "Unified theory of torque production in switched reluctance and synchronous reluctance motors," *Industry Applications, IEEE Transactions on*, vol. 31, pp. 329–337, Mar 1995.

[49] D. Staton, R. Deodhar, W. Soong, and T. Miller, "Torque prediction using the flux-mmf diagram in ac, dc, and reluctance motors," *Industry Applications, IEEE Transactions on*, vol. 32, pp. 180–188, Jan 1996.

[50] C. Cossar, M. Popescu, T. Miller, M. McGilp, and M. Olaru, "A general magnetic-energy-based torque estimator: Validation via a permanent-magnet motor drive," *Industry Applications, IEEE Transactions on*, vol. 44, pp. 1210–1217, July 2008.

[51] A. Parviainen, M. Niemela, and J. Pyrhonen, "Modeling of axial flux pm machines," in *Electric Machines and Drives Conference, 2003. IEMDC'03. IEEE International*, vol. 3, pp. 1955–1961 vol.3, June 2003.

[52] K. Tajima, K. Sato, T. Komukai, and O. Ichinokura, "Reluctance network analysis of an orthogonal-core type parametric induction motor," *Magnetics, IEEE Transactions on*, vol. 35, pp. 3706–3708, Sep 1999.

[53] K. Chau, M. Cheng, and C. Chan, "Nonlinear magnetic circuit analysis for a novel stator doubly fed doubly salient machine," *Magnetics, IEEE Transactions on*, vol. 38, pp. 2382–2384, Sep 2002.

[54] H. Polinder, J. Slootweg, M. Hoeijmakers, and J. Compter, "Modeling of a linear pm machine including magnetic saturation and end effects: maximum force-to-current ratio," *Industry Applications, IEEE Transactions on*, vol. 39, pp. 1681–1688, Nov 2003.

[55] B. Bekkouche, A. Chaouch, and Y. Mezari, "A switched reluctance motors analyse using permeance network method," *International Journal of Applied Engineering Research*, vol. 1, no. 2, pp. 137–152, 2006.

[56] K. Nakamura and O. Ichinokura, "Dynamic simulation of pm motor drive system based on reluctance network analysis," in *Power Electronics and Motion Control Conference, 2008. EPE-PEMC 2008. 13th*, pp. 758–762, Sept 2008.

[57] N. Bracikowski, M. Hecquet, P. Brochet, and S. Shirinskii, "Multiphysics modeling of a permanent magnet synchronous machine by using lumped models," *Industrial Electronics, IEEE Transactions on*, vol. 59, pp. 2426–2437, June 2012.

[58] H. Derbas, J. Williams, A. Koenig, and S. Pekarek, "A comparison of nodal- and mesh-based magnetic equivalent circuit models," *Energy Conversion, IEEE Transactions on*, vol. 24, pp. 388–396, June 2009.

[59] E. Ilhan, J. Paulides, L. Encica, and E. Lomonova, "Tooth contour method implementation for the flux-switching pm machines," in *Electrical Machines (ICEM), 2010 XIX International Conference on*, pp. 1–6, Sept 2010.

[60] V. Ostovic, *Dynamics of saturated machines*. Springer-Verlag, 1989.

[61] Z. Zhu, Y. Pang, D. Howe, S. Iwasaki, R. Deodhar, and A. Pride, "Analysis of electromagnetic performance of flux-switching permanent-magnet machines by nonlinear adaptive lumped parameter magnetic circuit model," *Magnetics, IEEE Transactions on*, vol. 41, pp. 4277–4287, Nov 2005.

[62] M. Bash, J. Williams, and S. Pekarek, "Incorporating motion in mesh-based magnetic equivalent circuits," *Energy Conversion, IEEE Transactions on*, vol. 25, pp. 329–338, June 2010.

[63] J. Perho, *Reluctance nework for analysing induction machines*. PhD thesis, Helsinki University of Technology, 2002.

[64] M. Amrhein and P. Krein, "Magnetic equivalent circuit modeling of induction machines design-oriented approach with extension to 3-d," in *Electric Machines Drives Conference, 2007. IEMDC '07. IEEE International*, vol. 2, pp. 1557–1563, May 2007.

[65] D. Gomez, A. Rodriguez, I. Villar, A. Lopez-de Heredia, I. Etxeberria-Otadui, and Z. Zhu, "Improved permeance network model for embedded magnet synchronous machines," in *Electrical Machines (ICEM), 2014 International Conference on*, pp. 1231–1237, Sept 2014.

[66] F. Trutt, E. Erdelyi, and R. Hopkins, "Representation of the magnetization characteristic of dc machines for computer use," *Power Apparatus and Systems, IEEE Transactions on*, vol. PAS-87, pp. 665–669, March 1968.

[67] J. Rivas, J. Zamarro, E. Martin, and C. Pereira, "Simple approximation for magnetization curves and hysteresis loops," *Magnetics, IEEE Transactions on*, vol. 17, pp. 1498–1502, Jul 1981.

[68] L. Rayleigh, "The behaviour of iron and steel under the operation of feeble magnetic force," *Phil. Mag.*, vol. 23, pp. 225–245, 1887.

[69] P. Weiss and R. Forrer, "Loi d'approche a la saturation," *Ann. Phys.*, vol. 12, pp. 279–374, 1929.

[70] J. Cale, S. Sudhoff, and J. Turner, "An improved magnetic characterization method for highly permeable materials," *Magnetics, IEEE Transactions on*, vol. 42, pp. 1974–1981, Aug 2006.

[71] A. Ben-Israel, "A newton-raphson method for the solution of systems of equations," *Journal of Mathematical Analysis and Applications*, vol. 15, no. 2, pp. 243 – 252, 1966.

[72] C. Steinmetz, "On the law of hysteresis," *Proceedings of the IEEE*, vol. 72, pp. 197–221, Feb 1984.

[73] J. Reinert, A. Brockmeyer, and R. De Doncker, "Calculation of losses in ferro- and ferrimagnetic materials based on the modified steinmetz equation," *Industry Applications, IEEE Transactions on*, vol. 37, pp. 1055–1061, Jul 2001.

[74] G. Bertotti, "General properties of power losses in soft ferromagnetic materials," *Magnetics, IEEE Transactions on*, vol. 24, pp. 621–630, Jan 1988.

[75] D. Lin, P. Zhou, W. Fu, Z. Badics, and Z. Cendes, "A dynamic core loss model for soft ferromagnetic and power ferrite materials in transient finite element analysis," *Magnetics, IEEE Transactions on*, vol. 40, pp. 1318–1321, March 2004.

[76] E. Hoang, *Étude, modélisation et mesure des pertes magnétiques dans les moteurs à réluctance variable à double saillance.* Thèse, École normale supérieure de Cachan - ENS Cachan, Dec. 1995.

[77] J. Lavers, P. Biringer, and H. Hollitscher, "A simple method of estimating the minor loop hysteresis loss in thin laminations," *Magnetics, IEEE Transactions on*, vol. 14, pp. 386–388, Sep 1978.

[78] C. Hernandez-Aramburo, T. Green, and S. Smith, "Assessment of power losses of an inverter-driven induction machine with its experimental validation," *Industry Applications, IEEE Transactions on*, vol. 39, pp. 994–1004, July 2003.

[79] C. Simao, N. Sadowski, N. Batistela, and J. Bastos, "Evaluation of hysteresis losses in iron sheets under dc-biased inductions," *Magnetics, IEEE Transactions on*, vol. 45, pp. 1158–1161, March 2009.

[80] S. K. Mukerji, M. George, and M. B. Ramamurthy, "Eddy ccurrent in ssolid rectangular cores," *Progress in Electromagnetics Research B*, vol. 7, pp. 117–131, 2008.

[81] A. Boglietti, A. Cavagnino, D. Staton, M. Shanel, M. Mueller, and C. Mejuto, "Evolution and modern approaches for thermal analysis of electrical machines," *Industrial Electronics, IEEE Transactions on*, vol. 56, pp. 871–882, March 2009.

[82] J. E. Vrancik, "Prediction of windage power loss in alternators," tech. rep., NASA, October 1968.

[83] SKF. http://www.skf.com.

[84] P. Mellor, D. Roberts, and D. Turner, "Lumped parameter thermal model for electrical machines of tefc design," *Electric Power Applications, IEE Proceedings B*, vol. 138, pp. 205–218, Sep 1991.

[85] A. Boglietti, A. Cavagnino, M. Lazzari, and M. Pastorelli, "A simplified thermal model for variable-speed self-cooled industrial induction motor," *Industry Applications, IEEE Transactions on*, vol. 39, pp. 945–952, July 2003.

[86] P. H. Mellor and D. R. Turner, "Real time prediction of temperatures in an induction motor using a microprocessor," *Electric Machines and Power Systems*, vol. 15, no. 4-5, pp. 333–352, 1988.

[87] Y. Çengel and A. Ghajar, *Heat and Mass Transfer: Fundamentals and Applications*. McGraw-Hill, 2011.

[88] G. I. Taylor, "Distribution of velocity and temperature between concentric cylinders," in *Proc. Roy. Soc*, pp. 546–578, 1935.

[89] C. Gazley, "Heat transfer characteristic of rotating and axial flow between concentric cylinder," *Trans. ASME*, pp. 79–89, 1958.

[90] D. Staton, A. Boglietti, and A. Cavagnino, "Solving the more difficult aspects of electric motor thermal analysis in small and medium size industrial induction motors," *Energy Conversion, IEEE Transactions on*, vol. 20, pp. 620–628, Sept 2005.

[91] S. Kreuawan, F. Gillon, F. Moussouni, S. Brisset, and P. Brochet, "Optimal design of traction motor in railway propulsion system," in *Electrical Machines and Power Electronics, 2007. ACEMP '07. International Aegean Conference on*, pp. 343–348, Sept 2007.

[92] J. Aubry, H. B. Ahmed, and B. Multon, "Bi-objective sizing optimization of a pm machine drive on an operating profile," in *Electrical Machines (ICEM), 2010 XIX International Conference on*, pp. 1–7, Sept 2010.

[93] J. Aubry, *Optimisation du dimensionnement d'une chaîne de conversion électrique directe incluant un système de lissage de production par supercondensateurs. Application au houlogénérateur SEAREV*. Thèse, École normale supérieure de Cachan - ENS Cachan, Nov. 2011.

[94] A. Saxena, "Performance and cost comparison of pm bldc motors for ceiling fan," in *Power Electronics, Drives and Energy Systems (PEDES), 2014 IEEE International Conference on*, pp. 1–5, Dec 2014.

[95] M. Bierhoff and F. Fuchs, "Semiconductor losses in voltage source and current source igbt converters based on analytical derivation," in *Power Electronics Specialists Conference, 2004. PESC 04. 2004 IEEE 35th Annual*, vol. 4, pp. 2836–2842, 2004.

[96] M. Ned, U. T. M., and R. W. P., *Power electronics: converters, applications, and design*. John Wiley & Sons, 2003.

[97] D. Graovac and M. Purschel, "Igbt power losses calculation using the data-sheet parameters." Infineon application note, January 2009.

[98] J. V. Gragger, A. Haumer, and M. Einhorn, "Averaged model of a buck converter for efficiency analysis." Engineering letters, 2010.

[99] K. Deb, A. Pratap, S. Agarwal, and T. Meyarivan, "A fast and elitist multiobjective genetic algorithm: Nsga-ii," *IEEE Transactions on Evolutionary Computation*, vol. 6, pp. 182–197, Apr 2002.

[100] R. Eberhart and Y. Shi, "Particle swarm optimization: developments, applications and resources," in *Evolutionary Computation, 2001. Proceedings of the 2001 Congress on*, vol. 1, pp. 81–86 vol. 1, 2001.

[101] J. R. Schott, "Faults tolerant design using single and multicrimulti genetic algorithm optimization," Master's thesis, Massachusetts Institute of Technology, 1995.